Structure and Reactivity Correlations of

High-valent Manganese and Cobalt Complexes

By

Yuri Lee

Submitted to the graduate degree program in Chemistry and the Graduate Faculty of the University of Kansas in partial fulfillment of the requirements for the degree of Doctor of Philosophy.

_____

Chairperson: Dr. Timothy A. Jackson

_____

Dr. Mikhail V. Barybin

_____

Dr. James D. Blakemore

_____

Dr. Cindy L. Berrie

_____

Dr. Prajnaparamita Dhar

Date Defended: November 19, 2021

The Dissertation Committee for Yuri Lee
certifies that this is the approved version of the following dissertation:

Structure and Reactivity Correlations of High-valent Manganese and Cobalt Complexes

_____

Chairperson: Dr. Timothy A. Jackson

Date approved: December 16, 2021

Abstract

Earth-abundant transition metals have attracted a great attention for decades due to their versatile nature that enables them to carry out a variety of reactions in metalloenzymes. Accordingly, various model systems have been developed to investigate reactivities of earth-abundant transition metals in different platforms, towards the pursuit of efficient catalysts in industrial applications. Although there are well-established structure-reactivity relationships for a couple of earth-abundant transition metals, more information is needed to better understand their reactivities and design selective metal catalysts with earth-abundant transition metals. Therefore, recent developments as well as experimental and theoretical results on structure-reactivity relationships of high-valent manganese and cobalt model complexes are delivered in this dissertation.

Formation, characterization, and reactivity investigations on high-valent bis(μ-oxo)dimanganese complexes and mononuclear manganese oxo complexes were investigated. Equatorial ligand field effects on O–H bond activation reactivity of $Mn^{III}Mn^{IV}(\mu\text{-}O)_2$ complexes were studied. Two mononuclear species, $[Mn^{II}(OTf)(N4py)](OTf)$ and $[Mn^{II}(OTf)(^{DMM}N4py)](OTf)$, were used to prepare $[Mn^{III}Mn^{IV}(\mu\text{-}O)_2(N4py)_2]^{3+}$ and $[Mn^{III}Mn^{IV}(\mu\text{-}O)_2(^{DMM}N4py)_2]^{3+}$, respectively, with H_2O_2 and a base. Structural features are compared between the two bis(μ-oxo)dimanganese complexes, which are nearly identical. Reduction potentials of the two bis(μ-oxo)dimanganese complexes are also comparable. Reactivity studies towards O–H bond activation with the two bis(μ-oxo)dimanganese complexes show marginal differences, presumably due to the divided equatorial ligand field effects by the bis(μ-oxo) bridge. Formation of a high-valent Mn^{IV}-oxo species was explored using $[Mn^{II}(OTf)(^{DMM}N4py)](OTf)$, different amounts of ceric(IV) ammonium nitrate (CAN), and water

in acetonitrile. Upon the addition of 2 equiv. CAN to $[Mn^{II}(OTf)(^{DMM}N4py)](OTf)$, a broad near-IR band was instantly shown, which is a characteristic feature of $[Mn^{IV}(O)(^{DMM}N4py)]^{2+}$. This intermediate decayed to $[Mn^{III}Mn^{IV}(\mu\text{-}O)_2(^{DMM}N4py)_2]^{3+}$ (at room temperature) or $[Mn^{IV}Mn^{IV}(\mu\text{-}O)_2(^{DMM}N4py)_2]^{3+}$ (at 0 °C). Addition of 4 equiv. CAN to $[Mn^{II}(OTf)(^{DMM}N4py)](OTf)$ also generates a broad near-IR band; however, the intermediate decays to a new chromophore, which might be a Ce^{IV}-bound Mn^{IV}-oxo complex. Additional experiments are needed to further characterize this new chromophore. Two novel mononuclear Mn^{II} complexes were prepared to examine equatorial ligand field effects within a wide range of the ligand field strength. The C–H bond activation reactivity of $[Mn^{IV}(O)(N3pyQ)]^{2+}$ follows an oxidative reactivity trend that shows a linear correlation between the reactivity and equatorial ligand field strength.

The oxidation state and electronic structure of a high-valent cobalt complex, $[Co^{IV}(ONO_2)_2(NNN)]$, was studied using electron paramagnetic resonance (EPR) and computational methods. This high-valent cobalt complex shows an unusual high spin density at the Co center. The results of single- and multireference computations suggest that the unpaired electron is located at d_z^2 orbital, which may facilitate concerted proton-electron transfer (CPET) reactions between $[Co^{IV}(ONO_2)_2(NNN)]$ and substrates. Transition state (TS) structures with different proton accepting oxygens on the nitrate ligands were computationally investigated. Calculated activation parameters from those TSs are comparable to the experimental values for ethylbenzene oxidation reaction. However, a notable deviation was observed between experimental and calculated activation parameters for 9,10-dihydroanthracene (DHA) oxidation reaction. Preliminary multireference calculation data show more features of each transition state, which provides insight to propose the most probable TS for the oxidation reactions of $[Co^{IV}(ONO_2)_2(NNN)]$ and substrates.

Acknowledgements

First, I would like to thank my research advisor and mentor, Professor Tim Jackson. I cannot think of any words that properly describe how grateful I have been to learn many aspects of chemistry and beyond that from you. You have taught me bioinorganic chemistry, (very challenging) spectroscopic techniques, computational methods, and a lot more; however, beyond those your drive and passion to excellence have been inspiring me to be a better researcher with your thoughtful guidance. I am also very thankful for the research opportunity in the Nordlander group at Lund University in Sweden, which helps me do much better at ligand synthesis. I will keep all that I learned from you in mind and be always proud of myself to have you as my Ph.D. mentor and have been a member of your group.

I would like to thank all my committee members. Professor Misha Barybin, thank you for allowing me to attend your class a couple of times and helping me find job opportunities as an international student. Professor James Blakemore, thank you for your lectures and assignments that helped me learn a lot about inorganic chemistry and electrochemistry. My special thanks to Professor Barybin and Professor Blakemore for their serving on my research committee and offering me any help in research when I needed. I also want to thank Professor Cindy Berrie and Professor Prajnaparamita Dhar for serving on my dissertation defense committee. Dr. Justin Douglas, thank you for helping me run EPR samples and many times of trouble shooting. Dr. Victor Day, thank you for solving a crystal structure and answering all the questions I had.

Professor Ebbe Nordlander, I appreciate you for your kind invitation to Lund and allowing me to work in your lab for three months. I am very grateful for my time at Lund University while learning ligand synthesis and working with your group members. Dr. Reena Singh, thank you

teaching me ligand synthesis and related chemistry. I became a better scientist while going through the time working with you. Dr. Ahibur Rahaman and Dr. Kamal Hossain, thank you for your hospitality when I started working in the group. Chuanshuai, Abishek, Yong, Jessica, Hasn, and Ida, I enjoyed working with all of you in lab. Stefan, we became good friends so fast! Thank you for helping me in a lot of ways and making a great time in Malmö. Yesol, you are an amazing friend, and I am blessed to meet you in Lund. Thank you for sharing such great memories together! I will keep praying for your wonderful adventures in Sweden.

I must thank all the past and current Jackson group members. Allyssa, thank you for teaching me experimental skills in lab and helping me in my first project, even though you were very busy with writing. Derek, thank you for teaching me a lot of English and helping me with computations. I hope you, Allyssa, and I have another trip together for good waffles in the future. Melissa, I don't think I could make my Ph.D. progress this far without you. Thank you for your unwavering support inside and outside the lab. I will go see you whichever city you will move to. Josh, thank you for helping me throughout my orals exam and making a good XAS trip when it was my first time at the beam line. Abraham, my dear friend, I already miss your singing and giggling in our office. Thank you for being such a faithful person and encouraging me a lot of times. Jaycee, thank you for the help whenever I needed to stab for EPR experiments. Also, I will keep the HEY Y'ALL mug wherever I go. Liz, thank you for helping me so many times in lab with so many things. You will be a great senior in Jackson group as you already are. Priya, thank you for lending me your KU ID card for a number of times. Let me know when you are going to Japan. Sam (Crowell), thank you for sharing a lot of delicious cupcakes, blondies, pies, etc. I will miss those a lot. Sam (Brunclik), I wish all the best for your research in Jackson group. Shannon

and Ellie, I appreciate our time in lab. Thank you for being great undergrad researchers with good vibes. Javier, you have just one more year to go! I wish all my best in your endeavors.

I am blessed to have great friends in the chemistry department. Amit, it was my best decision during the orientation week to go say hi to you and other friends. Thank you for a million times for being such a great friend and being there whenever I needed someone to talk to. I pray for you to publish a lot of fantastic works during the postdoc years. Shrikant, thank you for all the encouragement with your wonderful smile! I wish you my best for your research. Pasha, we had a great time crashing inorganic chemistry! Thank you for being a good friend and I hope you achieve fruitful works during your postdoc. Galina, I will never forget the time I stayed in your place. Thank you for the help and I hope you have a wonderful adventure ahead! Nate, thank you for being a good friend, helping me during my orals exam, letting me borrow chemicals, and so many more.

To my friends outside the department, I appreciate all fellowships I have through Bridges International. Cliff and Connie, Kali and Matheus, Alison and Jake, Greg, Misun, June, thank you so much for your prayers and all the encouragement. Tianlu and Chen, I appreciate you for everything and the great time we spent together. You were great housemates! Kui, we have so many memories together and I really appreciate all your supports and sincere friendship. Thank you for being there whenever I need a person to talk and praying with me. Andy, I appreciate you for coming to Kansas to spend some time with me. It was great! Thank you for being so patient, understanding me so many times, and supporting me with prayers. I am very excited to see you soon!

To my dear friends in Korea, Anna, Sara, Young-Eun, Hee-Kyung, Gippeum, Hyo-Sun, Ji-Yeon, Jin-Young, thank you for your friendship and supports. Sunny, you would not know how much I appreciate you for so many things. I was able to start my Ph.D. adventure as you helped me along the way. I will keep you in my prayers always and wish you my best for your new adventure ahead. I am sure you will do great!

To my dear family, Mom and Dad, thank you for your never-ending prayers and supports in all aspects of my life. I was able to come this far because of your love and support. I am so blessed to have you as my parents, and I am always proud to be your daughter. Brother, you are an awesome brother I could ever ask for. Thank you for always being there for me and supporting me in a lot of ways.

God, I am indebted for your love and blessings. Thank you for guiding me to this far, and now I am ready to start another journey with you.

Table of Contents

Abbreviations and Acronyms

Abs	absorption
BDFE	bond dissociation free energy
CH_2Cl_2	dichloromethane
CV	cyclic voltammetry
DFT	density functional theory
DHA	9,10-dihydroanthracene
EPR	electron paramagnetic resonance
ESI-MS	electrospray ionization mass spectrometry
EtBn	ethyl benzene
EtOAc	ethyl acetate
EXAFS	extended X-ray absorption fine structure
HAT	hydrogen atom transfer
HOTf	triflic acid
mCPBA	*meta*-chloroperoxybenzoic acid
MeCN	acetonitrile
Mn-RNR	manganese ribonucleotide reductase
NMR	nuclear magnetic resonance
OEC	oxygen evolving center
PhIO	iodosylbenzene
PSII	Photosystem II
SSRL	Stanford Synchrotron Radiation Lightsource
TD-DFT	time dependent density functional theory
TFE	2,2,2-trifluoroethanol
UV-Vis	ultraviolet-visible
XANES	X-ray absorption near-edge structure
XAS	X-ray absorption spectroscopy
XRD	X-ray diffraction

Chapter 1

High-valent Manganese and Cobalt Intermediates in Catalysis

1.1 Earth Abundant Transition metals in Catalysis

Catalysis is a process that increases a rate of a chemical reaction to reduce the time that takes to complete the reaction.[1] As in the oxidation of water to evolve dioxygen (O_2) or reduction of dinitrogen (N_2) to generate ammonia, catalytic reactions are occurring prevalently to maintain the fundamental part of life. In nature, most catalytic reactions take place through enzymes under benign conditions. To perform catalytic reactions under mild conditions, one of the strategies nature uses is implementing transition metals as cofactors in the active sites of enzymes, as depicted in Figure 1.1.[2, 3]

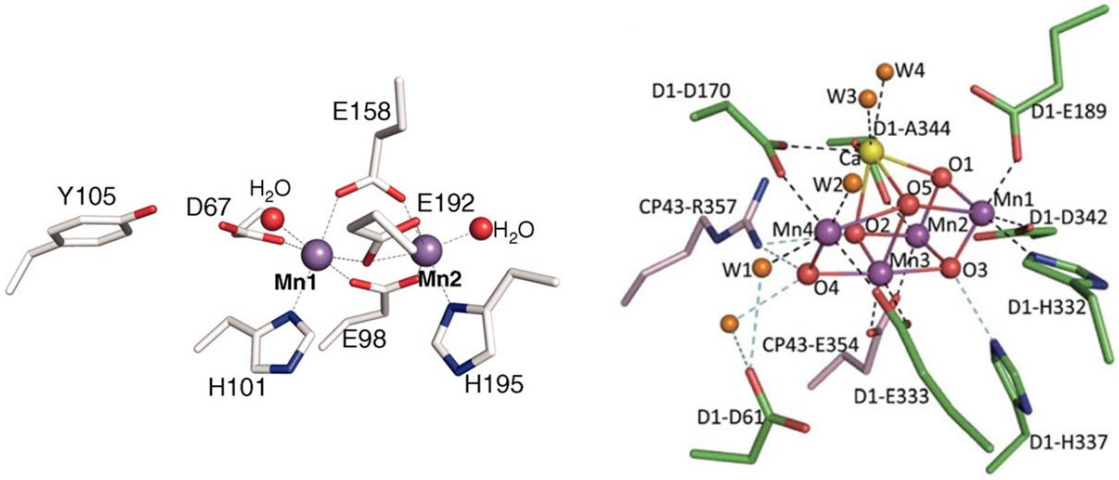

Figure 1.1. An active site XRD structures of Class Ib manganese ribonucleotide reductase as modeled by Boal *et al.* from ref. 2 (left) and oxygen evolving complex in photosystem II reported by Umena *et al.* from ref. 3 (right). Each structure shows the coordination sphere of the manganese ions. Reprinted with permissions from AAAS and Springer Nature.

These transition metals found in active sites of enzymes are mostly earth-abundant metals, including most of the first row transition metals and several early second and third row transition metals.[4] These findings reflect the redox reactivities of earth-abundant transition metals by

changing oxidation state readily.[5] Further, they show adequately tuned reactivities from the combinations of various factors including electronic structure, second coordination sphere effects, and thermodynamics.[4]

Likewise, researchers have developed a variety of synthetic catalysts to achieve demanding reactions in a timely manner under benign conditions using earth-abundant, 3d transition metals. Oxidative C–H bond functionalization is one of the research areas of investigating synthetic catalysts with 3d transition metals in purpose of synthesizing pharmaceuticals, chemical building blocks, and bioactive compounds.[6] Specifically, a substantial amount of efforts have been invested in high-valent transition-metal oxo species to accomplish selective C–H bond activation reactions. High-valent transition metal oxo units, either terminal or bridged forms, are prevalent in metallocofactors in nature.[7] Therefore, by studying and adapting imperative factors that affect reactivities of these core units selective C–H bond activation becomes possible even under mild and sustainable conditions, as the way nature does.[8]

The chemistry of high-valent 3d transition metal oxo complexes are divergent, interestingly, based on their intrinsic electronic structures. Several theoretical studies published recently support inherently different reactivities among the 3d transition-metal oxo species. Miliordos and Claveau studied differences in electronic structure of dicationic oxides (MO^{2+} unit) with first row transition metals by multireference computations.[9] In their calculations numerical data are reported from recalculating the potential energy curves (PECs) at equilibrium with quintuple-ζ basis sets. It is proposed that the first row transition metals can be categorized in three different groups based on their calculated ground states. First, TiO^{2+}, VO^{2+}, and CrO^{2+} feature stable oxo ground states (O^{2-}). For MnO^{2+} and FeO^{2+}, oxyl ground states ($O^{\bullet-}$) are shown in longer bond lengths between metal and oxygen, as well as low-lying excited states with an oxo character. Lastly, oxyl ground states

are computed for CoO^{2+}, NiO^{2+}, and CuO^{2+}. The differences in the ground state among the first row transition metals are also observed in molecular orbitals (MOs) of MO^{2+} systems (Figure 1.2). In this figure MOs of TiO^{2+} and NiO^{2+} represent MOs for MO^{2+} with early and late transition metals, respectively. The σ and π orbitals and σ* and π* orbitals in the figure show opposite features in directions that the orbitals are polarized. Additionally, these categories correspond well with experimental observations that tetragonal oxo complexes are frequently reported with 3d transition metals up to group 8. In metal complexes these intrinsic ground states become affected by ligand field strength and geometry-imposed steric hindrance, which are potent ways to tune the reactivity and selectivity of transition metal oxo species.

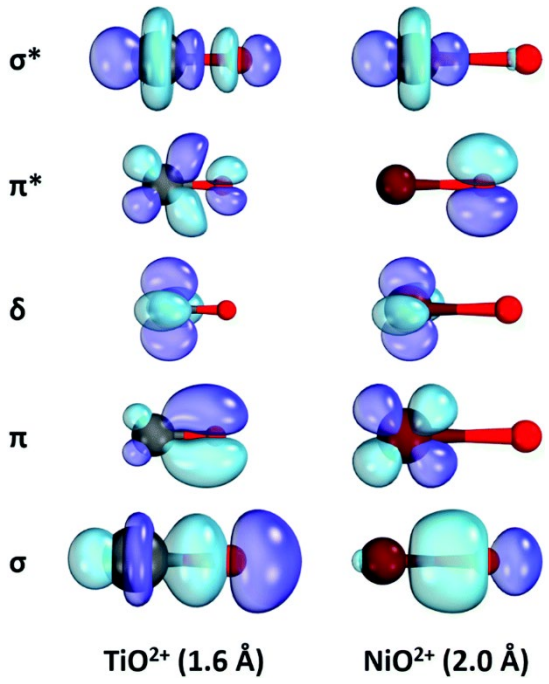

Figure 1.2. Representative molecular orbitals (MOs) at equilibrium showing differences between early and late MO^{2+} units, TiO^{2+} and NiO^{2+}, respectively, reported by Claveau and Miliordos from ref. 9. The MOs are taken at the bond distances indicated at the bottom of the corresponding MOs. Reproduced from ref. 9 with permission from the Royal Society of Chemistry.

Another theoretical study by Nam and co-workers describes reactivity patterns of several 3d transition-metal oxo complexes towards C–H bond cleavage related to their electronic properties.[10] Using a series of $[M^{IV}(O)(N4py)]^{2+}$ (M = Mn, Fe, Co, and Ni; N4py = *N*,*N*-bis(2-pyridylmethyl)-*N*-bis(2-pyridyl)methylamine), the authors compare early (Mn^{IV} and Fe^{IV}) and late (Co^{IV} and Ni^{IV}) transition metal oxo complexes regarding the M–O bond orders and bond dissociation enthalpies (BDEs), as well as spin densities on M and O atoms. Among the species, Co^{IV} and Ni^{IV} complexes show weaker M–O bonds and higher spin densities on O atom. Correspondingly, these two complexes display significantly higher cyclohexane oxidation reactivity determined by the calculated energies of activation barrier for each complex (9.3 and 4.3 kcal mol^{-1}, respectively). Additionally, the BDE for the O–H bond of $[M^{III}(OH)(N4py)]^{2+}$ is calculated as 92.0, 92.1, 110.6, and 112.8 kcal mol^{-1} for the corresponding Mn, Fe, Co, and Ni species, which supports higher reactivities of the Co^{IV} and Ni^{IV} complexes due to their larger driving forces. Based on these studies, there is much room to investigate high-valent 3d transition metals with respect to their intrinsic electronic structures to devise and design sustainable catalysts that can be used to perform demanding reactions involved with a wide range of the BDE values of substrates.

1.2 Bioinspired Synthetic Bis(μ-oxo)dimanganese Complexes

Manganese is the third most abundant transition metal among 3d transition metals. It is found often as multinuclear cofactors in multiple enzymes in nature.[11, 12] A number of bis(μ-oxo)dimanganese complexes have been synthesized as structural and functional models to investigate the mechanisms of several enzymes of interest. Representatives of these enzymes are

the oxygen evolving complex (OEC) in photosystem II (PSII) and manganese catalase.[13-15] The former enzyme takes water to evolve molecular oxygen under mild conditions and the latter enzyme converts hydrogen peroxide to water and molecular oxygen. Accordingly, a large amount of attention has been paid to proton-coupled electron transfer (PCET) reactivity of synthetic dimanganese species to reveal reasons of the abundance and prevalence of this metal in multinuclear structures in nature.[16-18] An important example of PCET process by dimanganese species includes the PCET process at the initial step to generate a tyrosyl radical in ribonucleotide reductases (RNRs) to reduce ribonucleotides to deoxyribonucleotides for DNA repair and replication.[16, 19, 20] Consequently, experimental results of the PCET reactivity of dimanganese species based on their structural features can provide knowledge to better understand specific roles of the dimanganese intermediate in the radical generation process.

A couple of studies were conducted to investigate PCET reactivity of bis(μ-oxo)dimanganese complexes with organic substrates. Mayer *et al.* inspected thermodynamic contributions for PCET reactivity of $[Mn^{III}Mn^{IV}(\mu\text{-}O)_2(phen)_4]^{3+}$ by measuring reduction potential and pK_a of the complex (Figure 1.3A). The authors reported mechanistic deviations, including electron, hydrogen, and hydride transfers, depending on the redox potentials (−0.03 ~ +0.90 V vs. $Fc^{+/0}$) and pK_as (11.5 ~ 14.6) of the complexes with different oxidation states due to intrinsic barriers of each PCET process (Figure 1.3B).

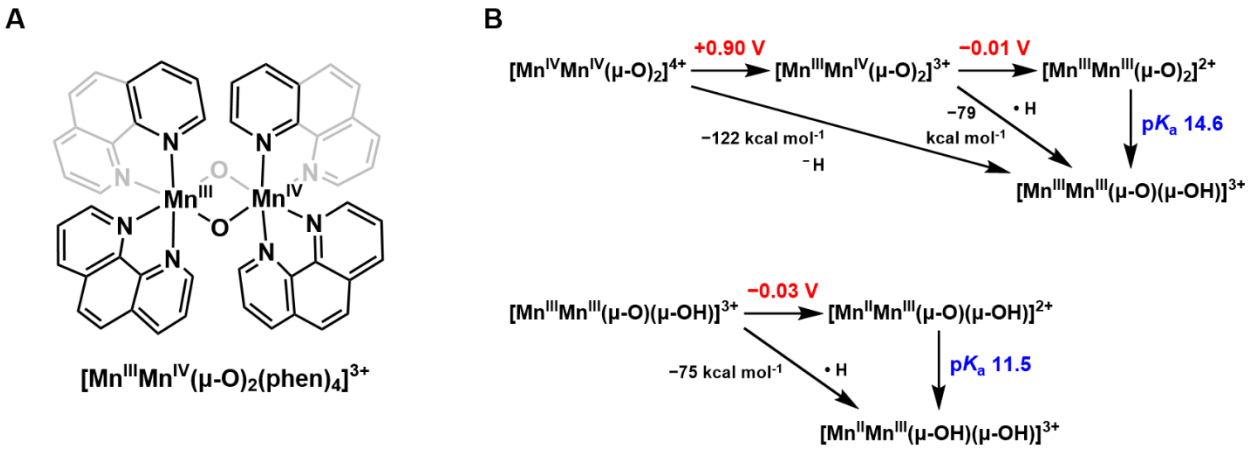

Figure 1.3. Structure of $[Mn^{III}Mn^{IV}(\mu\text{-}O)_2(phen)_4]^{3+}$ (A) and reduction potentials (vs. $Fc^{+/0}$), pK_a values, and thermodynamic affinity values related to reduced and/ or protonated bis(μ-oxo)dimanganese complexes from $[Mn^{IV}Mn^{IV}(\mu\text{-}O)_2(phen)_4]^{3+}$ (B).

Prior to the study described above Brudvig, Crabtree, and co-workers investigated the multiple proton-coupled electron transfers with the same dimanganese system by electrochemistry in aqueous solvent.[21, 22] This complex, $[Mn^{III}Mn^{IV}(\mu\text{-}O)_2(phen)_4]^{3+}$, shows two reversible protonation processes, and each protonation occurring upon one e^- reduction. They compared the results among other bis(μ-oxo)dimanganese(III,IV) species with different ligands (Figure 1.4A, B), and a pH-dependent proton-electron coupled transfer or kinetically proton-electron decoupled transfer is shown from other bis(μ-oxo)dimanganese(III,IV) systems (Figure 1.4C). The authors contributed these differences to the pK_a of oxo bridge in each system, which is also related to the ligand properties. Specifically, contrary to $[Mn^{III}Mn^{IV}(\mu\text{-}O)_2(phen)_4]^{3+}$ which shows two reversible proton and electron transfers, $[Mn^{III}Mn^{IV}(\mu\text{-}O)_2(bpy)_4]^{3+}$ did not form $[Mn^{II}Mn^{III}(\mu\text{-}OH)_2(bpy)_4]^{3+}$ due to the higher pK_a of its oxo bridge (pK_a = 11.0 was reported for $[Mn^{III}Mn^{III}(\mu\text{-}O)(\mu\text{-}OH)(bpy)_4]^{3+}$).[23] If p$K_a$ of an oxo bridge is relatively low (pK_a = 8.35 was reported for $[Mn^{III}Mn^{III}(\mu\text{-}O)(\mu\text{-}OH)(bispicen)_4]^{3+}$),[22] there is no proton-electron coupled transfer (Figure

1.4C). Together, this study signifies the effects of ligand properties on PCET reactivities of bis(μ-oxo)dimanganese(III,IV) species, which affects basicity of the oxo bridges.

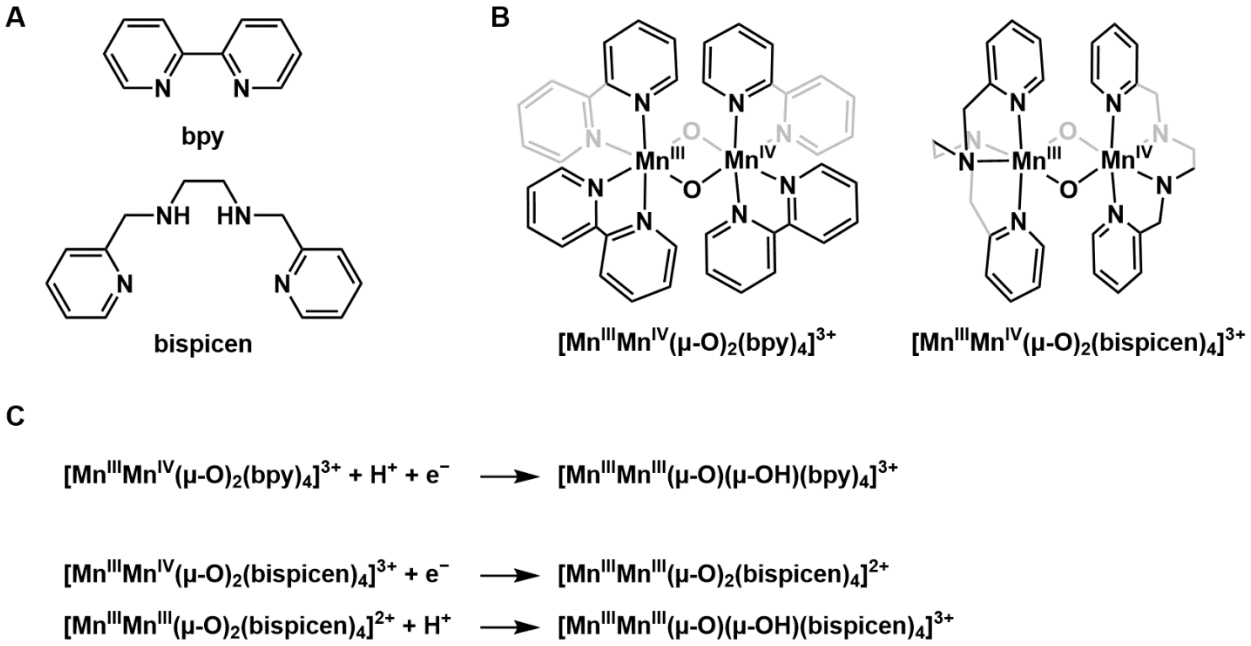

Figure 1.4. Structures of ligands (A) and dimanganese complexes (B). Proton-electron coupled and decoupled transfers occurring with the corresponding bis(μ-oxo)dimanganese(III,IV) systems (C).

Reactivities towards C–H bond oxidation had been studied using bis(μ-oxo)dimanganese complexes with different ligand scaffolds. One of the well-designed studies is using $[Mn^{IV}Mn^{IV}(\mu\text{-}O)_2(OH_2)_2(L)_2](NO_3)_4$ (see Figure 1.5A for the structure of L) by Crabtree, Brudvig, and co-workers.[24] This complex shows catalytic oxidizing ability towards the C–H bonds of ibuprofen and (4-methylcyclohexyl)acetic acid in a regioselective way under the excess amounts of the substrates and oxone (potassium peroxomonosulfate, $KHSO_5$), a two e^- oxidant. It was previously reported that an analogous dimanganese complex, $[Mn^{III}Mn^{IV}(\mu\text{-}O)_2(OH_2)_2(L')_2](NO_3)_3$ (L′ =

2,2′:6′,2″-terpyridine), catalyzes dioxygen evolution, and a Mn^{V}-oxo species was strongly suggested as a key intermediate.[25, 26] Accordingly, although the authors mentioned $Mn_2(\mu\text{-}O)_2$ as a reactive center in the present work, it is likely that a water ligand is deprotonated to a terminal oxo ligands which reacts with the C–H bonds of substrates as proposed in the previous study (Figure 1.5B). Consequently, this study shows the reactivity of a bis(μ-oxo)dimanganese complex potentially with terminal and bridging oxo units, which can activate C–H bonds of organic substrates, while further studies are needed to elucidate the key intermediate species of these reactions.

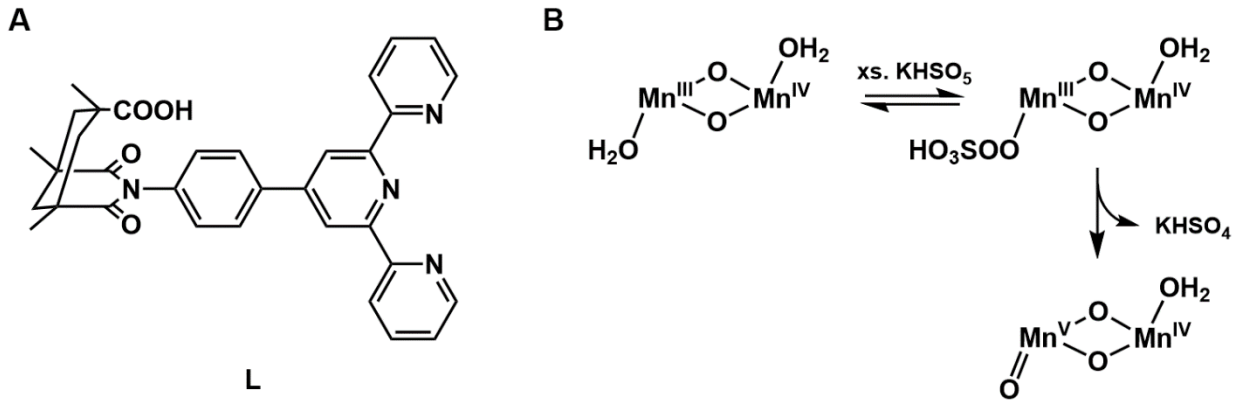

Figure 1.5. Structure of a terpyridine derivative ligand (A) and a proposed mechanism for the formation of terminal oxo ligand (B).[25, 26]

Comparatively more amounts of efforts have been made to investigate structural and electrochemical properties of the bis(μ-oxo)dimanganese species and the studies have been delineated in depth with different ligands and various oxidation states.[27] In particular, structural characteristics of mixed valence bis(μ-oxo)dimanganese(III,IV) complexes show localized valences based on Jahn-Teller distortions on Mn^{III} ions of the complexes. Further, bond distances

between Mn and O atoms reflect the different oxidation state, with a range of 1.82 – 1.86 Å for Mn^{III}–$O_{bridging}$ and 1.77 – 1.80 Å for Mn^{IV}–$O_{bridging}$. Both Mn^{III} and Mn^{IV} centers are high spin and antiferromagnetically coupled, affording $S = 1/2$ ground spin state with a sixteen-line hyperfine splitting on electron paramagnetic (EPR) spectra. Magnetic coupling constants are ranged from −159 to −146 cm^{-1}, where an isotropic Heisenberg exchange Hamiltonian $H = -2JS_1S_2$. Reduction potentials of bis(μ-oxo)dimanganese(III,IV) complexes show dependence on the chemical properties of ligands, which may further modulate PCET reactivities of bis(μ-oxo)dimanganese(III,IV) species. Nevertheless, a direct comparison of oxidation reactivities of bis(μ-oxo)dimanganese(III,IV) complexes with systematically modified ligand scaffolds, in my best knowledge, had not been carried out.

1.3 Formation of High-valent Manganese Intermediates

High-valent manganese species are frequently proposed as a key intermediate that carries out C–H bond activation. Due to this reason, researchers have focused on understanding reactivities of high-valent manganese complexes, as well as generating high-valent manganese species, which is pre-requisite to study the reactivities. Different types of terminal oxidants, which *in situ* produce a high-valent oxo complex by oxidizing a low-valent manganese complex, are utilized under various formation conditions. Commonly used oxidants include hydrogen peroxide (H_2O_2; and peroxides in general), iodosylbenzene (PhIO; and its derivatives), and ceric(IV) ammonium nitrate (CAN) with water (as an O atom donor), which are briefly introduced below with their reaction conditions.

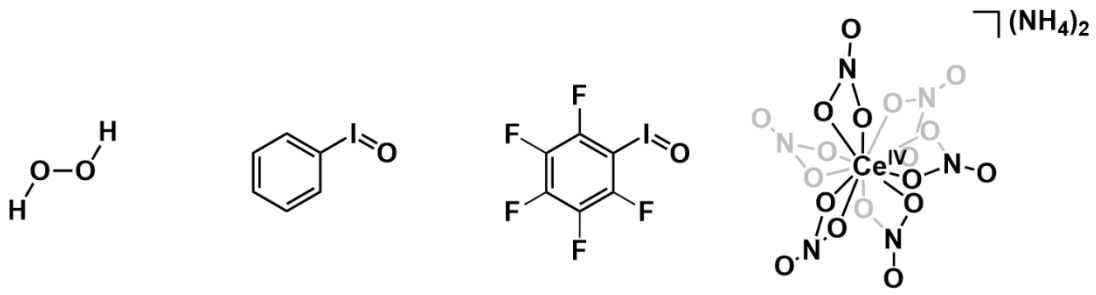

Figure 1.6. Chemical structures of commonly used oxidants for the formation of high-valent manganese oxo complexes; hydrogen peroxide, iodosylbenzene, iodosylpentafluorobenzene (an iodosylbenzene derivative), and ceric(IV) ammonium nitrate (left to right).

Inspired from nature, H_2O_2 has been utilized to generate high-valent manganese intermediate including bis(μ-oxo)dimanganese species. As an example, Hodgson, Michelsen, and co-workers prepared $[Mn^{III}Mn^{IV}(\mu\text{-}O)_2(bispictn)_2]^{3+}$ (bispictn = *N*,*N*′-bis(2-pyridylmethyl)-l,3-propanediamine) using H_2O_2.[28] Specifically, the formation conditions of this complex include H_2O_2 that is added to a mixture of the ligand (bispictn·4HCl·2H_2O), sodium carbonate, and $MnCl_2{\cdot}4H_2O$. More recently, my group reported formation and characterization of a bis(μ-oxo)dimanganese(III,IV) complex that is prepared using 5 equiv. 30% H_2O_2 and 0.5 equiv. triethylamine (TEA) in an aqueous solution of $[Mn^{II}(OTf)(N4py)](OTf)$ at 5 °C (Figure 1.7).[29, 30] Under these reaction conditions, $[Mn^{III}Mn^{IV}(\mu\text{-}O)_2(N4py)_2]^{3+}$ was formed quantitatively, based on absence of EPR signals from a Mn^{II} starting complex after the reaction. Additionally, the formation of this bis(μ-oxo)dimanganese was observed as a decay product from $[Mn^{III}(O_2)(N4py)]^+$ formed with 1 equiv. KO_2 in MeCN at −40 °C (Figure 1.7).

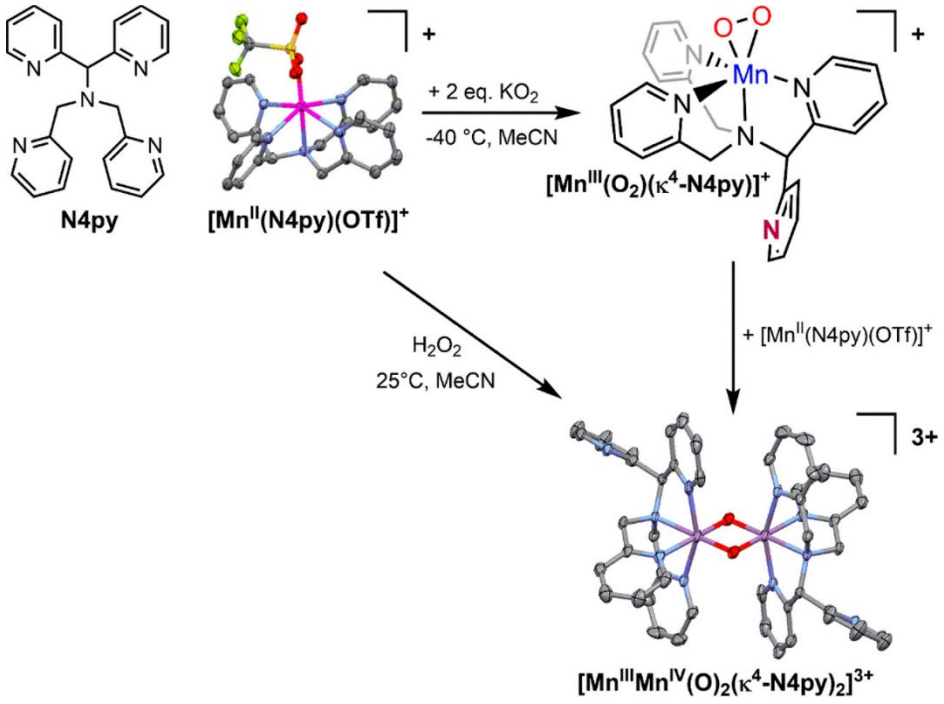

Figure 1.7. Formation of $[Mn^{III}Mn^{IV}(\mu\text{-}O)_2(N4py)_2]^{3+}$. Reprinted with permission from ref. 30. Copyrights 2017 American Chemical Society.

PhIO and its derivatives are frequently used to prepare high-valent oxo complexes. PhIO can be synthesized from iodosodiacetate, replacing the two acetate groups with an oxygen in basic aqueous conditions.[31] Formation conditions are often 2,2,2-trifluoroethanol (TFE) at 25 °C,[32-34] but CH_2Cl_2,[35, 36] 19:1 or 1:1 (v:v) TFE:MeCN,[37, 38] and MeCN (at −10 °C)[39] have been applied to prepare high-valent Mn^{IV}- or Mn^{V}-oxo complexes. Additionally, it has been discussed that metal-iodosylarene adducts could also participate in oxidative reactions.[40-43] Further, the formation of these metal iodosylarene adducts is supported by XRD structures of Mn^{III} and Mn^{IV} iodosylarene species (Figure 1.8).[43-46] Another iodosylarene compound, iodosylpentafluorobenzene, has been also used for the formation of high-valent manganese oxo complexes (Figure 1.6). Solomon, Nam, and co-workers reported Mn^{V}-oxo porphyrin species that were prepared using various oxidants

including *m*-chloroperbenzoic acid (*m*-CPBA), iodosylarenes, and H_2O_2. One of these oxidants, including iodosylpentafluorobenzene, was added to [Mn^{III}(TDCPP](Cl)] (TDCPP = *meso*-tetrakis(2,6-dichlorophenyl)porphinato dianion) to generate [Mn^{V}(O)(TDCPP)]$^+$ in 1:1 CH_2Cl_2:MeCN at 25 °C in the presence of tetrabutylammonium hydroxide (TBAH).

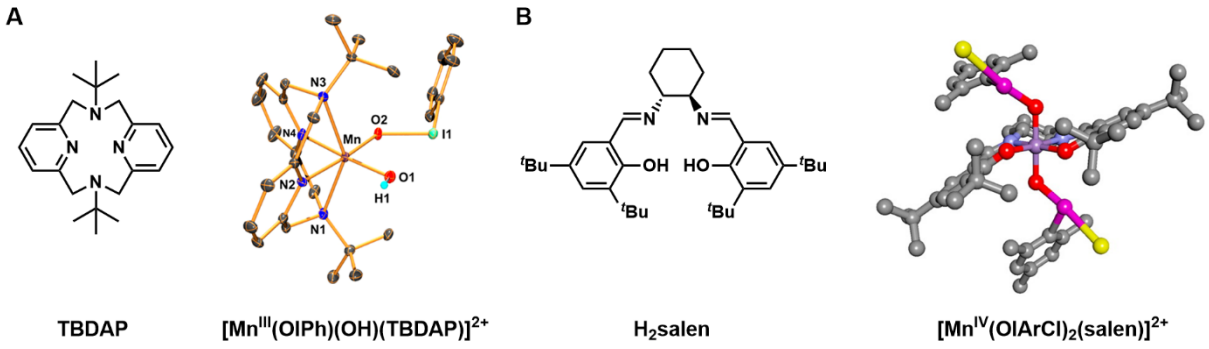

Figure 1.8. Ligand and XRD structures for [Mn^{III}(OIPh)(OH)(TBDAP)]$^{2+}$ reported by Cho *et al.* (A)[46] and [Mn^{IV}(OIArCl)$_2$(salen)] from previously reported study by Fujii *et al.* (B).[47] Reprinted with permissions from ref. 46 and 47. Copyrights 2018 and 2013 American Chemical Society.

Ceric(IV) ammonium nitrate (CAN) with water is another approach to prepare high-valent oxo species as well as to study their catalytic reactivities. In a typical mechanism, high-valent oxo species are formed by oxidation reaction of a low-valent metal complex and CAN as a one e^- oxidant (eq. 1)

$$[M^{II}(OH_2)L]^{2+} + 2 \text{ equiv. } Ce^{IV} \rightarrow [M^{IV}(O)L]^{2+} + 2 \text{ equiv. } Ce^{III} + 2H^+ \quad \text{(eq. 1)}$$

where water provides the oxygen atom. Because of this mechanism CAN has been applied as a sacrificial one e^- oxidant in water oxidation reactions to investigate O–O bond formation. Further, it has been suggested that Ce^{IV} also works as a Lewis acid, which attracts a water molecule close

to a metal catalyst to proceed water oxidation reaction. A similar role has been discussed for Ca^{2+} in several mechanistic models of the OEC in photosystem II, which promotes attacking a water or hydroxide ligand coordinated to a Mn^{IV}-oxo unit .[48, 49] These two features of Ce^{IV}, as a strong one electron oxidant and a Lewis acid, was probed by an equilibrium state found with an iron complex and CAN in MeCN with water:

$$[Fe^{IV}(O)(N4py)]^{2+} + Ce^{III}(ONO_2)_3 \rightleftharpoons [(N4py)Fe^{III}(O)Ce^{IV}(OH_2)(ONO_2)_4]^{2+}$$

where the equilibrium position changes depending on the amount of water in solution.[50] Similarly, either high-valent terminal oxo complexes or Ce^{IV}-bound high-valent manganese complexes was reported from oxidation reactions of low-valent manganese species and CAN with water, as briefly introduced below.[51-53]

Nam, Fukuzumi, Kim, Pushkar, and co-workers recently reported formation of a Ce^{IV}-bound high-valent manganese oxo complex.[53] This complex, which the authors proposed a Ce^{IV} is bound to the Mn^{IV}-oxo unit, was prepared by adding 2 equiv. CAN to $[Mn^{III}(OH)(dpaq)]^{+}$ in MeCN with water (40 μL) at −40 °C. The EPR spectrum of this Ce^{IV}-bound complex shows axial-type characteristics of high spin $S = 3/2$ Mn^{IV} species ($g_{eff} = 5.4$) and a typical feature of Mn^{II} species ($g_{eff} = 2.0$) of which the origin is not clear. The resonance Raman (rRaman) spectrum with ^{18}O labeling experiments exhibits a band with shift of 30 cm^{-1} from 675 cm^{-1} to 645 cm^{-1} upon the ^{18}O substitution. XANES data show a decreased pre-edge intensity relative to the Mn^{III}-hydroxo complex, and a feature at 3.67 Å in EXAFS data is attributed to the interaction between the Mn^{IV} and Ce^{IV} atoms. Although additional data are needed to support the mechanism of formation, in this study the authors show the potential of Ce^{IV} binding to a Mn^{IV}-oxo core in a high-valent manganese oxo complex.

1.4 Factors Influencing Reactivities of High-valent Manganese Species

Formations of high-valent manganese intermediates, as described earlier, enable to prepare a variety of model complexes with different geometries, steric features, electronic structures, and other chemical properties.[43, 44, 54, 55] Along the side, investigations of oxidizing reactivities of those intermediates allowed us to better understand what factors are imperative to their oxidizing reactivities. As those reactivities introduced above, C–H bond activation reactivities of high-valent manganese species have been studied more in depth than other oxidative reactivities. There are several mechanistic pathways that the C–H bond activation step has been studied.[56] Among those pathways a concerted proton–electron transfer (CPET) pathway is considered in general for C–H bond oxidations by high-valent manganese intermediates.[57] This pathway defines that both a proton and electron from a C–H bond are transferred in the same kinetic step. Based on this concept, several factors that affect this CPET mechanism have been postulated.

Thermodynamic influences are the most classical approach to analyze C–H bond activation reactivity, pointing out how thermodynamic driving force influences the kinetics of each step in C–H bond activation.[58] The thermodynamic driving force in C–H bond activation reactions can be gauged by experimentally or theoretically measuring the homolytic bond dissociation free energies (BDFE) (Figure 1.9),[56]

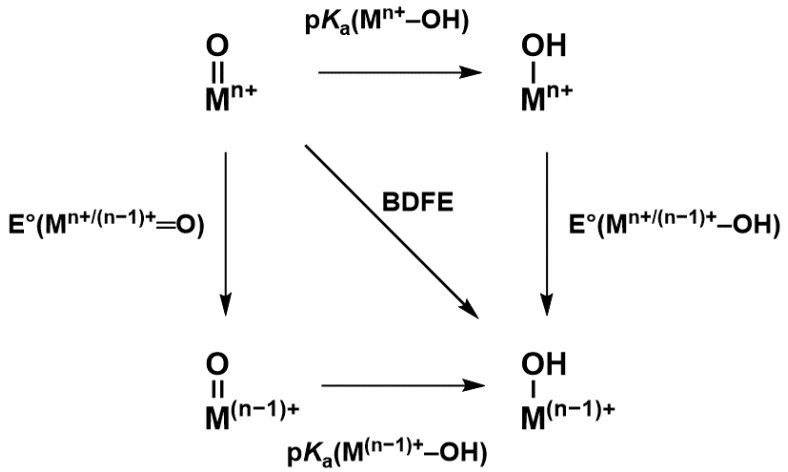

Figure 1.9. Thermochemical scheme showing thermodynamic driving force parameters for a metal oxo complex in a C–H bond activation reaction.

which is applied to, given this context, both a high-valent manganese intermediate and organic substrate involved in the C–H bond oxidative reaction. The experimental determination of a BDFE in a given solvent is generally from the following equation, originally developed by Bordwell and further modified by others.[59-62]

$$\mathrm{BDFE_{sol}(X–H)} = 1.37\mathrm{p}K_a + 23.06E^\circ + C_{G,sol}$$

where C_G is a constant in a given solvent. One representative example of thermodynamic influences on C–H bond activation reactivity is shown in Figure 1.10.[63]

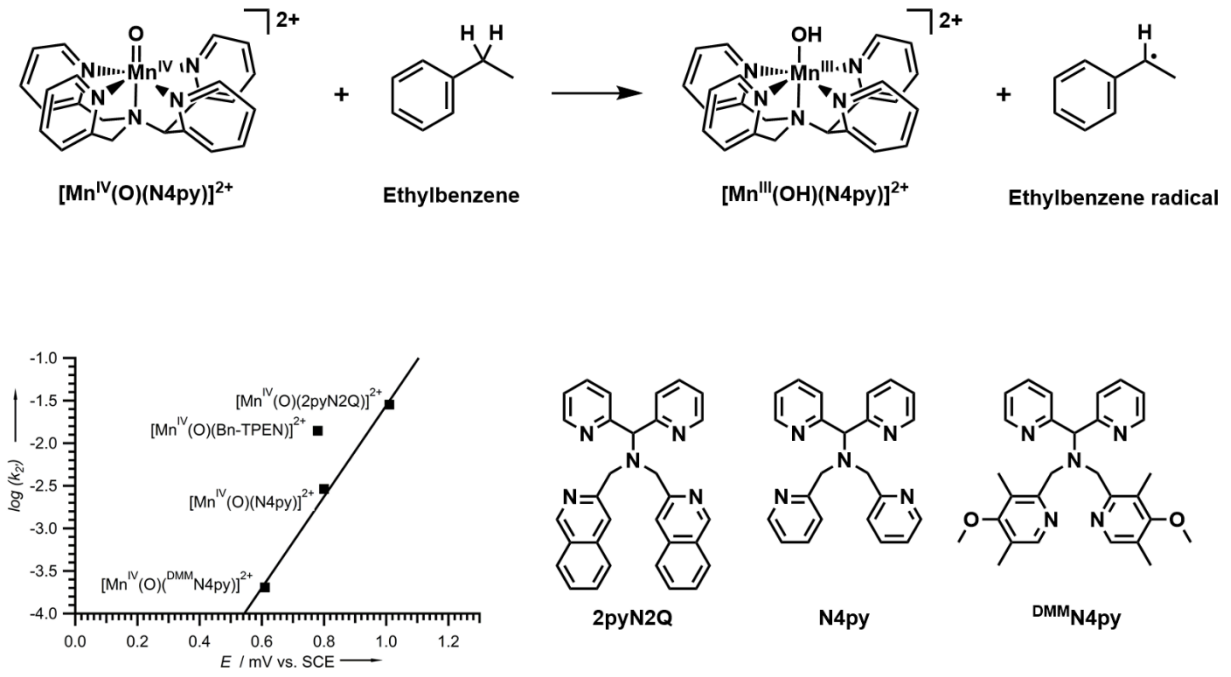

Figure 1.10. A reaction equation for the C–H bond activation reaction of $[Mn^{IV}(O)(N4py)]^{2+}$ and ethylbenzene (top). A plot of log(k_2) from ethylbenzene oxidation reactions against reduction potentials of a series of Mn^{IV}-oxo complexes with different ligand systems, displaying a linear correlation between the two experimental results (bottom left). The ligand structures applied in the study (bottom right). Plot is reprinted from ref. 63. Copyright 2017 Wiley. Used with permission from Wiley-VCH.

Published previously from my group, in this work the rate of ethylbenzene oxidation by a series of Mn^{IV}-oxo complexes, $[Mn^{IV}(O)(2pyN2Q)]^{2+}$, $[Mn^{IV}(O)(N4py)]^{2+}$, and $[Mn^{IV}(O)(^{DMM}N4py)]^{2+}$, shows a linear relationship with the experimentally determined potentials of $Mn^{IV/III}$ reduction for those Mn^{IV}-oxo complexes (Figure 1.10).[63] This relationship implies that the $Mn^{IV/III}$ reduction potential can be the major driving force of the kinetics of ethylbenzene oxidation reaction by those Mn^{IV}-oxo complexes.

Another important factor influencing C–H bond oxidation reactivities of high-valent manganese intermediates is equatorial ligand field strengths. The influences of equatorial ligand

field strengths were examined with the set of Mn^{IV}-oxo complexes in the study introduced above.[63] It was revealed that the C–H bond activation reactivity of a Mn^{IV}-oxo complex with a weak equatorial ligand field strength shows up to a hundred times faster rate than that of a Mn^{IV}-oxo complex with a strong equatorial ligand field strength (Figure 1.11). In other words, C–H bond oxidation reactivity can be modulated by applying different ligand field strengths. This equatorial ligand field effect shows correlations with the energy level of ^4E excited state among the series of Mn^{IV}-oxo complexes. The $Mn^{IV/III}$ reduction potentials are as well correlated with the rate enhancements as introduced earlier, which is attributed to differences in the ligands. Additional studies would be beneficial to find possible factors to overrule the equatorial ligand field effects on enhancing reaction rates, e.g., steric encumbrance.

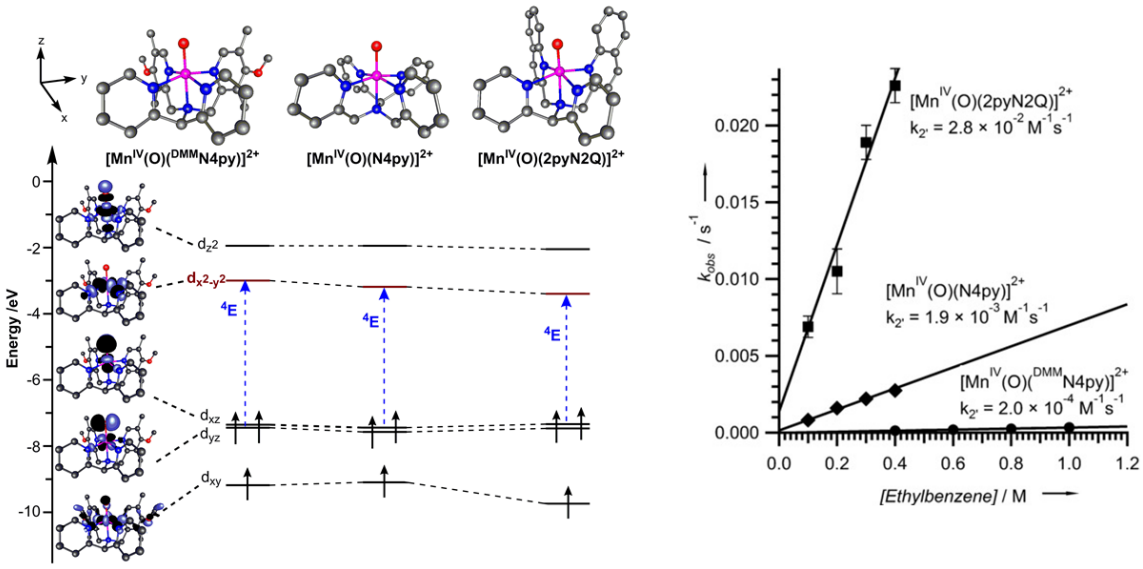

Figure 1.11. Changes in the energy level of ^4E excited state (left) and the rates of ethylbenzene oxidation among a series of Mn^{IV}-oxo species (right). Reprinted from ref. 63. Copyright 2017 Wiley. Used with permission from Wiley-VCH.

The binding effects of Lewis or Brønsted acids to high-valent manganese species show significant changes in their reactivities.[38, 64] Nam, Fukuzumi, and co-workers reported C–H bond oxidation is the main reaction process when they checked the reactivity of $[Mn^{IV}(O)(N4py)]^{2+}$ or $[Mn^{IV}(O)(Bn\text{-}TPEN)]^{2+}$ with cyclohexene, which can undergo either C–H bond hydroxylation or olefin epoxidation. In contrast, olefin epoxidation becomes the major reaction process from the same reaction except a Brønsted acid (triflic acid, CF_3SO_3H) was added (Figure 1.12). The authors claim this shift of selectivity based on the protonation of Mn^{IV}-oxo center due to the presence of Brønsted acid. Further, they propose that the C–H bond strength of substrate is another factor that affects in determining reaction pathways. Oxidation reactions with cyclohexene-d_{10} or cyclooctene produced only epoxide products due to their higher BDEs than that of cyclohexene (Figure 1.12).

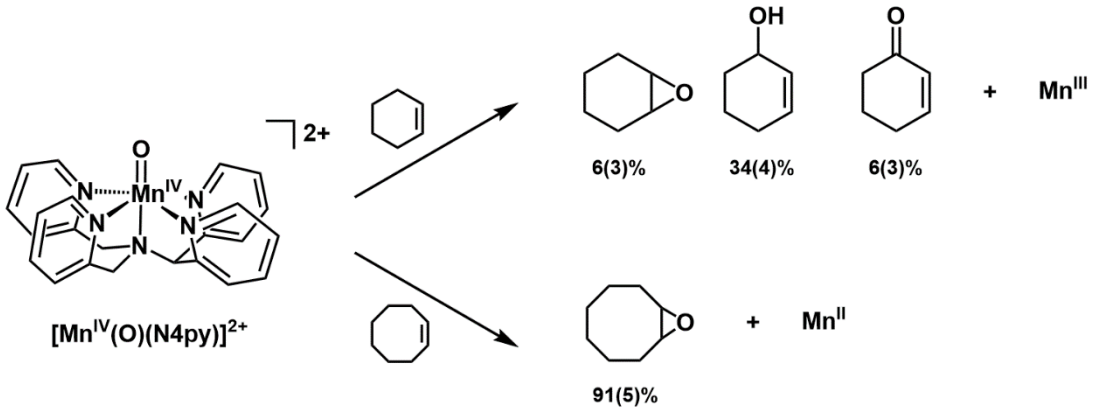

Figure 1.12. Comparisons of oxidation reactivities of $[Mn^{IV}(O)(N4py)]^{2+}$ towards C–H bond and C═C bond activation with cyclohexene and cyclooctene.

On the other hand, the influences of Lewis acidic metals on C–H bond activation reactivity of high-valent manganese oxo species were studied.[34, 53, 65-67] Nam and co-workers reported characterizations and reactivity studies of one or two $Sc(CF_3SO_3)_3$ bound $[Mn^{IV}(O)(N4py)]^{2+}$. The

cyclohexadiene (CHD) oxidation reactivities of those manganese species slow down by ca. 5 and 180 times for $[Mn^{IV}(O)(N4py)]^{2+}$ with 1 equiv. $Sc(CF_3SO_3)_3$ and $[Mn^{IV}(O)(N4py)]^{2+}$ with 2 equiv. $Sc(CF_3SO_3)_3$, respectively. The authors attribute the slower reactivities to steric hindrance due to the presence of $Sc(CF_3SO_3)_3$, which could hinder the approach of CHD to the Mn^{IV}-oxo unit to proceed oxidation reactions (Figure 1.13A).

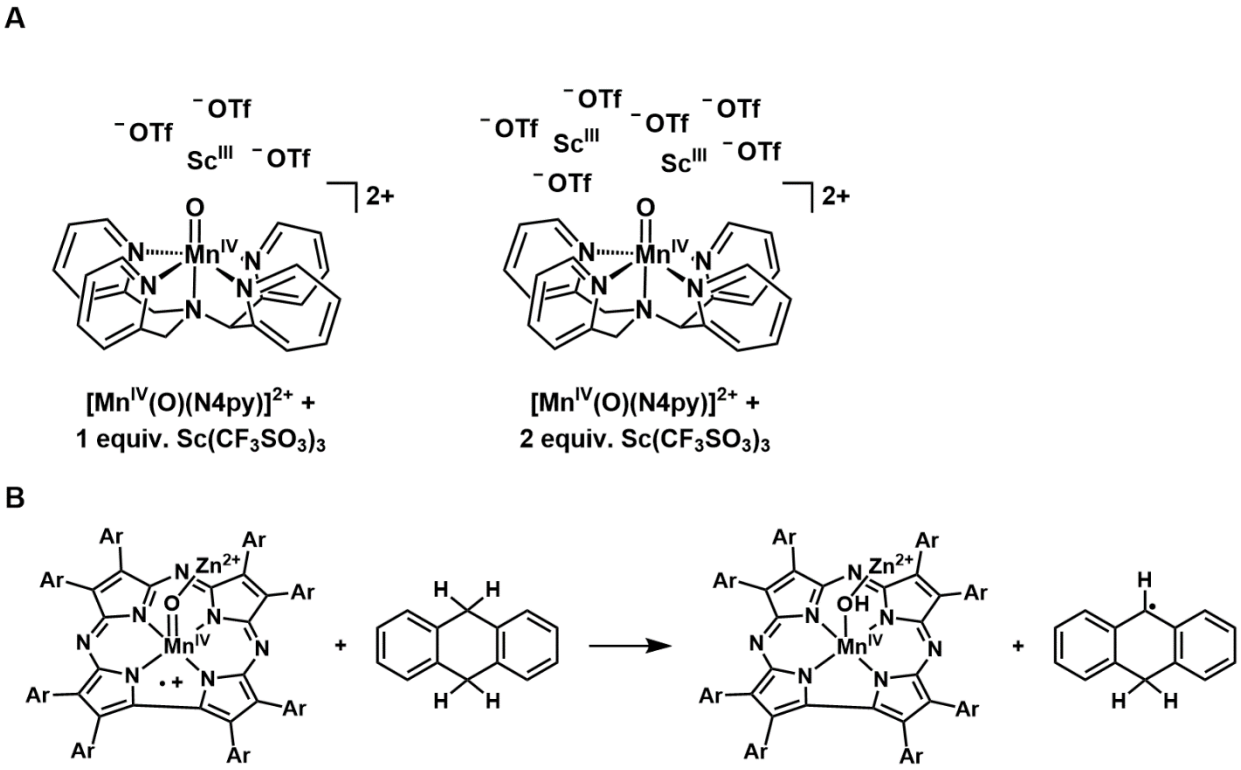

Figure 1.13. Structures of a Brønsted acid bound $[Mn^{IV}(O)(N4py)]^{2+}$ (A) and a Lewis acid bound $[Mn^{IV}(O)(TBP_8Cz^{\bullet+})]$ (B).

In contrast, Goldberg and co-workers reported of the binding effects of Zn^{2+} on C–H bond activation reactivity of a high-valent manganese oxo species, using $[(TBP_8Cz^{\bullet+})Mn^{IV}(O)–Zn^{2+}]$ and $[(TBP_8Cz^{\bullet+})Mn^{IV}(O)–B(C_6F_5)_3]$ (TBP_8Cz = octakis(p-*tert*-butylphenyl)corrolazinato).[67, 68]

Organic substrates with varied BDEs were used and the authors reported that the oxidizing reactivity is enhanced by a factor of 4 to 28, when [($TBP_8Cz^{\bullet+}$)Mn^{IV}(O)–Zn^{2+}] or [($TBP_8Cz^{\bullet+}$)Mn^{IV}(O)–$B(C_6F_5)_3$] is examined, respectively (Figure 1.13B). The degree of increments in C–H bond oxidation reaction rates of these complexes is contributed to the strengths of Lewis acidity. Together, the influences of Lewis or Brønsted acids bound to high-valent manganese oxo complexes are varied in opposite directions. More investigations on high-valent manganese oxo species with different ligand systems will be helpful to understand the determinants of these variations in reactivities.

1.5 High-valent Cobalt Species in C–H Bond Activation

As another earth abundant transition-metal, low- and high-valent cobalt species have gained much attention for their catalytic activities in a number of reactions.[69] Among the catalytic reactions, as an example, a high-valent Co multinuclear complex is proposed as an active intermediate to evolve O_2 by oxidizing H_2O.[70] Furthermore, Co species has been studied intensively with their catalytic C–H bond activation ability in organometallic transformations over 70 years.[71, 72] However, their bond activation mechanisms with respect to CPET have not been much explored. This lack of information could be attributed to its high d-electron counts. In the case of a tetragonal Co^{IV} complex an oxo ligand cannot be formed because the d^5 electron configuration results in the π-bond order between Co and O atoms less than one.[73-76] A proposed Co^{III}-oxyl complex, [$Co^{III}(O^{\bullet})$(N4py)]$^{2+}$, showed a markedly strong oxidizing reactivity towards C–H bonds of cyclohexane in gas phase, which may represent reactivities of late transition metal-oxyl complexes.[77] Only a handful of studies on high-valent Co oxo or oxyl species in various

geometries have been reported,[77-81] yet with very interesting experimental findings, which will be covered briefly in this section.

Anderson and Goetz reported C–H bond activation reactivity by a rare Co^{III}-oxo complex, $[Co^{III}(O)\{PhB(^{t}BuIm)_3\}]$.[79] In this work the authors proposed a basic asynchronous CPET pathway for the Co^{III}-oxo complex to cleave C–H bond, which is different from a thermodynamically driven CPET pathway. If C–H bond activation reactions of a metal-oxo complex and substrates are thermodynamically driven, a linear correlation is found between the reaction rate and BDE values of substrates. However, in this work the authors observed no correlation between the reaction rates and substrate BDE values (Figure 1.14A). Instead, they reported a linear relationship between the reaction rates and pK_a values of substrates, which can be interpreted as a stepwise PTET mechanism or a basic asynchronous CPET mechanism.

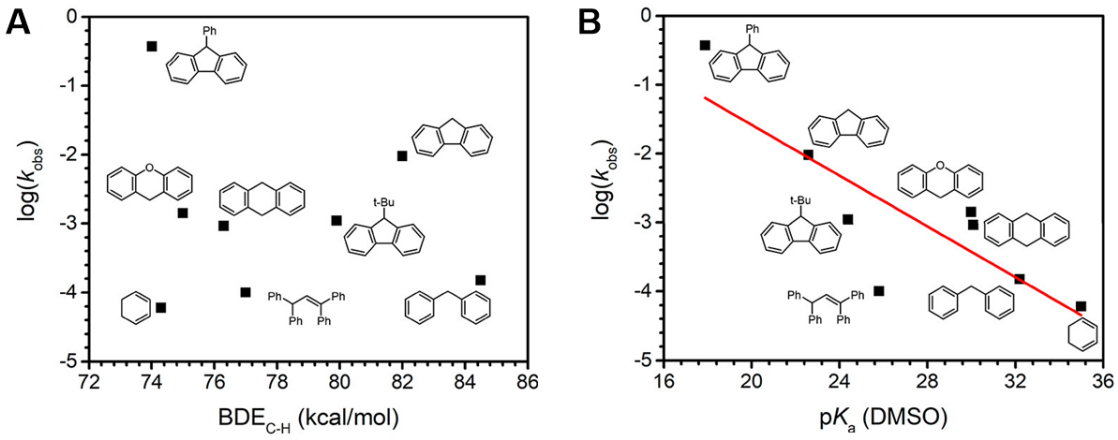

Figure 1.14. Plots of observed rate for C–H bond activation by $[Co^{III}(O)\{PhB(^{t}BuIm)_3\}]$ versus BDE of C–H bond (A) and pK_a of C–H bond (B).[79] Reprinted with permission from ref. 79. Copyrights 2020 American Chemical Society.

The asynchronous mechanism focuses on which character is found more between proton and electron transfer driving forces at the transition state (so-called "imbalanced transition state") of a C–H bond oxidation reaction in a concerted pathway. Therefore, there are basic asynchronous CPET, which is a more pK_a-driven pathway, and oxidative asynchronous CPET, which is a more reduction potential-driven pathway. Furthermore, it is proposed that the activation barriers are lower for the asynchronous mechanism than the synchronous mechanism.[82] The authors support this asynchronous mechanism with experimental and theoretical results of C–H bond activation by $[Co^{III}(O)\{PhB(^tBuIm)_3\}]$. Experimentally determined pK_a of $[Co^{III}(OH)\{PhB(^tBuIm)_3\}]^+$ shows highly basic properties of the complex (ca. 25.6 in MeCN), while the reduction potential of $[Co^{III}(O)\{PhB(^tBuIm)_3\}]$ was determined at −230 mV vs. $Fc^{+/0}$.[78] When the authors measured the activation parameters of DHA oxidation reaction, the values fall into the range of activation parameter values collected with various high-valent oxo complexes for DHA oxidation (11 kcal mol^{-1} for $\Delta H^{\ddagger}$ and −27 e.u. for $\Delta S^{\ddagger}$). The unusual linear relationship between log(k_{obs}) and pK_as of the substrates provided a possibility of either the stepwise PTET pathway or the basic asynchronous CPET mechanism. The authors carried out more experimental mechanistic studies for oxidation reactions by $[Co^{III}(O)\{PhB(^tBuIm)_3\}]$ and reported that there is no accumulation of $[Co^{III}(OH)\{PhB(^tBuIm)_3\}]^+$ or substrate carbanion, which can be seen in a stepwise PTET mechanism. Together, this work thoroughly interrogates and shows intriguing CPET reactivity of a Co^{III}-oxo system. More importantly, the study provides us further questions, e.g., a structure-reactivity relationship, related to the reasons behind the distinctive CPET reactivity of high-valent Co species.

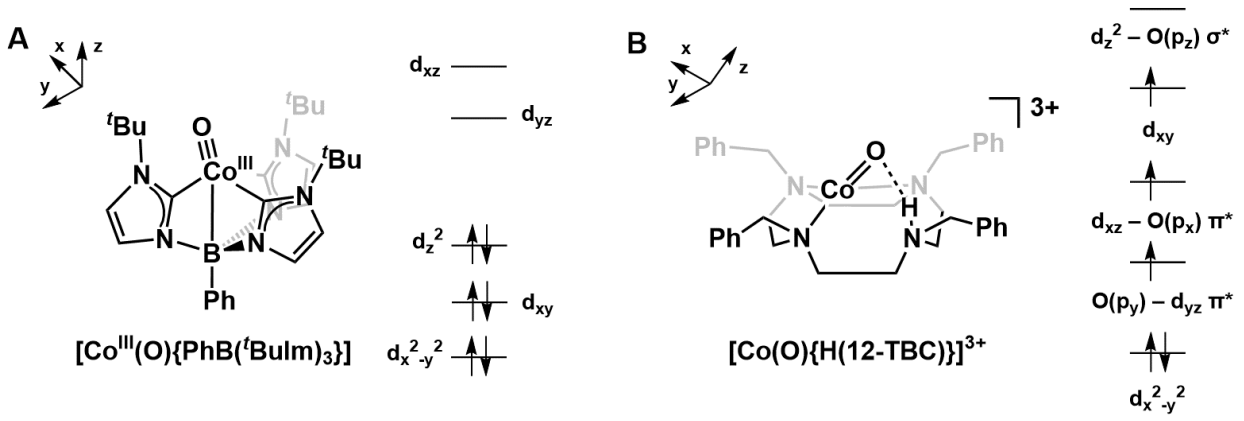

Figure 1.15. XRD characterized chemical structure for $[Co^{III}(O)\{PhB(^tBuIm)_3\}]$ (A) and a proposed chemical structure for $[Co(O)\{H(12\text{-}TBC)\}]^{3+}$ (B).[78, 81] DFT-calculated MO diagrams of the corresponding complexes are shown next to each structure.

Another high-valent Co oxo species was reported by Nam and co-workers (Figure 1.15). Using a macrocyclic ligand, 13-TMC (13-TMC = 1,4,7,10-tetramethyl-1,4,7,10-tetraazacyclotridecane), the authors reported formation of a Co^{IV}-oxo complex in square-pyramidal geometry by a photocatalytic oxidation, with $[Ru^{II}(bpy)_3]^{2+}$ and $Na_2S_2O_8$ in 1:1 (v/v) acetone:water at −20 °C. Alternatively, the complex was formed by the addition of 3 equiv. PhIO and 1.2 equiv. triflic acid (HOTf) in acetone at −40 °C. However, in their later study the authors suggested that this Co^{IV}-oxo complex, $[Co^{IV}(O)(13\text{-}TMC)]^{2+}$, might not have the square-pyramidal geometry since 1.2 equiv. HOTf could protonate the ligand and change the geometry.[81] Nevertheless, $[Co^{IV}(O)(13\text{-}TMC)]^{2+}$ shows C–H bond oxidation reactivity in the same acidic conditions with 1.2 equiv. HOTf in acetone at −40 °C. As an example, the second order rate constant (k_2) for DHA oxidation by $[Co^{IV}(O)(13\text{-}TMC)]^{2+}$ is 0.083 $M^{-1}s^{-1}$ under the corresponding conditions. Among the C–H bond oxidation reactions, the substrate with the highest BDE value is fluorene of which a calculated BDE value is 80 kcal mol^{-1}.[83] On the basis of a linear correlation between log(k_2') and BDEs of substrates hydrogen atom transfer (HAT) step was concluded as the

rate-determining step in the oxidation reactions. The authors examined the product metal complex from xanthene oxidation reaction, and the spectroscopic results suggest $[Co^{II}(13\text{-TMC})]^{2+}$. Additional investigation may be needed to confirm the structural characterization to elucidate the role of HOTf in formation of this complex. Further, the structural information will be beneficial to better understand the oxidizing reactivity of this high-valent Co complex.

Recently, another Co^{IV} complex was reported by Nam and co-workers.[81] Similar to the study mentioned above, a macrocyclic ligand, 12-TBC (12-TBC = 1,4,7,10-tetrabenzyl-1,4,7,10-tetraazacyclododecane) was used in this study to prepare a high-valent Co complex (Figure 1.15B). However, in this work the authors proposed a protonated four-coordinated geometry, which is different from what they reported for their earlier work on a Co^{IV} complex with 13-TMC ligand. Computational studies suggest the electronic structure of the complex, in which the authors pointed out a normal Co–O π interaction due to the hydrogen bond between the oxo ligand and proton on the ligand nitrogen (Figure 1.15B). However, they predicted an inverted metal-ligand bonding without the hydrogen bond, which would generate an oxyl ligand. The C–H bond activation reactivity of this complex was examined with xanthene and 1,4-cyclohexadiene (CHD) in acetone at −40 °C. The reactions show slower rates than the reactions of $[Co^{IV}(O)(13\text{-TMC})]^{2+}$ and the corresponding substrates (0.032 and 0.020 $M^{-1}s^{-1}$, respectively).

Above studies with high-valent Co species unambiguously show that there is a lack of knowledge about the reactivity of these complexes, especially with respect to their structure-reactivity relationships. Given that low- and high-valent Co catalysts are used in a variety of organic transformations, elucidating the structure-reactivity relationships for Co complexes can be a critical step to developing novel catalysts to perform desirable reactions. Therefore, more investigations are required for formations and reactivities of high-valent Co species to better

understand structural and electronic factors imperative to their reactivities, which will help us design more efficient Co catalysts for variable applications.

1.6 Notes and References

1. Anslyn, E. V.; Dougherty, D. A., *Modern Physical Organic Chemistry*. University Science Books: 2006.

2. Boal, A. K.; Cotruvo, J. A.; Stubbe, J.; Rosenzweig, A. C., Structural Basis for Activation of Class Ib Ribonucleotide Reductase. *Science* **2010,** *329* (5998), 1526-1530.

3. Umena, Y.; Kawakami, K.; Shen, J.-R.; Kamiya, N., Crystal structure of oxygen-evolving photosystem II at a resolution of 1.9 Å. *Nature* **2011,** *473* (7345), 55-60.

4. Bullock, R. M.; Chen Jingguang, G.; Gagliardi, L.; Chirik Paul, J.; Farha Omar, K.; Hendon Christopher, H.; Jones Christopher, W.; Keith John, A.; Klosin, J.; Minteer Shelley, D.; Morris Robert, H.; Radosevich Alexander, T.; Rauchfuss Thomas, B.; Strotman Neil, A.; Vojvodic, A.; Ward Thomas, R.; Yang Jenny, Y.; Surendranath, Y., Using nature's blueprint to expand catalysis with Earth-abundant metals. *Science* **2020,** *369* (6505), eabc3183.

5. Likhtenshteĭn, G. I., Chemical physics of redox metalloenzyme catalysis. Likhtenshteĭn, G. I., Ed. Berlin, New York : Springer-Verlag: Berlin, New York, 1988.

6. Karimov, R. R.; Hartwig, J. F., Transition-Metal-Catalyzed Selective Functionalization of C(sp3)−H Bonds in Natural Products. *Angewandte Chemie International Edition* **2018,** *57* (16), 4234-4241.

7. Huang, X.; Liu, W.; Ren, H.; Neelamegam, R.; Hooker, J. M.; Groves, J. T., Late Stage Benzylic C–H Fluorination with [18F]Fluoride for PET Imaging. *Journal of the American Chemical Society* **2014,** *136* (19), 6842-6845.

8. Gunay, A.; Theopold, K. H., C-H Bond Activations by Metal Oxo Compounds. *Chem. Rev. (Washington, DC, U. S.)* **2010,** *110* (2), 1060-1081.

9. Claveau, E. E.; Miliordos, E., Electronic structure of the dicationic first row transition metal oxides. *Physical Chemistry Chemical Physics* **2021,** *23* (37), 21172-21182.

10. Li, X.-X.; Cho, K.-B.; Nam, W., Electronic properties and reactivity patterns of high-valent metal-oxo species of Mn, Fe, Co, and Ni. *Bulletin of the Korean Chemical Society* **2021,** *42* (11), 1506-1512.

11. Sheng, Y.; Abreu, I. A.; Cabelli, D. E.; Maroney, M. J.; Miller, A.-F.; Teixeira, M.; Valentine, J. S., Superoxide Dismutases and Superoxide Reductases. *Chemical Reviews* **2014,** *114* (7), 3854-3918.

12. Signorella, S.; Hureau, C., Bioinspired functional mimics of the manganese catalases. *Coordination Chemistry Reviews* **2012,** *256* (11), 1229-1245.

13. Cady, C.; Crabtree, R.; Brudvig, G., Functional models for the oxygen-evolving complex of photosystem II. *Coordination Chemistry Reviews* **2008,** *252* (3-4), 444-455.

14. Pecoraro, V. L.; Baldwin, M. J.; Gelasco, A., Interaction of Manganese with Dioxygen and Its Reduced Derivatives. *Chemical Reviews* **1994,** *94* (3), 807-826.

15. Wu, A. J.; Penner-Hahn, J. E.; Pecoraro, V. L., Structural, Spectroscopic, and Reactivity Models for the Manganese Catalases. *Chemical Reviews* **2004,** *104* (2), 903-938.

16. Dempsey, J. L.; Winkler, J. R.; Gray, H. B., Proton-Coupled Electron Flow in Protein Redox Machines. *Chemical Reviews* **2010,** *110* (12), 7024-7039.

17. Wang, K.; Mayer, J. M., Oxidation of Hydrocarbons by [(phen)2Mn(μ-O)2Mn(phen)2]$^{3+}$ via Hydrogen Atom Abstraction. *Journal of the American Chemical Society* **1997,** *119* (6), 1470-1471.

18. Larsen, A. S.; Wang, K.; Lockwood, M. A.; Rice, G. L.; Won, T.-J.; Lovell, S.; Sadilek, M.; Turecek, F.; Mayer, J. M., Hydrocarbon oxidation by bis-μ-oxo manganese dimers: electron transfer, hydride transfer, and hydrogen atom transfer mechanisms. *J. Am. Chem. Soc.* **2002,** *124* (34), 10112-10123.

19. Nordlund, P.; Reichard, P., Ribonucleotide Reductases. *Annual Review of Biochemistry* **2006,** *75* (1), 681-706.

20. Cotruvo, J. A.; Stich, T. A.; Britt, R. D.; Stubbe, J., Mechanism of Assembly of the Dimanganese-Tyrosyl Radical Cofactor of Class Ib Ribonucleotide Reductase: Enzymatic Generation of Superoxide Is Required for Tyrosine Oxidation via a Mn(III)Mn(IV) Intermediate. *Journal of the American Chemical Society* **2013,** *135* (10), 4027-4039.

21. Manchanda, R.; Thorp, H. H.; Brudvig, G. W.; Crabtree, R. H., An unusual example of multiple proton-coupled electron transfers in a high-valent oxomanganese dimer, [(phen)2MnIII(O)2MnIV(phen)2](ClO4)3 (phen = 1,10 phenanthroline). *Inorganic Chemistry* **1992,** *31* (20), 4040-4041.

22. Manchanda, R.; Thorp, H. H.; Brudvig, G. W.; Crabtree, R. H., Proton-coupled electron transfer in high-valent oxomanganese dimers: role of the ancillary ligands. *Inorganic Chemistry* **1991,** *30* (3), 494-497.

23. Thorp, H. H.; Sarneski, J. E.; Brudvig, G. W.; Crabtree, R. H., Proton-coupled electron transfer in manganese complex [(bpy)2Mn(O)2Mn(bpy)2]$^{3+}$. *Journal of the American Chemical Society* **1989,** *111* (26), 9249-9250.

24. Das, S.; Incarvito, C. D.; Crabtree, R. H.; Brudvig, G. W., Molecular Recognition in the Selective Oxygenation of Saturated C-H Bonds by a Dimanganese Catalyst. *Science* **2006,** *312* (5782), 1941-1943.

25. Limburg, J.; Vrettos John, S.; Liable-Sands Louise, M.; Rheingold Arnold, L.; Crabtree Robert, H.; Brudvig Gary, W., A Functional Model for O-O Bond Formation by the O2-Evolving Complex in Photosystem II. *Science* **1999,** *283* (5407), 1524-1527.

26. Limburg, J.; Vrettos, J. S.; Chen, H.; De Paula, J. C.; Crabtree, R. H.; Brudvig, G. W., Characterization of the O2-Evolving Reaction Catalyzed by [(terpy)(H2O)Mn^{III}(O)2Mn^{IV}(OH2)(terpy)](NO3)3 (terpy = 2,2‘:6,2‘ ‘-Terpyridine). *Journal of the American Chemical Society* **2001,** *123* (3), 423-430.

27. Wieghardt, K., The Active Sites in Manganese-Containing Metalloproteins and Inorganic Model Complexes. *Angewandte Chemie International Edition in English* **1989,** *28* (9), 1153-1172.

28. Goodson, P. A.; Glerup, J.; Hodgson, D. J.; Michelsen, K.; Weihe, H., Syntheses and characterization of binuclear manganese(III,IV) and -(IV,IV) complexes with ligands related to N,N'-bis(2-pyridylmethyl)-1,2-ethanediamine. *Inorganic Chemistry* **1991,** *30* (26), 4909-4914.

29. Leto, D. F.; Chattopadhyay, S.; Day, V. W.; Jackson, T. A., Reaction landscape of a pentadentate N5-ligated Mn^{II} complex with O2˙− and H2O2 includes conversion of a peroxomanganese(iii) adduct to a bis(μ-oxo)dimanganese(iii,iv) species. *Dalton Transactions* **2013,** *42* (36), 13014-13025.

30. Rice, D. B.; Massie, A. A.; Jackson, T. A., Manganese–Oxygen Intermediates in O–O Bond Activation and Hydrogen-Atom Transfer Reactions. *Accounts of Chemical Research* **2017,** *50* (11), 2706-2717.

31. Saltzman, H.; Sharefkin, J. G., Iodosobenzene. *Organic Syntheses* **1963,** *43*, 60.

32. Wu, X.; Seo, M. S.; Davis, K. M.; Lee, Y.-M.; Chen, J.; Cho, K.-B.; Pushkar, Y. N.; Nam, W., A Highly Reactive Mononuclear Non-Heme Manganese(IV)–Oxo Complex That Can Activate the Strong C–H Bonds of Alkanes. *Journal of the American Chemical Society* **2011,** *133* (50), 20088-20091.

33. Leto, D. F.; Ingram, R.; Day, V. W.; Jackson, T. A., Spectroscopic properties and reactivity of a mononuclear oxomanganese(iv) complex. *Chemical Communications* **2013,** *49* (47), 5378-5380.

34. Chen, J.; Lee, Y.-M.; Davis, K. M.; Wu, X.; Seo, M. S.; Cho, K.-B.; Yoon, H.; Park, Y. J.; Fukuzumi, S.; Pushkar, Y. N.; Nam, W., A Mononuclear Non-Heme Manganese(IV)–Oxo

Complex Binding Redox-Inactive Metal Ions. *Journal of the American Chemical Society* **2013,** *135* (17), 6388-6391.

35. Zaragoza, J. P. T.; Siegler, M. A.; Goldberg, D. P., A Reactive Manganese(IV)–Hydroxide Complex: A Missing Intermediate in Hydrogen Atom Transfer by High-Valent Metal-Oxo Porphyrinoid Compounds. *Journal of the American Chemical Society* **2018,** *140* (12), 4380-4390.

36. Groves, J. T.; Kruper, W. J.; Haushalter, R. C., Hydrocarbon oxidations with oxometalloporphinates. Isolation and reactions of a (porphinato)manganese(V) complex. *Journal of the American Chemical Society* **1980,** *102* (20), 6375-6377.

37. Yoon, H.; Lee, Y.-M.; Wu, X.; Cho, K.-B.; Sarangi, R.; Nam, W.; Fukuzumi, S., Enhanced Electron-Transfer Reactivity of Nonheme Manganese(IV)–Oxo Complexes by Binding Scandium Ions. *Journal of the American Chemical Society* **2013,** *135* (24), 9186-9194.

38. Kim, S.; Cho, K.-B.; Lee, Y.-M.; Chen, J.; Fukuzumi, S.; Nam, W., Factors Controlling the Chemoselectivity in the Oxidation of Olefins by Nonheme Manganese(IV)-Oxo Complexes. *Journal of the American Chemical Society* **2016,** *138* (33), 10654-10663.

39. Sankaralingam, M.; Lee, Y.-M.; Pineda-Galvan, Y.; Karmalkar, D. G.; Seo, M. S.; Jeon, S. H.; Pushkar, Y.; Fukuzumi, S.; Nam, W., Redox Reactivity of a Mononuclear Manganese-Oxo Complex Binding Calcium Ion and Other Redox-Inactive Metal Ions. *Journal of the American Chemical Society* **2019,** *141* (3), 1324-1336.

40. Smegal, J. A.; Schardt, B. C.; Hill, C. L., Isolation, purification, and characterization of intermediate (iodosylbenzene)metalloporphyrin complexes from the (tetraphenylporphinato)manganese(III)-iodosylbenzene catalytic hydrocarbon functionalization system. *Journal of the American Chemical Society* **1983,** *105* (11), 3510-3515.

41. Kang, Y.; Wang, F.; Reinhard, F. G. C.; Xia, C.; De Visser, S. P.; Wang, Y., Can Manganese(III)-Iodosylarene Act as an Oxidant Alongside High-Valent Manganese(V)-Oxo Complexes? *ChemistrySelect* **2018,** *3* (11), 3208-3213.

42. Collman, J. P.; Zeng, L.; Decréau, R. A., Multiple active oxidants in competitive epoxidations catalyzed by porphyrins and corroles. *Chem. Commun.* **2003,** (24), 2974-2975.

43. Guo, M.; Lee, Y.-M.; Fukuzumi, S.; Nam, W., Biomimetic metal-oxidant adducts as active oxidants in oxidation reactions. *Coordination Chemistry Reviews* **2021,** *435*, 213807.

44. Fukuzumi, S.; Cho, K.-B.; Lee, Y.-M.; Hong, S.; Nam, W., Mechanistic dichotomies in redox reactions of mononuclear metal–oxygen intermediates. *Chemical Society Reviews* **2020,** *49* (24), 8988-9027.

45. Wang, C.; Kurahashi, T.; Fujii, H., Structure and Reactivity of an Iodosylarene Adduct of a Manganese(IV)-Salen Complex. *Angewandte Chemie International Edition* **2012,** *51* (31), 7809-7811.

46. Jeong, D.; Ohta, T.; Cho, J., Structure and Reactivity of a Mononuclear Nonheme Manganese(III)–Iodosylarene Complex. *Journal of the American Chemical Society* **2018,** *140* (47), 16037-16041.

47. Wang, C.; Kurahashi, T.; Inomata, K.; Hada, M.; Fujii, H., Oxygen-Atom Transfer from Iodosylarene Adducts of a Manganese(IV) Salen Complex: Effect of Arenes and Anions on I(III) of the Coordinated Iodosylarene. *Inorganic Chemistry* **2013,** *52* (16), 9557-9566.

48. Fillol, J. L.; Codolà, Z.; Garcia-Bosch, I.; Gómez, L.; Pla, J. J.; Costas, M., Efficient water oxidation catalysts based on readily available iron coordination complexes. *Nature Chemistry* **2011,** *3* (10), 807-813.

49. Codolà, Z.; Gómez, L.; Kleespies, S. T.; Que Jr, L.; Costas, M.; Lloret-Fillol, J., Evidence for an oxygen evolving iron–oxo–cerium intermediate in iron-catalysed water oxidation. *Nature Communications* **2015,** *6* (1), 5865.

50. Draksharapu, A.; Rasheed, W.; Klein, J. E. M. N.; Que Jr, L., Facile and Reversible Formation of Iron(III)–Oxo–Cerium(IV) Adducts from Nonheme Oxoiron(IV) Complexes and Cerium(III). *Angewandte Chemie International Edition* **2017,** *56* (31), 9091-9095.

51. Sawant, S.; Wu, X.; Cho, J.; Cho, K.-B.; Kim, S.; Seo, M.; Lee, Y.-M.; Kubo, M.; Ogura, T.; Shaik, S.; Nam, W., Water as an Oxygen Source: Synthesis, Characterization, and Reactivity Studies of a Mononuclear Nonheme Manganese(IV) Oxo Complex. *Angewandte Chemie* **2010,** *122* (44), 8366-8370.

52. Barman, P.; Vardhaman, A. K.; Martin, B.; Wörner, S. J.; Sastri, C. V.; Comba, P., Influence of Ligand Architecture on Oxidation Reactions by High-Valent Nonheme Manganese Oxo Complexes Using Water as a Source of Oxygen. *Angewandte Chemie* **2015,** *127* (7), 2123-2127.

53. Karmalkar, D. G.; Sankaralingam, M.; Seo, M. S.; Ezhov, R.; Lee, Y.-M.; Pushkar, Y. N.; Kim, W.-S.; Fukuzumi, S.; Nam, W., A High-Valent Manganese(IV)–Oxo–Cerium(IV) Complex and Its Enhanced Oxidizing Reactivity. *Angewandte Chemie International Edition* **2019,** *58* (45), 16124-16129.

54. Bryliakov, K. P.; Talsi, E. P., Active sites and mechanisms of bioinspired oxidation with H2O2, catalyzed by non-heme Fe and related Mn complexes. *Coordination Chemistry Reviews* **2014,** *276*, 73-96.

55. Cho, K.-B.; Hirao, H.; Shaik, S.; Nam, W., To rebound or dissociate? This is the mechanistic question in C–H hydroxylation by heme and nonheme metal–oxo complexes. *Chemical Society Reviews* **2016,** *45* (5), 1197-1210.

56. Warren, J. J.; Tronic, T. A.; Mayer, J. M., Thermochemistry of Proton-Coupled Electron Transfer Reagents and its Implications. *Chemical Reviews* **2010,** *110* (12), 6961-7001.

57. Mayfield, J. R.; Grotemeyer, E. N.; Jackson, T. A., Concerted proton–electron transfer reactions of manganese–hydroxo and manganese–oxo complexes. *Chemical Communications* **2020,** *56* (65), 9238-9255.

58. *Biomimetic Oxidations Catalyzed by Transition Metal Complexes*. Imperial College Press: 2000.

59. Bordwell, F. G.; Cheng, J. P.; Harrelson, J. A., Homolytic bond dissociation energies in solution from equilibrium acidity and electrochemical data. *Journal of the American Chemical Society* **1988,** *110* (4), 1229-1231.

60. Wayner, D. D. M.; Parker, V. D., Bond energies in solution from electrode potentials and thermochemical cycles. A simplified and general approach. *Accounts of Chemical Research* **1993,** *26* (5), 287-294.

61. Tilset, M., The Thermodynamics of Organometallic Systems Involving Electron-Transfer Paths. *Electron Transfer in Chemistry* **2001**, 677-713.

62. Tilset, M., 1.11 - Organometallic Electrochemistry: Thermodynamics of Metal–Ligand Bonding. Elsevier Ltd: 2007; pp 279-305.

63. Massie, A. A.; Denler, M. C.; Cardoso, L. T.; Walker, A. N.; Hossain, M. K.; Day, V. W.; Nordlander, E.; Jackson, T. A., Equatorial Ligand Perturbations Influence the Reactivity of Manganese(IV)-Oxo Complexes. *Angewandte Chemie International Edition* **2017,** *56* (15), 4178-4182.

64. Guo, M.; Corona, T.; Ray, K.; Nam, W., Heme and Nonheme High-Valent Iron and Manganese Oxo Cores in Biological and Abiological Oxidation Reactions. *ACS Central Science* **2019,** *5* (1), 13-28.

65. Hong, S.; Lee, Y.-M.; Sankaralingam, M.; Vardhaman, A. K.; Park, Y. J.; Cho, K.-B.; Ogura, T.; Sarangi, R.; Fukuzumi, S.; Nam, W., A Manganese(V)–Oxo Complex: Synthesis by Dioxygen Activation and Enhancement of Its Oxidizing Power by Binding Scandium Ion. *Journal of the American Chemical Society* **2016,** *138* (27), 8523-8532.

66. Liu, Y.; Lau, T.-C., Activation of Metal Oxo and Nitrido Complexes by Lewis Acids. *Journal of the American Chemical Society* **2019,** *141* (9), 3755-3766.

67. Leeladee, P.; Baglia, R. A.; Prokop, K. A.; Latifi, R.; de Visser, S. P.; Goldberg, D. P., Valence Tautomerism in a High-Valent Manganese–Oxo Porphyrinoid Complex Induced by a Lewis Acid. *Journal of the American Chemical Society* **2012,** *134* (25), 10397-10400.

68. Baglia, R. A.; Krest, C. M.; Yang, T.; Leeladee, P.; Goldberg, D. P., High-Valent Manganese–Oxo Valence Tautomers and the Influence of Lewis/Brönsted Acids on C–H Bond Cleavage. *Inorganic Chemistry* **2016,** *55* (20), 10800-10809.

69. Holzwarth, M. S.; Plietker, B., Biorelevant Metals in Sustainable Metal Catalysis-A Survey. *ChemCatChem* **2013,** *5* (7), 1650-1679.

70. Nocera, D. G., The Artificial Leaf. *Accounts of Chemical Research* **2012,** *45* (5), 767-776.

71. Moselage, M.; Li, J.; Ackermann, L., Cobalt-Catalyzed C–H Activation. *ACS Catalysis* **2016,** *6* (2), 498-525.

72. Gandeepan, P.; Müller, T.; Zell, D.; Cera, G.; Warratz, S.; Ackermann, L., 3d Transition Metals for C–H Activation. *Chemical Reviews* **2019,** *119* (4), 2192-2452.

73. Ballhausen, C. J.; Gray, H. B., The Electronic Structure of the Vanadyl Ion. *Inorganic Chemistry* **1962,** *1* (1), 111-122.

74. Winkler, J. R.; Gray, H. B., Electronic Structures of Oxo-Metal Ions. In *Molecular Electronic Structures of Transition Metal Complexes I*, Mingos, D. M. P.; Day, P.; Dahl, J. P., Eds. Springer Berlin Heidelberg: Berlin, Heidelberg, 2012; pp 17-28.

75. Gray, H. B.; Winkler, J. R., Living with Oxygen. *Accounts of Chemical Research* **2018,** *51* (8), 1850-1857.

76. Larson, V. A.; Battistella, B.; Ray, K.; Lehnert, N.; Nam, W., Iron and manganese oxo complexes, oxo wall and beyond. *Nature Reviews Chemistry* **2020,** *4* (8), 404-419.

77. Andris, E.; Navrátil, R.; Jašík, J.; Srnec, M.; Rodríguez, M.; Costas, M.; Roithová, J., M−O Bonding Beyond the Oxo Wall: Spectroscopy and Reactivity of Cobalt(III)-Oxyl and Cobalt(III)-Oxo Complexes. *Angewandte Chemie International Edition* **2019,** *58* (28), 9619-9624.

78. Goetz, M. K.; Hill, E. A.; Filatov, A. S.; Anderson, J. S., Isolation of a Terminal Co(III)-Oxo Complex. *Journal of the American Chemical Society* **2018,** *140* (41), 13176-13180.

79. Goetz, M. K.; Anderson, J. S., Experimental Evidence for pKa-Driven Asynchronicity in C–H Activation by a Terminal Co(III)–Oxo Complex. *Journal of the American Chemical Society* **2019,** *141* (9), 4051-4062.

80. Wang, B.; Lee, Y.-M.; Tcho, W.-Y.; Tussupbayev, S.; Kim, S.-T.; Kim, Y.; Seo, M. S.; Cho, K.-B.; Dede, Y.; Keegan, B. C.; Ogura, T.; Kim, S. H.; Ohta, T.; Baik, M.-H.; Ray, K.; Shearer, J.; Nam, W., Synthesis and reactivity of a mononuclear non-haem cobalt(IV)-oxo complex. *Nature Communications* **2017,** *8* (1), 14839.

81. Yang, J.; Dong, H. T.; Seo, M. S.; Larson, V. A.; Lee, Y.-M.; Shearer, J.; Lehnert, N.; Nam, W., The Oxo-Wall Remains Intact: A Tetrahedrally Distorted Co(IV)–Oxo Complex. *Journal of the American Chemical Society* **2021,** *143* (41), 16943-16959.

82. Bím, D.; Maldonado-Domínguez, M.; Rulíšek, L.; Srnec, M., Beyond the classical thermodynamic contributions to hydrogen atom abstraction reactivity. *Proceedings of the National Academy of Sciences* **2018,** *115* (44), E10287.

83. Luo, Y.-R., Comprehensive Handbook of Chemical Bond Energies. **2007**.

Chapter 2

Ligand Influence on Structural Properties and Reactivity of Bis(μ-oxo)dimanganese(III,IV) Species and Comparison of Reactivity with Terminal Mn^{IV}-oxo Complexes

2.1 Introduction

In nature, manganese-dependent enzymes function in vital biological processes. These processes include eliminating toxic reactive oxygen species (H_2O_2 and $O_2^{\bullet-}$), initiating the synthesis of DNA components, and generating protons, electrons, and O_2 through water oxidation.[1-4] Manganese-oxo species are proposed as intermediates in several of these manganese-dependent enzymes. In the majority of these enzymes, these manganese-oxo units are found in di- or multi-manganese clusters. For example, class Ib ribonucleotide reductase (RNR), which carries out nucleotide reduction in pathways for DNA synthesis and repair, employs a dimanganese cofactor known as $Mn^{III}Mn^{III}$-$Y^{\bullet}$.[2, 5] This cofactor is assembled through $O_2^{\bullet-}$ reduction by a $Mn^{II}Mn^{II}$ center, where it is proposed that a transient (μ-O)(μ-OH)$Mn^{III}Mn^{IV}$ intermediate oxidizes an adjacent tyrosine residue to generate the dimanganese(III,III)-tyrosyl radical cofactor.[2] The oxygen-evolving complex (OEC) in photosystem II contains a Mn_4Ca cluster with bridging oxo ligands and protein-derived capping ligands.[3, 5, 6] Stepwise oxidation of the OEC proceeds by proton-coupled electron transfer (PCET) reactions involving a tyrosine radical.[78] Thus, a primary role of multinuclear manganese species in nature is proton-coupled electron transfer (PCET) reactions with phenols or phenoxyl radicals. Because of their biological relevance, a number of manganese model complexes bearing oxo and/ or hydroxo ligands have been synthesized and studied.[6, 9-15]

In spite of the PCET reactivity of a $Mn^{III}Mn^{IV}$ unit in Mn-RNR, there are only a handful of investigations of the reactivity of synthetic bis(μ-oxo)dimanganese(III,IV) complexes toward C–H or O–H bonds.[16-19] The majority of studies of bis(μ-oxo)dimanganese(III,IV) complexes have focused on the synthesis and characterization of the $(\mu\text{-O})_2Mn_2$ unit with different supporting ligands, with the goal of structurally mimicking active-site motifs of manganese catalase and/ or

the OEC.[6, 20-23] Only for a subset of complexes has PCET reactivity been explored, but these have shown interesting results. Mayer and coworkers performed studies on the oxidation of weak C–H bonds with a mixed-valent $[Mn^{III}Mn^{IV}(\mu\text{-}O)_2(phen)_4]^{3+}$ complex (phen = 1,10-phenanthroline), which afforded accessibility to different Mn oxidation and ligand protonation states.[16] In particular, they showed that the $[Mn^{III}Mn^{III}(\mu\text{-}O)(\mu\text{-}OH)(phen)_4]^{3+}$ complex could act as a hydrogen atom transfer (HAT) agent in the oxidation of hydrocarbons with weak C–H bonds, generating the $[Mn^{II}Mn^{III}(\mu\text{-}OH)_2(phen)_4]^{3+}$ complex as a product.[16] In a more recent study by the Nam group, the mixed-valent $[Mn^{III}Mn^{IV}(\mu\text{-}O)_2(dpaq)_2]^{+}$ complex (dpaq = 2-[bis(pyridin-2-yl-methyl)]amino-*N*-quinolin-8-yl-acetamidate) was shown to have an amphoteric reactivity toward phenol and aldehyde derivatives.[18] For phenol oxidation, $[Mn^{III}Mn^{IV}(\mu\text{-}O)_2(dpaq)_2]^{+}$ functioned as an electrophile, as indicated by Hammett plot of *para*-substituted phenols with a ρ value of –1.0. Depending on the phenol substrates, the organic products were identified as phenoxyl radical species or dimerized phenol derivatives, and the metal product was proposed as $[Mn^{III}(OH)(dpaq)]^{+}$ based on the absence of an EPR signal. In contrast, the $[Mn^{III}Mn^{IV}(\mu\text{-}O)_2(dpaq)_2]^{+}$ complex showed nucleophilic character in aldehyde deformylation, giving a ρ value of +0.89 in a Hammett correlation for *para*-substituted benzaldehydes. The reaction of $[Mn^{III}Mn^{IV}(\mu\text{-}O)_2(dpaq)_2]^{+}$ with 2-PPA (2-phenylpropionaldehyde) generated the deformylated product, acetophenone, along with $[Mn^{III}(dpaq)]^{2+}$, as confirmed by ESI-MS.[18] These studies imply that the reactivity of mixed-valent bis(m-oxo)dimanganese(III,IV) complexes is strongly modulated by the properties of both metal complex and substrate.

In contrast to the paucity of studies of the HAT reactivity of dinuclear bis(μ-oxo)dimanganese(III,IV) adducts, the ability of mononuclear Mn^{IV}-oxo/hydroxo complexes to effect HAT reactions has been more extensively investigated.[14, 24-32] As high-valent manganese-

oxo species are often proposed as intermediates in C–H bond activation, olefin epoxidation, and oxygenation of hydrocarbons, one aim of such studies is the development of C–H functionalization catalysts for synthetic transformations.[28, 33-35] It is now well known that high-valent manganese-oxo species have a broad spectrum of reactivity, with some complexes showing slow rates of reaction with activated C–H bonds, and others capable of cleaving the strong C–H bonds in cyclohexane.[9, 14, 24, 28, 29, 36-38] In a recent study, our group systematically investigated the reactivities of manganese(IV)-oxo species with the series of pentadentate N5 ligands shown in Figure 2.1 (N4py = *N*,*N*-bis(2-pyridylmethyl)-*N*-bis(2-pyridyl)methylamine, ^{DMM}N4py = *N*,*N*-bis(4-methoxy-3,5-dimethyl-2-pyridylmethyl)-*N*-bis(2-pyridyl)methylamine, and 2pyN2Q = bis(2-pyridyl)-*N*,*N*-bis(2-quinolylmethyl)methanamine).[9] For both HAT and oxygen-atom transfer (OAT) reactions, these complexes showed an order of reactivity of $[Mn^{IV}(O)(2pyN2Q)]^{2+}$ > $[Mn^{IV}(O)(N4py)]^{2+}$ > $[Mn^{IV}(O)(^{DMM}N4py)]^{2+}$. This result was understood in terms of the modulation of the equatorial ligand field strength, with a weaker field corresponding to a more reactive Mn^{IV}-oxo unit.

In this study, we investigated the role of similar ligand perturbations on the structural properties and chemical reactivity of the corresponding bis(μ-oxo)dimanganese(III,IV) complexes, $[Mn^{III}Mn^{IV}(\mu\text{-}O)_2(N4py)_2]^{3+}$ (**1**) and $[Mn^{III}Mn^{IV}(\mu\text{-}O)_2(^{DMM}N4py)_2]^{3+}$ (**2**). In addition, the structural and reactivity differences between the bis(μ-oxo)dimanganese species and their terminal-oxo counterparts, $[Mn^{IV}(O)(N4py)]^{2+}$ and $[Mn^{IV}(O)(^{DMM}N4py)]^{2+}$, were also explored. Complexes **1** and **2** displayed nearly identical spectroscopic properties, which is suggestive of only very minor geometric and electronic changes between these species. These complexes also displayed very similar rates for O–H bond activation of a phenolic substrate. However, a comparison of the reactivity of the terminal Mn^{IV}-oxo complex $[Mn^{IV}(O)(^{DMM}N4py)]^{2+}$ and the

bridging Mn^{IV}-oxo analogue, **2**, showed the former complex to be more reactive for phenol oxidation by roughly five orders of magnitude.

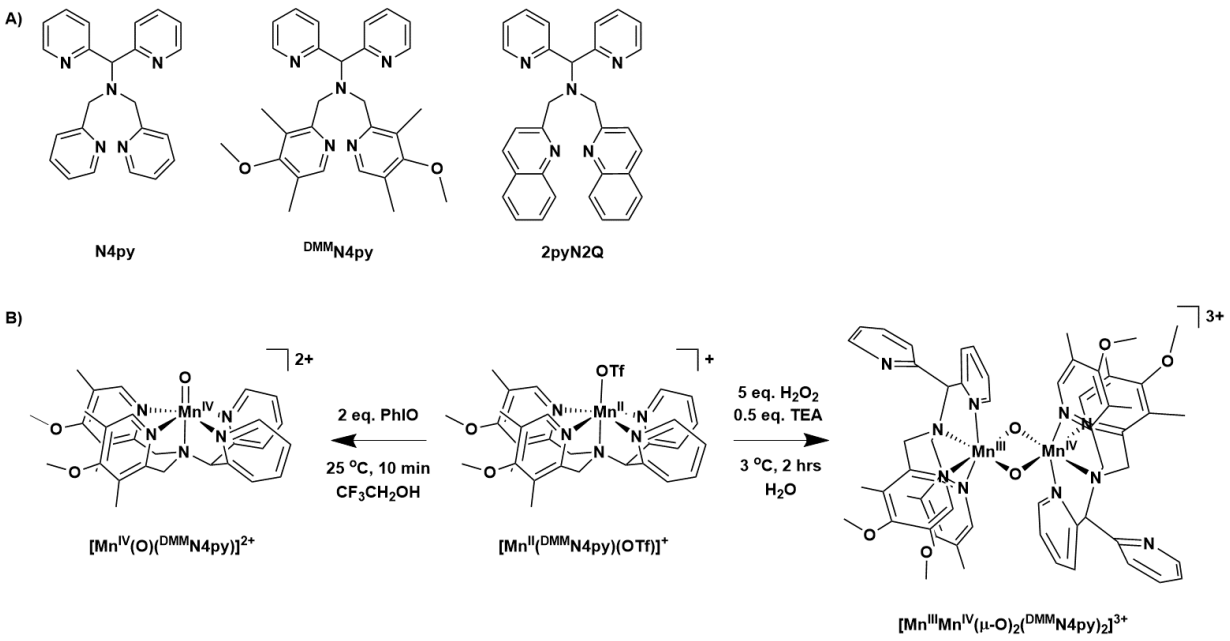

Figure 2.1. A) Structures of the N4py ligand and its derivatives ^{DMM}N4py and 2pyN2Q. B) Formation scheme of $[Mn^{IV}(O)(^{DMM}N4py)]^{2+}$ and $[Mn^{III}Mn^{IV}(\mu\text{-}O)_2(^{DMM}N4py)_2]^{2+}$ from $[Mn^{II}(^{DMM}N4py)(OTf)]^{+}$.

2.2 Experimental and Computational Methods

2.2.1 Materials and Instrumentation. All chemicals and solvents were ACS reagent grade or better and used as received after purchased from commercial vendors. All kinetic data were obtained using an Agilent 8453 spectrophotometer or a Varian Cary 50 Bio thermally controlled by a Unisoku cryostat (USP-203-A). A Quattro Micro GC mass spectrometer (Micromass Ltd, Manchester, UK) with an Agilent 6890 N gas chromatograph was used for product analysis. A 15 meter HP-5MS column (15 m × 250 μm × 0.25 μm) was equipped with

helium as a carrier gas, which constantly flowed at 2 mL min−1 rate. The temperature of the injector port was 250 °C and the column temperature was heated by 25 °C min-1 from 50 to 310 °C. Electron impact ionization was applied for 50 to 420 m/z mass range.

2.2.2 Formation of 1 and 2. The syntheses of the N4py and ^{DMM}N4py ligands and the formation of corresponding [Mn^{II}(N4py)(OTf)](OTf) and [Mn^{II}(^{DMM}N4py)(OTf)](OTf) complexes were performed following previously reported procedures.[9] Recrystallization of each [Mn^{II}(N4py)(OTf)](OTf) and [Mn^{II}(^{DMM}N4py)(OTf)](OTf) was conducted by dissolving the crude product in a small amount of CH_3CN and layering this solution with ether, and further recrystallization was performed with vapor diffusion of ether into CH_3CN solution containing each metal complex.

Complex **1** and **2** were formed according to a previous literature report for the generation of **1**.[39] In this procedure, 5 equiv. H_2O_2 (30% H_2O_2 solution in H_2O) and 0.5 equiv. triethylamine (Et_3N) were added to aqueous solutions of [Mn^{II}(N4py)(OTf)](OTf) or [Mn^{II}(^{DMM}N4py)(OTf)](OTf) at 3 °C. After 2 hours of stirring, the solvent was removed under vacuum. Crystals of **1** were obtained from vapor diffusion of diethyl ether into an CH_3CN solution of **1**. Recrystallization of **2** by this procedure failed to yield crystals suitable for X-ray diffraction, hence characterization of **2** was carried out spectroscopically.

2.2.3 EPR Spectroscopy. EPR samples of **1** and **2** were prepared as follows. After generation of **1** and **2** in aqueous solution, H_2O was removed under vacuum. The resulting solid was dissolved in CF_3CH_2OH (TFE) to make 3 mM samples, and an aliquot of this solution (300 μL) was transferred to an EPR tube (4 mm, quartz). The samples were frozen by slow submersion in liquid nitrogen and were stored in a liquid N_2 dewar. An X-band Bruker EMXPlus spectrometer

(9.4 GHz), with a dual-mode cavity (Bruker ER4116DM), was used for collecting EPR spectra of the samples. The temperature (10 K) of an Oxford ESR900 continuous-flow liquid helium cryostat was monitored and controlled by an Oxford ITC503 cryostat controller. Detailed experimental parameters used in each experiment are included in the caption of the figure containing the EPR spectra (Figure 2.3).

2.2.4 Mn K-edge X-ray Absorption Spectroscopy. XAS samples of **1** (5 mM) and **2** (4 mM) were prepared in TFE, using the same procedure as detailed for the preparation of EPR samples (vide supra). A sample container, supported with Kapton tape, was used and filled with sample solutions, then frozen and stored under liquid N_2. XAS experiments were performed on beamline 9-3 at Stanford Synchrotron Radiation Lightsource (SSRL) with a Si(220) monochromator cooled by liquid nitrogen and a 31- or 100-element Ge array detector. The Mn K-edge X-ray absorption spectra were collected with the energy range of 6300 – 7250 eV, through fluorescence excitation at 7 K. Manganese foil spectra were also taken as a reference, and the internal calibration was achieved by setting the first inflection point of the K-edge energy to 6539.0 eV. The pre-edge areas were fitted using the Fityk curve fitting program with a pseudo Voigt function for the background fit, which was subtracted from pre-edge fit.[40] EXAFS data were processed using the *DEMETER* software.[41] EXAFS data were refined using $k^3\chi(k)$, with *FEFF6* calculations for the phase and amplitude functions.[42] Density Functional Theory (DFT) optimized coordinates of **1** and **2**, obtained by energy-minimizing the previously reported XRD structure, were used to obtain the *FEEF* functions. In each fit, the average distance of scattering paths, r, and the Debye-Waller factor, σ^2, were optimized, while n (the number of scatterers per shell) was systematically varied. The E_0 value was allowed to vary for each fit.

2.2.5 Density Functional Theory (DFT) Calculations. DFT geometry optimizations for **1** and **2** were carried out using the ORCA 4.0.1 software package.[43] All geometry optimizations and frequency calculations were performed at the spin-unrestricted level, using the Becke−Perdew (BP86) functional with the Ahlrichs def2-SVP basis sets for C and H atoms and the Ahlrichs def2-TZVP basis sets for Mn, O, and N atoms.[44-46] The resolution of identity (RI) approximation and the def2/J auxiliary basis set were applied.[47, 48] X-ray coordinates of **1** from a previous study were used as initial coordinates for **1**. For **2**, the previously reported X-ray coordinates for **1** were modified by adding two methyl groups and one methoxy group at the meta- and para- position on the appropriate pyridine rings. Both models were converged to the broken-symmetry S = 1/2 spin state. Solvation effects were not included in the optimizations. The optimized structures were confirmed by the absence of any negative frequencies. The Cartesian coordinates for **1** and **2** are provided in Appendix 2 (Tables A2.1 and A2.2).

2.2.6 Cyclic Voltammetry. Cyclic voltammograms were recorded using an Epsilon potentiostat (BAS) at room temperature. The working electrode was a glassy carbon electrode with a Pt wire as the counter electrode. A Ag/AgCl quasi-reference electrode was used and $Fc^{+/0}$ potential was measured as an external reference. For each electrochemical experiment, the working electrode was carefully polished and then rinsed with deionized water and ethanol. The experiments employed 2 mM solutions of **1** or **2** in 100 mM Bu_4NPF_6 electrolyte solution (in TFE).

2.2.7 Kinetics Experiments. All kinetic measurements were carried out with freshly made 0.5 mM solutions of **1** and **2** in TFE. This solvent was chosen to permit the most balanced comparison with the reactivity of $[Mn^{IV}(O)(N4py)]^{2+}$ and $[Mn^{IV}(O)(^{DMM}N4py)]^{2+}$, which were also examined in TFE.[37] In a typical experiment, 100 μL of a CH_2Cl_2 solution containing various concentrations of substrate, 2,4-di-*tert*-butylphenol (0.01 – 0.08 M) or 4-*tert*-butylphenol (0.05 –

0.15 M), was added to the cuvette. Each reaction was performed in duplicate (at a minimum) in a temperature-controlled cryostat at 298 K. First-order rate constants for each reaction, k_{obs}, were obtained by fitting the decay of the electronic absorption intensity at 565 nm. All the reactions performed in this study showed pseudo-first-order decay profiles to at least five half-lives. The second-order rate constant, k_2, was derived from a plot of k_{obs} versus various concentrations of substrate, which displayed a linear correlation. The reactivity of $[Mn^{IV}(O)(^{DMM}N4py)]^{2+}$ towards the O–H bond of 4-*tert*-butylphenol was measured following a previously reported procedure for hydrocarbon oxidation by this complex.[37] 1 mM of $[Mn^{II}(^{DMM}N4py)(OTf)](OTf)$ in 1 mL TFE was combined with 2 equiv. PhIO in 1 mL TFE at room temperature to form the Mn^{IV}-oxo complex. After 10 minutes, which was the point of maximum formation of the electronic absorption bands of $[Mn^{IV}(O)(^{DMM}N4py)]^{2+}$, the cuvet containing the solution of the Mn^{IV}-oxo complex was put in a cryostat temperature-controlled at –40 °C. The substrate was added in a 100 µL aliquot of CH_2Cl_2 and k_{obs} was calculated by fitting the decay of the electronic absorption signal of $[Mn^{IV}(O)(^{DMM}N4py)]^{2+}$ at 940 nm. The second-order rate constant was obtained from the linear correlation between a plot of k_{obs} versus four different concentrations of the substrate (Figure 2.10). Reactions with the same substrate concentration were repeated three times (at a minimum). An Eyring plot for the reaction of **2** with 0.15 M 4-*tert*-butylphenol were determined by collecting pseudo-first order rate constants for this reaction over the 288 – 303 K temperature range (Figure 2.11). Each reaction was carried out in triplicate (at a minimum). An estimate of k_2 for the reaction of **2** with at 4-*tert*-butylphenol at –40 °C was derived using the Eyring equation (equation 1) with the $\Delta H^{\ddagger}$ obtained from the from Eyring plot and the k_2 of **2** at 25 °C.[49, 50]

$$\frac{k_2{}^{T_2}}{k_2{}^{T_1}} = \frac{T_2}{T_1} \times e^{\left(\frac{\Delta H^{\ddagger}}{RT_1} - \frac{\Delta H^{\ddagger}}{RT_2}\right)} \qquad \text{(equation 1)}$$

2.2.8 Product Analysis. Quantification of organic products and analysis of Mn products from the reaction mixtures of **1** or **2** with 2,4-di-*tert*-butylphenol (10 equiv.) were performed by GC-MS and iodometric titration,[51] respectively. Organic products were injected onto the GC-MS after separating Mn products by passing the crude reaction solution through a silica plug and eluting with an excess of ethyl acetate. The oxidized organic product was identified as the dimerized phenol (4,4',6,6'-tetra-*tert*-butyl-2,2'-biphenyldiol) by comparing GC and ^{1}H NMR data with those of authentic sample. The organic product was quantified using a calibration curve made using authentic sample and naphthalene as an internal standard. Quantification and iodometric titration of organic and manganese product were performed in triplicate.

2.3 Results and Discussion

2.3.1 Formation and Optical Properties of 1and 2. The formation of **1** was performed following a previously reported procedure, where 5 equiv. 30% H_2O_2 (in H_2O) and 0.5 equiv. Et_3N are added to an 0.57 mM aqueous solution of [Mn^{II}(OTf)(N4py)](OTf) at 3°C.[39] Following this reaction by electronic absorption spectroscopy reveals the formation of bands at 439, 563, and 666 nm (22 800, 17 800, and 15 000 cm^{-1}). The positions of these transitions are essentially identical to those previously reported for **1** in MeCN.[39] The only difference we observe is a decrease in the extinction coefficients for the 17 800 and 15 000 cm^{-1} bands (from respective values of 830 and 680 M^{-1} cm^{-1} in MeCN to 570 and 480 M^{-1} cm^{-1} in water). This change in extinction coefficient might imply a lower formation of **1** in this case; however, as described below, EPR and Mn K-edge XAS data are both supportive of high formation of **1** under these conditions. Thus, we attribute the change in extinction coefficient to the change in solvent polarity.

Treatment of an aqueous solution of $[Mn^{II}(OTf)(^{DMM}N4py)](OTf)$ with 5 equiv. 30% H_2O_2 and 0.5 equiv. Et_3N at 3°C results in the appearance of a new, dark green chromophore (**2**) with electronic absorption features essentially identical to those of **1** (Figure 2.2 and Table 2.1). After its formation in aqueous solution, the solvent is removed in vacuo and the isolated solid is dissolved in TFE for reactivity studies. **2** is remarkably stable in TFE, with a half-life of at least 17 hours at 25 °C. This stability is similar to that reported for **1**.[39] The only appreciable difference between the electronic absorption spectra of **1** and **2** is the slightly higher absorption intensity for **2**. For example, the electronic absorption band at 17 800 cm^{-1} for **2** has an extinction coefficient of 600 M^{-1} cm^{-1}, which is increased by ca. 5% compared to that of **1**. This change in intensity could reflect an intrinsic difference between the extinction coefficients of **1** and **2** or could be due to a marginally lower formation of **1** under these reaction conditions. In any case, the nearly identical electronic absorption signals of **1** and **2** are suggestive of strong similarities in the geometric and electronic structures of these complexes. For comparison, the analogous Mn^{IV}-oxo complexes, $[Mn^{IV}(O)(N4py)]^{2+}$ and $[Mn^{IV}(O)(^{DMM}N4py)]^{2+}$ showed noticeable differences by optical spectroscopy, with the former complex having a lower energy near-infrared absorption maxima (red-shift of ca. 300 cm^{-1} relative to $[Mn^{IV}(O)(^{DMM}N4py)]^{2+}$).[9] In addition, $[Mn^{IV}(O)(^{DMM}N4py)]^{2+}$ showed the onset of more intense optical signals at energies above 21 000 cm^{-1}, while $[Mn^{IV}(O)(N4py)]^{2+}$ contained only weak electronic absorption bands from 15 000–25 000 cm^{-1}.[9] Thus, the optical perturbations of the mononuclear Mn^{IV}-oxo complexes are far greater than those observed for **1** and **2**.

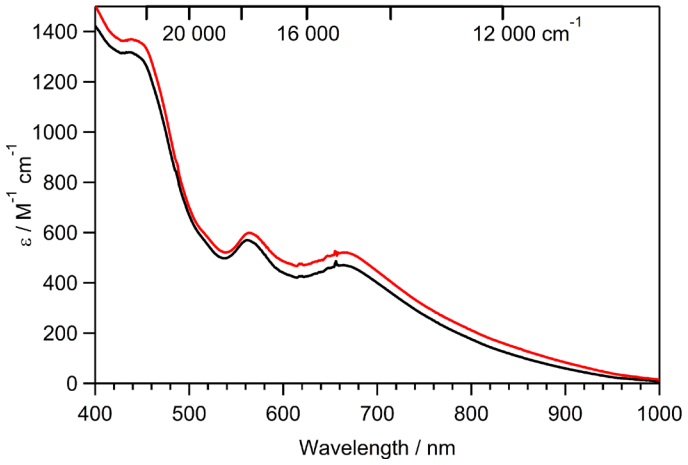

Figure 2.2. UV/vis spectra of 1 (black line) and **2** (red line) in H_2O at 3 °C.

Table 2.1. Spectroscopic characteristics of **1** and **2**.

complex	λ_{max} [cm^{-1}]	g_{eff}	a [mT]
1	22 800, 17 800, 15 000	2.01	7.7
2	22 700, 17 800, 15 000	2.01	7.7

We also investigated the reactivity of $[Mn^{II}(OH_2)(2pyN2Q)](OTf)_2$ with H_2O_2 under these conditions. However, the addition of 5 equiv. H_2O_2 and 0.5 equiv. Et_3N to an aqueous solution of $[Mn^{II}(OH_2)(2pyN2Q)](OTf)_2$ at 3°C resulted in the formation of broad, weak electronic absorption bands near 400 and 700 nm region (Appendix 2, Figure A2.1). The resulting solution was a pale yellow color, distinct from the dark green solutions observed for **1** and **2**. While the exact nature of the product of this reaction is unclear at present, we can conclude that the reaction of $[Mn^{II}(OH_2)(2pyN2Q)](OTf)_2$ with H_2O_2 under these conditions does not result in the formation of the $[Mn^{III}Mn^{IV}(\mu\text{-}O)_2(2pyN2Q)_2]^{3+}$ complex. We speculate that the 2pyN2Q ligand is too bulky to support a bis(μ-oxo)dimanganese(III,IV) species.

2.3.2 Characterization of 1 and 2 by EPR and X-ray absorption spectroscopies. Our previous investigations of **1** included the characterization of the structure of this complex using Mn K-edge X-ray absorption spectroscopy (XAS) and X-ray crystallography.[39] Despite our efforts, we have been unable to obtain crystals of **2** suitable for X-ray crystallography. Nonetheless, we have determined electronic and structural properties for **2** utilizing spectroscopic methods, including electron paramagnetic resonance (EPR) and XAS techniques. In addition, we describe here the spectroscopic characterization of **1** in TFE, as this solvent was used for the kinetic experiments.

In TFE, the perpendicular-mode, X-band EPR spectra of both **1** and **2** display sixteen-line signals centered at 342.5 mT (g=2.011) and 342.2 mT (g=2.012), respectively (Figure 2.3 and Table 2.1). The *g*-value and number of signals are characteristic of the mixed-valent bis(μ-O)$Mn^{III}Mn^{IV}$ core.[52-54] Spectra for both **1** and **2** show an absence of features from Mn^{II} starting materials. In the frozen TFE solution, **1** showed a hyperfine splitting of 7.7 mT centered at 342.5 mT, which is quite similar to the EPR parameters previously reported for a sample in butyronitrile (*g*=2.089 with a hyperfine splitting of 7.6 mT).[39] The frozen TFE solution of **2** afforded essentially identical EPR parameters to those of **1** (hyperfine splitting of 7.7 mT with *g*=2.012). A recently reported mixed-valent bis(μ-oxo)dimanganese(III,IV) species with the dpaq ligand (dpaq=2-[bis(pyridin-2-yl-methyl)]amino-*N*-quinolin-8-yl-acetamidate) also showed a characteristic sixteen-line EPR signal near *g*=2, but with *g*-values and hyperfine parameters perturbed compared to those of **1** and **2** (*g*=1.996 and 15 mT hyperfine splitting).[18]

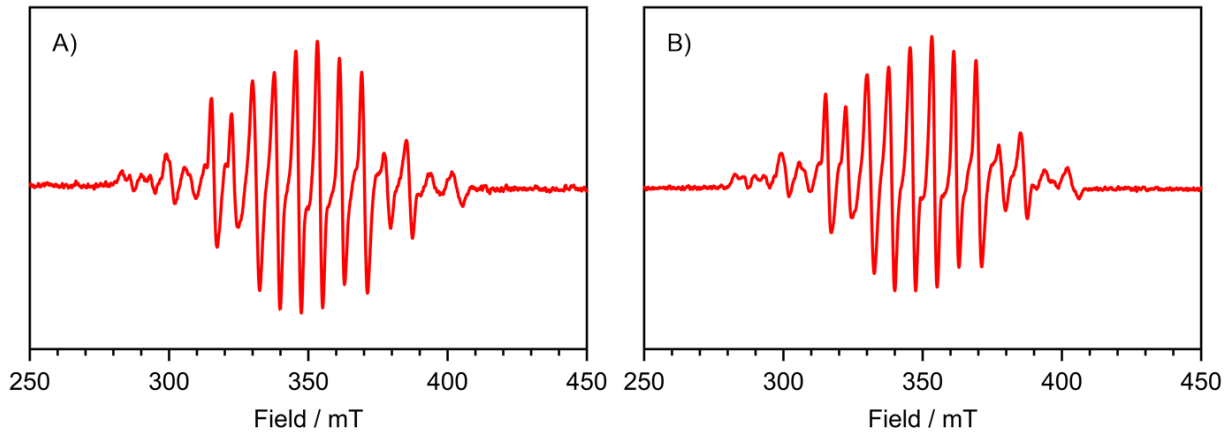

Figure 2.3. Perpendicular-mode X-band EPR spectra of 3 mM frozen TFE solutions of $[Mn^{III}Mn^{IV}(\mu\text{-}O)_2(N4py)_2]^{3+}$ (A) and $[Mn^{III}Mn^{IV}(\mu\text{-}O)_2(^{DMM}N4py)_2]^{3+}$ (B). Experimental conditions: 9.6419 GHz microwave frequency (A), 9.6397 GHz microwave frequency (B), 10 K, 0.002 mW microwave power, 0.3 mT modulation amplitude, 100 kHz modulation frequency, 81.92 ms time constant, and 10 000 point resolution.

Further comparison of the geometric and electronic structures of **1** and **2** in frozen TFE solution were obtained from analysis of Mn K-edge XAS data. X-ray absorption near edge structure (XANES) of **1** and **2** revealed nearly identical edge and pre-edge properties (Figure 2.4 and Table 2.2). The pre-edge peak, which arises from Mn-based 1s → 3d excitations, appears at an energy comparable to that of the pre-edge feature observed for the superoxidized Mn^{III}/Mn^{IV} form of manganese catalase (ca. 6540 eV).[55] Each pre-edge feature of complexes **1** and **2** is best fit to two electronic transitions (Table 2.2). The total area of these pre-edge features are comparable between **1** and **2** and are also quite similar to the areas observed for the mono-nuclear Mn^{IV}-oxo complexes $[Mn^{IV}(O)(N4py)]^{2+}$ and $[Mn^{IV}(O)\ (^{DMM}N4py)]^{2+}$ (Table 2.2). The total pre-edge area for **1** and **2** is within the rage of the pre-edge values of reported for superoxidized Mn catalase and other bis(μ-oxo)dimanganese(III,IV) model complexes.[55-57] The edge energies, from the first inflection point, of **1** and **2** were 6549.8 eV and 6550.1 eV, respectively. The edge energy of **1** in

TFE compares well with that reported for **1** in water (6550.6 eV), which implies that there is no significant solvent effect on the edge energy.[39] These edge energies are also comparable to those of the mononuclear Mn^{IV}-oxo complexes, $[Mn^{IV}(O)(N4py)]^{2+}$ and $[Mn^{IV}(O)(^{DMM}N4py)]^{2+}$ complex (Table 2.2).

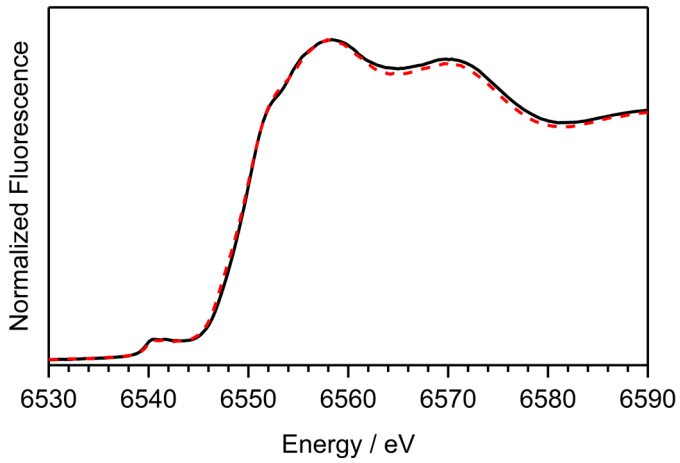

Figure 2.4. Normalized Mn K-edge XANES spectra of **1** (black solid trace) and **2** (red dashed trace) in CF_3CH_2OH at 7 K.

Table 2.2. Mn K-edge XANES properties of **1**, **2**, $[Mn^{IV}(O)(N4py)]^{2+}$ and $[Mn^{IV}(O)(^{DMM}N4py)]^{2+}$.

complex	**pre-edge [eV]**	**pre-edge area[a]**	**edge [eV]**
1[b]	6540.3, 6542.0	22.9	6549.8
2[b]	6540.3, 6541.5	19.6	6550.6
$[Mn^{IV}(O)(N4py)]^{2+}$[c]	6541.6	18.9	6550.8
$[Mn^{IV}(O)(^{DMM}N4py)]^{2+}$[c]	6541.3	19.6	6550.3
[a] Pre-edge area was multiplied by 100 after obtaining from fits of the XAS spectrum normalized to the post-edge line. [b] This work. [c] Reference 9.			

The Fourier transform (FT) of the EXAFS spectrum for **1** shows four major peaks at radial distances (*R*') of 1.3, 1.7, 2.1 (shoulder), and 2.4 Å (Figure 2.5). The inner peaks at 1.3 and 1.7 Å

are attributed to O and N shells, while the peaks at 2.1 and 2.4 Å have contributions from C and Mn scattering, respectively. The EXAFS data for **1** are best fit with shells at 1.82 Å (2 atom, O shell), 2.12 (2 atom, N shell), 2.91 (7 atom, C shell), and 2.63 Å (1 atom, Mn shell). Table 2.3 and Appendix 2, Table A2.3 contain information regarding the EXAFS fits. (Acceptable fits could also be obtained with 4 and 3 atom nitrogen shells at distances of 2.18 and 2.14 Å, respectively. These fits are shown in Appendix 2, Table A2.3. However, these fits showed larger σ^2 values than the 2 atom shell included in Table 2.3). These Mn-scatterer distances are in excellent agreement with those previously reported from an EXAFS analysis of **1** in H_2O, which are included in Table 2.3 for comparison. The previously reported X-ray crystal structure of the $[PF6]^-$ salt of **1** ($[Mn^{III}Mn^{IV}(\mu\text{-}O)_2(N4py)_2](PF_6)_3$) showed average Mn–O and Mn–N bond lengths of 1.81 and 2.12 Å, respectively,[39] which are in excellent agreement with the EXAFS-derived distances (Table 2.3).

The FT EXAFS spectrum of **2** has several features in the Mn–O/N or Mn···C scattering regions, which are quite similar in appearance to those of **1** (Figure 2.5). The data are well fit with Mn-scattering distances essentially identical to those of **1** (Table 2.3 and Appendix 2, Table A2.4). The only difference between the fits is the resolution of a second N shell at 2.22 Å in the case of **2**. Therefore, the results of this analysis of EXAFS data for **1** and **2** confirms the conclusion, based on electronic absorption and EPR data, that the Mn centers in these complexes have remarkably similar geometric and electronic structures.

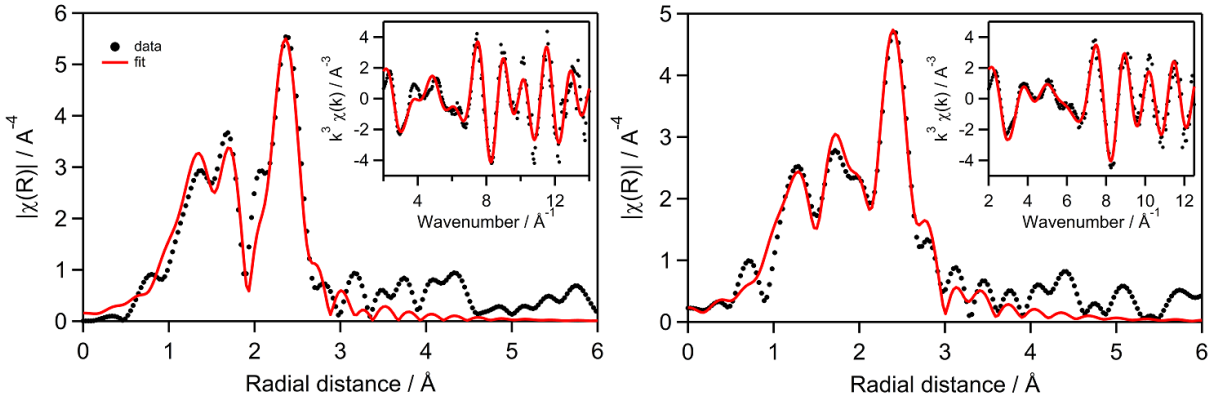

Figure 2.5. Fourier transforms of EXAFS data [$k^3\chi(k)$] and raw EXAFS spectra (inset) of **1** (left) and **2** (right). Experimental data are in black dots while fits are red traces.

Table 2.3. EXAFS fitting data for dimanganese(III,IV) complexes **1** and **2**.[a]

	Mn···Mn			**Mn–O**			**Mn–N**			**Mn···C**		
	n	*r* (Å)	σ^2 (Å^2)	*n*	*r* (Å)	σ^2 (Å^2)	*n*	*r* (Å)	σ^2 (Å^2)	*n*	*r* (Å)	σ^2 (Å^2)
1	1	2.63	2.4	2	1.82	4.8	2	2.12	7.9	7	2.91	8.3
1-H$_2$O	1	2.63	1.8	2	1.79	4.3	2	2.00	3.6	4	2.81	4.4
							1	2.17	3.7	5	2.96	4.2
2	1	2.65	3.0	2	1.82	6.0	2	2.05	6.1	6	2.92	4.2
							2	2.22	2.5			

[a] Fourier transform range: $k = 2 – 14$ Å^{-1} for 1 and $k = 2 – 12.5$ Å^{-1} for 2. Debye-Waller factors are reported as × 10^3. Data for $[Mn^{III}Mn^{IV}(\mu\text{-}O)_2(N4py)_2]^{3+}$ in H_2O (1-H_2O) are from reference 39.

2.3.3 DFT structures of 1 and 2. DFT optimized structures of **1** and **2** were derived to yield further geometric information for the two complexes (Figure 2.6 and Table 2.4). Overall, there is excellent agreement between the DFT-derived metric parameters and those determined experimentally (i.e., by X-ray crystallography for **1** and EXAFS analysis for **2**). For example, the Mn···Mn (2.7 Å for **1** and **2**), average Mn–O (1.82 Å for **1** and **2**), and average Mn–N (2.13 Å for **1** and 2.12 Å for **2**) separations from the DFT structures are essentially the same as the corresponding bond lengths from the EXAFS analysis performed in this study (Table 2.3). No

distinguishable bond angle distortion was observed between the DFT structures of **1** and **2** (Table 2.4). It should be noted that the DFT-computed structures provide slightly different values of Mn–O and Mn–N distances on each Mn center, suggesting valence localization of the Mn^{III} and Mn^{IV} states. In complex **1**, the mean of Mn(1)–O and Mn(1)–N distances are 1.84 and 2.20 Å, respectively, while the corresponding bond distances for the Mn(2) center are 1.80 and 2.06 Å. Similarly, **2** displayed a small difference in Mn-ligand bond lengths between the two metal centers (average Mn–O lengths of 1.84 and 1.81 Å and average Mn–N lengths of 2.20 and 2.05 Å for Mn(1) and Mn(2), respectively). For comparison, the previously reported DFT-derived structure of $[Mn^{IV}(O)(N4py)]^{2+}$ showed Mn–O and average Mn–N of 1.69 and 2.19 Å, respectively, while the DFT structure of $[Mn^{IV}(O)(^{DMM}N4py)]^{2+}$ had slightly shorter Mn–O and average Mn–N distances of 1.68 and 2.03 Å.[9, 58] The most notable difference between the structures of the mononuclear Mn^{IV}-oxo and bis(μ-oxo)dimanganese(III,IV) complexes is the large change in average Mn–N distance for the former. In those systems, the shorter Mn–N distances in $[Mn^{IV}(O)(^{DMM}N4py)]^{2+}$, which are in accordance with the more electron-donating properties of this ligand, were associated with noticeable changes in spectroscopic properties, $Mn^{IV/III}$ reduction potential, and hydrogen- and oxygen-atom transfer reactivity.[9] For the bis(μ-oxo)dimanganese(III,IV) complexes **1** and **2**, their very similar DFT structures are consistent with the nearly identical spectroscopic properties of these complexes.

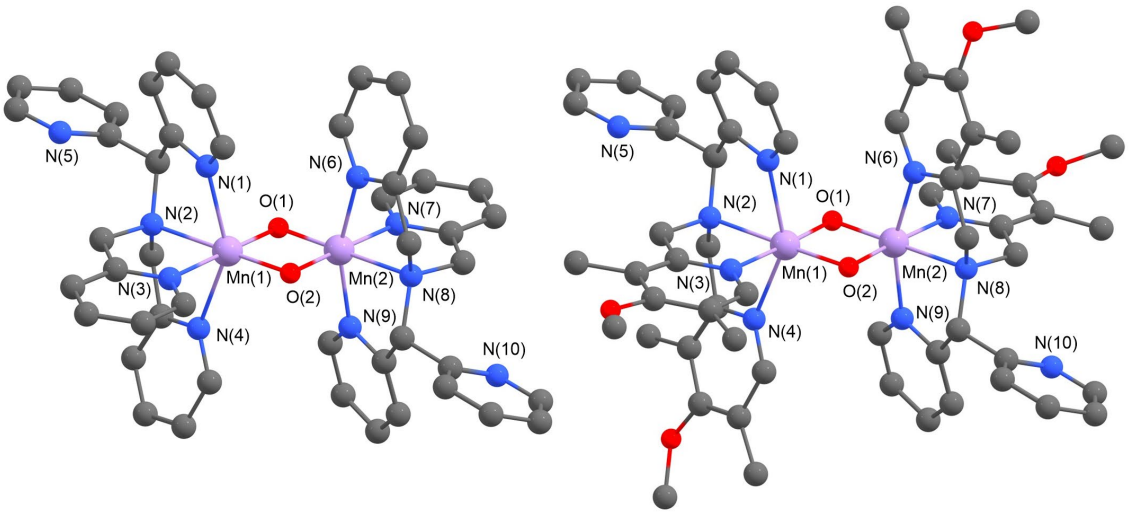

Figure 2.6. Optimized molecular structures of **1** (left) and **2** (right) from DFT calculations.

Table 2.4. Metric parameters of bond distances (Å) and angles (°) for **1** and **2** from DFT calculation and X-ray diffraction data of **1** $[Mn^{III}Mn^{IV}(\mu\text{-}O)_2(N4py)_2](PF_6)_3$ for comparison.[a]

	1 XRD	**1 DFT**	**2 DFT**
Mn [1] ··· Mn [2]	2.648(2)	2.701	2.695
Mn [1] – O [1]	1.834(5)	1.846	1.851
Mn [1] – O [2]	1.835(6)	1.835	1.835
Mn [2] – O [1]	1.767(6)	1.799	1.797
Mn [2] – O [2]	1.787(5)	1.806	1.813
Mn [1] – N [1]	2.236(8)	2.260	2.289
Mn [1] – N [2]	2.129(6)	2.192	2.176
Mn [1] – N [3]	2.091(5)	2.069	2.057
Mn [1] – N [4]	2.274(8)	2.290	2.258
Mn [2] – N [6]	2.045(7)	2.045	2.027
Mn [2] – N [7]	2.055(5)	2.059	2.046
Mn [2] – N [8]	2.094(7)	2.106	2.094
Mn [2] – N [9]	2.012(6)	2.033	2.041
O [1] – Mn [1] – O [2]	84.0(2)	83.22	83.64
O [1] – Mn [2] – O [2]	87.4(2)	85.38	85.80
Mn [1] – O [1] – Mn [2]	94.6(2)	95.63	95.28
Mn [1] – O [2] – Mn [2]	93.9(2)	95.77	95.28
N [1] – Mn [1] – N [4]	149.6(2)	148.52	148.79
N [6] – Mn [2] – N [9]	159.3(2)	159.16	159.23

[a] Reference 39.

2.3.4 Electrochemical Properties of 1and 2. Cyclic voltammetry (CV) experiments were carried out to reveal the electrochemical properties of **1** and **2** in TFE. The CV scan of **1** shows a quasi-reversible wave at E_{pc}= +0.84 V and $E_{1/2}$= +0.90 V vs. Fc^{+}/Fc (ΔE_p=0.122 V, with ΔE_p for Fc^{+}/Fc of 0.116 V under the same experimental conditions). The corresponding CV scan for **2** shows a similar, quasi-reversible process at a slightly lower potential (E_{pc}= +0.62 V and $E_{1/2}$= + 0.74 V vs. Fc^{+}/Fc; ΔE_p=0.189 V). In both cases, this redox event is attributed to the $Mn^{IV}Mn^{IV}$ / $Mn^{III}Mn^{IV}$ couple. The reduction potential of the $Mn^{IV}Mn^{IV}$ / $Mn^{III}Mn^{IV}$ couple of various bis(μ-oxo)dimanganese(III,IV) complexes has been shown to be strongly dependent on the identity of the supporting ligand. For example, CV investigations of $[Mn^{III}Mn^{IV}(\mu\text{-}O)_2(phen)_4]^{3+}$ revealed a quasi-reversible redox wave at +0.90 V (vs. Fc^{+}/Fc; $Ag/AgNO_3$ as reference electrode, $(C_5Me_5)_2Fe$ as internal standard, measured in MeCN), which was assigned as the $Mn^{IV}Mn^{IV}$ / $Mn^{III}Mn^{IV}$ couple.[16] Similar experiments for $[Mn^{III}Mn^{IV}(\mu\text{-}O)_2(bpy)_4]^{3+}$ in MeCN (bpy=2,2'-bipyridine) yielded a much lower $E_{1/2}$ of +1.32 V vs. SCE (approximately +0.27 V vs. Fc^{+}/Fc) for the $Mn^{IV}Mn^{IV}$ / $Mn^{III}Mn^{IV}$ couple.[59, 60] Bis(μ-oxo)dimanganese(III,IV) complexes with anionic salpn ligands (salpn=1,3-bis (salicylideneiminato)propane) and its derivatives showed much more negative $E_{1/2}$ values of −1.12 V to −0.58 V (vs. Fc^{+}/Fc; SCE as reference electrode, measured in CH_2Cl_2) for the $Mn^{IV}Mn^{IV}$ / $Mn^{III}Mn^{IV}$ couple.[61, 6263] For the salpn systems, the range of potentials reflected the values observed for the most electron-rich and electron-poor ligands, respectively. Thus, the $Mn^{IV}Mn^{IV}$ / $Mn^{III}Mn^{IV}$ reduction potentials observed for **1** and **2** fall within the broad range of values observed for this class of compound. The variation in potentials between **1** and **2** is also rather minor considering the large variations observed within the class. With respect to the ratio of cathodic peak and anodic peak current ratio, **1** and **2** showed values of 1.3 and 1.0,

respectively, which indicates both dimanganese species are chemically stable upon this redox process.

The CV traces of both **1** and **2** show an additional, prominent reduction wave at E_{pc}=−0.24 and E_{pc}=−0.40 V, respectively (vs. Fc^{+}/Fc; see Figure 2.7). These redox events are attributed to $Mn^{III}Mn^{IV}$ to $Mn^{III}Mn^{III}$ reduction. As we observed for the $Mn^{IV}Mn^{IV}$ / $Mn^{III}Mn^{IV}$ couples of **1** and **2**, complex **2**, which features the more electron-donating ^{DMM}N4py ligand, shows a more negative peak potential. We also note that the difference in peak potentials for the separate $Mn^{IV}Mn^{IV}$ / $Mn^{III}Mn^{IV}$ and $Mn^{III}Mn^{IV}$ / $Mn^{III}Mn^{III}$ couples of **1** and **2** is ca. 0.2 V for each couple. An additional, small reduction peak was observed at ca. +0.14 and −0.02 V in the CV traces of **1** and **2**, respectively (Figure 2.7, asterisks). These reduction peaks are not observed for CV scans that did not reach potentials where $Mn^{III}Mn^{IV}$ to $Mn^{IV}Mn^{IV}$ oxidation occurs (Appendix 2, Figure A2.2). Thus, we attribute these minor features to some decay product that results from formation of the $Mn^{IV}Mn^{IV}$ species.

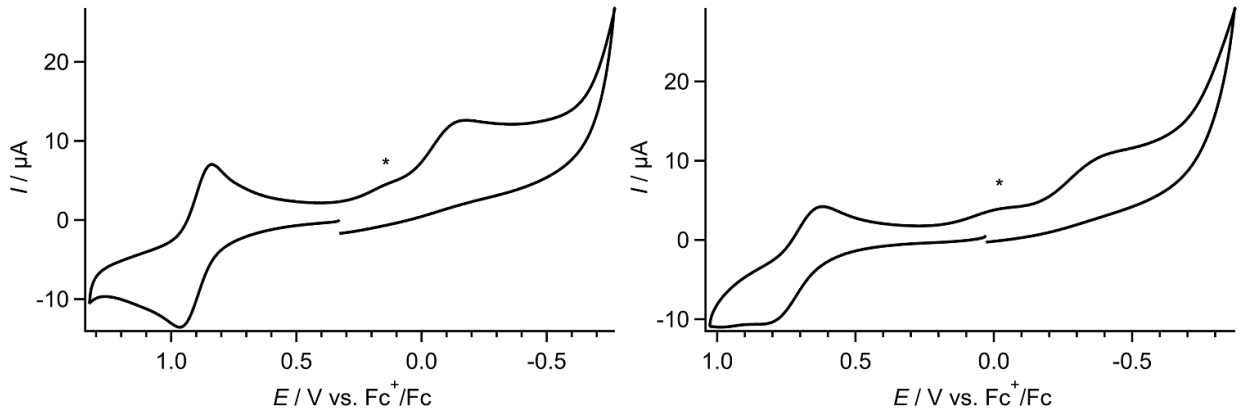

Figure 2.7. Cyclic voltammograms of **1** (left) and **2** (right). Solutions were 2 mM in CF_3CH_2OH with 0.1 M $TBAPF_6$. 0.1 V s^{-1} scan rate.

The $Mn^{III}Mn^{IV}$ to $Mn^{III}Mn^{III}$ peak potentials of **1** and **2** can be compared with the Mn^{IV}/Mn^{III} peak potentials of the mono-nuclear Mn^{IV}-oxo complexes $[Mn^{IV}(O)(N4py)]^{2+}$ and $[Mn^{IV}(O)(^{DMM}N4py)]^{2+}$. The $[Mn^{IV}(O)(N4py)]^{2+}$ complex showed a Mn^{IV}/Mn^{III} peak potential at +0.37 V (vs. Fc^{+}/Fc) in TFE:DCM electrolyte solution (1:1 with 0.1 M NBu_4PF_6), while the corresponding peak potential for $[Mn^{IV}(O)(^{DMM}N4py)]^{2+}$ was lower, at +0.06 V in TFE (with 0.1 M NBu_4PF_6).[9, 58] In general, the Mn^{IV}-oxo complexes have Mn^{IV}/Mn^{III} peak potentials ca. 0.5 V higher than their bis(μ-oxo)dimanganese(III,IV) analogues, which indicates substantially greater oxidizing power for the Mn^{IV}-oxo complexes. We also note that there is a smaller shift in potentials due to ligand perturbations for the bis(μ-oxo)dimanganese(III,IV) complexes compared to the Mn^{IV}-oxo species (0.16 V versus 0.31 V, respectively). This can be interpreted that two metal centers possibly level out the effect of ligand perturbations in bis(μ-oxo)dimanganese(III,IV) complexes.

2.3.5 Phenol Oxidation by 1 and 2. To assess the influence of variations between the N4py and ^{DMM}N4py ligands on the reactivity of **1** and **2**, we explored the reactions of these complexes with substituted phenols. Both of these complexes showed a very slow reaction with 2,4,6-tri-*tert*-butylphenol in CF_3CH_2OH at 25°C (Appendix 2, Figure A2.3). This comparatively slow reactivity (ca. two orders of magnitude slower when compared with k_{obs} for the corresponding reaction with 2,4-di-*tert*-butylphenol) is attributed to the steric bulk of this substrate and the metal complexes. Inspection of the space-filling models of the DFT structures of **1** and **2** shows that access to oxo ligands is hindered by pyridine groups of the N4py and ^{DMM}N4py ligands (Figure 2.6). Similarly, the mixed-valent $[Mn^{III}Mn^{IV}(\mu\text{-}O)_2(dpaq)_2]^{+}$ complex showed an order of magnitude difference of reactivity between 2,6-di-*tert*-butylphenol and 2,4-di-*tert*-butylphenol due to the steric encumbrance of the $[Mn^{III}Mn^{IV}(\mu\text{-}O)_2(dpaq)_2]^{+}$ complex and 2,6-di-*tert*-butylphenol

substrate.[18] Further reactivity studies were carried out with 2,4-di-*tert*-butylphenol and 4-*tert*-butylphenol, which showed faster reaction rates more amenable to kinetic interrogation.

The addition of the less bulky 2,4-di-*tert*-butylphenol substrate to **1** and **2** at 25 °C in CF_3CH_2OH resulted in the disappearance of the characteristic optical bands of each complex. Representative data for the reaction of **1** with 50 equivalents 2,4-di-*tert*-butylphenol are shown in Figure 2.8. For both **1** and **2**, the addition of an excess of 2,4-di-*tert*-butylphenol caused a first-order decay of the optical signals at 565 nm (Figure 2.8, inset). Fits of the change in absorbance versus time led to the determination of pseudo-first order rate constants (k_{obs}). Second-order rate constants (k_2) were obtained by plotting pseudo-first-order rate constants versus substrate concentration (Figure 2.9). This procedure yielded k_2 values of 2.7×10^{-1} and 2.2×10^{-1} M^{-1} s^{-1} for **1** and **2**, respectively. Thus, there is no significant difference in 2,4-di-*tert*-butylphenol oxidation rates for these complexes.

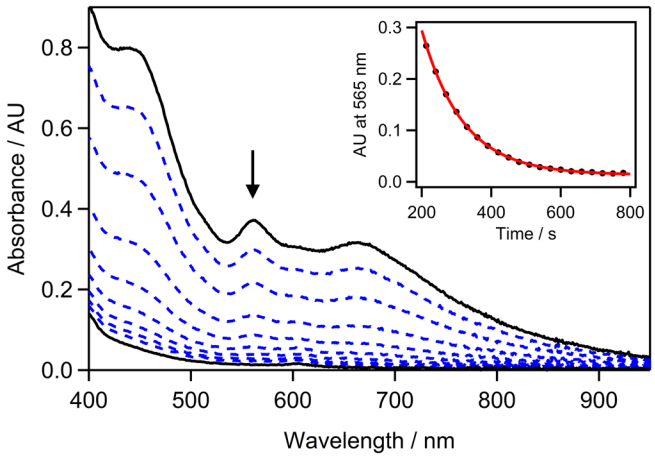

Figure 2.8. Electronic absorption spectra of 0.5 mM 1 upon the addition of 50 equiv. 2,4-di-*tert*-butylphenol in CF_3CH_2OH at 25 °C. Inset: Time trace of the change in absorbance at 565 nm (black solid circles) and fit to first-order decay process (solid red trace).

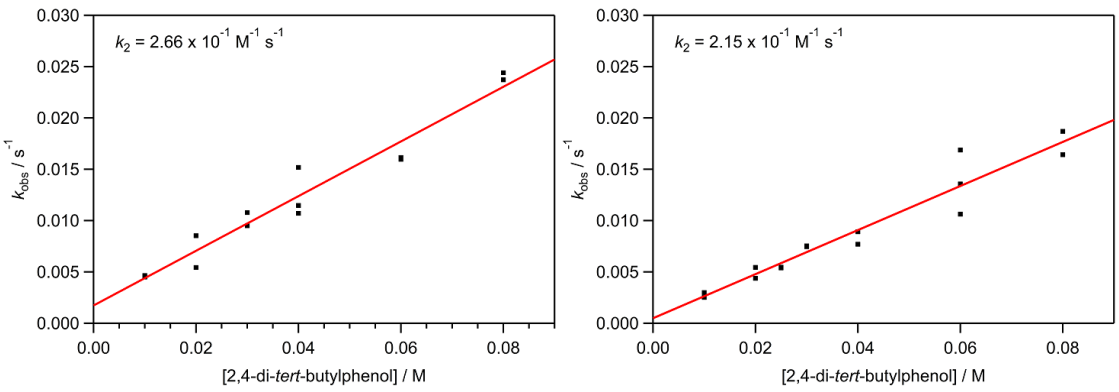

Figure 2.9. Pseudo-first order rates as a function of 2,4-di-*tert*-butylphenol concentration for **1** (left) and **2** (right) in CF_3CH_2OH at 25 °C.

The 2,4-di-*tert*-butylphenol oxidation rates of **1** and **2** can be compared with that reported for $[Mn^{III}Mn^{IV}(\mu\text{-}O)_2(dpaq)_2]^+$. That system showed a substantially larger second-order rate constant of 6.6(6) M^{-1} s^{-1} in CH_3CN at 25 °C.[18] The basis for the enhanced reactivity of $[Mn^{III}Mn^{IV}(\mu\text{-}O)_2(dpaq)_2]^+$ is unclear at present, although we note that the dpaq ligand is anionic, with an amide-donor, while the N4py and ^{DMM}N4py ligands are neutral. Product analysis was conducted to determine the reaction stoichiometry between 2,4-di-*tert*-butylphenol and complexes **1** and **2**. The manganese products were investigated by iodometric titration. A titration of solutions of **1** and **2** following reaction with 10 equiv. 2,4-di-*tert*-butylphenol afforded average Mn oxidation states of 2.10 ± 0.02 and 2.18 ± 0.08, respectively. Although these values can imply Mn^{II} as the metal products, we do not observe any signals typical of Mn^{II} in EPR spectra of reaction solutions (Appendix 2, Figure A2.4). Thus, the iodometric titration is consistent with a mixture of Mn^{II} and Mn^{III} products. A GC-MS analysis of these reaction solutions revealed the formation of ca. 1 equiv. dimerized phenol product (4,4',6,6'-tetra-*tert*-butyl-2,2'-biphenyldiol) relative to the initial concentration of the dimanganese(III,IV) complex. On the basis of these results, we concluded that

each bis(μ-O)$Mn^{III}Mn^{IV}$ complex reacts with 2 equiv. 2,4-di-*tert*-butylphenol to produce 1 equiv. dimerized phenol and a $Mn^{II}Mn^{III}$ product (which may or may not remain dinuclear).

The lack of variation in the reaction rates of **1** and **2** with 2,4-di-*tert*-butylphenol stands in contrast to that observed for hydrocarbon oxidation by the corresponding mononuclear Mn^{IV}-oxo complexes $[Mn^{IV}(O)(N4py)]^{2+}$ and $[Mn^{IV}(O)(^{DMM}N4py)]^{2+}$. In that case, the former complex reacted with hydrocarbons ca. 10-fold more rapidly.[9] The reactivity enhancement for the Mn^{IV}-oxo complex was related to the bond distances between the Mn^{IV} centers and equatorial N atom from the picolyl groups of the ligand, with an average Mn^{IV}–N contraction of 0.028 Å calculated for $[Mn^{IV}(O)^{DMM}N4py]^{2+}$ relative to that of $[Mn^{IV}(O)N4py]^{2+}$. In the DFT structures of the dimeric analogues **1** and **2**, the corresponding Mn^{IV}–N distances show a smaller difference of 0.016 Å, possibly due to intramolecular steric hindrance from the presence of two ligands. The DFT prediction of reduced ligand-field perturbations between **1** and **2** are fully compatible with the identical appearance of the electronic absorption spectra of these complexes (Table 2.4 and Figure 2.2). Gamelin and co-workers have assigned the visible electronic absorption features of bis(μ-oxo)dimanganese(III,IV) as predominantly deriving from Mn^{III} and Mn^{IV} ligand-field transitions.[64] Thus, the strong similarity between the electronic absorption band maxima and intensities of **1** and **2** are indicative of nearly identical ligand fields. Taken together, the spectroscopic, computational, and kinetic data demonstrate that electronic perturbations caused by the electron-rich ^{DMM}N4py ligand are muted in the bis(μ-oxo)dimanganese(III,IV) complexes as compared to the monomeric Mn^{IV}-oxo species.

2.3.5 Comparison of O-H Bond Reactivity of Bridging and Terminal Mn^{IV}-oxo Complexes. The oxidation reactivities of bridging and terminal manganese-oxo species was compared using **2** and $[Mn^{IV}(O)(^{DMM}N4py)]^{2+}$, the latter of which possesses lower oxidative

reactivity than $[Mn^{IV}(O)(N4py)]^{2+}$ and is thus amendable to kinetic investigations with phenols.[9] Due to the high reactivity of $[Mn^{IV}(O)^{DMM}N4py)]^{2+}$ compared to **2**, we chose 4-*tert*-butylphenol as the substrate for this comparison, as this substrate has a stronger O–H bond than 2,4-di-*tert*-butylphenol and thus reacts more slowly. With this choice of substrate, the reaction of $[Mn^{IV}(O)(^{DMM}N4py)]^{2+}$ with 4-*tert*-butylphenol was performed at −40 °C in CF3CH2OH. This reaction was kinetically well behaved (Figure 2.10 and Appendix 2, Figure A2.5), permitting the determination of a second-order rate constant (k_2) of 3.8×10^{-1} M^{-1} s^{-1} at −40 °C. Similar experiments performed for **2** at 25 °C in CF_3CH_2OH revealed a k_2 of 2.3×10^{-3} M^{-1} s^{-1} (Figure 2.10). Thus, even with a 65 unit increase in temperature, **2** reacts roughly 100-fold slower than $[Mn^{IV}(O)(^{DMM}N4py)]^{2+}$. To permit a more rigorous comparison between the reactivities of these complexes, we estimated the rate of reaction of **2** with 4-*tert*-butylphenol at −40°C using an Eyring plot assembled using k_{obs} values for the reaction of **2** with 300 equiv. 4-*tert*-butylphenol from 15 to 30 °C (Figure 2.11). The Eyring equation from the plot yields an estimated k_2 for O–H oxidation reactivity of **2** at −40 °C of 1.2 × 10–6 M^{-1} s^{-1}. Thus, the terminal Mn^{IV}-oxo adduct $[Mn^{IV}(O)(^{DMM}N4py)]^{2+}$ reacts with a common substrate five thousand-fold faster than its bridging analogue **2**. For comparison, a million-fold rate enhancement for C–H bond activation was previously reported by Que and co-workers in comparing an opened diamond core $[(HO)Fe^{III}(\mu\text{-}O)Fe^{IV}(O)]^{2+}$ complex relative to its closed-core $[Fe^{3.5}Fe^{3.5}(\mu\text{-}O)_2]^{3+}$ counterpart.[65]

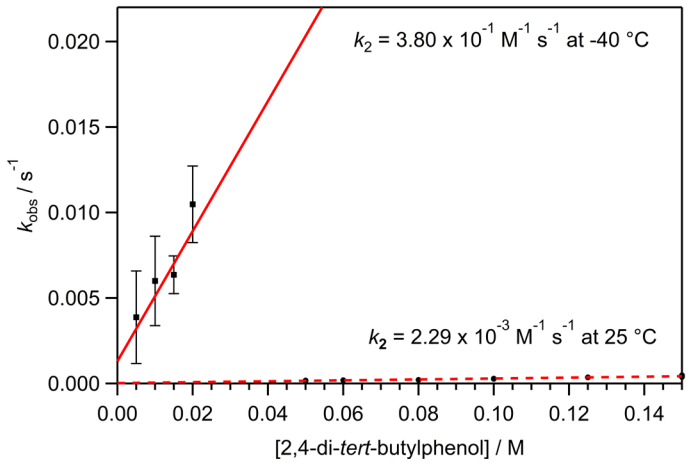

Figure 2.10. Pseudo-first order rates as a function of 4-*tert*-butylphenol concentration for **2** (0.5 mM, black solid circles) and $[Mn^{IV}(O)(^{DMM}N4Py)]^{2+}$ (0.5 mM, black solid squares) in CF_3CH_2OH at 25 and –40 °C, respectively. Error bars indicate ± standard deviation values from three replicates.

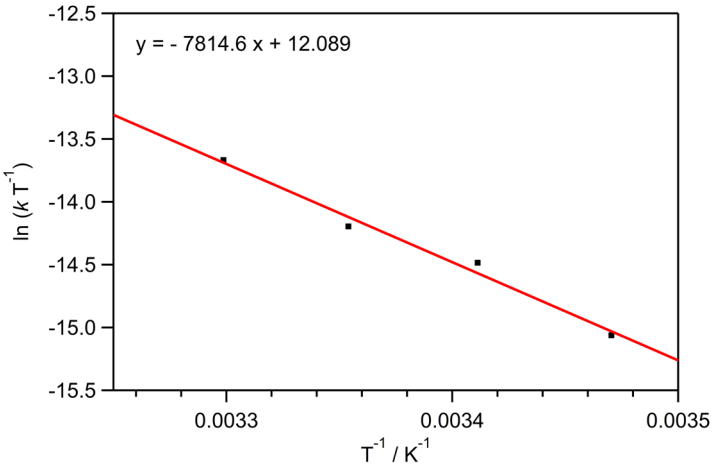

Figure 2.11. Eyring plot from the reaction of **2** and 4-*tert*-butylphenol (0.15 M) in CF_3CH_2OH at varied temperatures (288 K – 303 K).

2.4 Conclusion

In this paper we investigated geometric and electronic structures and O–H bond activation reactivity of bis(μ-O)dimanganese(III,IV) species coordinated by the N4py and ^{DMM}N4py ligands.

Spectroscopic data, including from electronic absorption, EPR, and Mn K-edge XAS experiments, revealed only marginal differences in the geometric and electronic structures of the two bis(μ-O)$Mn^{III}Mn^{IV}$ complexes. This conclusion is also supported by the DFT-computed structures of **1** and **2**, which showed only minor variations in Mn^{IV}–N bond distances when compared to DFT structures of the mono-nuclear Mn^{IV}-oxo analogues. Comparison of electrochemical properties of **1** and **2** showed a smaller gap between the reduction potential for the Mn_2(III,IV)/Mn_2(III,III) couple of **1** and **2** than that of Mn^{IV}/Mn^{III} reduction for $[Mn^{IV}(O)(N4py)]^{2+}$ and $[Mn^{IV}(O)(^{DMM}N4py)]^{2+}$. The oxidative reactivities of the bis(μ-O)$Mn^{III}Mn^{IV}$ complexes toward the O–H bond of 2,4-di-tert-butylphenol are barely distinguishable, reflecting the geometric and electronic similarities between **1** and **2**. These similar reactivities contrast with the more dramatic reactivity difference between $[Mn^{IV}(O)(N4py)]^{2+}$ and $[Mn^{IV}(O)(^{DMM}N4py)]^{2+}$, where the former reacts with hydrocarbons ten-fold more rapidly than the latter.[9] The generation of the bis(μ-O)$Mn^{III}Mn^{IV}$ complex **2** also allowed us to compare the relative oxidative capabilities of bridging and terminal Mn^{IV}-oxo units, with the latter being more reactive towards a common phenol substrate by a factor of 10^5.

2.5 Notes and References

1. Pecoraro, V. L.; Baldwin, M. J.; Gelasco, A., Interaction of Manganese with Dioxygen and Its Reduced Derivatives. *Chemical Reviews* **1994,** *94* (3), 807-826.

2. Cotruvo, J. A.; Stich, T. A.; Britt, R. D.; Stubbe, J., Mechanism of Assembly of the Dimanganese-Tyrosyl Radical Cofactor of Class Ib Ribonucleotide Reductase: Enzymatic Generation of Superoxide Is Required for Tyrosine Oxidation via a Mn(III)Mn(IV) Intermediate. *Journal of the American Chemical Society* **2013,** *135* (10), 4027-4039.

3. Young, I. D.; Ibrahim, M.; Chatterjee, R.; Gul, S.; Fuller, F. D.; Koroidov, S.; Brewster, A. S.; Tran, R.; Alonso-Mori, R.; Kroll, T.; Michels-Clark, T.; Laksmono, H.; Sierra, R. G.;

Stan, C. A.; Hussein, R.; Zhang, M.; Douthit, L.; Kubin, M.; De Lichtenberg, C.; Vo Pham, L.; Nilsson, H.; Cheah, M. H.; Shevela, D.; Saracini, C.; Bean, M. A.; Seuffert, I.; Sokaras, D.; Weng, T.-C.; Pastor, E.; Weninger, C.; Fransson, T.; Lassalle, L.; Bräuer, P.; Aller, P.; Docker, P. T.; Andi, B.; Orville, A. M.; Glownia, J. M.; Nelson, S.; Sikorski, M.; Zhu, D.; Hunter, M. S.; Lane, T. J.; Aquila, A.; Koglin, J. E.; Robinson, J.; Liang, M.; Boutet, S.; Lyubimov, A. Y.; Uervirojnangkoorn, M.; Moriarty, N. W.; Liebschner, D.; Afonine, P. V.; Waterman, D. G.; Evans, G.; Wernet, P.; Dobbek, H.; Weis, W. I.; Brunger, A. T.; Zwart, P. H.; Adams, P. D.; Zouni, A.; Messinger, J.; Bergmann, U.; Sauter, N. K.; Kern, J.; Yachandra, V. K.; Yano, J., Structure of photosystem II and substrate binding at room temperature. *Nature* **2016,** *540* (7633), 453-457.

4. Sheng, Y.; Abreu, I. A.; Cabelli, D. E.; Maroney, M. J.; Miller, A.-F.; Teixeira, M.; Valentine, J. S., Superoxide Dismutases and Superoxide Reductases. *Chemical Reviews* **2014,** *114* (7), 3854-3918.

5. Boal, A. K.; Cotruvo, J. A.; Stubbe, J.; Rosenzweig, A. C., Structural Basis for Activation of Class Ib Ribonucleotide Reductase. *Science* **2010,** *329* (5998), 1526-1530.

6. Wu, A. J.; Penner-Hahn, J. E.; Pecoraro, V. L., Structural, Spectroscopic, and Reactivity Models for the Manganese Catalases. *Chemical Reviews* **2004,** *104* (2), 903-938.

7. Weinberg, D. R.; Gagliardi, C. J.; Hull, J. F.; Murphy, C. F.; Kent, C. A.; Westlake, B. C.; Paul, A.; Ess, D. H.; McCafferty, D. G.; Meyer, T. J., Proton-Coupled Electron Transfer. *Chemical Reviews* **2012,** *112* (7), 4016-4093.

8. In this paper, we refer PCET reaction as a reaction indicating coupled movements of proton and electron encompassing related reactions, i.e. concerted proton-electron transfer (CPET) and sequential mechanism of proton transfer following by electron transfer (PT-ET or ET-PT).

9. Massie, A. A.; Denler, M. C.; Cardoso, L. T.; Walker, A. N.; Hossain, M. K.; Day, V. W.; Nordlander, E.; Jackson, T. A., Equatorial Ligand Perturbations Influence the Reactivity of Manganese(IV)-Oxo Complexes. *Angewandte Chemie International Edition* **2017,** *56* (15), 4178-4182.

10. Taguchi, T.; Stone, K. L.; Gupta, R.; Kaiser-Lassalle, B.; Yano, J.; Hendrich, M. P.; Borovik, A. S., Preparation and properties of an MnIV–hydroxide complex: proton and electron transfer at a mononuclear manganese site and its relationship to the oxygen evolving complex within photosystem II. *Chemical Science* **2014,** *5* (8), 3064-3071.

11. Kanady, J. S.; Tsui, E. Y.; Day, M. W.; Agapie, T., A Synthetic Model of the Mn3Ca Subsite of the Oxygen-Evolving Complex in Photosystem II. *Science* **2011,** *333* (6043), 733-736.

12. Gerey, B.; Gouré, E.; Fortage, J.; Pécaut, J.; Collomb, M.-N., Manganese-calcium/strontium heterometallic compounds and their relevance for the oxygen-evolving center of photosystem II. *Coordination Chemistry Reviews* **2016,** *319*, 1-24.

13. Sahu, S.; Goldberg, D. P., Activation of Dioxygen by Iron and Manganese Complexes: A Heme and Nonheme Perspective. *Journal of the American Chemical Society* **2016,** *138* (36), 11410-11428.

14. Yin, G., Understanding the Oxidative Relationships of the Metal Oxo, Hydroxo, and Hydroperoxide Intermediates with Manganese(IV) Complexes Having Bridged Cyclams: Correlation of the Physicochemical Properties with Reactivity. *Accounts of Chemical Research* **2013,** *46* (2), 483-492.

15. Pecoraro, V. L.; Hsieh, W.-Y., In Search of Elusive High-Valent Manganese Species That Evaluate Mechanisms of Photosynthetic Water Oxidation. *Inorganic Chemistry* **2008,** *47* (6), 1765-1778.

16. Larsen, A. S.; Wang, K.; Lockwood, M. A.; Rice, G. L.; Won, T.-J.; Lovell, S.; Sadilek, M.; Turecek, F.; Mayer, J. M., Hydrocarbon oxidation by bis-μ-oxo manganese dimers: electron transfer, hydride transfer, and hydrogen atom transfer mechanisms. *J. Am. Chem. Soc.* **2002,** *124* (34), 10112-10123.

17. Kang, H.; Cho, J.; Cho, K.-B.; Nomura, T.; Ogura, T.; Nam, W., Mononuclear Manganese-Peroxo and Bis(μ-oxo)dimanganese Complexes Bearing a Common N-Methylated Macrocyclic Ligand. *Chemistry - A European Journal* **2013,** *19* (42), 14119-14125.

18. Sankaralingam, M.; Jeon, S. H.; Lee, Y.-M.; Seo, M. S.; Ohkubo, K.; Fukuzumi, S.; Nam, W., An amphoteric reactivity of a mixed-valent bis(μ-oxo)dimanganese(iii,iv) complex acting as an electrophile and a nucleophile. *Dalton Transactions* **2016,** *45* (1), 376-383.

19. Caudle, M. T.; Pecoraro, V. L., Mechanism for the Reduction of the Mixed-Valent MnIIIMnIV[2-OHsalpn]2+Complex by Tertiary Amines. *Inorganic Chemistry* **2000,** *39* (25), 5831-5837.

20. Chen, H.; Tagore, R.; Das, S.; Incarvito, C.; Faller, J. W.; Crabtree, R. H.; Brudvig, G. W., General Synthesis of Di-μ-oxo Dimanganese Complexes as Functional Models for the Oxygen Evolving Complex of Photosystem II. *Inorganic Chemistry* **2005,** *44* (21), 7661-7670.

21. Limburg, J., A Functional Model for O-O Bond Formation by the O2-Evolving Complex in Photosystem II. *Science* **1999,** *283* (5407), 1524-1527.

22. Wieghardt, K., The Active Sites in Manganese-Containing Metalloproteins and Inorganic Model Complexes. *Angewandte Chemie International Edition in English* **1989,** *28* (9), 1153-1172.

23. Goodson, P. A.; Glerup, J.; Hodgson, D. J.; Michelsen, K.; Weihe, H., Syntheses and characterization of binuclear manganese(III,IV) and -(IV,IV) complexes with ligands related to N,N'-bis(2-pyridylmethyl)-1,2-ethanediamine. *Inorganic Chemistry* **1991,** *30* (26), 4909-4914.

24. Massie, A. A.; Sinha, A.; Parham, J. D.; Nordlander, E.; Jackson, T. A., Relationship between Hydrogen-Atom Transfer Driving Force and Reaction Rates for an Oxomanganese(IV) Adduct. *Inorganic Chemistry* **2018,** *57* (14), 8253-8263.

25. Leto, D. F.; Massie, A. A.; Rice, D. B.; Jackson, T. A., Spectroscopic and Computational Investigations of a Mononuclear Manganese(IV)-Oxo Complex Reveal Electronic Structure Contributions to Reactivity. *Journal of the American Chemical Society* **2016,** *138* (47), 15413-15424.

26. Rice, D. B.; Massie, A. A.; Jackson, T. A., Manganese–Oxygen Intermediates in O–O Bond Activation and Hydrogen-Atom Transfer Reactions. *Accounts of Chemical Research* **2017,** *50* (11), 2706-2717.

27. Yin, G.; Danby, A. M.; Kitko, D.; Carter, J. D.; Scheper, W. M.; Busch, D. H., Oxidative Reactivity Difference among the Metal Oxo and Metal Hydroxo Moieties: pH Dependent Hydrogen Abstraction by a Manganese(IV) Complex Having Two Hydroxide Ligands. *Journal of the American Chemical Society* **2008,** *130* (48), 16245-16253.

28. Wu, X.; Seo, M. S.; Davis, K. M.; Lee, Y.-M.; Chen, J.; Cho, K.-B.; Pushkar, Y. N.; Nam, W., A Highly Reactive Mononuclear Non-Heme Manganese(IV)–Oxo Complex That Can Activate the Strong C–H Bonds of Alkanes. *Journal of the American Chemical Society* **2011,** *133* (50), 20088-20091.

29. Cho, K.-B.; Shaik, S.; Nam, W., Theoretical Investigations into C–H Bond Activation Reaction by Nonheme MnIVO Complexes: Multistate Reactivity with No Oxygen Rebound. *The Journal of Physical Chemistry Letters* **2012,** *3* (19), 2851-2856.

30. Chen, J.; Lee, Y.-M.; Davis, K. M.; Wu, X.; Seo, M. S.; Cho, K.-B.; Yoon, H.; Park, Y. J.; Fukuzumi, S.; Pushkar, Y. N.; Nam, W., A Mononuclear Non-Heme Manganese(IV)–Oxo Complex Binding Redox-Inactive Metal Ions. *Journal of the American Chemical Society* **2013,** *135* (17), 6388-6391.

31. Kurahashi, T.; Kikuchi, A.; Shiro, Y.; Hada, M.; Fujii, H., Unique Properties and Reactivity of High-Valent Manganese−Oxo versus Manganese−Hydroxo in the Salen Platform. *Inorganic Chemistry* **2010,** *49* (14), 6664-6672.

32. Zaragoza, J. P. T.; Siegler, M. A.; Goldberg, D. P., A Reactive Manganese(IV)–Hydroxide Complex: A Missing Intermediate in Hydrogen Atom Transfer by High-Valent Metal-Oxo Porphyrinoid Compounds. *Journal of the American Chemical Society* **2018,** *140* (12), 4380-4390.

33. Borovik, A. S., Role of metal–oxo complexes in the cleavage of C–H bonds. *Chemical Society Reviews* **2011,** *40* (4), 1870-1874.

34. Du, J.; Miao, C.; Xia, C.; Lee, Y.-M.; Nam, W.; Sun, W., Mechanistic Insights into the Enantioselective Epoxidation of Olefins by Bioinspired Manganese Complexes: Role of Carboxylic Acid and Nature of Active Oxidant. *ACS Catalysis* **2018,** *8* (5), 4528-4538.

35. Milan, M.; Carboni, G.; Salamone, M.; Costas, M.; Bietti, M., Tuning Selectivity in Aliphatic C–H Bond Oxidation of N-Alkylamides and Phthalimides Catalyzed by Manganese Complexes. *ACS Catalysis* **2017,** *7* (9), 5903-5911.

36. Wu, X.; Seo, M. S.; Davis, K. M.; Lee, Y. M.; Chen, J.; Cho, K. B.; Pushkar, Y. N.; Nam, W., A highly reactive mononuclear non-heme manganese(IV)-oxo complex that can activate the strong C-H bonds of alkanes. *J Am Chem Soc* **2011,** *133* (50), 20088-91.

37. Massie, A. A.; Denler, M. C.; Cardoso, L. T.; Walker, A. N.; Hossain, M. K.; Day, V. W.; Nordlander, E.; Jackson, T. A., Equatorial Ligand Perturbations Influence the Reactivity of Manganese(IV)-Oxo Complexes. *Angew Chem Int Ed Engl* **2017,** *56* (15), 4178-4182.

38. Baglia, R. A.; Zaragoza, J. P. T.; Goldberg, D. P., Biomimetic Reactivity of Oxygen-Derived Manganese and Iron Porphyrinoid Complexes. *Chemical Reviews* **2017,** *117* (21), 13320-13352.

39. Leto, D.; Chattopadhyay, S.; Day, V.; Jackson, T., Reaction landscape of a pentadentate N5-ligated MnII complex with O2˙− and H2O2 includes conversion of a peroxomanganese(iii) adduct to a bis(μ-oxo)dimanganese(iii,iv) species. *Dalton Transactions* **2013,** *42* (36), 13014-undefined.

40. Wojdyr, M., Fityk: a general-purpose peak fitting program. *Journal of Applied Crystallography* **2010,** *43* (5-1), 1126-1128.

41. Ravel, B.; Newville, M., ATHENA, ARTEMIS, HEPHAESTUS: data analysis for X-ray absorption spectroscopy using IFEFFIT. *Journal of Synchrotron Radiation* **2005,** *12* (4), 537-541.

42. Rehr, J. J.; Mustre De Leon, J.; Zabinsky, S. I.; Albers, R. C., Theoretical x-ray absorption fine structure standards. *Journal of the American Chemical Society* **1991,** *113* (14), 5135-5140.

43. Neese, F., The ORCA program system. *WIREs Computational Molecular Science* **2012,** *2* (1), 73-78.

44. Becke, A. D., Density functional calculations of molecular bond energies. *The Journal of Chemical Physics* **1986,** *84* (8), 4524-4529.

45. Perdew, J. P., Density-functional approximation for the correlation energy of the inhomogeneous electron gas. *Physical Review B* **1986,** *33* (12), 8822-8824.

46. Weigend, F.; Ahlrichs, R., Balanced basis sets of split valence, triple zeta valence and quadruple zeta valence quality for H to Rn: Design and assessment of accuracy. *Physical Chemistry Chemical Physics* **2005,** *7* (18), 3297-3305.

47. Neese, F., An improvement of the resolution of the identity approximation for the formation of the Coulomb matrix. *Journal of Computational Chemistry* **2003,** *24* (14), 1740-1747.

48. Weigend, F., Accurate Coulomb-fitting basis sets for H to Rn. *Physical Chemistry Chemical Physics* **2006,** *8* (9), 1057-1065.

49. Eyring, H., The Activated Complex and the Absolute Rate of Chemical Reactions. *Chemical Reviews* **1935,** *17* (1), 65-77.

50. Eyring, H., The Activated Complex in Chemical Reactions. *The Journal of Chemical Physics* **1935,** *3* (2), 107-115.

51. Perez-Benito, J. F.; Brillas, E.; Arias, C., Iodimetric determinations in organic solvents: Determination of manganese oxidation states in methylene chloride solutions. *Canadian Journal of Chemistry* **1990,** *68* (1), 79-81.

52. Cooper, S. R.; Dismukes, G. C.; Klein, M. P.; Calvin, M., Mixed valence interactions in di-.mu.-oxo bridged manganese complexes. Electron paramagnetic resonance and magnetic susceptibility studies. *Journal of the American Chemical Society* **1978,** *100* (23), 7248-7252.

53. Usov, O. M.; Grigoryants, V. M.; Tagore, R.; Brudvig, G. W.; Scholes, C. P., Hyperfine Coupling to the Bridging 17O in the Di-μ-oxo Core of a MnIII−MnIV Model Significant to the Core Electronic Structure of the O2-Evolving Complex in Photosystem II. *Journal of the American Chemical Society* **2007,** *129* (39), 11886-11887.

54. Yano, J.; Sauer, K.; Girerd, J.-J.; Yachandra, V. K., Single Crystal X- and Q-Band EPR Spectroscopy of a Binuclear Mn2(III,IV) Complex Relevant to the Oxygen-Evolving Complex of Photosystem II. *Journal of the American Chemical Society* **2004,** *126* (24), 7486-7495.

55. Stemmler, T. L.; Sturgeon, B. E.; Randall, D. W.; Britt, R. D.; Penner-Hahn, J. E., Spectroscopic Characterization of Inhibitor Interactions with the Mn(III)/Mn(IV) Core inLactobacillus plantarumManganese Catalase. *Journal of the American Chemical Society* **1997,** *119* (39), 9215-9225.

56. Krewald, V.; Lassalle-Kaiser, B.; Boron, T. T.; Pollock, C. J.; Kern, J.; Beckwith, M. A.; Yachandra, V. K.; Pecoraro, V. L.; Yano, J.; Neese, F.; Debeer, S., The Protonation States of Oxo-Bridged MnIV Dimers Resolved by Experimental and Computational Mn K Pre-Edge X-ray Absorption Spectroscopy. *Inorganic Chemistry* **2013,** *52* (22), 12904-12914.

57. Plaksin, P. M.; Stoufer, R. C.; Mathew, M.; Palenik, G. J., Novel antiferromagnetic oxo-bridged manganese complex. *Journal of the American Chemical Society* **1972,** *94* (6), 2121-2122.

58. Leto, D. F.; Ingram, R.; Day, V. W.; Jackson, T. A., Spectroscopic properties and reactivity of a mononuclear oxomanganese(iv) complex. *Chemical Communications* **2013,** *49* (47), 5378-5380.

59. Morrison, M. M.; Sawyer, D. T., Redox reactions of di-.mu.-oxo bridged binuclear manganese(IV) and -(III) complexes. *Journal of the American Chemical Society* **1977,** *99* (1), 257-258.

60. Tsierkezos, N. G., Cyclic Voltammetric Studies of Ferrocene in Nonaqueous Solvents in the Temperature Range from 248.15 to 298.15 K. *Journal of Solution Chemistry* **2007,** *36* (3), 289-302.

61. Baldwin, M. J.; Gelasco, A.; Pecoraro, V. L., The effect of protonation on [Mn(IV)(?2-O)]2 complexes. *Photosynthesis Research* **1993,** *38* (3), 303-308.

62. Bao, D.; Millare, B.; Xia, W.; Steyer, B. G.; Gerasimenko, A. A.; Ferreira, A.; Contreras, A.; Vullev, V. I., Electrochemical Oxidation of Ferrocene: A Strong Dependence on the Concentration of the Supporting Electrolyte for Nonpolar Solvents. *The Journal of Physical Chemistry A* **2009,** *113* (7), 1259-1267.

63. The effect of supporting electrolyte on electrochemical measurements was not considered for conversion of reduction potentials.

64. Gamelin, D. R.; Kirk, M. L.; Stemmler, T. L.; Pal, S.; Armstrong, W. H.; Penner-Hahn, J. E.; Solomon, E. I., Electronic Structure and Spectroscopy of Manganese Catalase and Di-.mu.-oxo [MnIIIMnIV] Model Complexes. *Journal of the American Chemical Society* **1994,** *116* (6), 2392-2399.

65. Xue, G.; De Hont, R.; Münck, E.; Que, L., Million-fold activation of the [Fe2(μ-O)2] diamond core for C–H bond cleavage. *Nature Chemistry* **2010,** *2* (5), 400-405.

Chapter 3

Spectroscopic Characterization of Mono- and Dinuclear Manganese(IV) Adducts Formed by Ceric Ammonium Nitrate and Water

Electronic absorption spectra of the formation of a dinuclear manganese adduct were collected by Shannon D. Jones.

3.1 Introduction

Ceric ammonium nitrate (CAN) has been broadly utilized as a one-electron oxidant in organic synthesis and water oxidation.[1-7] The Ce^{IV} ion in CAN is useful due to its strong oxidizing ability (+1.37 V vs. SCE in aqueous 1 M HNO_3 for the $Ce^{IV/III}$ reduction potential)[8] and high Lewis acidity, which facilitates a number of oxidative transformations of organic molecules.[7-10] Based on these properties, CAN is commonly used as a sacrificial oxidant in water oxidation, where transition-metal complexes are employed as catalysts. Furthermore, it has been proposed that Ce^{IV} could play a role similar to that of Ca^{II} at the oxygen evolving complex (OEC) in photosystem II, by leading a water molecule close to a catalytic transition-metal center to initiate O–O bond formation.[1] Due to the increasing use of CAN in various oxidation reactions involving small molecules and transition metal complexes, there is much interest in understanding the transition metal intermediates formed in reactions with CAN.

Several recent studies have provided experimental evidence of intermediates generated by reacting CAN with metal complexes. Reactions of CAN with low-valent iron or manganese complexes (Fe^{II} and Mn^{II}) generate metal(IV)-oxo complexes, showing the strong oxidizing character of the Ce^{IV}. In those reactions, the oxo ligand is derived from water added to the reaction.[11-15] As an example, Nam and co-workers reported the formation of a mononuclear Mn^{IV}-oxo complex from the reaction of $[Mn^{II}(CF_3SO_3)_2(BQCN)]$ (BQCN = *N*,*N*'-dimethyl-*N*,*N*'-bis(8-quinolyl)cyclohexanediamine; Figure 3.1) with 4 equiv. CAN in 9:1 MeCN:H_2O or 9:1 acetone:H_2O at 0 °C.[11] Although the intermediate complex formed in the reaction is proposed as $[Mn^{IV}(O)(OH_2)(BQCN)]^{2+}$, it does not show a broad near-IR band which is a characteristic feature for Mn^{IV}-oxo species. The electron paramagnetic resonance (EPR) spectrum of the intermediate complex shows a positive signal at $g_{eff} \approx 4$, which is indicative of a manganese(IV) species. The

resonance Raman spectrum of the Mn^{IV} intermediate displays the Mn–O vibration at 707 cm^{-1}, although it is at the very low-end of those values reported for Mn^{IV}-oxo species (712 to 750 cm^{-1}).[16-19] The origin of the oxygen atom in the Mn^{IV} intermediate complex was speculated using the electrospray ionization mass spectrometry (ESI-MS) with $H_2{}^{18}O$. The experimental results show major peaks at m/z 242.5 and 484.1, which can account for $[Mn^{IV}(O)(OH_2)(BQCN)]^{2+}$ or $[Mn^{IV}(OH)_2(BQCN)]^{2+}$ and $[Mn^{IV}(O)(OH)(BQCN)]^{+}$, respectively. When the labeled water was added, peaks at m/z 244.5 and 488.1 were observed. As a result, the authors concluded that the oxygen atom in the Mn^{IV} intermediate is from water. In another study, Sastri, Comba, and co-workers reported the formation of two Mn^{IV}-oxo adducts from the reaction of two Mn^{II} complexes supported by pentadentate N5 ligands in the bispidine family with 4 equiv. CAN in 9:1 MeCN:H_2O or 9:1 acetone:H_2O at 5 °C.[12] Characterization of these Mn^{IV}-oxo species was conducted by electronic absorption spectroscopy and ESI-MS, which respectively showed broad near-IR bands at 970 and 975 nm and mass and isotope patterns consistent with $[Mn^{IV}(O)L]^{2+}$ ions (L = L^1 and L^2; Figure 3.1). Together, these studies demonstrate how CAN serves as an oxidant to make metal(IV)-oxo complexes.

A different type of intermediate generated in a reaction of metal(II) complex, CAN, and water is illustrated in a study with an iron complex. Fillol, Costas, Que, and co-workers have provided experimental evidence for Ce^{IV} acting as a Lewis acid and inner-sphere oxidant in an iron-oxo-cerium intermediate.[1] They reported a formation of $[(mcp)Fe^{IV}(O)(\mu\text{-}O)Ce^{IV}(NO_3)_3]^{+}$ (mcp = (*N*,*N*′-dimethyl-*N*,*N*′-bis(2-pyridylmethyl)-1,2-cis-diaminocyclohexane; Figure 3.1) from a reaction of $[Fe^{IV}(O)(mcp)]^{2+}$ and CAN in aqueous solution at 25 °C. They characterized this intermediate using cryospray ionization high-resolution mass spectrometry (CSI-HRMS) and resonance Raman (rR). The authors suggest an additional role of Ce^{IV} ion as a Lewis acid to initiate

water oxidation with the iron catalyst based on the formulation proposed for the Fe^{IV}-oxo intermediate.

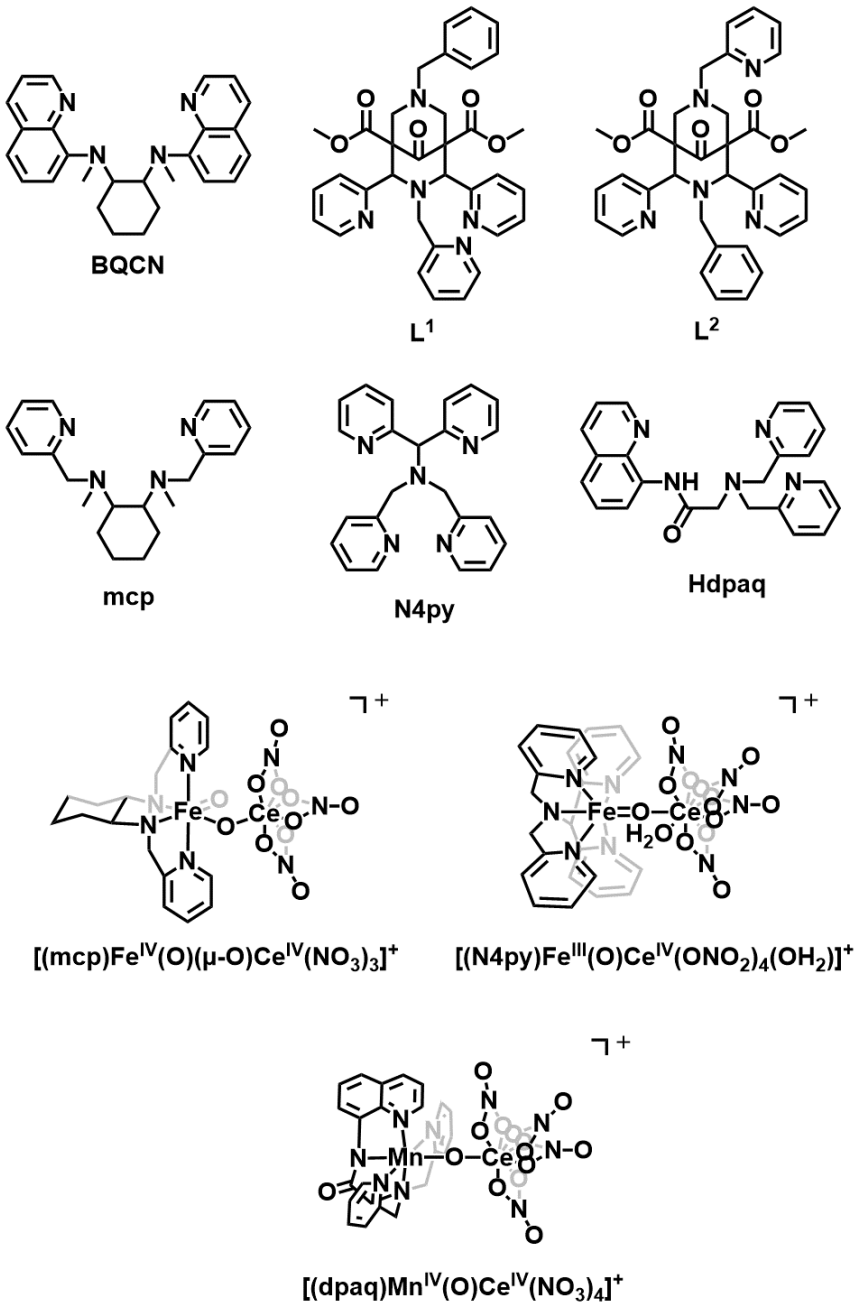

Figure 3.1. Ligand structures described in the context and characterized or proposed structures of Ce^{IV}-bound iron or manganese species.

Similarly, Que and co-workers reported an XRD structure of $[(N4py)Fe^{III}(O)Ce^{IV}(OH_2)(ONO_2)_4]^+$ (N4py = *N*,*N*-bis(2-pyridylmethyl)-*N*-bis(2-pyridyl)methylamine; Figure 3.1), where Ce^{IV} and Fe^{III} are bound to oxo ligand to form an oxo-bridged hetero-bi-metallic complex.[20] This intermediate complex was generated from a reaction of $[Fe^{II}(NCMe)(N4py)]^{2+}$ and 2 equiv. CAN with 10 μL water in MeCN or $[Fe^{IV}(O)(N4py)]^{2+}$ with 4.5 equiv. CAN in MeCN. Interestingly, the authors observed an equilibrium between the hetero-bi-metallic complex and $[Fe^{IV}(O)(N4py)]^{2+}$ dependent on the amount of H_2O in the reaction solution. This reversible electron transfer is possibly ascribed to the changes in the electronic environment of Ce^{IV} and Ce^{III}. The oxidizing ability of Ce^{IV} is greatly affected by ligand environments, shifting its reduction potentials from +1.63 to −0.69 V vs. SCE for the $Ce^{IV/III}$ couple under aqueous conditions.[8] A significant influence of ligands on the reduction potential of the $Ce^{IV/III}$ couple in non-aqueous conditions are also reported.[8] Accordingly, it is presumed that the increasing amount of H_2O could affect the ligand environment and reduction potential of Ce^{III}, and $[Fe^{IV}(O)(N4py)]^{2+}$ was able to oxidize Ce^{III} to Ce^{IV}.

The chemistry of Ce^{IV} as a Lewis acid was explored with a manganese complex by Fukuzumi, Nam, and co-workers.[13] They proposed a $[Mn^{IV}(O)(dpaq)]^+$–Ce^{IV} adduct (dpaq = 2-[bis(pyridin-2-ylmethyl)]amino-*N*-quinolin-8-yl-acetamidate; Figure 3.1) generated in a reaction of $[Mn^{III}(OH)(dpaq)]^+$ and 2 equiv. CAN in 49:1 (v/v) CH_3CN:H_2O at −40 ˚C. This manganese adduct was characterized by multiple spectroscopic methods, including cold-spray ionization time-of-flight mass spectrometry (CSI-MS), EPR spectroscopy, and X-ray absorption spectroscopy (XAS). The CSI-MS spectrum of the adduct suggests $[Mn(O)(dpaq)Ce(NO_3)_3(CH_3CN)]^+$, $[Mn(O)(dpaq)Ce(NO_3)_4]^+$, and $[Mn(O)(dpaq)Ce(NO_3)_4(NH_4)]^+$. The EPR spectrum reveals a high-spin S = 3/2 Mn^{IV} center with g_{eff} values of 5.4 and 4.0 for the manganese intermediate. The

oxidation state of this intermediate is also corroborated by X-ray absorption near-edge structure (XANES) spectrum, which shows the Mn *K*-edge shifted to a higher energy than that of $[Mn^{III}(OH)(dpaq)]^{+}$. The best fit of the extended X-ray absorption fine structure (EXAFS) shows that the Ce atom is 3.67 Å away from the absorber. Additionally, the binding of Ce^{IV} to the Mn^{IV}-oxo unit is examined with other Lewis acidic metals. Spectral changes were observed when CAN was added to $[Mn^{IV}(O)(dpaq)]^{+}$–Sc^{III} adduct, showing from a feature of $[Mn^{IV}(O)(dpaq)]^{+}$–Sc^{III} adduct to $[Mn^{IV}(O)(dpaq)]^{+}$–Ce^{IV} adduct. Altogether, these studies show the variable role of Ce^{IV} in reactions of CAN with metal complexes.

Above studies have provided critical information concerning the roles of Ce^{IV} ion from CAN in the formation of and/ or reactions with metal(IV)-oxo complexes. The strong oxidizing potential of CAN makes Ce^{IV} as an outer- or inner-sphere oxidant; furthermore, Ce^{IV} can react as a Lewis acid that binds to metal(IV)- or metal(III)-oxo complexes. On the basis of the variable role of Ce^{IV} ion from CAN in mind, we explored the reaction of an electron-rich Mn^{II} complex with CAN in this study. Previously, a series of Mn^{IV}-oxo complexes with pentadentate N5 ligands has been studied for their geometric and electronic structures and reactivities towards C–H bond activation.[21-24] However, the formation of those Mn^{IV}-oxo complexes has to be done in 2,2,2-trifluoroethanol (TFE), of which the role has been proposed to stabilize Mn^{IV}-oxo complexes through hydrogen-bonding interactions.[24] Therefore, it is beneficial to prepare Mn^{IV}-oxo complexes in different solvent systems to broaden the range of applications that Mn^{IV}-oxo complexes can be used. Additionally, the hazardous properties of the fluorinated solvent, TFE, pose a concern to keep using the solvent. In this study we examined the reactions of varied amounts of CAN with $[Mn^{II}(OTf)(^{DMM}N4py)](OTf)$ ($^{DMM}N4py$ = *N*,*N*-bis(4-methoxy-3,5-dimethyl-2-pyridylmethyl)-*N*-bis(2-pyridyl)methylamine) in MeCN:H_2O. The complex,

$[Mn^{II}(OTf)(^{DMM}N4py)](OTf)$, features a neutral pentadentate N5 ligand of electron-rich properties and has been used to prepare a Mn^{IV}-oxo complex, $[Mn^{IV}(O)(^{DMM}N4py)]^{2+}$, and a bis(μ-oxo)dimanganese(III,IV) complex, $[Mn^{III}Mn^{IV}(\mu\text{–}O)_2(^{DMM}N4py)_2]^{3+}$ (Figure 3.2).[21, 25, 26] Both complexes have been well-characterized with multiple spectroscopic techniques such as EPR and XAS. We took advantage of this established information for our current investigations of intermediates generated from the reactions of various amounts of CAN with $[Mn^{II}(OTf)(^{DMM}N4py)](OTf)$ in this report. Based on the experimental results, we propose that $[Mn^{II}(OTf)(^{DMM}N4py)](OTf)$ is converted to $[Mn^{III}Mn^{IV}(\mu\text{–}O)_2(^{DMM}N4py)_2]^{3+}$, $[Mn^{IV}Mn^{IV}(\mu\text{–}O)_2(^{DMM}N4py)_2]^{3+}$, or Ce^{IV}-bound $[Mn^{IV}(O)(^{DMM}N4py)]^{2+}$ by different amounts of CAN in the presence of water. Multiple spectroscopic results support the formulations of each intermediate.

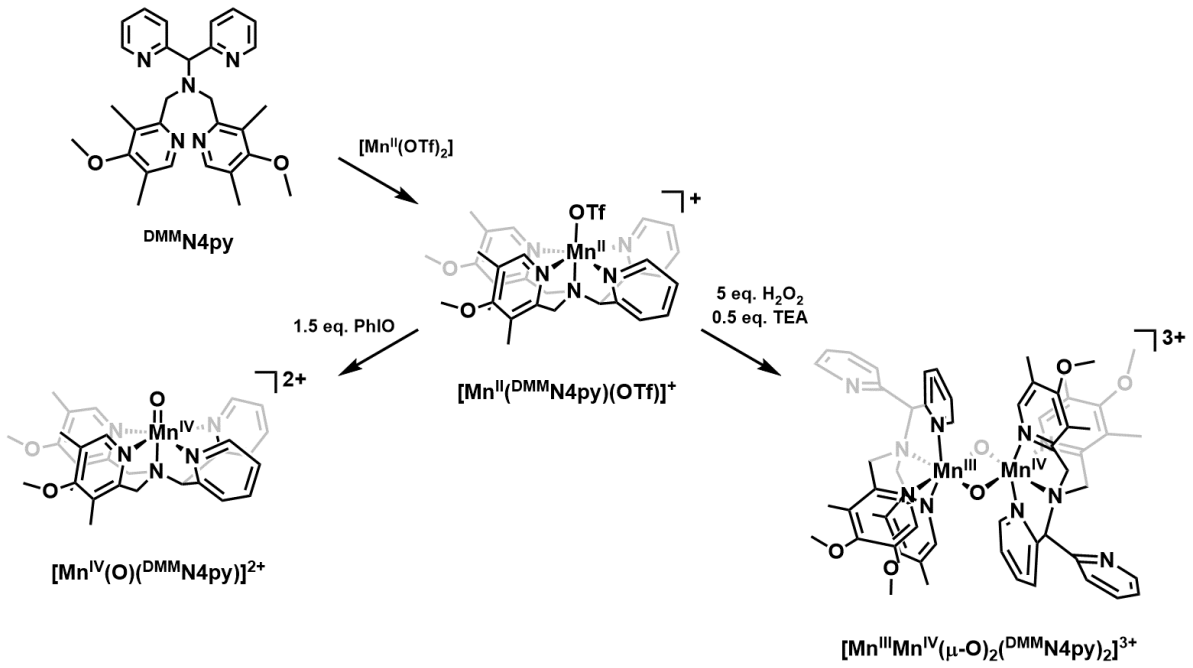

Figure 3.2. Structure of $^{DMM}N4py$ ligand and reported intermediates generated from $[Mn^{II}(OTf)(^{DMM}N4py)](OTf)$ under the given conditions.

3.2 Experimental Methods

3.2.1 Materials and Instrumentation. All chemicals and solvents were ACS reagent-grade or better and purchased from commercial vendors. Chemicals were used as received unless otherwise mentioned. Iodosobenzene (PhIO) was prepared according to a previous procedure.[27] Electronic absorption spectra were collected using either an Agilent 8453 or a Varian Cary 50 Bio spectrophotometer, both of which were equipped with a Unisoku cryostat (USP-203-A) for temperature control. Electron paramagnetic resonance experiments were carried out using an X-band Bruker EMXPlus spectrometer (9.4 GHz) equipped with a dual-mode cavity (Bruker ER4116DM). An Oxford ITC503 cryostat controller was used for adjusting temperature along with an Oxford ESR900 continuous-flow liquid helium cryostat. X-ray absorption spectra were obtained from experiments conducted at beamline 7-3 at Stanford Synchrotron Radiation Lightsource (SSRL) with a Si(220) monochromator and a 30-element Ge solid-state detector (Canberra) at 10 K.

3.2.2 Synthesis and Characterization. Synthesis and purification of ^{DMM}N4py were carried out according to published procedures.[21, 25, 26] Metalation of the ligand was performed with a smaller scale than that previously reported. Under an inert atmosphere, 1.2 equiv. $Mn^{II}(OTf)_2 \cdot 2CH_3CN$[28] was dissolved in acetonitrile (0.11g, 0.25 mmol; 15 mL) and added to ^{DMM}N4py ligand (0.1 g, 0.21 mmol) which was already dissolved in a small amount of acetonitrile (1 - 2 mL). The reaction solution was stirred overnight and filtered with a 0.45 μm PTFE syringe filter, which yields a clear brown solution of $[Mn^{II}(OTf)(^{DMM}N4py)](OTf)$. Recrystallization was carried out by evaporating acetonitrile from the solution of $[Mn^{II}(OTf)(^{DMM}N4py)](OTf)$, followed by re-dissolving the residues in 1 - 2 mL acetonitrile and layering the solution with diethyl ether. Crystals were found in the solution a couple of days later or in decanted diethyl ether solution.

Further purification of $[Mn^{II}(OTf)(^{DMM}N4py)](OTf)$ was achieved using vapor diffusion using acetonitrile/diethyl ether solvent system.

3.2.3 Electron Paramagnetic Resonance Experiments. EPR samples were prepared according to the following procedures, with the formation of each species monitored by electronic absorption spectroscopy. To prepare 6 mM samples of intermediates, 5 mg (0.006 mmol) $[Mn^{II}(OTf)(^{DMM}N4py)](OTf)$ was dissolved in 1 mL 7:3 (v/v) MeCN:H_2O, and the solution was transferred to a quartz cuvette with a 0.2 cm pathlength. Although the solvent system of 9:1 (v/v) MeCN:H_2O was used for 2 mM solutions of $[Mn^{II}(OTf)(^{DMM}N4py)](OTf)$, it was observed that different amount of water can affect the formation of intermediates. Thus, 7:3 (v/v) MeCN:H_2O was used to prepare 6 mM samples of intermediates. After cooling the solution to 0 ˚C, 6.6 mg or 13.3 mg (0.012 or 0.024 mmol, respectively) CAN dissolved in the same solvent was added to the cuvette, which was put into a spectrophotometer to monitor the formation reaction. Once the intensity at λ_{max} is maximized on the electronic absorption spectra, 250 μL of the solution was added to a 4 mm quartz EPR tube and flash-frozen in liquid N_2. Experimental parameters and conditions used for collecting the EPR data are provided in each caption below figures of EPR spectra.

3.2.4 Mn *K*-edge X-ray Absorption Spectroscopy. XAS samples of intermediates generated in the reactions of $[Mn^{II}(OTf)(^{DMM}N4py)](OTf)$ and different amounts of CAN were made according to the following procedures. A solution of $[Mn^{II}(OTf)(^{DMM}N4py)](OTf)$ was prepared by dissolving 12.6 mg (0.015 mmol) of $[Mn^{II}(OTf)(^{DMM}N4py)](OTf)$ in 2.5 mL of the same solvent. Then 13.3 mg of CAN (0.024 mmol) or 6.6 mg of CAN (0.012 mmol) dissolved in 100 μL of 7:3 (v/v) MeCN:H_2O was added to a 1 mL of 6 mM solution of $[Mn^{II}(OTf)(^{DMM}N4py)](OTf)$ (0.006 mmol). Once the λ_{max} of each intermediate shows the

maximum absorbance (confirmed using the electronic absorption band at 640 or 625 nm for the reactions with 2 equiv. and 4 equiv. CAN, respectively), approximately 300 μL of the reaction solution was transferred to an XAS container of which one side was covered with Kapton tape. Then the XAS container was flash-frozen in liquid N_2. The XAS data of intermediates were recorded using fluorescence excitation over a range of 6310 eV to 7300 eV. A reference spectrum using manganese foil was taken in each experiment for the internal calibration of edge energy, of which the energy was set to 6539.0 eV. The edge energy is determined by using the maximum inflection point. The obtained XAS data for both XANES and EXAFS regions were analyzed and processed using the *DEMETER* software package.[29] All the data were merged at the end of processing, and the post-edge line was used for normalization. EXAFS data were fit using *FEFF6* for the phase and amplitude calculations of the models, which were prepared from the DFT-optimized structures.[30] The best fit was determined by the *R*-factor and the σ^2 (Debye-Waller factor) parameter. The Fityk software was used to fit pre-edge region, the pre-edge peaks and background, with pseudo-Voigt line shapes of 1:1 Lorentzian to Gaussian functions.[31]

3.3 Results and Discussion

3.3.1 Reaction of [Mn^{II}(OTf)(^{DMM}N4py)](OTf) with 2 equiv. CAN. As the formation of [Mn^{IV}(O)(^{DMM}N4py)]$^{2+}$ from [Mn^{II}(OTf)(^{DMM}N4py)](OTf) is a two-electron process, we first investigated the reaction of [Mn^{II}(OTf)(^{DMM}N4py)](OTf) with 2 equiv. CAN at room temperature. Upon the addition of 2 equiv. CAN to a 2 mM solution of [Mn^{II}(OTf)(^{DMM}N4py)](OTf) in 9:1 (v/v) MeCN:H_2O at room temperature, we observed an instant growth of two electronic absorption bands at 600 nm and 960 nm (Figure 3.3, inset). The near-IR band at 960 nm is attributed to

$[Mn^{IV}(O)(^{DMM}N4py)]^{2+}$, similar to the λ_{max} of 920 nm observed for $[Mn^{IV}(O)(^{DMM}N4py)]^{2+}$ in TFE.[21] The 30% conversion from $[Mn^{II}(OTf)(^{DMM}N4py)](OTf)$ to $[Mn^{IV}(O)(^{DMM}N4py)]^{2+}$ was estimated based on the extinction coefficient value at 920 nm in TFE ($\varepsilon \approx 290$ $M^{-1}cm^{-1}$).[21] Under these conditions the broad band at 960 nm quickly starts decaying and the band at 600 nm evolves to give new features at 440, 562, and 660 nm (Figure 3.3). This conversion takes ca. 10 minutes. The new features are assigned to $[Mn^{III}Mn^{IV}(\mu\text{–}O)_2(^{DMM}N4py)_2]^{3+}$ (445, 564, and 667 nm observed in TFE).[26] About 95% formation of the bis(μ-oxo)dimanganese(III,IV) complex is formed, estimated by using the intensity at 564 nm and the previously reported extinction coefficient of $[Mn^{III}Mn^{IV}(\mu\text{–}O)_2(^{DMM}N4py)_2]^{3+}$ ($\varepsilon = 600$ $M^{-1}cm^{-1}$ at 564 nm).

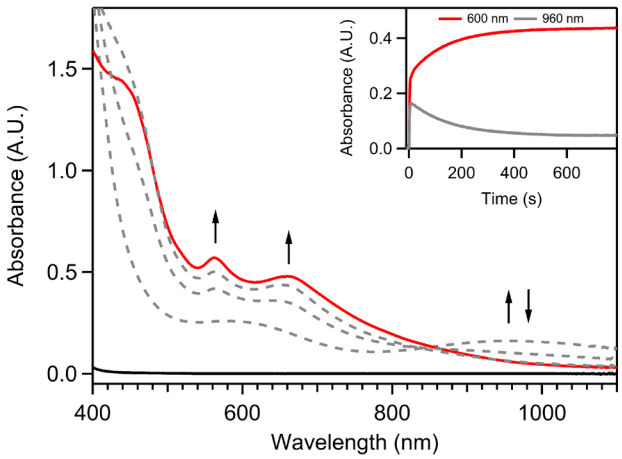

Figure 3.3. Formation of an intermediate with a broad near-IR band (dashed gray) from the reaction of a 2 mM of $[Mn^{II}(OTf)(^{DMM}N4py)](OTf)$ (black) and 2 equiv. CAN in 9:1 (v/v) MeCN:H_2O at room temperature. Dashed gray traces show a convesion to another intermediate (red). Inset shows changes in absorbance at 600 and 960 nm along the reaction.

On the basis of the observations from the electronic absorption spectra, we postulated a possible reaction pathway of $[Mn^{II}(OTf)(^{DMM}N4py)](OTf)$ and 2 equiv. CAN (Figure 3.4). In the

current solvent system, 9:1 (v/v) MeCN:H_2O, $[Mn^{II}(OTf)(^{DMM}N4py)]^{+}$ would become a H_2O-bound form as H_2O is a better ligand than OTf^{-} ion. Then, there will be two sequential one-electron oxidation of $[Mn^{II}(OH_2)(^{DMM}N4py)]^{2+}$ by CAN (Figure 3.4). From the first one-electron oxidation, $[Mn^{III}(OH)(^{DMM}N4py)]^{2+}$ is generated, which is followed by the second one-electron oxidation towards the formation of $[Mn^{IV}(O)(^{DMM}N4py)]^{2+}$ with one proton. When $[Mn^{IV}(O)(^{DMM}N4py)]^{2+}$ decays due to its instability in the given solvent system, $[Mn^{IV}(O)(^{DMM}N4py)]^{2+}$ reacts with $[Mn^{III}(OH)(^{DMM}N4py)]^{2+}$, which forms $[Mn^{III}Mn^{IV}(\mu\text{–}O)_2(^{DMM}N4py)_2]^{3+}$ and one proton.

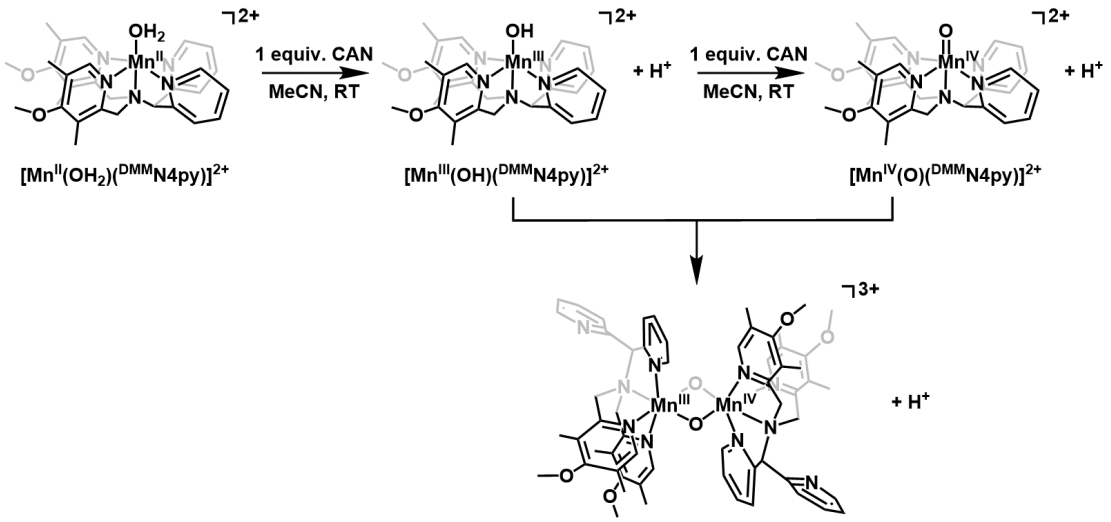

Figure 3.4. A proposed reaction scheme for the formation of $[Mn^{III}Mn^{IV}(\mu\text{–}O)_2(^{DMM}N4py)_2]^{3+}$.

Additionally, the same reaction was carried out at 0 °C. In this reaction $[Mn^{II}(OTf)(^{DMM}N4py)](OTf)$ is converted to an intermediate that exhibits a broad feature at near-IR region (Figure 3.5). The conversion from $[Mn^{II}(OTf)(^{DMM}N4py)](OTf)$ to $[Mn^{IV}(O)(^{DMM}N4py)]^{2+}$ is calculated as 40%, a slightly higher than what is shown in the previous reaction at room temperature. However, at 0 °C the broad near-IR feature decays to a different

intermediate, which has a characteristic electronic absorption feature at 640 nm. This electronic absorption band does not resemble those features reported previously for oxidation products of $[Mn^{II}(OTf)(^{DMM}N4py)](OTf)$.[21, 26] One possible candidate for this intermediate is a bis(μ-oxo)dimanganese(IV,IV) complex, $[Mn^{IV}Mn^{IV}(\mu\text{–}O)_2(^{DMM}N4py)_2]^{4+}$. Hodgson, Michelsen, and co-workers previously reported similar electronic absorption bands near 543 and 630 nm for bis(μ-oxo)dimanganese(IV,IV) complexes with *N*,*N*′-bis(2-pyridylmethyl)-1,2-ethanediamine ligand systems.[32]

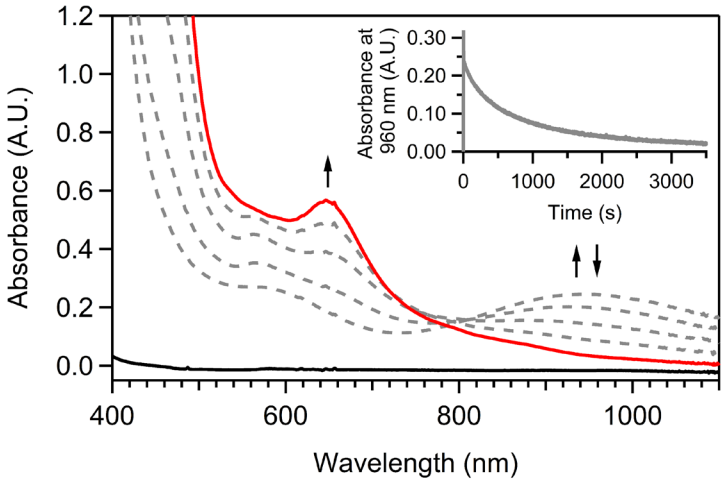

Figure 3.5. Electronic absorption spectra of the reaction between a 2 mM solution of $[Mn^{II}(OTf)(^{DMM}N4py)](OTf)$ (black) and 2 equiv. CAN in 9:1 (v/v) MeCN:H_2O at 0 °C. Dashed gray traces show the formation of $[Mn^{IV}(O)(^{DMM}N4py)]^{2+}$, based on the broad feature in near-IR region, which decays to another reaction intermediate in red trace.

This new intermediate was also observed when 2 equiv. CAN was added to the bis(μ-oxo)dimanganese(III,IV) complex (Figure 3.6). In this reaction $[Mn^{III}Mn^{IV}(\mu\text{–}O)_2(^{DMM}N4py)_2]^{3+}$ was prepared separately, following a previously reported procedure.[26] This bis(μ-oxo)dimanganese(III,IV) complex was dissolved in 9:1 (v/v) MeCN:H_2O at room temperature,

then 2 equiv. CAN was added to the $[Mn^{III}Mn^{IV}(\mu\text{–}O)_2(^{DMM}N4py)_2]^{3+}$ solution. More resolved electronic absorption spectra were shown in this reaction (with 535, 595, and 640 nm bands) than what was seen in the previous reaction at 0 °C (Appendix A3. Figure A3.1). Therefore, it is concluded that $[Mn^{IV}Mn^{IV}(\mu\text{–}O)_2(^{DMM}N4py)_2]^{4+}$ is formed in the reaction of $[Mn^{II}(OTf)(^{DMM}N4py)](OTf)$ and 2 equiv. CAN at 0 °C, which is also generated in the reaction of $[Mn^{III}Mn^{IV}(\mu\text{–}O)_2(^{DMM}N4py)_2]^{3+}$ and 2 equiv. CAN at room temperature. Additionally, another reaction was carried out where 2 equiv. CAN was added to $[Mn^{III}Mn^{IV}(\mu\text{–}O)_2(^{DMM}N4py)_2]^{3+}$ which was generated by reacting $[Mn^{II}(OTf)(^{DMM}N4py)](OTf)$ and 2 equiv. CAN in 9:1 (v/v) MeCN:H_2O at room temperature (Appendix A3. Figure A3.2). Comparable electronic absorption spectra to those in the reaction of $[Mn^{III}Mn^{IV}(\mu\text{–}O)_2(^{DMM}N4py)_2]^{3+}$ and 2 equiv. CAN were observed in the reaction.

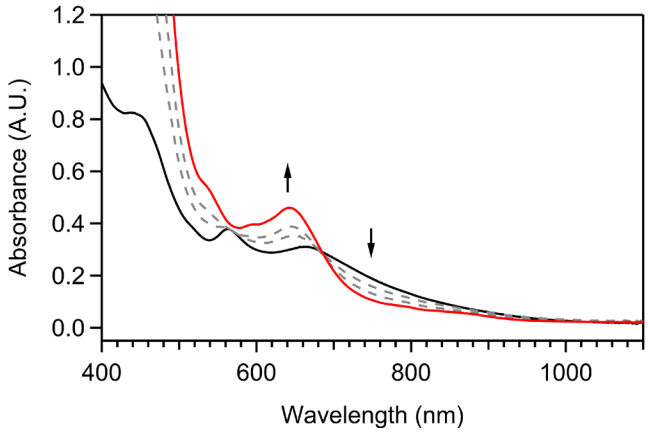

Figure 3.6. Electronic absorption spectra from the reaction of $[Mn^{III}Mn^{IV}(\mu\text{–}O)_2(^{DMM}N4py)_2]^{3+}$ (black) and 2 equiv. CAN in 9:1 (v/v) MeCN:H_2O at room temperature. Spectral changes (dashed gray) were observed after 2 equiv. CAN, which forms an intermediate in the red trace.

Further characterization of $[Mn^{IV}Mn^{IV}(\mu\text{–}O)_2(^{DMM}N4py)_2]^{4+}$ was carried out using EPR spectroscopy. The EPR spectrum of $[Mn^{IV}Mn^{IV}(\mu\text{–}O)_2(^{DMM}N4py)_2]^{4+}$ exhibits an admixture of $[Mn^{II}(OTf)(^{DMM}N4py)](OTf)$ and $[Mn^{III}Mn^{IV}(\mu\text{–}O)_2(^{DMM}N4py)_2]^{3+}$ without any other signals (Figure 3.7), which indicates that $[Mn^{IV}Mn^{IV}(\mu\text{–}O)_2(^{DMM}N4py)_2]^{4+}$ is EPR silent. Similarly, several bis(μ-oxo)dimanganese(IV,IV) complexes have been reported as EPR silent due to their antiferromagnetic coupling.[32, 33] Therefore, the geometric and electronic structure of $[Mn^{IV}Mn^{IV}(\mu\text{–}O)_2(^{DMM}N4py)_2]^{4+}$ was investigated using X-ray absorption spectroscopy, which is described below.

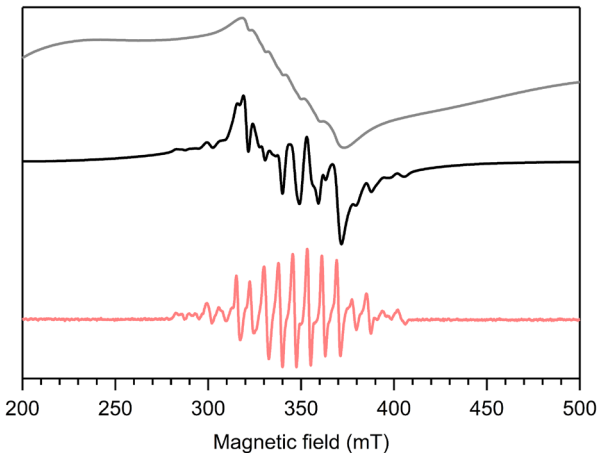

Figure 3.7. EPR spectrum of $[Mn^{IV}Mn^{IV}(\mu\text{–}O)_2(^{DMM}N4py)_2]^{4+}$ from the reaction of $[Mn^{II}(OTf)(^{DMM}N4py)](OTf)$ and 2 equiv. CAN at 0 °C (black). Gray trace shows 6 mM solution of $[Mn^{II}(OTf)(^{DMM}N4py)](OTf)$ in the same solvent system and rose trace shows $[Mn^{III}Mn^{IV}(\mu\text{–}O)_2(^{DMM}N4py)_2]^{3+}$ from a previous study.[26] Experimental conditions: 9.64 GHz microwave frequency, 4 G modulation amplitude, 100 kHz modulation frequency, 26 dB power attenuation, 20 dB receiver gain, 40.96 ms time constant.

Mn *K*-edge XAS data were collected for $[Mn^{IV}Mn^{IV}(\mu\text{–}O)_2(^{DMM}N4py)_2]^{4+}$ and the data were compared with the XAS data for $[Mn^{IV}(O)(^{DMM}N4py)]^{2+}$ and $[Mn^{III}Mn^{IV}(\mu$-

$O)_2(^{DMM}N4py)_2]^{3+}$ in TFE which were reported previously.[21, 26] The edge energy of $[Mn^{IV}Mn^{IV}(\mu–O)_2(^{DMM}N4py)_2]^{4+}$ is 6551.2 eV, which is slightly higher than the energies of $[Mn^{IV}(O)(^{DMM}N4py)]^{2+}$ and $[Mn^{III}Mn^{IV}(\mu\text{-}O)_2(^{DMM}N4py)_2]^{3+}$ (Table 3.1). The pre-edge region of $[Mn^{IV}Mn^{IV}(\mu–O)_2(^{DMM}N4py)_2]^{4+}$ shows a peak near 6541 eV (Figure 3.8). The fit of the pre-edge peak is achieved using three individual functions at 6540.5, 6541.6, and 6542.9 eV (Appendix A3; Figure A3.3). These pre-edge energies are nearly identical with the pre-edge energies previously reported for $[Mn^{IV}(O)(^{DMM}N4py)]^{2+}$ and $[Mn^{III}Mn^{IV}(\mu\text{-}O)_2(^{DMM}N4py)_2]^{3+}$, except the band near 6543 eV is not observed in the bis(μ-oxo)dimanganese(III,IV) complex (Table 3.1). Along the same line, the pre-edge area of $[Mn^{IV}Mn^{IV}(\mu–O)_2(^{DMM}N4py)_2]^{4+}$ is similar to those areas of the Mn^{IV}-oxo and bis(μ-oxo)dimanganese(III,IV) complexes, which indicates analogous geometric distortions among these complexes to allow comparable 3*d* and 4*p* mixing. Collectively, the edge energy and pre-edge features of $[Mn^{IV}Mn^{IV}(\mu–O)_2(^{DMM}N4py)_2]^{4+}$ correspond remarkably well to a high-valent manganese complex in a distorted octahedral environment.

Table 3.1. Mn *K*-edge pre-edge and edge properties of $[Mn^{IV}Mn^{IV}(\mu–O)_2(^{DMM}N4py)_2]^{4+}$ and related complexes.

Complex	Edge energy (eV)	Pre-edge energy (eV)	Pre-edge area	Ref.
$[Mn^{IV}Mn^{IV}(\mu–O)_2(^{DMM}N4py)_2]^{4+}$	6551.2	6540.5, 6541.6, 6542.9	19.0	this work
$[Mn^{III}Mn^{IV}(\mu–O)_2(^{DMM}N4py)_2]^{3+}$	6550.6	6540.3, 6541.5	19.6	[26]
$[Mn^{IV}(O)(^{DMM}N4py)]^{2+}$	6550.5	6539.9, 6541.6, 6543.2	20.1	[24]

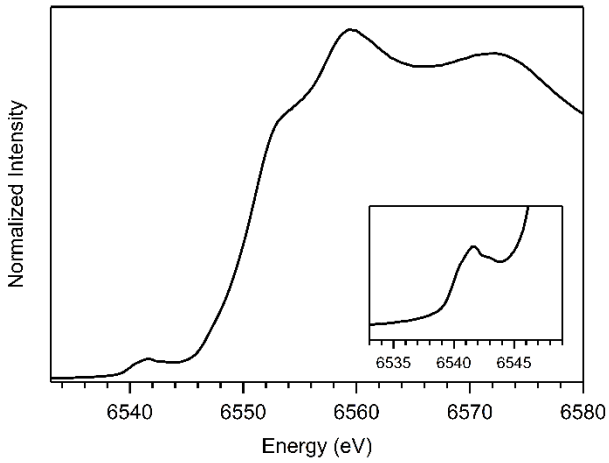

Figure 3.8. Mn *K*-edge XANES spectrum of $[Mn^{IV}Mn^{IV}(\mu\text{–}O)_2(^{DMM}N4py)_2]^{4+}$ prepared from the reaction of $[Mn^{II}(OTf)(^{DMM}N4py)](OTf)$ and 2 equiv. CAN in 7:3 (v/v) MeCN:H_2O at 0 °C. Inset shows enlarged view of the pre-edge region.

Analyzing the EXAFS data of $[Mn^{IV}Mn^{IV}(\mu\text{–}O)_2(^{DMM}N4py)_2]^{4+}$ gives geometric information of this complex. The Fourier transforms of the EXAFS region of $[Mn^{IV}Mn^{IV}(\mu\text{–}O)_2(^{DMM}N4py)_2]^{4+}$ show five peaks, including three prominent peaks approximately at R' of 1.3, 2.0, and 2.4 Å ($R' \approx R + 0.4$ Å) (Figure 3.9). The EXAFS fits of these data are summarized in Table 3.2. The best EXAFS fit results in four shells. There is an O shell at 1.78 Å with one O atom. A N shell is followed at 1.98 Å with two N atoms, presumably from the ligand of $[Mn^{IV}Mn^{IV}(\mu\text{–}O)_2(^{DMM}N4py)_2]^{4+}$. Next, a Mn atom fits well as the third nearest neighbor, which is at 2.64 Å. Lastly, one C shell is also used to fit the EXAFS data. Different numbers of C atom affect the Debye-Waller factors of other shells but give marginal effects on bond lengths (fits 1 and 2 in Table 3.2). Additionally, the bond distances of Mn–O and Mn–N derived from the best fit for the EXAFS data of $[Mn^{III}Mn^{IV}(\mu\text{-}O)_2(^{DMM}N4py)_2]^{3+}$ are slightly longer than those of $[Mn^{IV}Mn^{IV}(\mu\text{–}O)_2(^{DMM}N4py)_2]^{4+}$ by 0.04 and 0.07 Å, respectively (Table 3.3).[26] The corresponding bond distances of $[Mn^{IV}Mn^{IV}(\mu\text{–}O)_2(^{DMM}N4py)_2]^{4+}$ are longer than those of $[Mn^{IV}(O)(^{DMM}N4py)]^{2+}$ by

0.06 and 0.04 Å, respectively. As a result, EXAFS analysis for $[Mn^{IV}Mn^{IV}(\mu\text{–}O)_2(^{DMM}N4py)_2]^{4+}$ also supports a $Mn^{IV}Mn^{IV}(\mu\text{-}O)_2$ species.

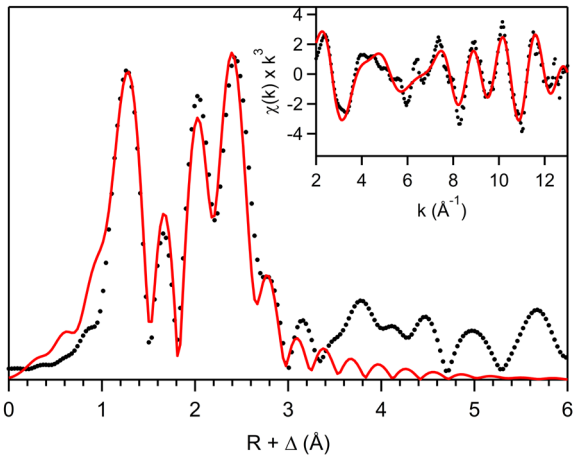

Figure 3.9. Fourier transforms of Mn *K*-edge EXAFS spectrum of $[Mn^{IV}Mn^{IV}(\mu\text{–}O)_2(^{DMM}N4py)_2]^{4+}$ (dotted black) and the fit (red). Inset shows raw *k*-space experimental data (dotted black) and the fit (red).

Table 3.2. Metric parameters from the EXAFS fits of $[Mn^{IV}Mn^{IV}(\mu\text{–}O)_2(^{DMM}N4py)_2]^{4+}$. The best EXAFS fit is indicated in bold.[a]

fit	n	Mn–O r (Å)	σ^2 (Å^2)	n	Mn–N r (Å)	σ^2 (Å^2)	n	Mn···Mn r (Å)	σ^2 (Å^2)	n	Mn···C r (Å)	σ^2 (Å^2)	R-factor
1	**1**	**1.78**	**1.98**	**2**	**1.98**	**5.86**	**1**	**2.65**	**3.47**	**6**	**2.89**	**6.07**	**0.11**
2	1	1.78	2.12	2	1.98	6.20	1	2.64	3.17	8	2.89	8.90	0.12
3	1	1.77	2.77	3	1.98	11.0	1	2.64	3.21	8	2.89	9.11	0.15
4	2	1.80	6.90	2	2.02	5.83	1	2.64	3.49	6	2.88	6.64	0.16
5	2	1.79	7.40	3	2.02	10.5	1	2.64	3.45	6	2.88	6.83	0.18
6	2	1.80	6.99	2	2.02	6.12	1	2.64	3.24	8	2.88	9.35	0.17

[a] Debye-Waller factors are given in × 10^3. The range of k = 2 - 13 Å^{-1} is used for the Fourier transform. The resolution of each fit is 0.12 Å.

Table 3.3. The best EXAFS fit results of **2**, $[Mn^{IV}(O)(^{DMM}N4py)]^{2+}$, $[Mn^{III}Mn^{IV}(\mu\text{-}O)_2(^{DMM}N4py)_2]^{3+}$.[a]

	n	Mn–O r (Å)	σ^2 (Å^2)	n	Mn–N r (Å)	σ^2 (Å^2)	n	Mn···Mn r (Å)	σ^2 (Å^2)	n	Mn···C r (Å)	σ^2 (Å^2)
$[Mn^{IV}Mn^{IV}(\mu\text{–}O)_2(^{DMM}N4py)_2]^{4+}$	1	1.78	1.98	2	1.98	5.86	1	2.65	3.47	6	2.89	6.07
$[Mn^{III}Mn^{IV}(\mu\text{-}O)_2(^{DMM}N4py)_2]^{3+}$	2	1.82	6.0	2 2	2.05 2.22	6.1 2.5	1	2.65	3.0	6	2.92	4.2
$[Mn^{IV}(O)(^{DMM}N4py)]^{2+}$	1	1.72	1.26	2 3	1.94 2.10	2.38 6.09	-	-	-	3 3	2.92 2.74	2.28 8.63

[a] Debye-Waller factors are given in × 10^3. Data for $[Mn^{IV}(O)(^{DMM}N4py)]^{2+}$ and $[Mn^{III}Mn^{IV}(\mu\text{-}O)_2(^{DMM}N4py)_2]^{3+}$ are from reference 24 and 26, respectively.

3.3.2 Reaction of $[Mn^{II}(OTf)(^{DMM}N4py)](OTf)$ and 4 equiv. CAN. From above experiments, it is revealed that $[Mn^{IV}(O)(^{DMM}N4py)]^{2+}$ is formed instantaneously when 2 equiv. CAN are added to $[Mn^{II}(OTf)(^{DMM}N4py)](OTf)$ at room temperature, but the Mn^{IV}-oxo complex decays promptly. We tried another reaction where $[Mn^{II}(OTf)(^{DMM}N4py)](OTf)$ reacts with 4 equiv. CAN to see what can be changed if the amount of $[Mn^{IV}(O)(^{DMM}N4py)]^{2+}$ is increased by adding a larger amount of CAN. Once 4 equiv. CAN is introduced, electronic absorption bands at 625 and 940 nm appear instantaneously (Figure 3.10). The band at 940 nm rapidly decays while the band at 625 nm gains intensity over 15 seconds. The electronic absorption feature of this new intermediate is shown as one broad band at 625 nm (16 000 cm^{-1}, ε = 610 M^{-1} cm^{-1}; Figure 3.10). This new chromophore is distinctive from what has been shown in the electronic absorption spectra of $[Mn^{IV}(O)(^{DMM}N4py)]^{2+}$ (λ_{max} at 10 900 cm^{-1}, ε = 290 M^{-1} cm^{-1}), $[Mn^{III}Mn^{IV}(\mu\text{–}O)_2(^{DMM}N4py)_2]^{3+}$ (λ_{max} at 17 800 and 15 000 cm^{-1}, ε = 600 M^{-1} cm^{-1} at 17 800 cm^{-1}), and $[Mn^{IV}Mn^{IV}(\mu\text{–}O)_2(^{DMM}N4py)_2]^{4+}$ (λ_{max} at 18 700, 16 800, and 15 600 cm^{-1}, ε = 380 M^{-1} cm^{-1} at 15 600 cm^{-1}).[21, 26] However, this electronic absorption feature is reminiscent to that of $[Mn^{IV}(O)(OH_2)(BQCN)]^{2+}$ (λ_{max} at 15 900 cm^{-1}; ε = 400 M^{-1} cm^{-1}), which was formed under

similar conditions (addition of 4 equiv. CAN to a 2 mM solution of $[Mn^{II}(BQCN)]^{2+}$ in 9:1 (v/v) MeCN:H_2O at 0 ˚C).[11]

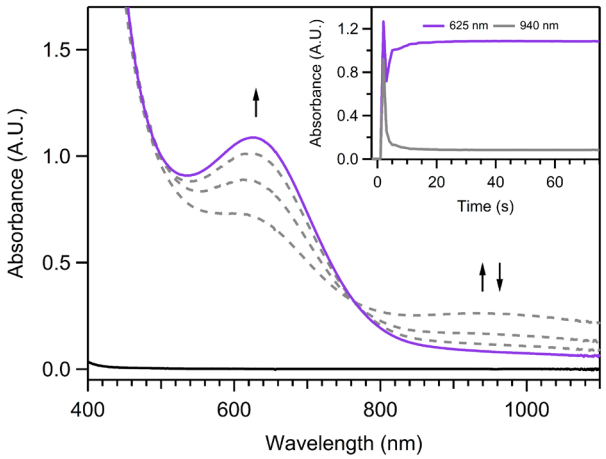

Figure 3.10. Instant formation of $[Mn^{IV}(O)(^{DMM}N4py)]^{2+}$ (dashed gray) from the reaction of a 2 mM solution of $[Mn^{II}(OTf)(^{DMM}N4py)](OTf)$ (black) and 4 equiv. CAN in 9:1 (v/v) MeCN:H_2O at room temperature. The near-IR band in dashed gray traces is decreased in absorbance, while the band at 625 nm gains intensity to form the final intermediate (purple).

EPR spectroscopy was used to further characterize the oxidation state and electronic environment of the intermediate prepared in frozen solution. The perpendicular-mode EPR spectrum of the intermediate consists of two resonances, one intense signal at g_{eff} = 3.6 and the other negative signal at g_{eff} = 2.0 (191 and 353 mT, respectively; Figure 3.11), which shows an axial EPR spectrum of an S = 3/2 Mn^{IV} system. Comparable EPR signals have been observed in manganese(IV) complexes.[34-36] In the former report by Chakravorty and co-workers, a manganese(IV) with a tridentate Schiff base, a ligand of four anionic oxygen and two neutral nitrogen (MnO_4N_2), shows g values of 3.86 and 2.02 in 1:1 DCM:toluene glass at 77 K. Specifically, a six-line hyperfine structure was found at g = 2.0, which is originated from ^{55}Mn.

Similarly, in the latter study by Garner, Trautwein, Weiss, and co-workers, an axial EPR signal of a Mn^{IV}-oxo porphyrinato complex is observed at $g \approx 4$ with a six-line pattern over a negative signal at $g \approx 2$, which are also indicative of a high-spin $S = 3/2$ Mn^{IV} species. Likewise, the ground state of $S = 3/2$ Mn^{IV} gives rise to an axial EPR signal of $g_{\perp}$ values over a range of 3.4 – 4.0 and $g_{\parallel}$ values near 2 in other studies.[11, 13, 21, 23, 37-39] The EPR spectrum of $[Mn^{IV}(O)(^{DMM}N4py)]^{2+}$ shows an axial EPR signal at $g_{\perp} = 4.4$ and $g_{\parallel} = 2.0$,[21, 37] although the intensity of axial signal is weaker than what is shown for the intermediate species in current reaction. In other Mn^{IV}-oxo complexes, $[Mn^{IV}(O)(OH_2)(BQCN)]^{2+}$ and $[Mn^{IV}(O)(dpaq)]^{+}$–Ce^{IV} provide $g_{\perp}$ values of 4.0.[11, 13] The marginal sixteen-line signal displayed at $g_{eff} = 2.0$ ($A = 8.5$ mT) in the EPR spectrum of the intermediate presumably corresponds to $[Mn^{III}Mn^{IV}(\mu\text{-}O)_2(^{DMM}N4py)_2]^{3+}$ as an impurity or a side product in the sample. When we tried to quantify the amount of the impurity using the EPR quantification method, the signal shows approximately 28% of the species in the solution. Although it seems the quantified amount of the $[Mn^{III}Mn^{IV}(\mu\text{-}O)_2(^{DMM}N4py)_2]^{3+}$ is overestimated, we assume that it could be due to the negative component of the axial signal of Mn^{IV} species, which is overlapped with the impurity signal. Altogether, the EPR spectrum of the intermediate species proves the presence of mononuclear Mn^{IV} species in the solution.

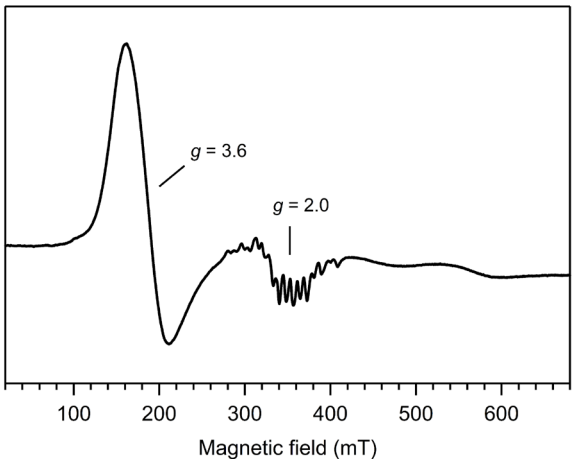

Figure 3.11. X-band EPR spectrum of the new intermediate at 10 K. Experimental conditions: 9.64 GHz microwave frequency, 4 G modulation amplitude, 100 kHz modulation frequency, 14 dB power attenuation, 20 dB receiver gain, 40.96 ms time constant.

Further investigation of the geometric and electronic characteristics of the intermediate was achieved through Mn *K*-edge XAS technique. The rising edge energy of the intermediate is 6552.0 eV, which is higher than not only that of $[Mn^{II}(OTf)(^{DMM}N4py)](OTf)$ (6546.8 eV), but that of $[Mn^{IV}(O)(^{DMM}N4py)]^{2+}$ (6550.5 eV) (Table 3.4). However, this edge energy is comparable to those of other Mn^{IV} complexes, $[Mn^{IV}(OH)_2(Me_2EBC)]^{2+}$ and $[Mn^{IV}(O)(OH)(Me_2EBC)]^{2+}$ (6552.0 and 6551.8 eV, respectively).[40] Among other studies of Mn^{IV}-oxo/hydroxo and -oxohydroxo complexes, the range of the edge energy is from 6550.3 to 6553.8 eV (Table 3.4). Although the rising-edge is used as a good indicator of the oxidation state of the central metal, the edge-energy can vary depending on other factors such as metal-ligand bond distance and covalency.[41] Furthermore, the EPR spectrum of the intermediate complex clearly shows the axial feature of mononuclear Mn^{IV} complex as described earlier. Therefore, we propose that the edge energy of the intermediate species still indicate Mn^{IV} oxidation state; however, it is unclear at the moment to determine which factor may attribute to the shift of the edge energy of the intermediate.

The pre-edge region of the intermediate complex reveals two pre-edge peaks at 6541.2 and 6543.1 eV (Figure 3.12). These pre-edge energies, from the quadrupole-allowed 1*s* to 3*d* electron transitions, are close to those values for $[Mn^{IV}(O)(^{DMM}N4py)]^{2+}$ (6539.9, 6541.6, and 6543.2 eV; Table 3.4). Similar pre-edge energies were previously reported for other Mn^{IV} species, e.g., $[Mn^{IV}(OH)_2Me_2EBC]^{2+}$ (6541.0 and 6543.2 eV) and $[Mn^{IV}(O)(OH)Me_2EBC]^{2+}$ (6541.2 and 6543.3 eV).[40] Therefore, pre-edge energies of the intermediate complex are within the range of the values for Mn^{IV} complexes. Additionally, the pre-edge area of the intermediate shows 14.9 and 8.5 for the first and second peak areas, respectively (Appendix A3. Figure A3.4). The sum of these values (23.4) is a little higher than that of $[Mn^{IV}(O)(^{DMM}N4py)]^{2+}$ (20.1), and much higher than those of $[Mn^{IV}(OH)_2(Me_2EBC)]^{2+}$ (5.0 and 2.0) and $[Mn^{IV}(O)(OH)(Me_2EBC)]^{2+}$ (10.5 and 3.7). The pre-edge peaks are known to be sensitive to the coordination number and symmetry of the metal. As an example, the pre-edge areas of $[Mn^{IV}(OH)_2(Me_2EBC)]^{2+}$ and $[Mn^{IV}(OH)_2(TBDAP)]^{2+}$ are almost identical (7.0 and 6.0; Table 3.4), which have the same geometry shown in their XRD structures. Accordingly, there is a possibility that the intermediate complex takes a different geometry, e.g., a five-coordinate structure regarding that less coordinated structures display higher intensity of their pre-edge peaks (O_h < 5-coordinate < T_d).[41-43] A five-coordinate complex, $[Mn^{IV}(OH)(H_3buea)]$, shows 21 units for the pre-edge area (Table 3.4).

Table 3.4. Mn *K*-edge XAS edge energy, pre-edge energy, and pre-edge area of the intermediate complex and other Mn^{IV}-oxo and/ or hydroxo complexes in different geometries.

Complex	Edge energy (eV)	Pre-edge energy (eV)	Pre-edge area	Reference
Intermediate complex	6552.0	6541.2, 6543.1	14.9, 8.5	this work
Six-coordinate complexes				
$[Mn^{IV}(O)(^{DMM}N4py)]^{2+}$	6550.5	6539.9, 6541.6, 6543.2	20.1	[23]
$[Mn^{III}Mn^{IV}(\mu\text{-}O)_2(^{DMM}N4py)_2]^{3+}$	6550.6	6540.3, 6541.5	19.6	[26]
$[Mn^{IV}(OH)_2(TBDAP)]^{2+}$	6551.4	-	6.0	[39]
$[Mn^{IV}(OH)_2(Me_2EBC)]^{2+}$	6552.0	6541.0, 6543.2	5.0, 2.0	[37]
$[Mn^{IV}(O)(OH)(Me_2EBC)]^{2+}$	6551.8	6541.2, 6543.3	10.5, 3.7	[37]
Five-coordinate complexes				
$[Mn^{IV}(O)(H_3buea)]^{-}$	6551.7	6541.0, 6542.8	33	[44]
$[Mn^{IV}(OH)(H_3buea)]$	6553.8	6540.9, 6542.7	21	[45]
$[Mn^{IV}(O)(T_{piv}PP)]$	6551.2	-	-	[35]

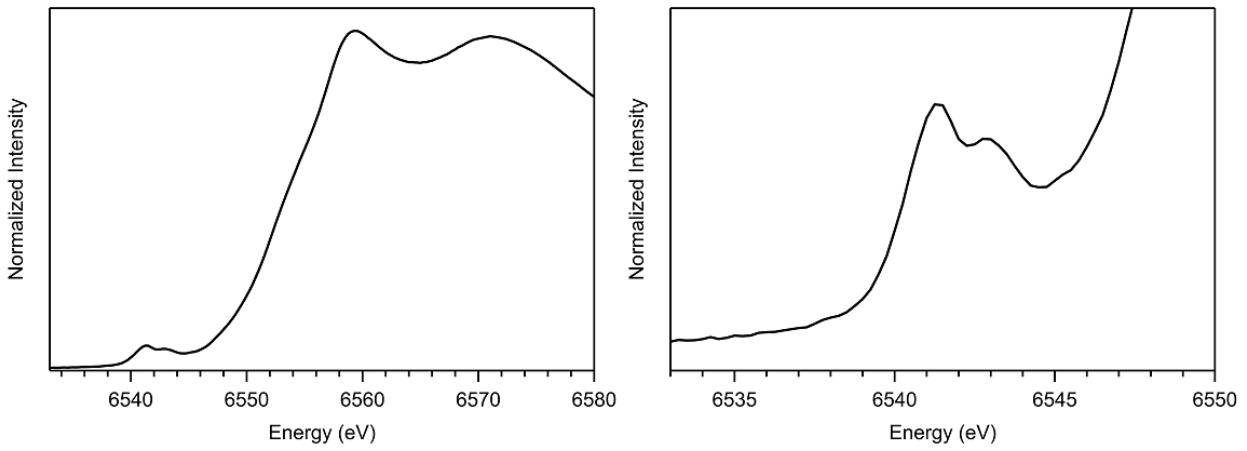

Figure 3.12. Mn *K*-edge XANES spectrum of the intermediate generated from the reaction of a 6 mM solution of $[Mn^{II}(OTf)(^{DMM}N4py)](OTf)$ and 4 equiv. CAN.

Analysis of the EXAFS data has provided the metric parameters of the intermediate. The phase-shifted Fourier-transformed EXAFS data of the intermediate species display a scattering profile with four major peaks at 1.3, 1.7, 2.0, and 2.4 Å in *R′* space (Figure 3.13). The metric

parameters from these EXAFS data were obtained using *FEFF* calculations on a DFT-optimized $[Mn^{IV}(O)(^{DMM}N4py)]^{2+}$ structure. Fitting these features was carried out with four shells of O, N, and C scatterers, where O and N scatterers are in the first coordination sphere and C scatterers are in the second coordination sphere (Table 3.5). The best fit displays that two O scatterers in the first shell are in the distance of 1.80 Å from the absorber. Three N scatterers are in the next shell at 2.01 Å, which presumably corresponds to the nitrogen atoms of the ligand. The last two shells have contributions from C scattering, with three scatters for each shell, at 2.79 and 2.94 Å, respectively. Increasing the number of C atoms in this shell does not significantly affect to the goodness-of-fit (GOF) which was determined by R-factor (Table 3.5). Additionally, no evidence for Ce or Mn scatterer was observed. The distances of the O and N scatterers from the absorber are longer than the reported distances in $[Mn^{IV}(O)(^{DMM}N4py)]^{2+}$ and other Mn^{IV}-oxo complexes from their EXAFS analyses. In a previous study from our group, the distance for Mn–O/N is 1.72 Å in $[Mn^{IV}(O)(^{DMM}N4py)]^{2+}$ from EXAFS measurements.[24] If it is considered with the corresponding bond distances from other Mn^{IV}-oxo complexes, the range of Mn–O bond distance is from 1.70 to 1.76 Å. On the other hand, EXAFS analysis on $[Mn^{IV}(OH)_2(Me_2EBC)]^{2+}$ shows 1.80 Å and $[Mn^{IV}(O)(OH)(Me_2EBC)]^{+}$ displays 1.71 and 1.84 Å for the distance of Mn–O.[40] Therefore, the distance derived from the best fit of EXAFS analysis for the intermediate, 1.80 Å, is most consistent with a $[Mn^{IV}–OH]$ distance.

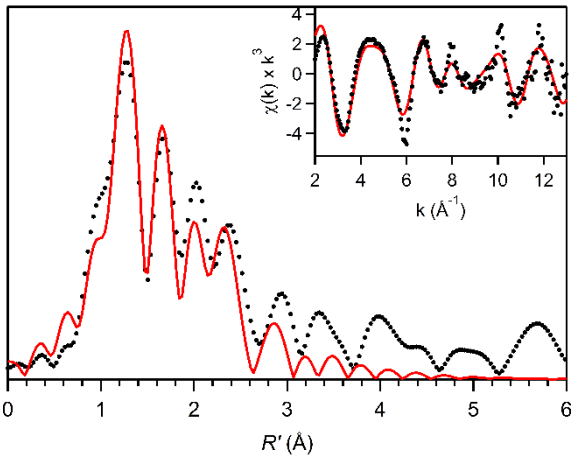

Figure 3.13. Fourier transforms of EXAFS data for the intermediate complex with experimental results (dotted black) and fitted results (red). Inset shows the experimental data (dotted black) and fit (red) in raw EXAFS spectrum.

Table 3.5. Metric parameters from the EXAFS fits for the intermediate species. The best EXAFS fit is indicated in bold.[a]

fit	n	Mn–O r (Å)	$\sigma^2 \times 10^3$ (Å^2)	n	Mn–N r (Å)	$\sigma^2 \times 10^3$ (Å^2)	n	Mn···C r (Å)	$\sigma^2 \times 10^3$ (Å^2)	n	Mn···C r (Å)	$\sigma^2 \times 10^3$ (Å^2)	R-factor
1	2	1.80	4.21	3	2.01	3.89	1	2.87	1.73	-	-	-	0.16
2	2	1.80	4.25	3	2.01	3.92	3	2.88	6.40	-	-	-	0.12
3	2	1.80	4.10	3	2.01	3.83	3	2.83	4.78	1	2.96	−0.88	0.11
4	**2**	**1.80**	**4.00**	**3**	**2.01**	**3.84**	**3**	**2.79**	**5.06**	**3**	**2.94**	**3.02**	**0.13**
5	2	1.80	3.97	3	2.01	3.86	3	2.77	5.46	4	2.93	5.07	0.15
6	2	1.80	3.97	3	2.01	3.91	4	2.78	7.72	4	2.93	5.07	0.15

[a] Debye-Waller factors are given in × 10^3. The range of k = 2 - 13 Å^{-1} is used for the Fourier transform.

Collectively, EPR and XAS data have shown that the intermediate complex is a Mn^{IV} complex. However, nearly 1.5 eV higher edge energy than that of $[Mn^{IV}(O)(^{DMM}N4py)]^{2+}$ poses uncertainty in the characterization of this intermediate, although similar values have been shown in other Mn^{IV}-oxo and -hydroxo systems. One possible complex for this intermediate is a $[Mn^{IV}(O)(OH)(^{DMM}N4py)]^{+}$–$Ce^{IV}$ adduct, which is comparable to $[Mn^{IV}(O)(dpaq)]^{+}$–Ce^{IV} that Nam and co-workers reported from the reaction of $[Mn^{III}(OH)(dpaq)]^{+}$ and 2 equiv. CAN.[13] In

their study the edge of the proposed $[Mn^{IV}(O)(dpaq)]^{+}$–Ce^{IV} adduct is shifted to a higher energy compared to the edge of $[Mn^{III}(OH)(dpaq)]^{+}$, although it is difficult to make a precise comparison without the exact edge energies from those two complexes. Thus, we tried a reaction of $[Mn^{IV}(O)(^{DMM}N4py)]^{2+}$ with a Ce^{IV} ion to examine the Ce^{IV} ion could react with or bind to $[Mn^{IV}(O)(^{DMM}N4py)]^{2+}$. For this experiment, $[Mn^{IV}(O)(^{DMM}N4py)]^{2+}$ was generated by adding 1.5 equiv. PhIO to a 2 mM solution of $[Mn^{II}(OTf)(^{DMM}N4py)](OTf)$ in 9:1 (v/v) MeCN:H_2O. The solution of 1.5 equiv. was prepared in 9:1 (v/v) MeCN:TFE to minimize the amount of TFE used for dissolving PhIO. The formation of $[Mn^{IV}(O)(^{DMM}N4py)]^{2+}$ was assured with an increase of the near-IR band at 920 nm, and approximately 55% yield for the formation of $[Mn^{IV}(O)(^{DMM}N4py)]^{2+}$ was determined under these conditions (Figure 3.14, left).[21] When 2 equiv. CAN was added to the solution, spectral changes occurred. A new band at 630 nm was observed, and the spectrum looks similar to that of the intermediate complex generated from the reaction between $[Mn^{II}(OTf)(^{DMM}N4py)](OTf)$ and 4 equiv. CAN (Figure 3.14, right). This experiment shows that a Ce^{IV} ion can bind to $[Mn^{IV}(O)(^{DMM}N4py)]^{2+}$. Additional experiments to obtain further evidence for Ce^{IV}-bound $[Mn^{IV}(O)(^{DMM}N4py)]^{2+}$, e.g., ESI-MS, will be conducted.

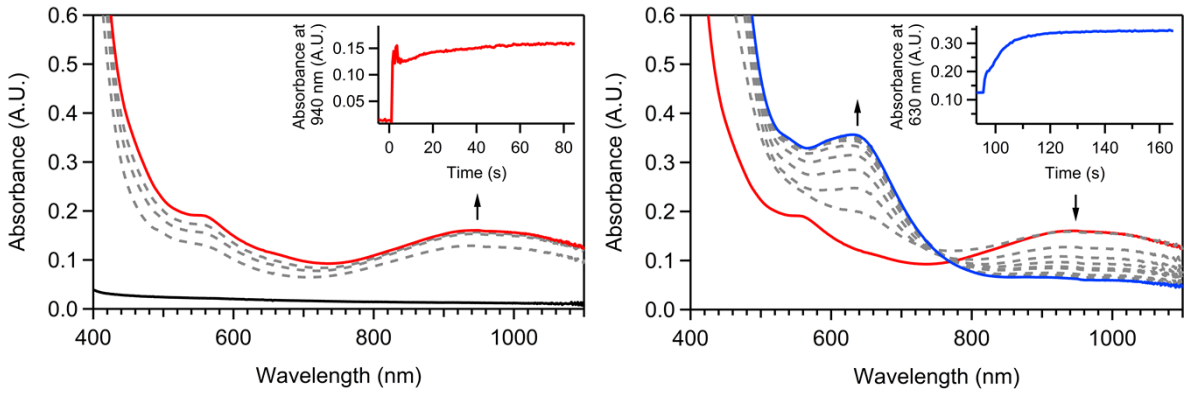

Figure 3.14. Formation of $[Mn^{IV}(O)(^{DMM}N4py)]^{2+}$ in 9:1 (v/v) MeCN:H_2O (red) from the reaction of 1.5 equiv. PhIO in 9:1 (v/v) MeCN:TFE and a 1 mM solution of $[Mn^{II}(OTf)(^{DMM}N4py)](OTf)$ in 9:1 (v/v) MeCN:H_2O (black) at room temperature (left). Electronic absorption spectra of $[Mn^{IV}(O)(^{DMM}N4py)]^{2+}$ (red) and after adding 2 equiv. CAN at room temperature (blue; right). Each inset shows the time trace of the corresponding reaction.

3.4 Conclusion

In this study the possibility to prepare $[Mn^{IV}(O)(^{DMM}N4py)]^{2+}$ in acetonitrile with water, using CAN as an oxidant, was explored. It has shown that $[Mn^{III}Mn^{IV}(\mu\text{–}O)_2(^{DMM}N4py)_2]^{3+}$ or $[Mn^{IV}Mn^{IV}(\mu\text{–}O)_2(^{DMM}N4py)_2]^{4+}$ is generated from the reaction of $[Mn^{II}(OTf)(^{DMM}N4py)](OTf)$ and 2 equiv. CAN in the solvent system depending on the reaction temperature. A quantitative amount of $[Mn^{III}Mn^{IV}(\mu\text{–}O)_2(^{DMM}N4py)_2]^{3+}$ is observed under the reaction conditions at room temperature, which shows a broad near-IR band, from $[Mn^{IV}(O)(^{DMM}N4py)]^{2+}$, as an intermediate species. This bis(μ-oxo)dimanganese(III,IV) complex is oxidized to $[Mn^{IV}Mn^{IV}(\mu\text{–}O)_2(^{DMM}N4py)_2]^{4+}$ by additional 2 equiv. CAN. At 0 °C, the formation of $[Mn^{IV}Mn^{IV}(\mu\text{–}O)_2(^{DMM}N4py)_2]^{4+}$ was observed. Characterization studies show $[Mn^{IV}Mn^{IV}(\mu\text{–}O)_2(^{DMM}N4py)_2]^{4+}$ is EPR silent, presumably due to a strong antiferromagnetic coupling which is frequently reported for high-valent bis(μ-oxo)dimanganese complexes.[46] Instead, XAS data of $[Mn^{IV}Mn^{IV}(\mu\text{–}$

$O)_2(^{DMM}N4py)_2]^{4+}$ reveal the high-valent oxidation state of the complex and shorter distances between manganese and atoms in the first coordination sphere than those reported for $[Mn^{III}Mn^{IV}(\mu\text{–}O)_2(^{DMM}N4py)_2]^{3+}$. Another intermediate species is formed from the reaction of $[Mn^{II}(OTf)(^{DMM}N4py)](OTf)$ and 4 equiv. CAN, which also exhibits a broad near-IR band from $[Mn^{IV}(O)(^{DMM}N4py)]^{2+}$ in its formation process. An axial EPR signal is attributed to Mn^{IV} oxidation state of this intermediate. However, XAS data show a higher edge energy of this intermediate than $[Mn^{IV}(O)(^{DMM}N4py)]^{2+}$ by 1.5 eV along with 1.80 Å for the Mn−O bond distance. Possible intermediates were explored by adding 2 equiv. CAN to $[Mn^{IV}(O)(^{DMM}N4py)]^{2+}$, which provides a comparable electronic absorption spectrum. Further experiment will be needed to characterize this intermediate, which might be a Ce^{IV}-bound $[Mn^{IV}(O)(^{DMM}N4py)]^{2+}$. Overall, this study shows the formation of $[Mn^{IV}(O)(^{DMM}N4py)]^{2+}$ in 9:1 (v/v) MeCN:H_2O, which decays to form more stable species. These results can be insightful to search for other experimental conditions with different solvent or oxidants to prepare Mn^{IV}-oxo species without using TFE.

3.5 Notes and References

1. Codolà, Z.; Gómez, L.; Kleespies, S. T.; Que Jr, L.; Costas, M.; Lloret-Fillol, J., Evidence for an oxygen evolving iron–oxo–cerium intermediate in iron-catalysed water oxidation. *Nature Communications* **2015,** *6* (1), 5865.

2. Moonshiram, D.; Alperovich, I.; Concepcion, J. J.; Meyer, T. J.; Pushkar, Y., Experimental demonstration of radicaloid character in a Ru^{V}=O intermediate in catalytic water oxidation. *Proceedings of the National Academy of Sciences* **2013,** *110*, 3765-3770.

3. Fillol, J. L.; Codolà, Z.; Garcia-Bosch, I.; Gómez, L.; Pla, J. J.; Costas, M., Efficient water oxidation catalysts based on readily available iron coordination complexes. *Nature Chemistry* **2011,** *3* (10), 807-813.

4. Ellis, W. C.; McDaniel, N. D.; Bernhard, S.; Collins, T. J., Fast Water Oxidation Using Iron. *Journal of the American Chemical Society* **2010,** *132* (32), 10990-10991.

5. Grotjahn, D. B.; Brown, D. B.; Martin, J. K.; Marelius, D. C.; Abadjian, M.-C.; Tran, H. N.; Kalyuzhny, G.; Vecchio, K. S.; Specht, Z. G.; Cortes-Llamas, S. A.; Miranda-Soto, V.; van Niekerk, C.; Moore, C. E.; Rheingold, A. L., Evolution of Iridium-Based Molecular Catalysts during Water Oxidation with Ceric Ammonium Nitrate. *Journal of the American Chemical Society* **2011,** *133* (47), 19024-19027.

6. Sridharan, V.; Menéndez, J. C., Cerium(IV) Ammonium Nitrate as a Catalyst in Organic Synthesis. *Chemical Reviews* **2010,** *110* (6), 3805-3849.

7. Nair, V.; Deepthi, A., Cerium(IV) Ammonium Nitrate-A Versatile Single-Electron Oxidant. *Chem. Rev. (Washington, DC, U. S.)* **2007,** *107* (5), 1862-1891.

8. Piro, N. A.; Robinson, J. R.; Walsh, P. J.; Schelter, E. J., The electrochemical behavior of cerium(III/IV) complexes: Thermodynamics, kinetics and applications in synthesis. *Coordination Chemistry Reviews* **2014,** *260*, 21-36.

9. Molander, G. A., Application of lanthanide reagents in organic synthesis. *Chemical Reviews* **1992,** *92* (1), 29-68.

10. Noyes, A. A.; Garner, C. S., Strong Oxidizing Agents in Nitric Acid Solution. I. Oxidation Potential of Cerous—Ceric Salts. *Journal of the American Chemical Society* **1936,** *58* (7), 1265-1268.

11. Sawant, S.; Wu, X.; Cho, J.; Cho, K.-B.; Kim, S.; Seo, M.; Lee, Y.-M.; Kubo, M.; Ogura, T.; Shaik, S.; Nam, W., Water as an Oxygen Source: Synthesis, Characterization, and Reactivity Studies of a Mononuclear Nonheme Manganese(IV) Oxo Complex. *Angewandte Chemie* **2010,** *122* (44), 8366-8370.

12. Barman, P.; Vardhaman, A. K.; Martin, B.; Wörner, S. J.; Sastri, C. V.; Comba, P., Influence of Ligand Architecture on Oxidation Reactions by High-Valent Nonheme Manganese Oxo Complexes Using Water as a Source of Oxygen. *Angewandte Chemie* **2015,** *127* (7), 2123-2127.

13. Karmalkar, D. G.; Sankaralingam, M.; Seo, M. S.; Ezhov, R.; Lee, Y.-M.; Pushkar, Y. N.; Kim, W.-S.; Fukuzumi, S.; Nam, W., A High-Valent Manganese(IV)–Oxo–Cerium(IV) Complex and Its Enhanced Oxidizing Reactivity. *Angewandte Chemie International Edition* **2019,** *58* (45), 16124-16129.

14. Wu, X.; Yang, X.; Lee, Y.-M.; Nam, W.; Sun, L., A nonheme manganese(IV)-oxo species generated in photocatalytic reaction using water as an oxygen source. *Chem. Commun. (Cambridge, U. K.)* **2015,** *51* (19), 4013-4016.

15. Lee, Y.-M.; Dhuri, S. N.; Sawant, S. C.; Cho, J.; Kubo, M.; Ogura, T.; Fukuzumi, S.; Nam, W., Water as an Oxygen Source in the Generation of Mononuclear Nonheme Iron(IV) Oxo Complexes. *Angewandte Chemie International Edition* **2009,** *48* (10), 1803-1806.

16. Parsell, T. H.; Yang, M.-Y.; Borovik, A. S., C−H Bond Cleavage with Reductants: Re-Investigating the Reactivity of Monomeric $Mn^{III/IV}$−Oxo Complexes and the Role of Oxo Ligand Basicity. *Journal of the American Chemical Society* **2009,** *131* (8), 2762-2763.

17. Czernuszewicz, R. S.; Su, Y. O.; Stern, M. K.; Macor, K. A.; Kim, D.; Groves, J. T.; Spiro, T. G., Oxomanganese(IV) porphyrins identified by resonance Raman and infrared spectroscopy. Weak bonds and the stability of the half-filled t2g subshell. *Journal of the American Chemical Society* **1988,** *110* (13), 4158-4165.

18. Makino, R.; Uno, T.; Nishimura, Y.; Iizuka, T.; Tsuboi, M.; Ishimura, Y., Coordination structures and reactivities of compound II in iron and manganese horseradish peroxidases. A resonance Raman study. *Journal of Biological Chemistry* **1986,** *261* (18), 8376-8382.

19. Groves, J. T.; Stern, M. K., Olefin epoxidation by manganese (IV) porphyrins: evidence for two reaction pathways. *Journal of the American Chemical Society* **1987,** *109* (12), 3812-3814.

20. Draksharapu, A.; Rasheed, W.; Klein, J. E. M. N.; Que Jr, L., Facile and Reversible Formation of Iron(III)–Oxo–Cerium(IV) Adducts from Nonheme Oxoiron(IV) Complexes and Cerium(III). *Angewandte Chemie International Edition* **2017,** *56* (31), 9091-9095.

21. Massie, A. A.; Denler, M. C.; Cardoso, L. T.; Walker, A. N.; Hossain, M. K.; Day, V. W.; Nordlander, E.; Jackson, T. A., Equatorial Ligand Perturbations Influence the Reactivity of Manganese(IV)-Oxo Complexes. *Angewandte Chemie International Edition* **2017,** *56* (15), 4178-4182.

22. Massie, A. A.; Sinha, A.; Parham, J. D.; Nordlander, E.; Jackson, T. A., Relationship between Hydrogen-Atom Transfer Driving Force and Reaction Rates for an Oxomanganese(IV) Adduct. *Inorganic Chemistry* **2018,** *57* (14), 8253-8263.

23. Denler, M. C.; Massie, A. A.; Singh, R.; Stewart-Jones, E.; Sinha, A.; Day, V. W.; Nordlander, E.; Jackson, T. A., Mn^{IV}-Oxo complex of a bis(benzimidazolyl)-containing N5 ligand reveals different reactivity trends for Mn^{IV}-oxo than Fe^{IV}-oxo species. *Dalton Transactions* **2019,** *48* (15), 5007-5021.

24. Massie, A. A.; Denler, M. C.; Singh, R.; Sinha, A.; Nordlander, E.; Jackson, T. A., Structural Characterization of a Series of N5-Ligated Mn^{IV}-Oxo Species. *Chem-Eur J* **2020,** *26* (4), 900-912.

25. Rana, S.; Dey, A.; Maiti, D., Mechanistic elucidation of C–H oxidation by electron rich non-heme iron(iv)–oxo at room temperature. *Chemical Communications* **2015,** *51* (77), 14469-14472.

26. Lee, Y.; Jackson, T. A., Ligand Influence on Structural Properties and Reactivity of Bis(μ-oxo)dimanganese(III,IV) Species and Comparison of Reactivity with Terminal Mn^{IV}-oxo Complexes. *ChemistrySelect* **2018,** *3* (47), 13507-13516.

27. Saltzman, H.; Sharefkin, J. G., Iodosobenzene. *Organic Syntheses* **1963,** *43*, 60.

28. Dixon, N. E.; Lawrance, G. A.; Lay, P. A.; Sargeson, A. M.; Taube, H., Trifluoromethanesulfonates and Trifluoromethanesulfonato-O Complexes. *Inorganic Syntheses* **1990**, 70-76.

29. Ravel, B.; Newville, M., ATHENA, ARTEMIS, HEPHAESTUS: data analysis for X-ray absorption spectroscopy using IFEFFIT. *Journal of Synchrotron Radiation* **2005,** *12* (4), 537-541.

30. Rehr, J. J.; Mustre De Leon, J.; Zabinsky, S. I.; Albers, R. C., Theoretical x-ray absorption fine structure standards. *Journal of the American Chemical Society* **1991,** *113* (14), 5135-5140.

31. Wojdyr, M., Fityk: a general-purpose peak fitting program. *Journal of Applied Crystallography* **2010,** *43* (5-1), 1126-1128.

32. Goodson, P. A.; Glerup, J.; Hodgson, D. J.; Michelsen, K.; Weihe, H., Syntheses and characterization of binuclear manganese(III,IV) and -(IV,IV) complexes with ligands related to *N*,*N*′-bis(2-pyridylmethyl)-1,2-ethanediamine. *Inorganic Chemistry* **1991,** *30* (26), 4909-4914.

33. Cooper, S. R.; Dismukes, G. C.; Klein, M. P.; Calvin, M., Mixed valence interactions in di-.mu.-oxo bridged manganese complexes. Electron paramagnetic resonance and magnetic susceptibility studies. *Journal of the American Chemical Society* **1978,** *100* (23), 7248-7252.

34. Chandra, S. K.; Basu, P.; Ray, D.; Pal, S.; Chakravorty, A., A family of mononuclear manganese(IV) complexes: an $Mn^{IV}O4N2$ sphere assembled via phenolate-imine-carboxylate coordination. *Inorganic Chemistry* **1990,** *29* (13), 2423-2428.

35. Charnock, J. M.; Garner, C. D.; Trautwein, A. X.; Bill, E.; Winkler, H.; Ayougou, K.; Mandon, D.; Weiss, R., Characterization of an Oxo(porphyrinato)manganese(IV) Complex by X-ray Absorption Spectroscopy. *Angewandte Chemie International Edition in English* **1995,** *34* (3), 343-346.

36. Lassalle-Kaiser, B.; Hureau, C.; Pantazis, D. A.; Pushkar, Y.; Guillot, R.; Yachandra, V. K.; Yano, J.; Neese, F.; Anxolabéhère-Mallart, E., Activation of a water molecule using a mononuclear Mn complex: from Mn-aquo, to Mn-hydroxo, to Mn-oxyl via charge compensation. *Energy & Environmental Science* **2010,** *3* (7), 924-938.

37. Yin, G.; McCormick, J. M.; Buchalova, M.; Danby, A. M.; Rodgers, K.; Day, V. W.; Smith, K.; Perkins, C. M.; Kitko, D.; Carter, J. D.; Scheper, W. M.; Busch, D. H., Synthesis, Characterization, and Solution Properties of a Novel Cross-Bridged Cyclam Manganese(IV) Complex Having Two Terminal Hydroxo Ligands. *Inorganic Chemistry* **2006,** *45* (20), 8052-8061.

38. Garcia-Bosch, I.; Company, A.; Cady, C. W.; Styring, S.; Browne, W. R.; Ribas, X.; Costas, M., Evidence for a Precursor Complex in C–H Hydrogen Atom Transfer Reactions Mediated by a Manganese(IV) Oxo Complex. *Angewandte Chemie International Edition* **2011,** *50* (25), 5648-5653.

39. Jeong, D.; Yan, J. J.; Noh, H.; Hedman, B.; Hodgson, K. O.; Solomon, E. I.; Cho, J., Oxidation of Naphthalene with a Manganese(IV) Bis(hydroxo) Complex in the Presence of Acid. *Angewandte Chemie International Edition* **2018,** *57* (26), 7764-7768.

40. Leto, D. F.; Jackson, T. A., Mn K-Edge X-ray Absorption Studies of Oxo- and Hydroxo-manganese(IV) Complexes: Experimental and Theoretical Insights into Pre-Edge Properties. *Inorganic Chemistry* **2014,** *53* (12), 6179-6194.

41. Sarangi, R., X-ray absorption near-edge spectroscopy in bioinorganic chemistry: Application to M–O2 systems. *Coordination Chemistry Reviews* **2013,** *257* (2), 459-472.

42. Westre, T. E.; Kennepohl, P.; Dewitt, J. G.; Hedman, B.; Hodgson, K. O.; Solomon, E. I., A Multiplet Analysis of Fe K-Edge 1s → 3d Pre-Edge Features of Iron Complexes. *Journal of the American Chemical Society* **1997,** *119* (27), 6297-6314.

43. Roe, A. L.; Schneider, D. J.; Mayer, R. J.; Pyrz, J. W.; Widom, J.; Que, L., X-ray absorption spectroscopy of iron-tyrosinate proteins. *Journal of the American Chemical Society* **1984,** *106* (6), 1676-1681.

44. Gupta, R.; Taguchi, T.; Lassalle-Kaiser, B.; Bominaar, E. L.; Yano, J.; Hendrich, M. P.; Borovik, A. S., High-spin Mn–oxo complexes and their relevance to the oxygen-evolving complex within photosystem II. *Proceedings of the National Academy of Sciences* **2015,** *112* (17), 5319-5324.

45. Taguchi, T.; Stone, K. L.; Gupta, R.; Kaiser-Lassalle, B.; Yano, J.; Hendrich, M. P.; Borovik, A. S., Preparation and properties of an Mn^{IV}–hydroxide complex: proton and electron transfer at a mononuclear manganese site and its relationship to the oxygen evolving complex within photosystem II. *Chemical Science* **2014,** *5* (8), 3064-3071.

46. Wieghardt, K., The Active Sites in Manganese-Containing Metalloproteins and Inorganic Model Complexes. *Angewandte Chemie International Edition in English* **1989,** *28* (9), 1153-1172.

Chapter 4

Formation, Characterization, and C–H Bond Activation Reactivity of Mononuclear Oxomanganese(IV) Species

4.1 Introduction

Catalysis with earth-abundant transition metals for hydrocarbon activation has been one of the most sustainable and efficient strategies to access synthetic feedstocks, fine chemicals, and pharmaceutical compounds.[1-4] This area of research has gained much attention as cytochrome P450 (CYP) heme proteins and methane monooxygenases (MMOs) were found to perform transformations involving inert C–H bond activation with great selectivity under ambient conditions.[5] With the aim of developing metal catalysts that function like CYP enzymes and MMOs, a number of transition metal model complexes have been developed and their C–H bond activation mechanisms have been investigated to understand the oxidative chemistry by those enzymes in nature.[6-11] From those studies, high-valent metal-oxo species have been proposed to be the active intermediates that react with organic substrates, and many studies have been conducted to reveal the significant factors of hydrocarbon activation reaction by using synthetic high-valent metal-oxo complexes.[12-16]

High-valent oxomanganese model complexes in mono- or multi-nuclear form have evolved in line with the investigations for biological metalloenzymes to develop synthetic catalysts for C–H bond transformations.[13, 14, 17-21] These model complexes have shown critical factors that can modulate the C–H bond activation reactivity of metal catalysts. Among the efforts made to reveal those critical factors, our group had developed a series of oxomanganese(IV) complexes with different degrees of perturbations on equatorial ligand-field.[22-24] In these studies, the kinetic experiments with the oxomanganese(IV) complexes showed considerably different C–H bond activation reactivities depending on the equatorial ligand-field strength of each oxomanganese(IV) complex. The oxomanganese(IV) complex with relatively weak equatorial ligand-field exhibits

the fastest reactivity towards C–H bond activation among the three oxomanganese(IV) complexes used in the study. In other studies, it has been shown that C–H bond activation reactivity can be varied dependent on the central transition metal of metal-oxo complex. Within the same ligand scaffold, 2pyN2B ((*N*-bis(1-methyl-2-benzimidazolyl)methyl-*N*-(bis-2-pyridylmethyl)amine), the oxomanganese(IV) complex reacts as a sluggish oxidant to abstract H atom from substrates. In contrast, oxoiron(IV) complex shows higher reactivities than not only the oxomanganese(IV) complex but also other oxoiron(IV) complexes with similar ligand frameworks, showing the potential of a strong oxidant. Possible rationales have been proposed to explain this variation between oxomanganese(IV) and oxoiron(IV) complexes, which can be summarized as: i) both oxometal complexes take different reaction channels to activate C–H bond and ii) the major factor that influences the C–H bond activation reactivity the most is not the same for each oxometal complex.[25] However, there is no systematic studies yet with oxomanganese(IV) and oxoiron(IV) complexes to confirm whether these proposals hold true and are applicable to other oxometal systems with different ligands.

Studies to discern the major determinant of the C–H bond activation reactivity of oxo-metal species have been carried out to establish essential requirements for highly efficient synthetic catalysts. Since the classical thermodynamic contributions were introduced to describe the reactivity by oxo-metal complexes,[26-29] other factors have been explored to explain the C–H bond activation, including geometric and electronic structural parameters,[22, 30-32] basicity of the one-electron reduced form,[33, 34] multistate reactivity,[35] tunneling contributions,[36, 37] and (a)synchronicity.[38, 39] Based on those previous studies, it is clearly shown that multiple factors are contributing to the reactivity of oxo-metal species towards C–H bond activation. Although it is not applicable in every C–H bond activation reaction, the most generic model, so far, to interpret the

C–H bond activation reactivity by oxometal species comes from the thermodynamic contributions to cleave substrate C–H bond and form metal O–H bond in the catalytic reaction.

Intending to identify the dominant factor that determines the C–H bond activation reactivity of oxomanganese(IV) complexes, in this study we have prepared two newly generated oxomaganese(IV) species and investigated the oxidative reactivity of one oxomanganese(IV) species experimentally. Two oxomanganese(IV) complexes are chosen from another computational study that investigated thermodynamic contributions to postulate the generic reactivity trend towards C–H bond activation by the oxomanganese(IV) complexes.[40] The C–H bond activation reactivity of the eight oxomanganese(IV) complexes were predicted based on their calculated $Mn^{IV/III}$ reduction potentials and pK_a values of the corresponding Mn^{III}–hydroxo complexes.[41] Among the eight complexes, three oxomanganese(IV) complexes were targeted to be synthesized, and two of the complexes, $[Mn^{IV}(O)(N3pyQ)]^{2+}$ (N3pyQ = 1,1-di(pyridin-2-yl)-*N*-(pyridin-2-ylmethyl)-*N*-(quinolin-2-ylmethyl)methanamine) and $[Mn^{IV}(O)(N4py^{2Me})]^{2+}$ ($N4py^{2Me}$ = *N*,*N*-Bis((1-methyl-1H-imidazol-2-yl)methyl)-1,1-di(pyridin-2-yl)methanamine), were experimentally prepared and are described in this chapter. The C–H bond activation reactivities of one of the two complexes were explored with a series of organic substrates that encompasses a wide range of bond dissociation enthalpies (BDEs). The experimental results were compared with theoretical predictions of their C–H bond activation reactivity based on the expected thermodynamic driving forces of the reaction.

4.2 Experimental Methods

4.2.1 Materials and Instrumentation. Chemicals and solvents were ACS reagent, or better, and were purchased from commercial vendors. Chemicals were used as received, except 9,10-dihydroanthracene (DHA) which was recrystallized from hot ethanol.[42] Iodosobezene (PhIO) was synthesized from iodosobenzene diacetate following the reported procedure.[43] A Varian Cary 50 Bio or an Agilent 8453 spectrophotometer equipped with a Unisoku cryostat, USP-203-A, was used to collect electronic absorption spectra for kinetic experiments at a desired temperature. Electron paramagnetic resonance (EPR) spectra were collected using a Bruker EMXPlus spectrometer (X-band; 9.4 GHz) with a Bruker ER4116DM dual-mode cavity. Temperatures were controlled with an Oxford ESR900 continuous flow cryostat and an Oxford ITC503 cryostat controller. Detailed recording conditions are in the caption of each EPR spectrum (*vide infra*). Nuclear magnetic resonance (NMR) spectra were obtained using a Bruker 400 MHz AVIIIHD NMR instrument.

4.2.2 Synthesis and Characterization. A neutral N5 pentadentate ligand, N3pyQ, was prepared by the following procedure. Di-2-pyridyl ketone oxime and di-2-pyridylmethanamine were synthesized according to literature procedures.[44] Di-2-pyridylmethanamine was transferred to a scintillation vial (1.8 g, 10 mmol) and put into an ice bath. 2-Pyridinecarboxaldehyde was added (1.1 mL, 12 mmol; 1.2 equiv.) for a neat reaction to generate (*E*)-*N*-(di(pyridin-2-yl)methyl)-1-(pyridin-2-yl)methanimine. The reaction vial was stored in a refrigerator at 5 °C overnight. The pale-yellow product (1.7 g, 6.2 mmol) was rinsed with cyclohexane and transferred to a three-necked round-bottom flask. After the product was dissolved in MeOH (23 mL), $NaBH_4$ was added (0.49 g, 13 mmol; 2.1 equiv.). The reaction solution was stirred for three hours at room temperature. During the reaction, the color of the solution changed from magenta to sangria. The

reaction flask was cooled, and conc. HCl was added until acidic (pH < 2). The addition of acid caused gas evolution and the reaction solution changed color from sangria to orange, to sage, and to mauve over time. The reaction solution was stirred an additional 30 minutes. 5 M NaOH solution was added dropwise to make the reaction solution basic (pH > 10) and the color of the solution was changed from grey-purple to green, to yellow, to orange, and to brown in the end. Afterward, the solvent of the reaction solution was evaporated in vacuo and the product was extracted with ethyl acetate and water. The organic layer was rinsed with brine and dried with Na_2SO_4. Evaporation of the organic solvent gave 1,1-di(pyridin-2-yl)-*N*-(pyridin-2-ylmethyl)methanamine (91% yield).

The final step of N3pyQ ligand synthesis was carried out by reacting the crude product of the former step (1.7 g, 6 mmol) and 2-(chloromethyl)quinoline hydrochloride (1.5 g, 6.8 mmol; 1.1 equiv.) in 5 M NaOH solution (60 mL). The reaction mixture was refluxed at 80 °C for 30 hours then stirred under N_2 for 42 hours. Extraction was performed with CH_2Cl_2 followed by brine wash and dried with Na_2SO_4 (63% yield). The crude ligand was purified using basic alumina using CH_2Cl_2/MeOH solvent mixture. The product was obtained as a brown oil (59% yield). ^{1}H NMR ($CDCl_3$): δ 8.58 (dq, 2H), 8.50 (dt, 1H), 8.09 (d, 1H), 8.04 (d, 1H), 7.82 (d, 1H), 7.77-7.65 (m, 6H), 7.61-7.55 (m, 2H), 7.49 (ddd, 1H), 7.15 (ddd, 2H), 7.08 (ddd, 1H), 5.42 (s, 1H), 4.19 (s, 2H), 4.04 (s, 2H); ^{13}C NMR ($CDCl_3$): δ 149.45, 149.10, 136.43, 129.42, 129.11, 127.58, 127.41, 126.16, 124.31, 123.26, 122.26, 121.95, 121.23, 72.17, 58.12, 57.68.

The 2pyN2I ligand (2pyN2I = *N*,*N*-bis((6-methylpyridin-2-yl)methyl)-1,1-di(pyridin-2-yl)methanamine), which features two 1-methyl-imidazolyl moieties, was prepared by modification of the synthesis of a similar ligand.[45] Di-2-pyridylamine (1 g, 5.4 mmol) was stirred with $NaBH(CH_3COO)_3$ (8 g, 38 mmol; 7 equiv.) in CH_2Cl_2 (200 mL). The reaction mixture was cooled

in an ice bath followed by the addition of 1-methyl-2-imidazolecarboxaldehyde (1.2 g, 11 mmol; 2 equiv.). The reaction mixture was stirred for 48 hours under N_2. A saturated $NaHCO_3$ aqueous solution was added to quench the reaction, which formed gas. Extraction of the product was performed with ethyl acetate, and the organic extracts were dried over Na_2SO_4 followed by evaporation of the organic solvent. The crude product was gained as a pale-yellow oil (92% yield). Product purification was carried out using column chromatography on basic alumina with MeOH/CH_2Cl_2 as the eluent (32% yield). ^{1}H NMR ($(CD_3)_2SO$): δ 8.52 (dq, 2H), 7.77 (td, 2H), 7.57 (dt, 2H), 7.27 (ddd, 2H), 7.02 (d, 2H), 6.81 (d, 2H), 5.23 (s, 1H), 3.81 (s, 4H), 3.31 (s, 6H).

Metal complexes with the preceding ligands were prepared by combining 1 equiv. $Mn^{II}(OTf)_2 \cdot 2CH_3CN$ (208 mg and 233 mg for N3pyQ and 2pyN2I ligands, respectively)[46] with 1 equiv. ligand (200 mg) in CH_3CN (25 mL) and stirring overnight under an inert atmosphere. For metalation of 2pyN2I ligand, 1 equiv. $Mn^{II}(ClO_4) \cdot 6H_2O$ (194 mg) was also used in MeOH (10 mL) to promote recrystallization of the complex in the next step. ***Caution!*** *Perchlorate salts of metal complexes are potentially explosive. This metalation step must be performed in small quantities.* The solvent was filtered with a 0.45 μm PTFE syringe filter and evaporated in vacuo. The residual solid was redissolved with a small amount of CH_3CN (approximately 1 - 2 mL) and layered with diethyl ether. The obtained crystals were purified further by slow evaporation and/ or vapor diffusion, both using CH_3CN/Et_2O until the crystals were not contaminated by brown ligand residues.

4.2.3 Electron Paramagnetic Resonance Experiments. EPR samples for oxomanganese(IV) species were prepared by adding PhIO in TFE to each Mn(II) complex (5 or 3 mM, see Figures 4.6 and 4.7) in TFE. After checking the maximum oxomanganese(IV) complex formation on the electronic absorption spectra, an aliquot of the solution containing

oxomanganese(IV) complex (approximately 300 μL) was transferred to a 4 mm quartz EPR tube and flash frozen using liquid N_2.

4.2.4 C–H Bond Activation Kinetic Experiments. Kinetic studies were carried out to determine the reactivity of oxomanganese(IV) complexes towards C–H bonds of organic substrates with different bond dissociation free energies. For general procedures, the addition of 1 mL PhIO in TFE to 1 mL $[Mn^{II}(N3pyQ)]^{2+}$ or $[Mn^{II}(N4py^{2Me})]^{2+}$ in TFE was performed to generate 1 mM oxomanganese(IV) complex. Different amounts of PhIO were used to achieve maximized yield and stability of the oxomanganese(IV) complex; e.g., 2.5 equiv. PhIO for $[Mn^{IV}(O)(N3pyQ)]^{2+}$ and 10 equiv. PhIO for $[Mn^{IV}(O)(2pyN2I)]^{2+}$. All the formation and kinetic experiments were performed in a quartz cuvette at 25 °C. The formation of oxomanganese(IV) complex in the solution was monitored by electronic absorption spectroscopy using the characteristic near-IR band of each complex. Once the formation reached its maximum, an excess amount of organic substrate in 100 μL CH_2Cl_2 or TFE was added to the solution. The reaction between oxomanganese(IV) complex and organic substrate was observed by tracking the decay of the near-IR absorption signal of the oxomanganese(IV) complex. The pseudo-first order rate constant (k_{obs}) was obtained by fitting the decay time trace over approximately five half-lives. The second-order rate constant (k_2) was attained by collecting k_{obs} at a minimum of four different substrate concentrations. The k_{obs} values were plotted against the substrate concentration used and the k_2 value was determined from the slope. The added substrate in CH_2Cl_2 or TFE was of varied volume (from 100 μL to 200 μL), depending on the solubility of substrate in TFE. Although we varied volume of the solution of substrate, the total volume of the reaction solution was set as 2.1 mL by reducing the volume of the solution of PhIO used to generate the oxomanganese(IV) complex.

4.3 Results and Discussion

4.3.1 X-ray Diffraction Characterization of $[Mn^{II}(N3pyQ)(OH_2)](ClO_4)_2$. An XRD structure for $[Mn^{II}(N3pyQ)(OH_2)](ClO_4)_2$ reveals a Mn^{II} center in a distorted octahedral geometry, with the Mn atom bound to five N atoms from the N3pyQ ligand and one O atom from a water molecule (Figure 4.1).[47] The average $Mn–N_{equatorial}$ bond distance is 2.26 Å, with a range from 2.217(2) to 2.299(2) Å. The bond distances of the Mn center with the axial N1 and O1W ligands are 2.269(2) and 2.096(3) Å, respectively. These bond distances in the primary sphere are similar to those reported for $[Mn^{II}(N4py)(OTf)](OTf)$ and $[Mn^{II}(2pyN2Q)(OH_2)](ClO_4)_2$ (N4py = 1,1-di(pyridin-2-yl)-*N*,*N*-bis(pyridin-2-ylmethyl)methanamine; 2pyN2Q = 1,1-di(pyridin-2-yl)-*N*,*N*-bis(quinolin-2-ylmethyl)methanamine).[22, 48] The average $Mn–N_{equatorial}$ bond distance from the XRD structure of $[Mn^{II}(N4py)(OTf)](OTf)$ is 2.26 Å. A little longer bond distances are observed for $[Mn^{II}(2pyN2Q)(OH_2)](ClO_4)_2$, affording the average $Mn–N_{equatorial}$ bond distance of 2.28 Å. This slightly elongated $Mn–N_{equatorial}$ bond distance of $[Mn^{II}(2pyN2Q)(OH_2)](ClO_4)_2$ was attributed previously to the two bulky quinolinyl moieties giving less donation to the center Mn atom.[22] The same steric effect is observed in $[Mn^{II}(N3pyQ)(OH_2)](ClO_4)_2$, as the bond distance of Mn–N4 (from the quinolinyl moiety) is slightly longer (by 0.042 Å) than that of Mn–N5 (from the pyridinyl moiety). The axial angle of $[Mn^{II}(N3pyQ)(OH_2)](ClO_4)_2$ is 165.8° (for N1–Mn–O1W). This angle is slightly larger than the axial angle of $[Mn^{II}(2pyN2Q)(OH_2)](ClO_4)_2$, which is 163.8°. Additionally, the axial water ligand is away from the quinolinyl moiety. The angle of the N atom of the quinolinyl moiety and the axial water ligand, N4–Mn–O1W, is 116.6°. In contrast, the angle between the N atom of the pyridinyl moiety and the axial water, N4–Mn–O1W, is 100.4°. These two different angles show the steric hinderance caused by the quinolinyl group. The same steric effect has been also seen in an XRD structure of $[Mn^{II}(2pyN2Q)(OH_2)](ClO_4)_2$, due to the two

quinolinyl moieties on the ligand scaffold. As an example, the angles between N atoms from the two quinolinyl moieties and the axial water, N4–Mn–O1W and N5–Mn–O1W are 113.6° and 114.5°, respectively, reflecting the steric encumbrance within the 2pyN2Q ligand frame. Together, an XRD structure analysis of one of the new manganese(II) complexes, $[Mn^{II}(N3pyQ)(OH_2)](ClO_4)_2$, provides the metric parameters that are in between those of $[Mn^{II}(2pyN2Q)(OH_2)](ClO_4)_2$ and $[Mn^{II}(N4py)(OTf)](OTf)$, as we expected based on the ligand structure of the complex.

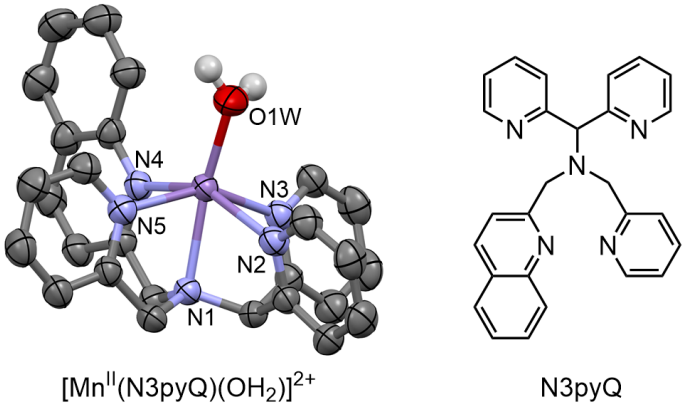

Figure 4.1. X-ray structure of $[Mn^{II}(N3pyQ)(OH_2)]^{2+}$ and N3pyQ ligand structure. Hydrogens on carbon atoms are omitted for clarity.

The crystal structure of $[Mn^{II}(2pyN2I)(OTf)](OTf)$ was also determined to reveal the geometric characteristics of this complex (Figure 4.2). The N5 pentadentate 2pyN2I ligand and a triflate ion are coordinated to the center Mn atom through a distorted octahedral geometry. The average $Mn–N_{equatorial}$ bond distance is 2.24 Å from the four coordinate bond distances from 2.177(3) Å to 2.314(2) Å. The smaller average bond distance than that of other crystallographically

characterized manganese(II) complexes (average Mn–$N_{equatorial}$ bond distances are from 2.25 Å to 2.28 Å)[24] is attributed to the short bond distances between the Mn and N atoms from the two (*N*-methyl)imidazolyl moieties, 2.177(3) and 2.181(2) Å. The short distance of Mn–N bond implies that more donation is made by the (*N*-methyl)imidazolyl group to the Mn center, reflecting the high basicity of this nitrogen heterocycle similar to that of (*N*-methyl)benzimidazole.[49] Slight longer bond distances (2.193(2) Å) are found between the Mn and the N atoms from (*N*-methyl)benzimidazolyl moieties in the previous study with $[Mn^{II}(2pyN2B)(OH_2)](OTf)$, which is very likely due to the steric bulkiness of the (*N*-methyl)benzimidazolyl group.[24] The short bond distances of Mn–$N_{(N\text{-methyl})imidazolyl}$ cause some *trans* influence to the opposite side Mn–$N_{pyridinyl}$ distances, resulting in 2.314(2) and 2.286(3) Å. Besides, the axial bond of Mn–N1 shows much longer distance of 2.380(3) Å compared to the equatorial Mn–N bond distances in the structure (average Mn–$N_{equatorial}$ = 2.24 Å). This elongation of the axial bond is also observed in $[Mn^{II}(2pyN2B)(OH_2)](OTf)$, which displays bond distances nearly identical to those of $[Mn^{II}(2pyN2I)(OTf)](OTf)$ (2.38 Å and 2.25 Å for the axial Mn–N1 and average Mn–$N_{equatorial}$ bonds, respectively). This similarity might originate from the comparable angular restrictions imposed by the imidazole and benzimidazole moieties in the 2pyN2I and 2pyN2B ligands. The selected bond distances and angles of $[Mn^{II}(N3pyQ)(OH_2)](ClO_4)_2$ and $[Mn^{II}(2pyN2I)(OTf)](OTf)$ are shown in Table 4.1.

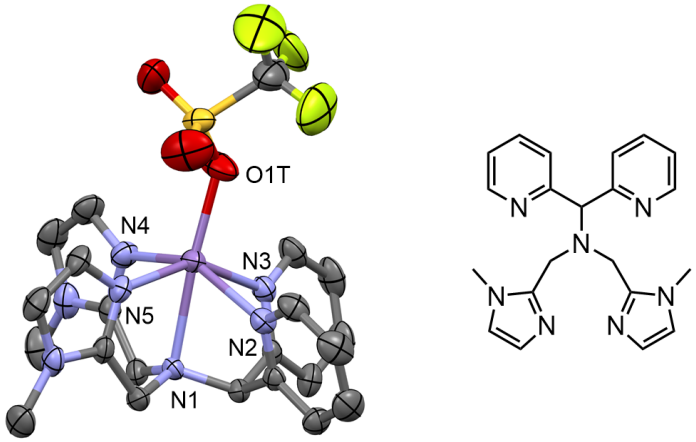

Figure 4.2. X-ray structure of $[Mn^{II}(2pyN2I)(OTf)]^{+}$ and 2pyN2I ligand structure. Hydrogens are omitted for clarity.

Table 4.1. Selected bond distances and angles of $[Mn^{II}(N3pyQ)(OH_2)](ClO_4)_2$ and $[Mn^{II}(2pyN2I)(OTf)](OTf)$.

$[Mn^{II}(N3pyQ)(OH_2)](ClO_4)_2$					
Bond	Distance (Å)	Angles (°)			
Mn–O1W	2.096(3)	N1–Mn–O1W	165.8(1)	N2–Mn–N3	79.33(8)
Mn–N1	2.269(2)	N2–Mn–O1W	92.5(1)	N4–Mn–N5	86.67(8)
Mn–N2	2.299(2)	N3–Mn–O1W	107.8(1)	N2–Mn–N4	150.23(8)
Mn–N3	2.272(2)	N4–Mn–O1W	116.6(1)	N3–Mn–N5	151.25(8)
Mn–N4	2.259(2)	N5–Mn–O1W	100.4(1)	N2–Mn–N5	94.14(8)
Mn–N5	2.217(2)			N3–Mn–N4	85.74(8)
$[Mn^{II}(2pyN2I)(OTf)](OTf)$					
Bond	Distance (Å)	Angles (°)			
Mn–O1T	2.106(3)	N1–Mn–O1T	172.5(1)	N2–Mn–N3	79.08(9)
Mn–N1	2.380(3)	N2–Mn–O1T	107.4(1)	N4–Mn–N5	91.3(1)
Mn–N2	2.286(3)	N3–Mn–O1T	99.9(1)	N2–Mn–N4	148.6(1)
Mn–N3	2.314(2)	N4–Mn–O1T	102.0(1)	N3–Mn–N5	148.64(9)
Mn–N4	2.177(3)	N5–Mn–O1T	111.3(1)	N2–Mn–N5	88.23(9)
Mn–N5	2.181(2)			N3–Mn–N4	85.3(1)

4.3.2 Formation and Characterization of Oxomanganese(IV) Complexes. The addition of 10 equiv. PhIO caused two electronic absorption bands to appear in the visible region at 390 and 467 nm (25600 and 21400 cm^{-1}, respectively) and one broad band to arise in the near-IR region at 1050 nm (9524 cm^{-1}) (Figure 4.3). The increase of absorbance at the three wavelengths occurs with the same rate (Appendix A4. Figure A4.1). The molar absorptivities of the three electronic absorption bands are 1350, 780, and 220 M^{-1} cm^{-1} for 390, 467, and 1050 nm bands, respectively. In previous studies, broad electronic absorption bands in the near-IR region have been shown to be characteristic of oxomanganese(IV) complexes with pentadentate N5 ligands.[22-24, 48] As an example, $[Mn^{IV}(O)(2pyN2Q)]^{2+}$ shows an electronic absorption band at 1180 nm (8475 cm^{-1}). Thus, we assigned the new chromophore as $[Mn^{IV}(O)(N3pyQ)]^{2+}$. Compared with λ_{max} of other oxomanganese(IV) species, $[Mn^{IV}(O)(N3pyQ)]^{2+}$ displays the near-IR maximum wavelength in between those of $[Mn^{IV}(O)(2pyN2Q)]^{2+}$ and $[Mn^{IV}(O)(N4py)]^{2+}$ (Figure 4.4). In a previous study, this near-IR absorption band of oxomanganese(IV) complex was attributed to the one-electron excitation from the $^4B_1$ ground state $(b_2(d_{xy})^1e(d_{yz},d_{xz})^2b_1(d_{x2-y2})^0a_1(d_{z2})^0)$ to the ^4E state $(b_2(d_{xy})^1e(d_{yz},d_{xz})^1b_1(d_{x2-y2})^1a_1(d_{z2})^0)$. On the basis of this assignment, we expect the $^4B_1 \rightarrow {}^4E$ transition energy for $[Mn^{IV}(O)(N3pyQ)]^{2+}$ to be between those of $[Mn^{IV}(O)(2pyN2Q)]^{2+}$ and $[Mn^{IV}(O)(N4py)]^{2+}$, as $[Mn^{IV}(O)(N3pyQ)]^{2+}$ has an intermediate equatorial ligand-field strength. The decay process of $[Mn^{IV}(O)(N3pyQ)]^{2+}$ was monitored using the near-IR maximum band at 1050 nm. When 10 equiv. PhIO was used in this formation reaction, when $[Mn^{IV}(O)(N3pyQ)]^{2+}$ is fully formed, the half-life ($t_{1/2}$) of the oxomanganese(IV) complex was approximately 30 minutes. In contrast, a much longer $t_{1/2}$ of ca. 2.3 hours was observed when a reduced amount of PhIO (2.5 equiv.) was added in the formation reaction, achieving a moderate formation of the

oxomanganese(IV) complex (> 85%). Thus, we used 2.5 equiv. PhIO for kinetic studies of the complex, as it provides better experimental conditions (see section **4.3.3**).

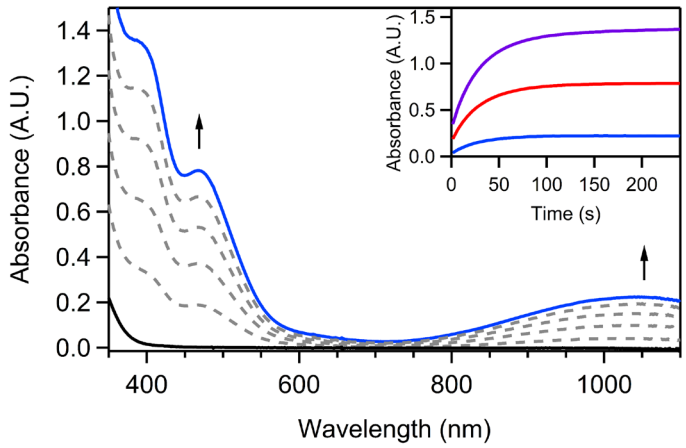

Figure 4.3. Formation of $[Mn^{IV}(O)(N3pyQ)]^{2+}$ (blue) from 1 mM $[Mn^{II}(N3pyQ)(OTf)]^{+}$ (black, solid) and 10 equiv. PhIO in TFE solution at 25 °C. The inset shows time traces at 390 nm (purple), 467 nm (red), and 1050 nm (blue) for the formation reaction.

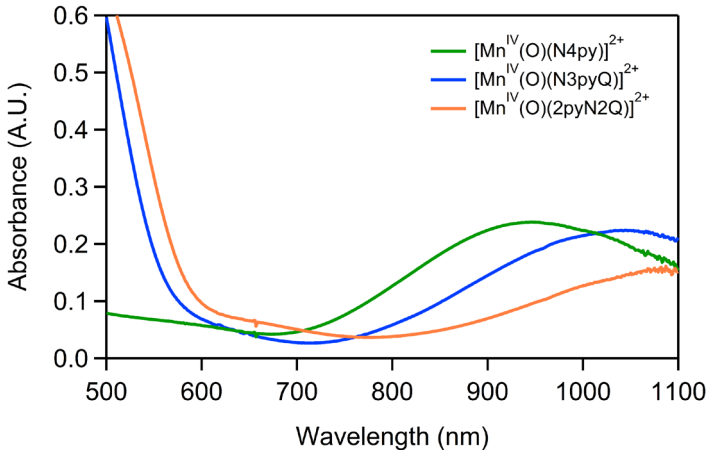

Figure 4.4. Comparison of the near-IR electronic absorption bands of $[Mn^{IV}(O)(N4py)]^{2+}$ (green), $[Mn^{IV}(O)(N3pyQ)]^{2+}$ (blue), and $[Mn^{IV}(O)(2pyN2Q)]^{2+}$ (orange).

On the other hand, $[Mn^{II}(2pyN2I)(OTf)](OTf)$ is also used to observe the reaction with an excess amount of PhIO in TFE. Upon the addition of 10 equiv. PhIO, we observed an absorption band in the near-IR region and two additional bands in the visible region at 445 and 650 nm (22470 and 15400 cm^{-1}, respectively; Figure 4.5). Similar to what mentioned earlier, the $^4B_1 \rightarrow {}^4E$ transition for $[Mn^{IV}(O)(2pyN2I)]^{2+}$ is expected to occur at a lower energy than the transition energies of $[Mn^{IV}(O)(N4py)]^{2+}$, due to the stronger equatorial ligand-field strength of $[Mn^{IV}(O)(2pyN2I)]^{2+}$ than that of $[Mn^{IV}(O)(N4py)]^{2+}$. (See Appendix A4. Figure A4.2 for DFT-optimized metric parameters of $[Mn^{IV}(O)(2pyN2I)]^{2+}$ and $[Mn^{IV}(O)(N4py)]^{2+}$). Indeed, the band is shown at 915 nm (10900 cm^{-1}). However, the electronic absorption band shown at 650 nm attains comparable intensity with the near-IR band, which is not observed in the electronic absorption spectra of other oxomanganese(IV) species. Moreover, the formation of the bands at 650 and 915 nm occur at different rates (Figure 4.5, inset). The rate difference indicates that more than one species is formed in the reaction. Additionally, while the intensity of the band at 915 nm decreases, the intensity of the band at 650 nm does not nearly change. Therefore, the absorbance at 650 nm does not originate from the decay process of the chromophore with the band at 915 nm. We tried to change the solvent of the reaction to see whether there are any changes in the formation reaction. Interestingly, changing the solvent from TFE to 1:1 TFE:CH_2Cl_2 of the reaction increased the absorbance intensity at 915 nm (by ~30 %) and reduced the absorbance at 650 nm slightly (Appendix 4; Figure A4.3). However, the ratio of these two products remains unclear. To better understand the percent formation of each product, spin quantification of EPR spectroscopy could be useful.

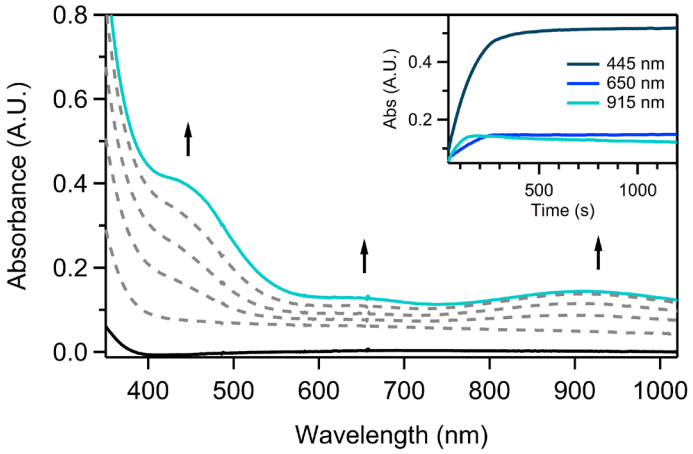

Figure 4.5. Formation of $[Mn^{IV}(O)(2pyN2I)]^{2+}$ (cyan) from 1 mM solution of $[Mn^{II}(2pyN2I)(OTf)]^{+}$ (black) and 10 equiv. PhIO in TFE solution at 25 °C. Time traces at 445 nm (denim blue), 650 nm (blue), and 915 nm (cyan) are shown in the inset.

The geometric and electronic structures of $[Mn^{IV}(O)(N3pyQ)]^{2+}$ in TFE solution was investigated using X-band EPR in the perpendicular mode. A positive signal with six-line hyperfine splitting is displayed at g_{eff} = 5.53, along with other signals at g_{eff} = 4.48, 2.68, and 2.0 (Figure 4.6). The hyperfine coupling constant, A, is observed as 7.2 mT from the six-line splitting at g_{eff} = 5.53. The g_{eff} values and hyperfine coupling constant of this complex are comparable with those values reported for other S = 3/2 Mn^{IV} species, which spans from 5.79 to 5.15 for the g_{eff} value of the six-line signal and from 7.7 mT to 6.6 mT for the A value.[22, 24, 50-52] The observed g_{eff} = 5.53 indicates that the Mn^{IV} species shows rhombic electronic properties. This signal is from either the ground state or excited state doublets expected to be seen in S = 3/2 spin manifold, m_s = ±1/2 and ±3/2, for four different spin energy levels. Two separated doublets are not always shown for high-spin Mn^{IV} species; however, it requires moderate to large zero-field splitting (ZFS) from the Mn^{IV} system. A couple of studies in literature where overlapped signals from the two doublets are shown report the axial zero-field splitting parameter (D) of 1.2 and 3.0 cm^{-1} obtained from

spectral simulations and temperature dependencies.[51, 52] Additionally, the signal from $m_s = \pm 3/2$ doublet appears at lower field than that from $m_s = \pm 1/2$ doublet. Based on these previously reported data, the signal at $g_{eff} = 4.48$ could be attributed to one of the two doublets, $m_s = \pm 1/2$ or $\pm 3/2$, possibly shown at low-field area.[51, 53] However, the signal could also originate from another $S = 3/2$ Mn^{IV} complex in a different conformation. Borovik and co-workers suggest two $S = 3/2$ Mn^{IV} conformers present for $[Mn^{IV}(H_3buea)(OH)]$ based on the simulations of the corresponding EPR spectrum.[54] Spectral simulations along with temperature-dependent EPR experiments will help us identify the origin of this signal. The broad signal at $g_{eff} = 2.68$ has been observed from other $S = 3/2$ Mn^{IV} species, with the position varying from $g_{eff} = 3.09$ to 2.44.[50, 51] The overall features of the EPR spectrum for $[Mn^{IV}(O)(N3pyQ)]^{2+}$ are similar to those of $[Mn^{IV}(O)(Bn\text{-}TPEN)]^{2+}$,[50] which suggests that the geometric and electronic structures of the two oxomanganese(IV) complexes are similar. We attribute the multi-line signals at $g_{eff} = 2.0$ ($A = 7.8$ mT) to μ-oxodimanganese(III,IV) species based on the g_{eff} and A values shown, which are nearly identical to the reported g_{eff} and A values for μ-oxodimanganese(III,IV) species with similar ligands (2.0 and 7.7 mT, respectively).[55] The μ-oxodimanganese(III,IV) complex can be formed as a decay product, as observed for similar systems.[24] It is possible that this multi-line signal has contributions from both the Mn^{II} center and μ-oxodimanganese(III,IV) species,[56] although it is difficult to identify the signals as they are very weak resonances.

As the generation of $[Mn^{IV}(O)(2pyN2I)]^{2+}$ may contain more than one species, we prepared two EPR samples from the formation reaction to identify which species corresponds to the near-IR absorption band and which to the 650 nm band shown (*vide supra*). For this purpose, one sample was made when the near-IR absorption band was at its maximum; the other sample was made when the 650 nm band was maximized. The perpendicular mode EPR spectrum of the sample with

the maximum near-IR absorption band shows a positive component at g_{eff} = 5.24, which most likely derives from S = 3/2 Mn^{IV} species (Figure 4.7). However, the intensity of the signal is weak and there is no hyperfine splitting observed in the spectrum. Another signal that can correspond to S = 3/2 Mn^{IV} is seen at g_{eff} = 3.38. Other resonances are found at g_{eff} = 2.0; however, the signals are too weak in intensity to be assigned. The second EPR sample prepared when the formation solution with the maximized 650 nm band absorption is EPR silent in the perpendicular mode (Appendix 4, Figure A4.4). This observation is corroborated with our tentative assignment of the absorption band from a Mn^{III} complex (*vide supra*). An attempt to obtain better signals by using a higher concentrated sample proved futile, as a weaker Mn^{IV} signal and the more intense impurity signal around g_{eff} = 2.0 were observed in the EPR spectrum (Appendix 4, Figure A4.5).

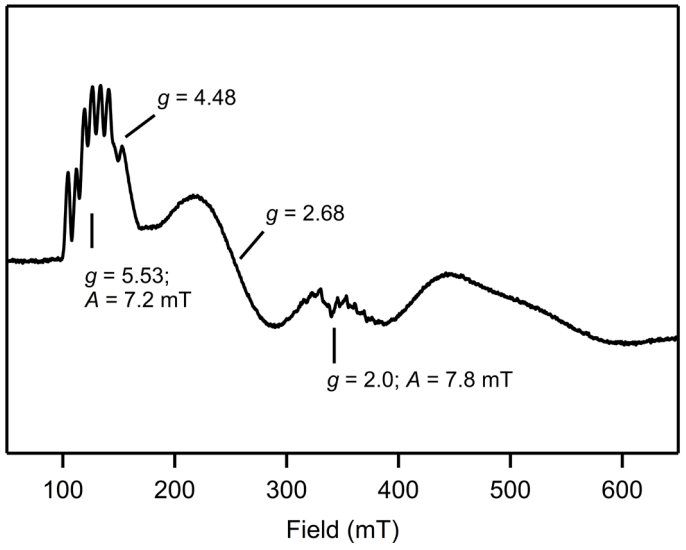

Figure 4.6. X-band EPR spectrum of 5 mM $[Mn^{IV}(O)(N3pyQ)]^{2+}$ generated by 2.5 equiv. PhIO in TFE. Experimental conditions: 9.64 GHz microwave frequency, 4 G modulation amplitude, 100 kHz modulation frequency, 14 dB power attenuation, 20 dB receiver gain, 40.96 ms time constant, and 13 K temperature.

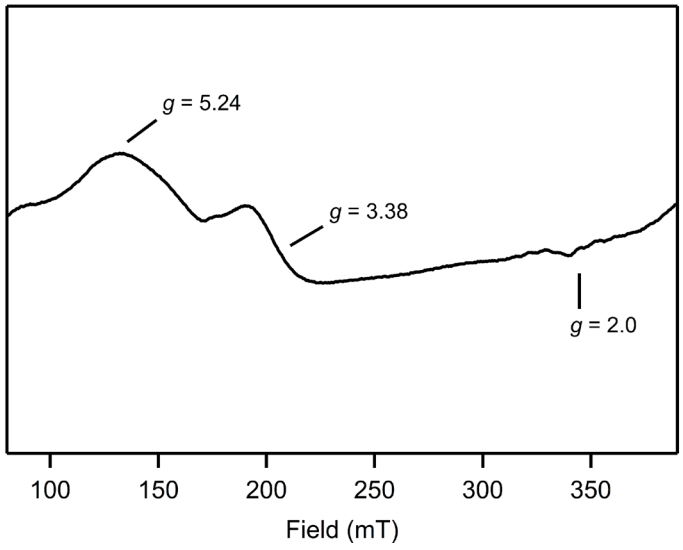

Figure 4.7. X-band EPR spectrum of $[Mn^{IV}(O)2pyN2I)]^{2+}$ generated from 3 mM solution of $[Mn^{II}(2pyN2I)(OTf)]^{+}$ and 10 equiv. PhIO in TFE. Experimental conditions: 9.64 GHz microwave frequency, 4 G modulation amplitude, 100 kHz modulation frequency, 14 dB power attenuation, 20 dB receiver gain, 40.96 ms time constant, and 10 K temperature.

4.3.3 C–H Bond Activation by Oxomanganese(IV) Species. The reactivity of $[Mn^{IV}(O)(N3pyQ)]^{2+}$ towards C–H bonds was investigated using a series of four organic substrates with BDE values from 78 to 94 kcal mol^{-1} (based on the reported calculated values).[23] This is a sufficient range of BDE values to study the linear free energy relationship in C–H bond activation, as it has been discussed that a small range of substrate BDE values could lead to erroneous interpretation of the linear free energy relationship between metal complex and the substrates.[23] Upon the addition of an excess amount of organic substrate to 1 mM solution of $[Mn^{IV}(O)(N3pyQ)]^{2+}$ in TFE at 25 °C, the electronic absorption band in the near-IR region decayed following pseudo-first-order kinetics (Figure 4.8). The time trace of this decay process at 1050 nm was fit to obtain the k_{obs} value for the reaction (Figure 4.8, inset) which is used to determine k_2 value (Figure 4.9). The k_2' values are given by dividing the k_2 values by the number of H atoms of

corresponding substrate that can be cleaved in the reaction. We started exploring the reactivity of $[Mn^{IV}(O)(N3pyQ)]^{2+}$ towards a weak C–H bond using 9,10-dihydroanthracene (DHA). When excess DHA (10 - 40 equiv.) was injected into a 1 mM $[Mn^{IV}(O)(N3pyQ)]^{2+}$ solution, a rapid decay of the near-IR absorption band occured, representing fast kinetics. The k_2' value of the reaction is 2.3(3) M^{-1} s^{-1}. The k_2' values for DHA oxidized by $[Mn^{IV}(O)(2pyN2Q)]^{2+}$ and $[Mn^{IV}(O)(N4py)]^{2+}$ were determined as 5.6(7) M^{-1} s^{-1} and 0.90(9) M^{-1} s^{-1}, respectively, although in the latter 1:1 TFE:CH_2Cl_2 solvent was used for the reactions.[22, 23] In a previous study, the solvent dependence on the k_2 was discussed comparing the k_2 values from the reaction of $[Mn^{IV}(O)(2pyN2B)]^{2+}$ and DHA in TFE and 1:1 TFE:CH_2Cl_2 as the solvent.[24] The k_2 value is enhanced by 1.7 times when TFE was used in the reaction, which is a marginal increase. Together, the k_2' values of the three oxomanganese(IV) complexes place the reactivity of $[Mn^{IV}(O)(N3pyQ)]^{2+}$ towards weak C–H bond activation as the second fastest among the complexes.

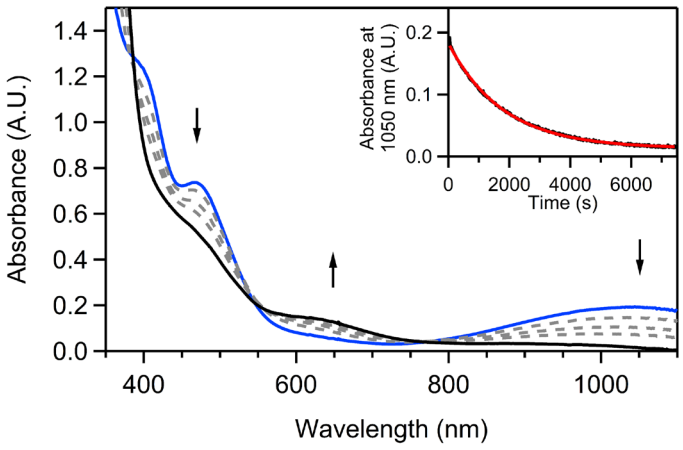

Figure 4.8. Electronic absorption spectra of 1 mM solution of $[Mn^{IV}(O)(N3pyQ)]^{2+}$ (blue) upon the addition of 100 equiv. ethylbenzene in TFE at 25 °C. Time trace at 1050 nm is shown in the inset (black) with fit to the first-order kinetic model (red).

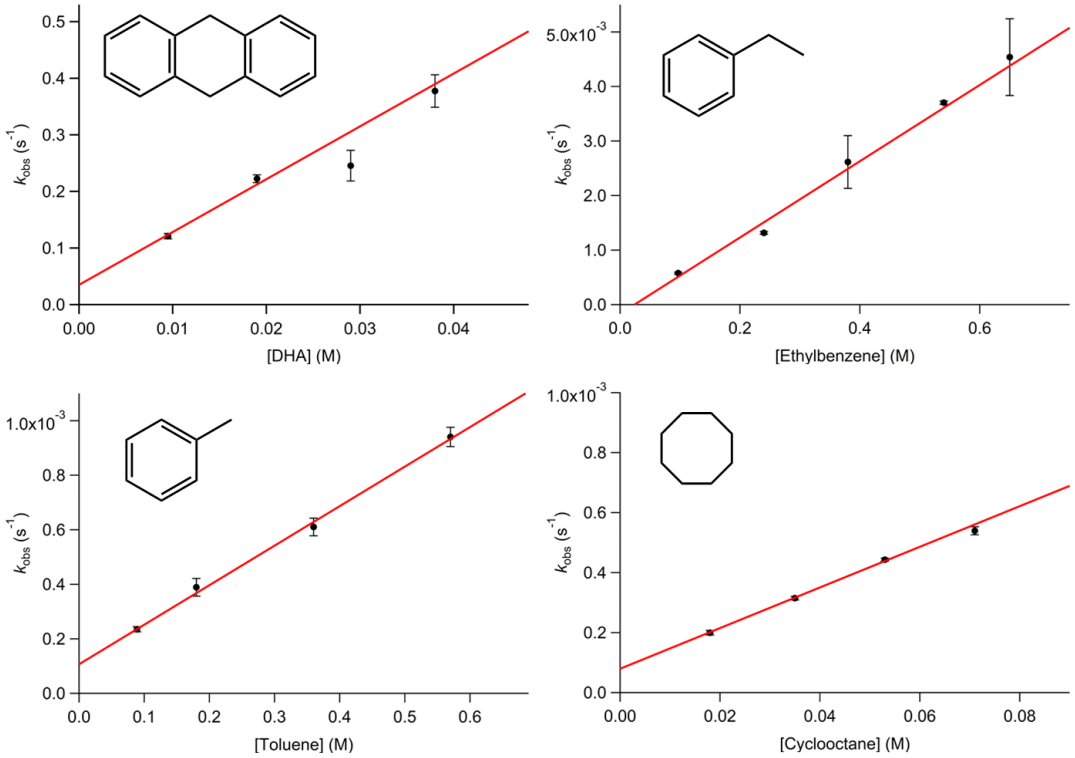

Figure 4.9. Plots of k_{obs} vs. substrate concentration for each C–H bond activation reaction. Substrate structures are shown in the corresponding plot.

The reactivity towards strong C–H bond activation was examined with ethylbenzene, toluene, and cyclooctane. Among these substrates, cyclooctane takes the highest calculated BDE value of 94 kcal mol^{-1}. Due to the high BDE value, only a few of the k_2' values have been reported for the reaction with cyclooctane by oxomanganese(IV) complexes.[22, 50] The k_2' values obtained with $[Mn^{IV}(O)(N3pyQ)]^{2+}$ are: 3.4(9) × 10^{-3} M^{-1} s^{-1} from the rection with ethylbenzene, 4.8(3) × 10^{-4} M^{-1} s^{-1} with toluene, and 4.2(3) × 10^{-4} M^{-1} s^{-1} with cyclooctane (Table 4.2). When comparisons of the k_2' values made with other oxomanganese(IV) complexes, the k_2' values of $[Mn^{IV}(O)(N3pyQ)]^{2+}$ are two to eight times slower than those of $[Mn^{IV}(O)(2pyN2Q)]^{2+}$ and two

or three times faster than those of $[Mn^{IV}(O)(N4py)]^{2+}$ (except the k_2' of $[Mn^{IV}(O)(N4py)]^{2+}$ with cyclooctane which was not determined previously). Therefore, the reactivity of $[Mn^{IV}(O)(N3pyQ)]^{2+}$ takes an intermediate position between $[Mn^{IV}(O)(2pyN2Q)]^{2+}$ and $[Mn^{IV}(O)(N4py)]^{2+}$ for C–H bond oxidation. A linear correlation is found from the plot of $\log(k_2')$ of $[Mn^{IV}(O)(N3pyQ)]^{2+}$ versus substrate BDE values (Figure 4.10). The $\log(k_2')$ values of $[Mn^{IV}(O)(N3pyQ)]^{2+}$ between those of $[Mn^{IV}(O)(2pyN2Q)]^{2+}$ and $[Mn^{IV}(O)(N4py)]^{2+}$ were expected, following a recent discussion about the multi-state reactivity model.[35] As the energy of the near-IR band represents a relative energy level of the excited state ^4E to the ground state $^4B_1$, it is postulated that the lower energies of the near-IR band, the faster C–H bond cleavage. The collected k_2, k_2', and calculated BDE values used in the reactivity studies of $[Mn^{IV}(O)(N3pyQ)]^{2+}$ are shown in Table 4.2. The reactivity trend is in agreement with the energy trend of the electronic absorption band at the near-IR region where the electronic absorption band of $[Mn^{IV}(O)(2pyN2Q)]^{2+}$ is shown at the lowest energy and that of $[Mn^{IV}(O)(^{DMM}N4py)]^{2+}$ is found at the highest energy among the three oxomanganese(IV) complexes considered here (Figure 4.11). The electronic absorption band at the near-IR region has been assigned as a ^4E excited state (d_{xz}, $d_{yz} \rightarrow d_{x2-y2}$) (*vide supra*). Since this ^4E excited state has been proposed to be the electronic state at the transition state of hydrogen atom transfer (HAT) reaction,[35, 57-59] the reactivity of the HAT reaction is expected to be faster as the energy of the ^4E transition is lowered. This correlation between the HAT reactivity and the energy of the ^4E excited state has been observed in previous studies and $[Mn^{IV}(O)(N3pyQ)]^{2+}$ follows this correlation as well.[22, 24]

Table 4.2. Second-order rate constants, corrected second-order rate constants, and calculated BDE values of substrates from the reaction of $[Mn^{IV}(O)(N3pyQ)]^{2+}$ and the corresponding substrate.

Substrate	k_2 (M^{-1} s^{-1})	k_2' (M^{-1} s^{-1})	Calculated BDE (kcal mol^{-1})
DHA	9.3(4)	2.3(3)	78
Ethylbenzene	$6.9(9) \times 10^{-3}$	$3.4(9) \times 10^{-3}$	86.4
Toluene	$1.4(4) \times 10^{-3}$	$4.8(3) \times 10^{-4}$	90.5
Cyclooctane	$6.7(7) \times 10^{-3}$	$4.2(3) \times 10^{-4}$	94

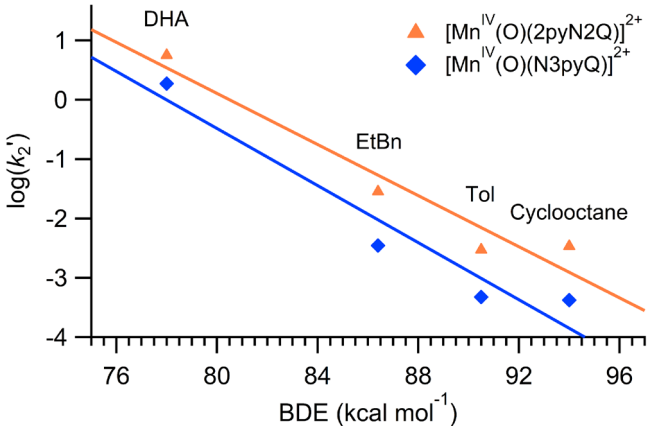

Figure 4.10. Plot of log k_2' as a function of substrate BDE values from each C–H bond activation reaction by $[Mn^{IV}(O)(N3pyQ)]^{2+}$ (blue) and $[Mn^{IV}(O)(2pyN2Q)]^{2+}$ (orange) with trend lines for each complex.

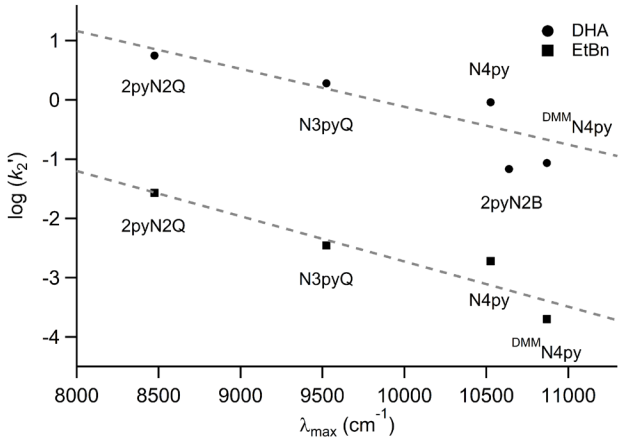

Figure 4.11. Plot of log k_2' against the electronic absorption band energy at the near-IR region for various oxomanganese(IV) complexes.

4.4 Conclusion

We prepared two novel manganese(II) complexes and their corresponding oxomanganese(IV) adducts to investigate the C–H bond oxidation reactivity of Mn^{IV}-oxo centers in different equatorial ligand field environments. The formation of oxomanganese(IV) complexes was confirmed by electronic absorption and EPR spectroscopies, which showed spectral signatures comparable to those of oxomanganese(IV) complexes with similar coordination spheres. We found that the log(k_2') values of $[Mn^{IV}(O)(N3pyQ)]^{2+}$ are following the reactivity trend shown by other oxomanganese(IV) complexes. Therefore, the reactivity of $[Mn^{IV}(O)(N3pyQ)]^{2+}$ signifies the correlation between reactivity and the energy of near-IR band of each oxomanganese(IV) complex, which represents the strength of equatorial ligand field. Nonetheless, possible contributions from other factors, e.g., reduction potential or pK_a of the Mn^{IV}-oxo complexes, are computationally and experimentally under investigation with a broader range of oxomanganese(IV) complexes.

4.5 Notes and References

1. Gandeepan, P.; Müller, T.; Zell, D.; Cera, G.; Warratz, S.; Ackermann, L., 3d Transition Metals for C–H Activation. *Chemical Reviews* **2019,** *119* (4), 2192-2452.

2. Arndtsen, B. A.; Bergman, R. G.; Mobley, T. A.; Peterson, T. H., Selective Intermolecular Carbon-Hydrogen Bond Activation by Synthetic Metal Complexes in Homogeneous Solution. *Accounts of Chemical Research* **1995,** *28* (3), 154-162.

3. Das, S., Molecular Recognition in the Selective Oxygenation of Saturated C-H Bonds by a Dimanganese Catalyst. *Science* **2006,** *312* (5782), 1941-1943.

4. Mandelli, D.; Kirillov, A. M., Preface to Special Issue: C–H functionalization in modern molecular catalysis. *Journal of Molecular Catalysis A: Chemical* **2017,** *426*, 271-272.

5. Denisov, I. G.; Makris, T. M.; Sligar, S. G.; Schlichting, I., Structure and Chemistry of Cytochrome P450. *Chemical Reviews* **2005,** *105* (6), 2253-2278.

6. Neu, H. M.; Yang, T.; Baglia, R. A.; Yosca, T. H.; Green, M. T.; Quesne, M. G.; de Visser, S. P.; Goldberg, D. P., Oxygen-Atom Transfer Reactivity of Axially Ligated Mn(V)–Oxo Complexes: Evidence for Enhanced Electrophilic and Nucleophilic Pathways. *Journal of the American Chemical Society* **2014,** *136* (39), 13845-13852.

7. Sahu, S.; Goldberg, D. P., Activation of Dioxygen by Iron and Manganese Complexes: A Heme and Nonheme Perspective. *Journal of the American Chemical Society* **2016,** *138* (36), 11410-11428.

8. Gray, H. B.; Winkler, J. R., Living with Oxygen. *Accounts of Chemical Research* **2018,** *51* (8), 1850-1857.

9. Zaragoza, J. P. T.; Siegler, M. A.; Goldberg, D. P., A Reactive Manganese(IV)–Hydroxide Complex: A Missing Intermediate in Hydrogen Atom Transfer by High-Valent Metal-Oxo Porphyrinoid Compounds. *Journal of the American Chemical Society* **2018,** *140* (12), 4380-4390.

10. Mandal, D.; Mallick, D.; Shaik, S., Kinetic Isotope Effect Determination Probes the Spin of the Transition State, Its Stereochemistry, and Its Ligand Sphere in Hydrogen Abstraction Reactions of Oxoiron(IV) Complexes. *Accounts of Chemical Research* **2018,** *51* (1), 107-117.

11. Milan, M.; Salamone, M.; Costas, M.; Bietti, M., The Quest for Selectivity in Hydrogen Atom Transfer Based Aliphatic C–H Bond Oxygenation. *Accounts of Chemical Research* **2018,** *51* (9), 1984-1995.

12. Collins, T. J.; Ryabov, A. D., Targeting of High-Valent Iron-TAML Activators at Hydrocarbons and Beyond. *Chemical Reviews* **2017,** *117* (13), 9140-9162.

13. Rice, D. B.; Massie, A. A.; Jackson, T. A., Manganese–Oxygen Intermediates in O–O Bond Activation and Hydrogen-Atom Transfer Reactions. *Accounts of Chemical Research* **2017,** *50* (11), 2706-2717.

14. Borovik, A. S., Role of metal–oxo complexes in the cleavage of C–H bonds. *Chemical Society Reviews* **2011,** *40* (4), 1870-1874.

15. Gunay, A.; Theopold, K. H., C-H Bond Activations by Metal Oxo Compounds. *Chem. Rev. (Washington, DC, U. S.)* **2010,** *110* (2), 1060-1081.

16. Fukuzumi, S.; Cho, K.-B.; Lee, Y.-M.; Hong, S.; Nam, W., Mechanistic dichotomies in redox reactions of mononuclear metal–oxygen intermediates. *Chemical Society Reviews* **2020,** *49* (24), 8988-9027.

17. Guo, M.; Lee, Y.-M.; Fukuzumi, S.; Nam, W., Biomimetic metal-oxidant adducts as active oxidants in oxidation reactions. *Coordination Chemistry Reviews* **2021,** *435*, 213807.

18. Chen, J.; Jiang, Z.; Fukuzumi, S.; Nam, W.; Wang, B., Artificial nonheme iron and manganese oxygenases for enantioselective olefin epoxidation and alkane hydroxylation reactions. *Coordination Chemistry Reviews* **2020,** *421*, 213443.

19. Mayfield, J. R.; Grotemeyer, E. N.; Jackson, T. A., Concerted proton–electron transfer reactions of manganese–hydroxo and manganese–oxo complexes. *Chemical Communications* **2020,** *56* (65), 9238-9255.

20. Bryliakov, K. P.; Talsi, E. P., Active sites and mechanisms of bioinspired oxidation with H2O2, catalyzed by non-heme Fe and related Mn complexes. *Coordination Chemistry Reviews* **2014,** *276*, 73-96.

21. Shul'pin, G. B., Metal-catalyzed hydrocarbon oxygenations in solutions: the dramatic role of additives: a review. *J. Mol. Catal. A: Chem.* **2002,** *189* (1), 39-66.

22. Massie, A. A.; Denler, M. C.; Cardoso, L. T.; Walker, A. N.; Hossain, M. K.; Day, V. W.; Nordlander, E.; Jackson, T. A., Equatorial Ligand Perturbations Influence the Reactivity of Manganese(IV)-Oxo Complexes. *Angewandte Chemie International Edition* **2017,** *56* (15), 4178-4182.

23. Massie, A. A.; Sinha, A.; Parham, J. D.; Nordlander, E.; Jackson, T. A., Relationship between Hydrogen-Atom Transfer Driving Force and Reaction Rates for an Oxomanganese(IV) Adduct. *Inorganic Chemistry* **2018,** *57* (14), 8253-8263.

24. Denler, M. C.; Massie, A. A.; Singh, R.; Stewart-Jones, E.; Sinha, A.; Day, V. W.; Nordlander, E.; Jackson, T. A., Mn^{IV}-Oxo complex of a bis(benzimidazolyl)-containing N5 ligand reveals different reactivity trends for Mn^{IV}-oxo than Fe^{IV}-oxo species. *Dalton Transactions* **2019,** *48* (15), 5007-5021.

25. Barman, P.; Vardhaman, A. K.; Martin, B.; Wörner, S. J.; Sastri, C. V.; Comba, P., Influence of Ligand Architecture on Oxidation Reactions by High-Valent Nonheme Manganese Oxo Complexes Using Water as a Source of Oxygen. *Angewandte Chemie* **2015,** *127* (7), 2123-2127.

26. Mayer, J. M., Hydrogen Atom Abstraction by Metal−Oxo Complexes: Understanding the Analogy with Organic Radical Reactions. *Accounts of Chemical Research* **1998,** *31* (8), 441-450.

27. Warren, J. J.; Tronic, T. A.; Mayer, J. M., Thermochemistry of Proton-Coupled Electron Transfer Reagents and its Implications. *Chemical Reviews* **2010,** *110* (12), 6961-7001.

28. Bell, R. P., The theory of reactions involving proton transfers. *Proceedings of the Royal Society of London. Series A - Mathematical and Physical Sciences* **1936,** *154* (882), 414-429.

29. Evans, M. G.; Polanyi, M., Inertia and driving force of chemical reactions. *Transactions of the Faraday Society* **1938,** *34* (0), 11-24.

30. Rasheed, W.; Draksharapu, A.; Banerjee, S.; Young Jr, V. G.; Fan, R.; Guo, Y.; Ozerov, M.; Nehrkorn, J.; Krzystek, J.; Telser, J.; Que Jr, L., Crystallographic Evidence for a Sterically Induced Ferryl Tilt in a Non-Heme Oxoiron(IV) Complex that Makes it a Better Oxidant. *Angewandte Chemie International Edition* **2018,** *57* (30), 9387-9391.

31. Xue, S.-S.; Li, X.-X.; Lee, Y.-M.; Seo, M. S.; Kim, Y.; Yanagisawa, S.; Kubo, M.; Jeon, Y.-K.; Kim, W.-S.; Sarangi, R.; Kim, S. H.; Fukuzumi, S.; Nam, W., Enhanced Redox Reactivity of a Nonheme Iron(V)–Oxo Complex Binding Proton. *Journal of the American Chemical Society* **2020,** *142* (36), 15305-15319.

32. Sankaralingam, M.; Lee, Y.-M.; Pineda-Galvan, Y.; Karmalkar, D. G.; Seo, M. S.; Jeon, S. H.; Pushkar, Y.; Fukuzumi, S.; Nam, W., Redox Reactivity of a Mononuclear Manganese-Oxo Complex Binding Calcium Ion and Other Redox-Inactive Metal Ions. *Journal of the American Chemical Society* **2019,** *141* (3), 1324-1336.

33. Parsell, T. H.; Yang, M.-Y.; Borovik, A. S., C−H Bond Cleavage with Reductants: Re-Investigating the Reactivity of Monomeric $Mn^{III/IV}$−Oxo Complexes and the Role of Oxo Ligand Basicity. *Journal of the American Chemical Society* **2009,** *131* (8), 2762-2763.

34. Jaccob, M.; Ansari, A.; Pandey, B.; Rajaraman, G., Theoretical studies on concerted versus two steps hydrogen atom transfer reaction by non-heme $Mn^{IV/III}$=O complexes: how important is the oxo ligand basicity in the C–H activation step? *Dalton Transactions* **2013,** *42* (47), 16518-16526.

35. Rice, D. B.; Massie, A. A.; Jackson, T. A., Experimental and Multireference ab Initio Investigations of Hydrogen-Atom-Transfer Reactivity of a Mononuclear Mn^{IV}-oxo Complex. *Inorganic Chemistry* **2019,** *58* (20), 13902-13916.

36. Dhar, D.; Yee, G. M.; Spaeth, A. D.; Boyce, D. W.; Zhang, H.; Dereli, B.; Cramer, C. J.; Tolman, W. B., Perturbing the Copper(III)–Hydroxide Unit through Ligand Structural Variation. *Journal of the American Chemical Society* **2016,** *138* (1), 356-368.

37. Mandal, D.; Ramanan, R.; Usharani, D.; Janardanan, D.; Wang, B.; Shaik, S., How Does Tunneling Contribute to Counterintuitive H-Abstraction Reactivity of Nonheme Fe(IV)O Oxidants with Alkanes? *Journal of the American Chemical Society* **2015,** *137* (2), 722-733.

38. Bím, D.; Maldonado-Domínguez, M.; Rulíšek, L.; Srnec, M., Beyond the classical thermodynamic contributions to hydrogen atom abstraction reactivity. *Proceedings of the National Academy of Sciences* **2018,** *115* (44), E10287.

39. Goetz, M. K.; Anderson, J. S., Experimental Evidence for pKa-Driven Asynchronicity in C–H Activation by a Terminal Co(III)–Oxo Complex. *Journal of the American Chemical Society* **2019,** *141* (9), 4051-4062.

40. Manuscript in preparation

41. From an unpublished work by Mayfield, J. R. and Jackson, T. A.

42. Armarego, W. L. F.; Chai, C. L. L., *Purification of laboratory chemicals, fifth edition*. 5th ed. ed.; Burlington, Mass.?: Butterworth-Heinemann: Burlington, Mass.?, 2003.

43. Saltzman, H.; Sharefkin, J. G., Iodosobenzene. *Organic Syntheses* **1963,** *43*, 60.

44. Chang, J.; Plummer, S.; Berman, E. S. F.; Striplin, D.; Blauch, D., Synthesis and Characterization of Bis(di-2-pyridylmethanamine)ruthenium(II). *Inorganic Chemistry* **2004,** *43* (5), 1735-1742.

45. Singh, R.; Ganguly, G.; Malinkin, S. O.; Demeshko, S.; Meyer, F.; Nordlander, E.; Paine, T. K., A Mononuclear Nonheme Iron(IV)-Oxo Complex of a Substituted N4Py Ligand: Effect of Ligand Field on Oxygen Atom Transfer and C–H Bond Cleavage Reactivity. *Inorganic Chemistry* **2019,** *58* (3), 1862-1876.

46. Dixon, N. E.; Lawrance, G. A.; Lay, P. A.; Sargeson, A. M.; Taube, H., Trifluoromethanesulfonates and Trifluoromethanesulfonato-O Complexes. *Inorganic Syntheses* **1990**, 70-76.

47. The XRD structure of [Mn^{II}(N3pyQ)(OH2)](ClO4)2 was prepared and submitted by Shannon D. Jones.

48. Leto, D. F.; Ingram, R.; Day, V. W.; Jackson, T. A., Spectroscopic properties and reactivity of a mononuclear oxomanganese(iv) complex. *Chemical Communications* **2013,** *49* (47), 5378-5380.

49. Chen, L. Z.; Flammang, R.; Maquestiau, A.; Taft, R. W.; Catalan, J.; Cabildo, P.; Claramunt, R. M.; Elguero, J., Thermodynamic basicity vs. kinetic basicity of diazoles (imidazoles and pyrazoles). *The Journal of Organic Chemistry* **1991,** *56* (1), 179-183.

50. Wu, X.; Seo, M. S.; Davis, K. M.; Lee, Y.-M.; Chen, J.; Cho, K.-B.; Pushkar, Y. N.; Nam, W., A Highly Reactive Mononuclear Non-Heme Manganese(IV)–Oxo Complex That Can Activate the Strong C–H Bonds of Alkanes. *Journal of the American Chemical Society* **2011,** *133* (50), 20088-20091.

51. Parsell, T. H.; Behan, R. K.; Green, M. T.; Hendrich, M. P.; Borovik, A. S., Preparation and Properties of a Monomeric Mn^{IV}−Oxo Complex. *Journal of the American Chemical Society* **2006,** *128* (27), 8728-8729.

52. Leto, D. F.; Massie, A. A.; Colmer, H. E.; Jackson, T. A., X-Band Electron Paramagnetic Resonance Comparison of Mononuclear Mn^{IV}-oxo and Mn^{IV}-hydroxo Complexes and Quantum Chemical Investigation of Mn^{IV} Zero-Field Splitting. *Inorganic Chemistry* **2016,** *55* (7), 3272-3282.

53. Kessissoglou, D. P.; Li, X.; Butler, W. M.; Pecoraro, V. L., Mononuclear manganese(IV) complexes of hydroxyl-rich Schiff base ligands. *Inorganic Chemistry* **1987,** *26* (15), 2487-2492.

54. Gupta, R.; Taguchi, T.; Borovik, A. S.; Hendrich, M. P., Characterization of Monomeric $Mn^{II/III/IV}$–Hydroxo Complexes from X- and Q-Band Dual Mode Electron Paramagnetic Resonance (EPR) Spectroscopy. *Inorganic Chemistry* **2013,** *52* (21), 12568-12575.

55. Lee, Y.; Jackson, T. A., Ligand Influence on Structural Properties and Reactivity of Bis(μ-oxo)dimanganese(III,IV) Species and Comparison of Reactivity with Terminal Mn^{IV}-oxo Complexes. *ChemistrySelect* **2018,** *3* (47), 13507-13516.

56. Richens, D. T.; Sawyer, D. T., Bis(tetramethylammonium) tris(sorbitolato)manganate(IV), an EPR-active monomeric complex of manganese(IV). *Journal of the American Chemical Society* **1979,** *101* (13), 3681-3683.

57. Cho, K.-B.; Shaik, S.; Nam, W., Theoretical Investigations into C–H Bond Activation Reaction by Nonheme MnIVO Complexes: Multistate Reactivity with No Oxygen Rebound. *The Journal of Physical Chemistry Letters* **2012,** *3* (19), 2851-2856.

58. Chen, J.; Cho, K.-B.; Lee, Y.-M.; Kwon, Y. H.; Nam, W., Mononuclear nonheme iron(iv)–oxo and manganese(iv)–oxo complexes in oxidation reactions: experimental results prove theoretical prediction. *Chemical Communications* **2015,** *51* (66), 13094-13097.

59. Kim, S.; Cho, K.-B.; Lee, Y.-M.; Chen, J.; Fukuzumi, S.; Nam, W., Factors Controlling the Chemoselectivity in the Oxidation of Olefins by Nonheme Manganese(IV)-Oxo Complexes. *Journal of the American Chemical Society* **2016,** *138* (33), 10654-10663.

Chapter 5

Influences of Geometric and Electronic Structure on Concerted Proton-Electron Transfer by a Mononuclear Co(IV) Complex

Portions of this chapter have been reproduced with permission from Kwon, Y., Lee, Y., Evenson, G. E., Jackson, T. A., Wang, D. *J. Am. Chem. Soc*. **2020**, *142*, 13435–13441. Copyright 2020 American Chemical Society.

Experimental activation parameters were collected by Kwon, Y. at University of Montana.

5.1 Introduction

Structure-reactivity relationships for metal complexes bearing one or more late transition metals has been of great interest due to their high reactivity in a number of organic transformations and functionalizations.[1-5] Specifically, terminal oxo complexes comprising such late transition metals have been proposed as a highly reactive intermediate in those reactions, although there are restrictions for geometries that these intermediates could possess based on the molecular orbital (MO) theory. Developed by Ballhausen and Gray for tetragonal oxycations in 1962, this general MO theory predicts that as the number of d electrons exceeds four, the metal-oxo complex in tetragonal geometry becomes very unstable due to the half π–bond order (so-called "the oxo wall").[6, 7] Late transition metals, for example, Co and Ni, are often found with more than four d electrons, and due to this reason late transition metal-oxo species are scarce and must adopt geometries other than a tetragonal structure. Accordingly, an increasing amount of efforts has been made to prepare terminal oxo complexes by adapting various geometries and electronic structures except tetragonal systems.[8]

In a recent study Srnec, Costas, Roithova, and co-workers prepared a formally Co(IV)-oxo complex, $[Co^{IV}(O)(N4py)]^{2+}$, in gas phase and investigated its reactivity towards C–H bond activation.[9] This complex was characterized by infrared and visible photodissociation spectroscopies with an ^{18}O labeled complex, which revealed a significantly weak Co–O bond based on the shifted vibrational frequencies (< 660 cm^{-1}). The authors compared the vibration modes of this formally Co^{IV}-oxo species to those of $Fe^{III/IV}$- and Co^{III}-oxo systems of different spin states. The electronic structure of formally Co^{IV}-oxo species is proposed to be that of a Co^{III}-oxyl complex, in which an unpaired electron resides in a pπ* orbital of the oxyl ligand (Figure 5.1). Reactivity studies of this Co^{III}-oxyl species show a remarkable oxidizing power of this complex,

which activates a relatively strong C–H bond (99 kcal mol^{-1})[10] of cyclohexane even in gas phase. This study effectually represents high reactivity of a terminal oxyl complex bearing a late transition metal, which corroborates the predicted reactivity of this type of late transition metal species.

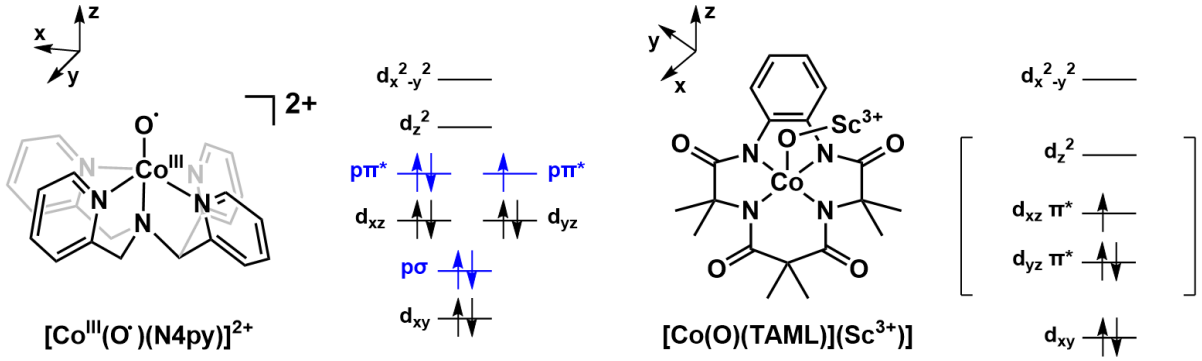

Figure 5.1. Structures and MO diagrams of previously reported high-valent Co complexes with a terminal oxo/oxyl ligand. Orbitals in blue show oxyl ligand based p orbitals. Brackets indicate a conjectural assignment of MO energy levels.[11]

Another approach used to study late transition metal species with an oxo/oxyl ligand is to add Lewis acidic metal ions to stabilize the ligand. Ray, Nam, and co-workers reported a high-valent Co adduct, $[Co(O)(TAML)]M^{n+}$ (M^{n+} = Sc^{3+}, Ce^{3+}, Y^{3+}, and Zn^{2+}; TAML = tetraamidomacrocyclic ligand), which they characterized by applying several spectroscopic methods.[12] This high-valent Co complex was prepared by addition of 3 equiv. PhIO to $Li(OH_2)_3[Co^{III}(TAML)]$ in acetone with 20 equiv. $Sc(CF_3SO_3)_3$ (or other Lewis acidic metal ions) at 5 °C. The authors proposed that the increased electrophilicity of the oxygen atom due to the binding of Sc^{3+} results in the bridging oxo ligand that is more stable than Co–O˙ core. They observed a rhombic signal in the EPR spectrum (g_x = 2.57, g_y = 2.16, and g_z = 2.03) at 5 K, which is often reported for square-pyramidal and -planar macrocyclic Co species.[13-15] Further, a higher

edge energy than that of $Li(OH_2)_3[Co^{III}(TAML)]$ in a Co K-edge X-ray absorption near-edge spectrum (XANES) indicates a higher oxidation state for the Co center in $[Co(O)(TAML)]Sc^{3+}$. The authors suggest the association of Sc^{3+} to the Co–O center from the best fit of the extended X-ray absorption fine structure (EXAFS) data (Sc^{3+} located at 3.38 Å away) along with an O scatterer (at 1.67 Å). Oxidizing ability of $[Co(O)(TAML)]Sc^{3+}$ was explored with respect to hydrogen and oxygen atom transfer reactions, albeit it shows a modest reactivity for these reactions ($k_2' = 0.053$ $M^{-1}s^{-1}$ for DHA oxidation and $k_2 = 1.5$ $M^{-1}s^{-1}$ for thioanisole oxidation; both reactions performed at 5 °C). Nevertheless, this study explored a possible strategy to prepare late transition metal-oxo/oxyl species and characterized geometry and reactivity of Lewis acid bound late transition metal-oxo complexes.

Likewise, other strategies that researchers devised have shown possibilities in adapting late transition metals to diverse geometric and electronic structures, aimed at developing highly reactive oxidation catalysts.[16-19] Although there is increasing interest in this area, only a handful of studies have elucidated the reactivity of late transition metal species in relation to their electronic structures. In this context, we investigated the influences of geometric and electronic structure towards C–H bond oxidation reactivity of mononuclear Co(IV) and Ni(IV) complexes. These two high-valent metal species are prepared with the same dianionic NNN pincer ligand which provides a rigid and effective platform for redox reactions occurring at a central atom (Figure 5.2). A strong sacrificial oxidant, ceric(IV) ammonium nitrate (CAN), is used to achieve the high oxidation state for both metal species. Spectroscopic studies using electron paramagnetic resonance spectroscopy (EPR), and Co K-edge X-ray absorption spectroscopy (XAS) were carried out to reveal geometric and electronic features of these high-valent Co species. These structural parameters collected are used to shed light on structure and reactivity relationship of these late transition metal species.

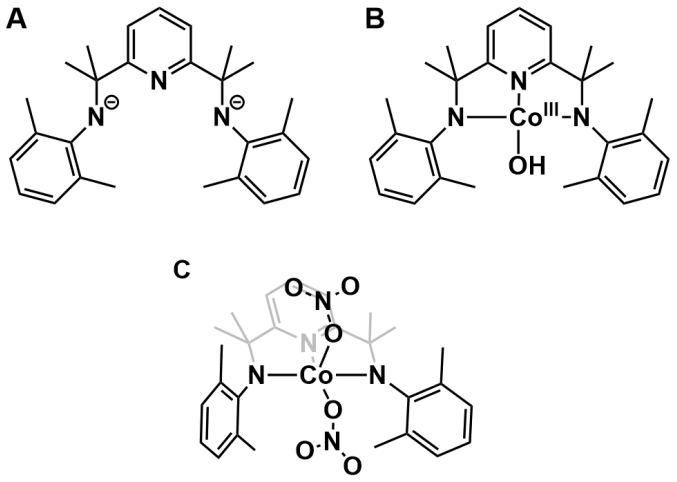

Figure 5.2. Structures of (A) dianionic pincer ligand, (B) [Co^{III}(OH)(NNN)], and (C) [$Co^{IV}(ONO_2)_2$(NNN)] used in this study.

5.2 Experimental and Computational Methods

5.2.1 Instrumentation. EPR spectra were collected using an X-band Bruker EMXPlus spectrometer with a Bruker ER4116DM dual-mode cavity. An Oxford ESR900 continuous-flow liquid helium cryostat was used to monitor applied temperature. Experimental temperatures were controlled with an Oxford ITC503 cryostat controller. Parameters used in collecting spectra are provided in the caption of Figure 5.3.

5.2.2 Electron Paramagnetic Resonance Experiments. EPR samples with 5 mM frozen solution of [$Co^{IV}(ONO_2)_2$(NNN)] was prepared and sent by the Wang group at University of Montana. EPR spectra for [$Co^{IV}(ONO_2)_2$(NNN)] were collected under non-saturating conditions at 9.640 GHz microwave frequency, 0.4 mT modulation amplitude, 100.00 kHz modulation frequency, 14.0 dB power attenuation, 20 dB receiver gain, and 163.84 ms time constant. Spectra were collected from 7.5 – 50 K. Spectra collected at different temperatures are very similar, but the hyperfine features are best observed in the 30 K spectrum (Appendix A5, Figure A5.1). EPR

spectral simulations were carried out using the EasySpin software developed by Stoll.[20] Simulations for EPR spectra of $[Co^{IV}(ONO_2)_2(NNN)]$ began with $g = 2.2$ and $A = 365$ MHz, which are the values obtained from spectral analysis, then these values were varied to find a better fit using the "pepper" function. The EPR spectrum of $[Co^{IV}(ONO_2)_2(NNN)]$ was simulated with the following parameters: g = [2.23, 2.08, 2.00]; S = 0.5; Nucs = '^{59}Co'; A (MHz) = [135, 165, 320]; lw = [8]; gStrain = [0.0011, 0.002, 0.002]; AStrain (MHz) = [125, 154, 75]; HStrain (MHz) = [450, 453, 180]. As noted in the text, the A = 135 and 165 MHz values are not as well defined as A = 320 MHz, the latter of which is required to fit the observed hyperfine splittings from ca. 320 – 400 mT. However, we are unable to properly fit the breadth of the experimental spectrum if A_1 and A_2 are set to zero. We can best accommodate the breadth of the EPR signal when A_1 and A_2 fall between 100 and 200 MHz (see Appendix A5, Figure A5.2). In addition, large Astrain and Hstrain components are required to fit the breadth of the EPR signal. The HStrain parameters correspond to unresolved hyperfine couplings, used to simulate line broadenings. Large HStrain parameter values have been used to simulate the broad EPR spectrum of a cuboidal Co complex containing Co(III) and Co(IV) centers, e.g. [682, 638, 435 MHz] and [645, 615, 408 MHz].[21, 22]

5.2.3 Co/Ni K-edge X-ray Absorption Spectroscopy. XAS samples in 4 – 5.8 mM frozen solutions were prepared by the Wang group at University of Montana. The Ni K-edge XANES spectra were collected on beam line 7-3 at the Stanford Synchrotron Radiation Lightsource (SSRL) in SLAC National Accelerator Laboratory. A range of 8050 eV to 8936 eV was used for data acquisition with fluorescence excitation, which was detected with a Lytle detector and a Si(220) double-crystal monochromator ($\varphi = 90°$). A nickel foil was taken in each experiment for internal calibration of edge energy, of which the first inflection point was set to 8333.0 eV. All XAS data were recorded at ca. 13 K, controlled by an Oxford Helium cryostat. Each sample was monitored

for evidence of photoreduction, and we did not observe a red-shift in edge energy of any samples. The rising edge energy is determined by the half-height with respect to the white-line intensity of each sample. The obtained XANES data were processed using the *DEMETER* software package.[23] All data were merged at the end of processing, and the intensity of white-line for each spectrum was used for normalization.

5.2.4 DFT calculations. All computational results were obtained from ORCA 4.1.2 and 4.2.1.[24] The crystal structure of $[Co^{IV}(ONO_2)_2(NNN)]$ was used to provide initial coordinates for DFT geometry optimization. The TPSS-D3 functional was employed with def2-TZVP basis sets on Co, O, and N, and def2-SVP on the rest of atoms.[25-30] The def2/J auxiliary basis sets were used for both basis sets.[31] The RI approximation and the conductor-like polarizable continuum model (CPCM) for solvation in acetonitrile were included. All DFT calculations were tightly converged to the $S = 1/2$ state. The DFT-optimized structure showed no imaginary frequencies in a numerical frequency calculation, which provides evidence that this structure represents a true minimum on the potential energy surface. Investigation of the electronic structure of $[Co^{IV}(ONO_2)_2(NNN)]$ was performed by analyzing the energies and compositions of the spin-up (α) and spin-down (β) Kohn-Sham (KS) orbitals. The frontier KS orbitals are described in Table A5.1 in Appendix A5. The analysis reveals that the singly occupied molecular orbital (SOMO) is of Co^{IV} $3d_z^2$ character, with admixtures of amido ligand character. The π-bonding molecular orbitals of the Co^{IV} $3d_{xz}$ orbital and the amido ligands and/or the axial ligand are found at lower energy than the SOMO. The Co^{IV}-based $3d_{xy}$ molecular orbital is essentially non-bonding (Appendix A5, Figure A5.3). The β-spin KS orbitals follow a similar splitting pattern as the α-spin KS orbitals, except that the Co^{IV} $3d_z^2$ orbital has a higher energy than the Co^{IV} d_{yz} orbital.

5.2.5 CASSCF Calculations. Complete-active space self-consistent field (CASSCF) calculations, with n-electron valence perturbation theory (NEVPT2) corrections, were performed to further evaluate the electronic structure of [$Co^{IV}(ONO_2)_2(NNN)$] and to calculate *g* values.[32] In this case, we considered a model using the X-ray structure coordinates where only the hydrogen atoms were subjected to energy-minimization by DFT methods (using the same DFT level of theory as described above).[25, 29, 30] This previously-employed approach is motivated by the strong sensitivity of ground-state spin Hamiltonian parameters to minor structural perturbations.[33, 34] It is also assumed that the positions of the hydrogen atoms are not as well defined from the X-ray crystal structure as the heavy-atom positions, necessitating the optimization of the hydrogen positions by DFT methods. We initially performed state-averaged CASSCF calculations, and then used the orbitals from the state-averaged solution as input for a state-specific CASSCF calculation. In the state-specific calculation, the weight of the ground state was set to unity while the weights of all other states were set to zero. All the CASSCF results reported in this work are for the state-specific solution. The active space for the CASSCF calculations consisted of 13 electrons in 9 orbitals, noted as CAS(13,9). The active space included the five CoIV-based 3d orbitals and their five electrons, the bonding counterpart to the Co^{IV}-based $d_{x^2-y^2}$ orbital (σ-bonding with respect to the equatorial ligands), the bonding counterpart to the Co^{IV}-based d_{yz} orbital (π-bonding with respect to the amido ligands), the bonding counterpart to the Co^{IV}-based d_{z^2} orbital (σ-bonding with the axial ligands), and a Co^{IV} π orbital with σ-interactions with the amido ligands. Surface contour plots of the active-space orbitals for the state-specific wavefunction are shown in Appendix A5, Figure 5.4. Calculations with larger active spaces were plagued by convergence issues, even with aggressive level shifting. The calculations considered twenty-five doublet states, twenty-four quartet states, and one sextet state. The CASSCF calculation converged to a doublet

ground state, consistent with the spin state observed for [$Co^{IV}(ONO_2)_2$(NNN)] from EPR spectroscopy. The calculated *g* and *A* values reported in the paper are for the state-specific CAS(13,9) calculation after NEVPT2 correction. The use of the core properties CP(PPP) basis set[35] for Co had little effect on the calculated *A* values when compared to a calculation using the def2-TZVP basis set for Co ($A_{CP(PPP)}$ = -66, -316, -441 MHz; $A_{def2\text{-}TZVP}$ = -61 -326, -451 MHz). Hyperfine values were also calculated using DFT computations. These calculations employed the core properties CP(PPP) basis set[35] for Co and def2-TZVP (O and N) and def2-SVP (C and H) basis sets for other atoms. Separate DFT calculations were performed that utilized the B3LYP and TPSSh functionals, and only modest (ca. 25%) differences in the A values were noted. In particular, the B3LYP calculations give *A* = -137, 125, and 451 MHz and the TPSSh calculations give *A* = -113, 88, and 414 MHz. The use of the DFT-optimized model for [$Co^{IV}(ONO_2)_2$(NNN)] also led to modest changes in the *A* values (-160, 108, and 417 MHz). In all cases, the DFT-computed *A* values give one value significantly larger in magnitude than the other two, which is in good agreement with experiment (|*A*| = 135, 165, and 320 MHz), although the magnitudes of the calculated A values deviate somewhat from their experimental counterparts. To assess the sensitivity of the CASSCF calculations to the model of [$Co^{IV}(ONO_2)_2$(NNN)] employed, we performed the same calculations for the DFT-optimized model of [$Co^{IV}(ONO_2)_2$(NNN)]. The results are essentially identical to those found when using the X-ray structure coordinates. For example, in both cases the ground state configuration from the state-specific calculations is of 61% from the $(d_{xy})^2(d_{xz})^2(d_{z^2})^1(d_{yz})^0(d_{x^2-y^2})^0$ configuration and 12% from the $(d_{xy})^2(d_{xz})^0(d_{z^2})^1(d_{yz})^2(d_{x^2-y^2})^0$ configuration. The calculated *g* values are also very similar: *g* = 2.01, 2.07, and 2.39 when using the X-ray structure coordinates and *g* = 2.01, 2.05, and 2.37 when using the DFT-optimized coordinates.

5.3 Results and Discussion

5.3.1 Characterization of [$Co^{IV}(ONO_2)_2$(NNN)] by Electron Paramagnetic Resonance Spectroscopy.

The perpendicular-mode, X-band EPR spectrum of [$Co^{IV}(ONO_2)_2$(NNN)] shows one broad resonance at $g \approx 2.2$ (320 mT) at 30 K (Figure 5.3). The negatively signed component of this signal shows seven resolved hyperfine lines attributed to the ^{59}Co ($I = 7/2$) nucleus (Figure 5.3). The EPR signal is unusually broad, spanning ca. 270 – 400 mT. The breadth of this signal as well as the observation of ^{59}Co hyperfine coupling are consistent with predominant localization of the unpaired spin on the Co center, as expected for Co(IV). While the EPR signal of [$Co^{IV}(ONO_2)_2$(NNN)] does not closely resemble any EPR signal previously reported for a Co(IV) complex, there are a limited number of examples of Co(IV) centers in square pyramidal environments for comparison (see Appendix A5, Table A5.2).[12, 14, 15, 36, 37] Two Co(IV)–corrole complexes with an axial PPh_3 or C_6H_5 ligand displayed rhombic signals,[14, 15] the latter was described as having a delocalized valence with the unpaired electron distributed between both the cobalt and the corrole macrocycle.[37] In another case, a Co(IV) bis(dithiolene) complex with an axial PPh_3 ligand showed a nearly axial EPR signal with resolved hyperfine splitting on both $g_\perp$ and $g_\parallel$.[36] Finally, a Co(IV)–oxo–Lewis acid complex with a tetraamido macrocyclic ligand showed a rhombic EPR signal with g values from 2.57 to 2.03.[12]

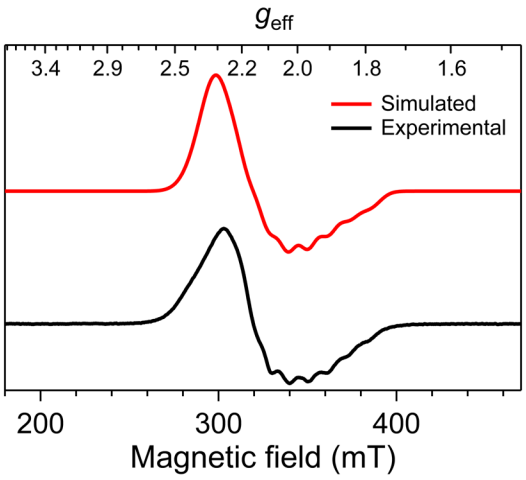

Figure 5.3. Perpendicular-mode X-band EPR spectrum of a 5 mM frozen solution of $[Co^{IV}(ONO_2)_2(NNN)]$ in acetonitrile at 30 K (black) and simulation (red). Experimental conditions: microwave frequency 9.6403 GHz, microwave power 7.962 mW, modulation amplitude 0.4 mT, modulation frequency 100 kHz, and time constant 163.84 ms.

The EPR spectrum of $[Co^{IV}(ONO_2)_2(NNN)]$ can be well simulated using $g_1 = 2.23$, $g_2 = 2.08$, and $g_3 = 2.00$ (Figures 5.3 and A5.6 in Appendix A5), which fall within the range of g values reported for square pyramidal, low-spin d^5 Co(IV) systems (Appendix A5, Table A5.2). The hyperfine coupling constant $A(^{59}Co)$ is simulated with $A_1 = 135$ MHz, $A_2 = 165$ MHz, and $A_3 = 320$ MHz. The large A_3 value is required to reproduce the hyperfine features readily observed in the experimental spectrum (the simulated values for A_1 and A_2 should be viewed with less certainty, although values in the range of 100 – 200 MHz were necessary to reproduce the breadth of the EPR signal; see Experimental Methods section and Figure 5.3). The A_3 value is higher than previously reported A values for Co(IV) centers (207, 156, and 72 MHz; see Table A5.2), which could be due to a higher spin density on the Co(IV) center in $[Co^{IV}(ONO_2)_2(NNN)]$.

5.3.2 Characterization of $[Co^{III}(OH)(NNN)]$, $[Co^{III}(ONO_2)(NNN)]$, and $[Co^{IV}(ONO_2)_2(NNN)]$ by Co K-edge X-ray absorption spectroscopy. Electronic structural

information was derived from XANES data.[38] An additional sample of [$Co^{III}(ONO_2)$(NNN)] was prepared to compare overall edge features with those of [Co^{III}(OH)(NNN)] and [$Co^{IV}(ONO_2)_2$(NNN)]. The X-ray absorption spectra of [Co^{III}(OH)(NNN)] and [$Co^{III}(ONO_2)$(NNN)] show nearly identical features, each containing several shoulders along the rising edge (Figure 5.4). The first peak (**1-pre** in Figure 5.4) with a low intensity at ca. 7710 eV is attributed to an electric dipole-forbidden 1s → 3d transition, which gains some intensity due to Co 3d and 4p orbital mixing.[38-41] The low intensity of this feature for [Co^{III}(OH)(NNN)] and [$Co^{III}(ONO_2)$(NNN)] may indicate the centrosymmetric geometry (square-planar) as shown in their XRD structures (Appendix A5, Table A5.4). Similarly, a low intensity pre-edge feature was observed in an X-ray near-edge spectrum of $[Co^{III}(TAML)]^{-}$ in a square-planar geometry.[12] The second peak (**2-pre** in Figure 5.4) with a much higher intensity is ascribed to an electric dipole-allowed one-electron transition from 1s to $4p_z$ orbital (around 7716 eV).[39, 40, 42] This transition commonly gains more intensity; however, some variations are observed among Co species within the same square-pyramidal geometry but different ligand fields.[39, 43-45] Other transitions straggling over the rising edge could be due to multiple scattering effects, as previously reported.[42] The rising edge energies are ca. 7721 eV for both complexes (7721.2 and 7720.9 eV for [Co^{III}(OH)(NNN)] and [$Co^{III}(ONO_2)$(NNN)], respectively). This value is about 2 eV higher than the edge energy reported for [Co^{II}HMD]$(ClO_4)_2$ but similar to that of [Co^{III}HMD(CO_3^{2-})](ClO_4) (HMD = 5,7,7,12,14,14-hexamethyl-1,4,8,11-tetraazacyclotetradeca-4,11-diene).[39] Other square-planar or -pyramidal Co^{III} complexes with TAML ligand and oxidized TAML ligand also showed an edge energy of 7721 eV for the edge energy.[45] Collectively, XANES data for [Co^{III}(OH)(NNN)] and [$Co^{IV}(ONO_2)_2$(NNN)] are consistent with a square-planar Co^{III} species, as shown in their XRD structures (Appendix A5, Figure A5.7 and Table A5.4).

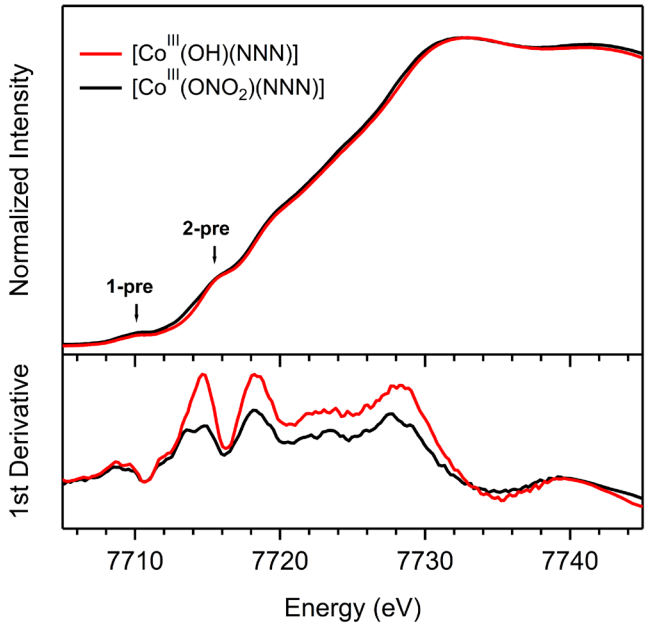

Figure 5.4. Co K-edge X-ray absorption near-edge spectra (XANES) of [Co^{III}(OH)(NNN)] and [$Co^{III}(ONO_2)$(NNN)] (top). The first derivative spectra of the near-edge region for the two complexes (bottom).

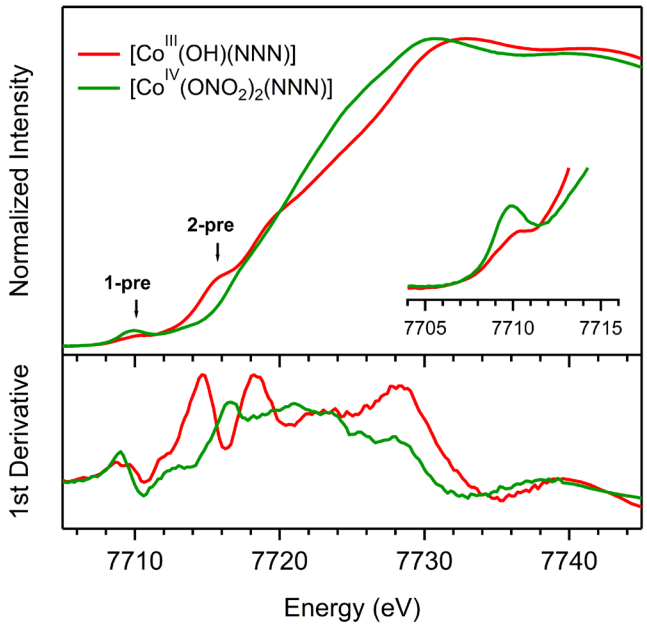

Figure 5.5. Co K-edge XANES of [Co^{III}(OH)(NNN)] and [$Co^{IV}(ONO_2)_2$(NNN)]. Inset shows magnified 1s → 3d one-electron transition peaks for [Co^{III}(OH)(NNN)] and [$Co^{IV}(ONO_2)_2$(NNN)] (top). The first derivative spectra of the near-edge region for the two complexes (bottom).

Further, the oxidation state and electronic structure of the Co center in $[Co^{IV}(ONO_2)_2(NNN)]$ was probed by its X-ray near-edge spectrum, which shows very distinct transitions from those observed in $[Co^{III}(OH)(NNN)]$ or $[Co^{III}(ONO_2)(NNN)]$. As shown in the inset of Figure 5.5, the first pre-edge feature of $[Co^{IV}(ONO_2)_2(NNN)]$ (**1-pre**) is more intense than that of $[Co^{III}(OH)(NNN)]$ or $[Co^{III}(ONO_2)(NNN)]$. The increased intensity is consistent with a change in the centrosymmetry around the Co ion, in accordance with the XRD structure of the complex that showed a square pyramidal geometry. Additionally, there is no resolved peak that could be correlated to a dipole-allowed $1s \rightarrow 4p_z$ one-electron transition. The absence of this transition has been reported for Co complexes with square pyramidal geometry, which implicates that the intensity of this transition varies depending on local coordination environments of each complex.[39, 41, 42, 46] As an example, comparable changes are observed in the XANES data of $[Co^{III}(TAML)]^-$ and $[Co(O)(TAML)]Sc^{3+}$. The first pre-edge feature of $[Co(O)(TAML)]Sc^{3+}$ gains more intensity relative to that of $[Co^{III}(TAML)]^-$, but no resolved peak or shoulder appears as another pre-edge peak.[12] The rising edge energy of $[Co^{IV}(ONO_2)_2(NNN)]$ is 7720.6 eV, although intense transitions along the rising edge make this value, or comparisons with the edge energies of other complexes, less meaningful (Appendix A5, Table A5.5). Together, the differences in the XANES data of $[Co^{III}(OH)(NNN)]$ and $[Co^{IV}(ONO_2)_2(NNN)]$ are consistent with the distinct geometries observed by XRD. Overall features in the near-edge region are parallel to those of XANES data for square pyramidal Co species. This geometry corresponds to that used in CASSCF/NEVPT2 calculations, of which the results are in good agreement with the EPR simulation parameters of $[Co^{IV}(ONO_2)_2(NNN)]$ (*vide infra*). Therefore, we conclude that $[Co^{IV}(ONO_2)_2(NNN)]$ remains the square pyramidal geometry in solution state as well as in solid state.

5.3.3 Computational Studies of Geometric and Electronic Structure of [$Co^{IV}(ONO_2)_2(NNN)$]. The electronic structure of [$Co^{IV}(ONO_2)_2(NNN)$] was examined using both DFT and CASSCF/NEVPT2 computations. The DFT-optimized structure of [$Co^{IV}(ONO_2)_2(NNN)$] (Figure 5.6A) shows metric parameters in excellent agreement with those observed in the X-ray crystal structure of [$Co^{IV}(ONO_2)_2(NNN)$] (Appendix A5, Figure A5.7). Notably, the long Co–ONO_2 axial distance is reproduced in the DFT structure, which suggests that this bond elongation is not an artifact of the solid-state sample but should persist in solution. This axial bond length plays an important role in defining the orbital ground state for an $S = 1/2$ Co(IV) system, as discussed below.

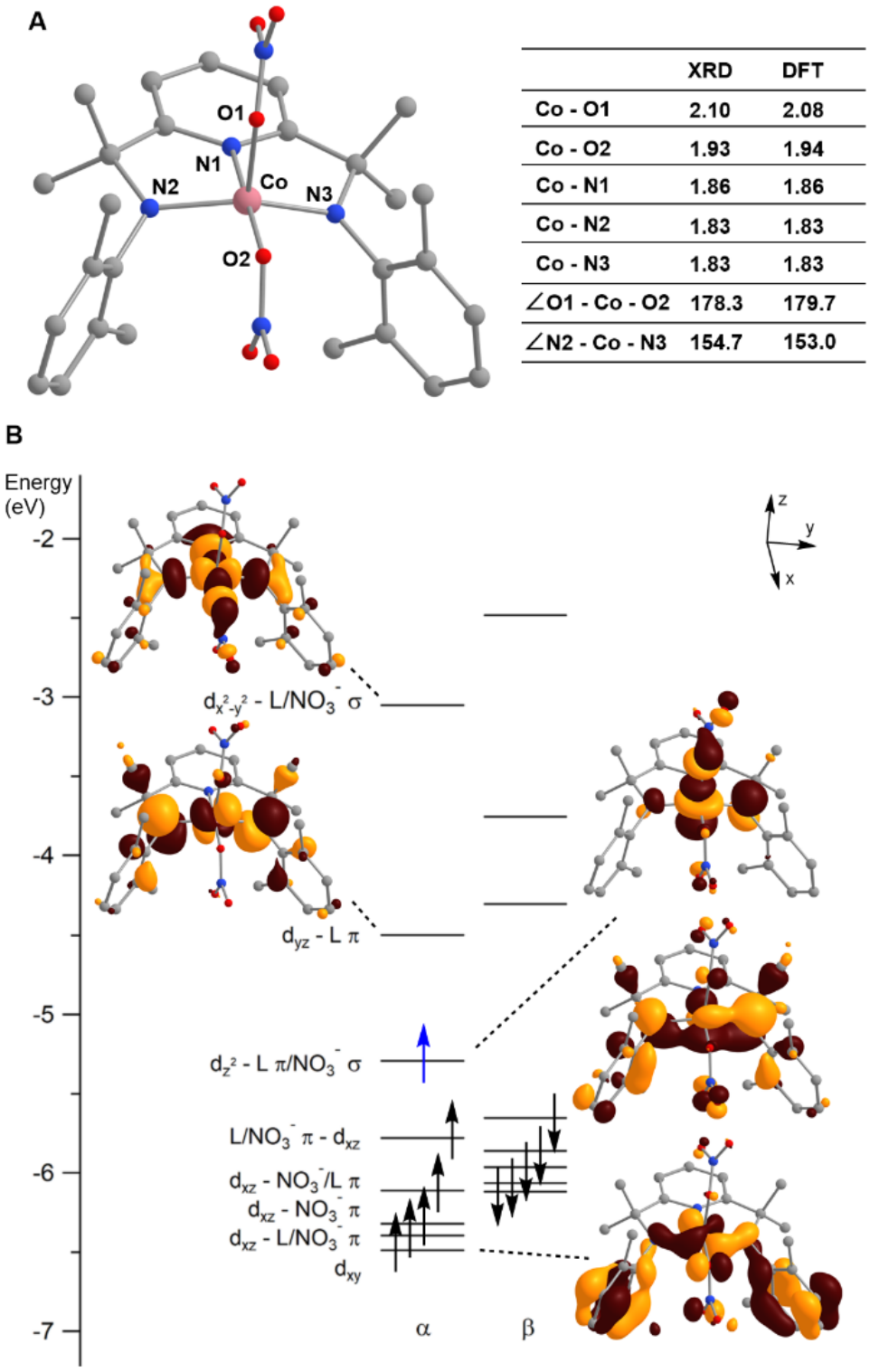

	XRD	DFT
Co - O1	2.10	2.08
Co - O2	1.93	1.94
Co - N1	1.86	1.86
Co - N2	1.83	1.83
Co - N3	1.83	1.83
∠O1 - Co - O2	178.3	179.7
∠N2 - Co - N3	154.7	153.0

Figure 5.6. (A) DFT-calculated structure of [$Co^{IV}(ONO_2)_2(NNN)$] with the corresponding bond distances (Å). (B) Co(IV) d orbital splitting pattern for [$Co^{IV}(ONO_2)_2(NNN)$] from DFT computations. Surface contour plots of quasi-restricted orbitals are shown for each d orbital.

The Co(IV) d-orbital splitting pattern for [$Co^{IV}(ONO_2)_2$(NNN)] reflects highly covalent interactions between the Co(IV) center and the N3 ligand. Using a conventional coordinate system, where the z axis is along the axial Co–ONO_2 bond and the x and y axes lie along the equatorial Co–ligand bonds (Figure 5.6B; also see Appendix A5, Figure A5.3 and Table A5.1), the d_{xy}, d_{xz}, and d_{yz} orbitals are of π-type and the d_z^2 and $d_{x^2-y^2}$ orbitals are of σ-type. The Co(IV) d_{xy} and d_{xz} orbitals have the weakest interactions with the ligands and are therefore at the lowest energy and doubly occupied. Each of these orbitals shows some mixing with the π-system of the pincer ligand but has only minor interactions with the nitrate ligands (Figure 5.6B). In contrast, the Co(IV) d_{yz} orbital is ideally suited for strong π-interactions with the pincer ligand (Figure 5.6B). The strength of these π-interactions, coupled with the weak Co–ONO_2 axial interaction places the Co(IV) d_{yz} MO at higher energy than the Co(IV) d_z^2 MO (Figure 5.6B). Consequently, the Co(IV) d_z^2 MO is the singly occupied MO (SOMO) for this complex. At the highest energy is the Co(IV) $d_{x^2-y^2}$ MO, which is σ-antibonding with the pincer ligand and the equatorial nitrate ligand.

CASSCF calculations with NEVPT2 corrections offer a complementary means of examining the electronic structure of [$Co^{IV}(ONO_2)_2$(NNN)] (Appendix A5, Figure A5.4 and Table A5.3). Using a moderately sized active space of 13 electrons in 9 orbitals (so-called CAS(13,9), see Experimental Methods for details), the CASSCF/NEVPT2 calculations converge to a doublet ground state, consistent with the EPR results described above. This ground state is well separated from other states; the lowest lying doublet and quartet excited states are near 5000 cm^{-1}. The ground state is dominated by a $(d_{xy})^2(d_{xz})^2(d_z^2)^1(d_{yz})^0(d_{x^2-y^2})^0$ configuration (61%), with a 12% admixture of a $(d_{xy})^2(d_{xz})^0(d_z^2)^1(d_{yz})^2(d_{x^2-y^2})^0$ configuration. Thus, these multireference calculations identify the Co(IV) d_z^2 MO as the SOMO, in accordance with the DFT results. The compositions of the CASSCF natural orbitals are similar to the DFT MOs and reveal the strong π-bonding

interaction between L and the Co(IV) d_{yz} orbital that places this orbital above the Co(IV) d_{z^2} MO (Figure A5.4). An isosurface plot of the spin density for the CASSCF wave function shows the localization of the spin on the Co(IV) d_{z^2} MO (Appendix A5, Figure A5.8). The CASSCF/NEVPT2 calculations predict *g* values of 2.39, 2.07, and 2.01, in reasonable agreement with the values obtained by spectral simulations (2.23, 2.08, and 2.00; see Appendix A5, Figure A5.6). The *A* values from the CASSCF/NEVPT2 computations are in more modest agreement with experiment ($|A_{NEVPT2}|$ = 61, 326, 451 MHz; $A_{simulation}$ = 135, 165, 320 MHz), although the uncertainty in two of the experimental components of the *A* matrix renders the comparison less meaningful. The electronic structure computations offer some important insights into the potential reactivity of $[Co^{IV}(ONO_2)_2(NNN)]$ in hydrogen-atom transfer reactions (*vide infra*). In these reactions, the Co(IV) d_{z^2} SOMO is expected to accept an electron from the substrate. The axial NO_3^- ligand could serve as the proton acceptor. The covalency between the Co(IV) d_{z^2} orbital and the axial NO_3^- ligand in the SOMO (Figure 5.6B) appears well suited for facilitating proton and electron transfer in a concerted fashion.

5.3.4 Transition State Structure of $[Co^{IV}(ONO_2)_2(NNN)]$ in CPET Reactions with ethylbenzene and 9,10-dihydroanthracene. The unusual oxidation reactivity of $[Co^{IV}(ONO_2)_2(NNN)]$ was investigated computationally by examining the potential transition state (TS) structures of $[Co^{IV}(ONO_2)_2(NNN)]$ using DFT methods (Figure 5.7A). To this end, the oxidation reaction with ethylbenzene (EtBn) was chosen first, and four oxygen atoms were set as the proton acceptors involved in the reaction, which are on the axial or equatorial nitrate ligands of $[Co^{IV}(ONO_2)_2(NNN)]$ (Figure 5.7B).

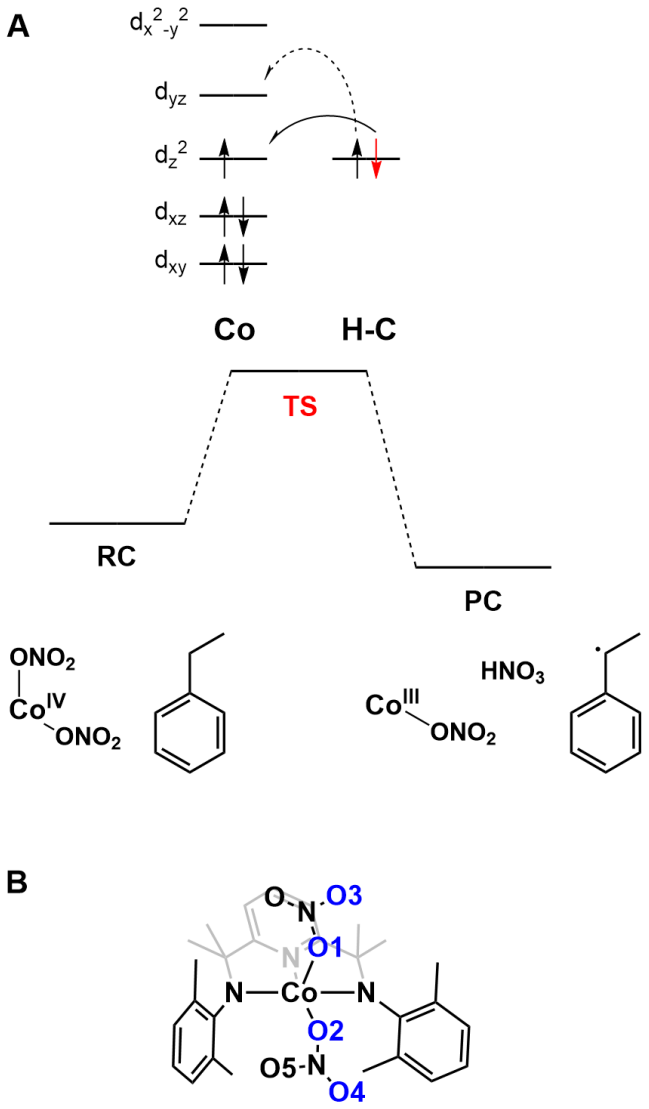

Figure 5.7. (A) Possible electron transfers at the transition state on a reaction coordinate of $[Co^{IV}(ONO_2)_2(NNN)]$ and a C–H bond of substrate. (B) Selected oxygen atoms as a proton acceptor in this study (O1 – O4).

Experimental activation parameters were collected to compare and complement the activation parameters obtained from the calculations (Table 5.1). The experimental values show the enthalpy of activation as 15.1 kcal mol^{-1} and the entropy contributions at 298.15 K ($T\Delta S^{\ddagger}$) as −6.9 kcal mol^{-1}. Five TS structures from the reaction of $[Co^{IV}(ONO_2)_2(NNN)]$ and EtBn (with O1,

O2, O3, and O4 as proton acceptors; each TS labeled as axial-O1, equatorial-O2, axial-O3, and equatorial-O4, correspondingly) were obtained by scanning potential energy surface for each reaction and applying transition state optimizations. Activation parameters for the calculated TSs are shown in Table 5.1, relative to infinitely separated reactants ([$Co^{IV}(ONO_2)_2$(NNN)] and EtBn).[47] The smallest $\Delta H^{‡}$ is gained from equatorial-O4 TS structure (19.1 kcal mol^{-1}), and the largest activation enthalpy is from axial-O1 (23.1 kcal mol^{-1}; Table 5.1). Thus, the energy gap between the experimental and calculated enthalpies of activation is 4 – 8 kcal mol^{-1}. In contrast, the entropies of activation among all experimental and theoretical values are marginally different, deviating within 1.5 kcal mol^{-1}. Correspondingly, structural features of each transition state are analyzed and compared in detail to better understand the variations in the activation enthalpy (*vide infra*).

Table 5.1. Experimental and calculated activation parameters at 298.15 K for the reaction of [$Co^{IV}(ONO_2)_2$(NNN)] and EtBn.[a]

	$\Delta H^{‡}$	$T\Delta S^{‡,b}$	$\Delta G^{‡}$
Experimental	15.1	−6.9[c]	22.0
axial-O1	23.1	−7.4	30.4
axial-O1′	21.3	−6.8	28.1
axial-O3	22.3	−7.1	29.4
equatorial-O2	20.4	−7.5	27.8
equatorial-O4	19.1	−6.2	25.3

[a] All values are in kcal mol^{-1}.
[b] Entropy values are calculated at 298.15 K.
[c] −23 cal mol^{-1} K^{-1} (e.u.).

From surface scans involving axial-O1, we explored two transition state structures, and each structure showed different structural features after the optimization calculations. One

structure has an axial nitrate ligand bound to the Co center and the other has an unbound axial nitrate (labeled as axial-O1 and axial-O1′, respectively; Figure 5.8). All TS structures show a late transition state, where the proton is already transferred to the acceptor atom. The shortest bond length of O–H bond is 1.15 Å among the five transition state structures, which correspondingly gives the longest separation between the C and H atoms (1.53 Å). Other transition state structures show comparable distances for O–H bonds (1.20 – 1.24 Å), and C···H interactions (1.41 – 1.46 Å). Additionally, TS structures with axial O atom acceptors show a large distance between Co–O1 and Co–O2 bond lengths. In contrast, Co–O1 and Co–O2 bond distances are comparable in the structures with equatorial O atom acceptors (< 0.05 Å differences; Table 5.1). Another discrepancy between the transition state structures with axial and equatorial O atom acceptors is the bond angle of N2–Co–N3. This bond angle with equatorial O acceptors is smaller than those of TS structures with axial O acceptors by 3 – 19°, indicating that the Co center lies out of the pincer ligand plane (Figure 5.9). This distortion can be measured with the index of the degree of trigonality (τ_5), which gives higher values to the TS structures with equatorial O acceptors, e.g., 0.47 for equatorial-O4 ($\tau_5 = 0$ implies ideal square planar geometry, while $\tau_5 = 1$ for ideal trigonal bipyramidal geometry; Table 5.2).[48, 49] For comparison, $\tau 5$ of $[Co^{IV}(ONO_2)_2(NNN)]$ is 0.39. These variations observed in geometric parameters between the TS structures with axial and equatorial O acceptors could mean different electronic structures between those TSs. Therefore, it could be beneficial to compare electronic structures of the TSs in order to interpret the differences in calculated $\Delta H^{\ddagger}$ for EtBn oxidation reaction (Table 5.1). To better understand the electronic structure of each TS, CASSCF with NEVPT2 corrections are being conducted to include multireference characters observed in $[Co^{IV}(ONO_2)_2(NNN)]$.

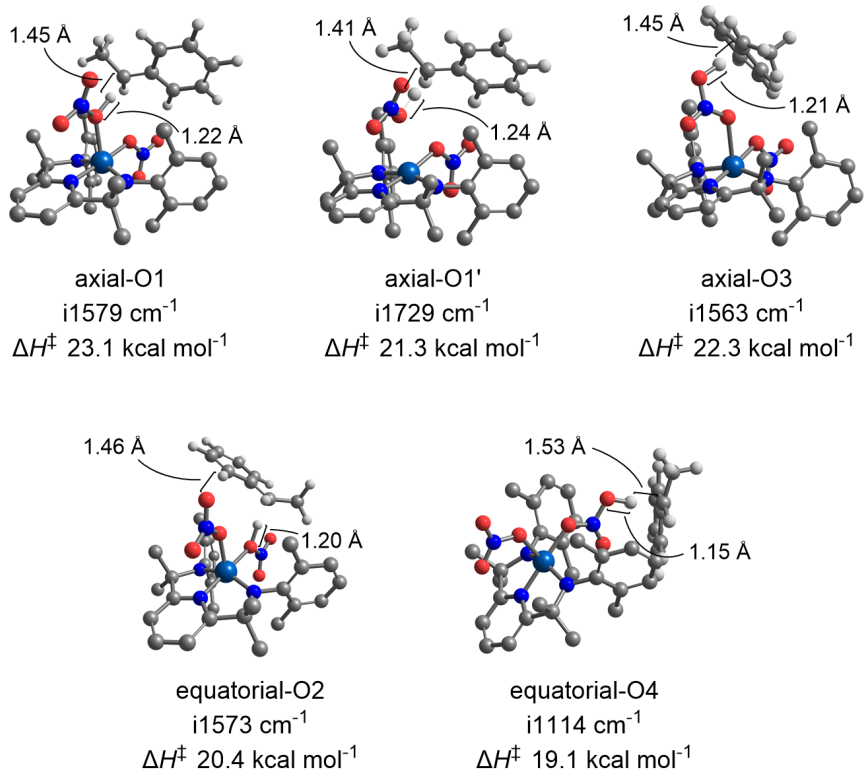

Figure 5.8. Calculated TS structures with different oxygen atoms as proton acceptors for the C–H bond oxidation reaction of $[Co^{IV}(ONO_2)_2(NNN)]$ and EtBn. The imaginary frequencies from each TS optimization and $\Delta H^{‡}$ are indicated.

Table 5.2. Selected bond distances (Å) and angles (°) for the computed TS structures of the C–H bond oxidation reaction of $[Co^{IV}(ONO_2)_2(NNN)]$ and EtBn.[a]

	O–H	C···H	Co–O1	Co–O2	∠N1–Co–O2	∠N2–Co–N3	τ_5[b]
axial-O1	1.22	1.45	2.26	1.92	176.6	154.7	0.37
axial-O1′	1.24	1.41	–	1.91	171.7	160.8	0.18
axial-O3	1.21	1.45	2.37	1.91	175.3	157.8	0.29
equatorial-O2	1.20	1.46	2.06	2.02	177.8	151.8	0.43
equatorial-O4	1.15	1.53	2.03	1.98	178.0	150.0	0.47

[a] Atom labels are referred to what is shown in Figure 5.6A.
[b] Index of the degree of trigonality = $(\beta - \alpha) \div 60$; where β and α are the largest angles.[48, 49]

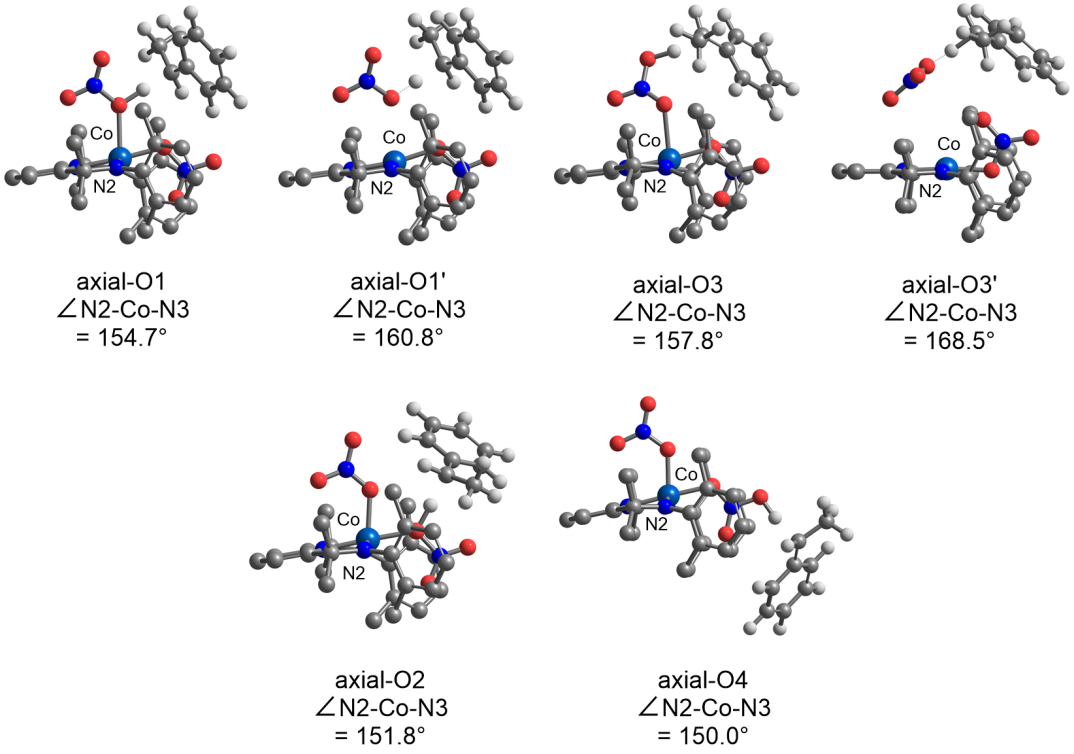

Figure 5.9. A side view of TS structures with their bond angle of ∠N2–Co–N3. N3 atom is located behind Co atom. A smaller bond angle of ∠N2–Co–N3 causes Co atom raised out of the pincer ligand plane.

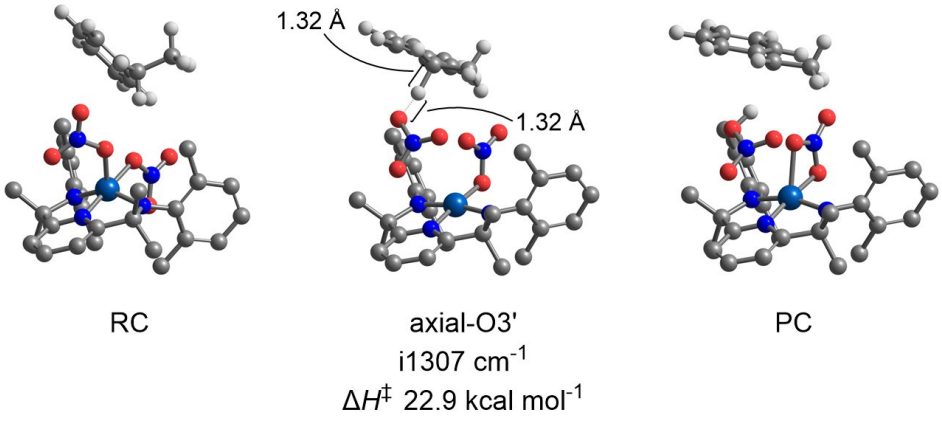

Figure 5.10. Structures of reactant complex (RC), TS (axial-O3′), and product complex (PC) in the NEB calculations.

Alternatively, a nudged elastic band (NEB) calculation was performed to inspect potential energy profile from reactant complex (RC) to product complex (PC) through TS. The O3 atom as a proton acceptor was chosen to achieve this TS comparisons, and DFT-optimized RC and PC were used for the NEB calculations (Figure 5.10). As expected, the potential energy profile attained from the NEB calculation shows a more detailed reaction path of the C–H bond activation by $[Co^{IV}(ONO_2)_2(NNN)]$ with O3 proton acceptor (this TS is labeled as axial-O3′). First, before reaching the TS of C–H bond activation, there is one intermediate species between two TSs (Figure 5.11; around image 7). The first TS is where the axial nitrate ligand dissociates from the Co center, and the equatorial nitrate ligand shifts to a bidentate binding mode (structure A in Figure 5.11). Correspondingly, another NEB calculation was carried out to understand this conformational change in detail (Figure 5.12).

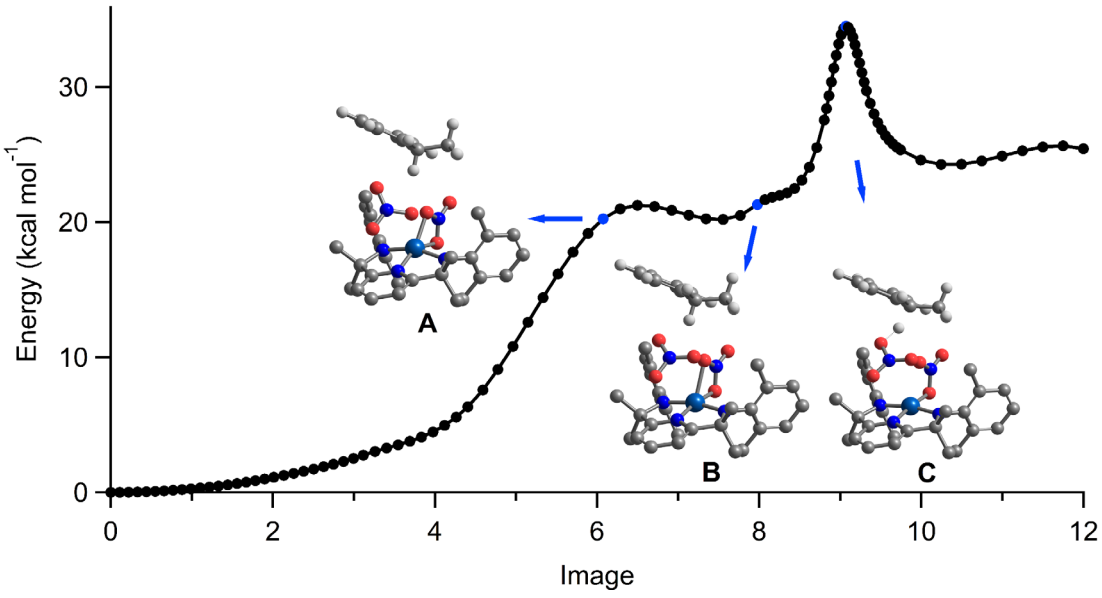

Figure 5.11. Potential energy profile for the reaction coordinate of $[Co^{IV}(ONO_2)_2(NNN)]$ and EtBn obtained from a converged NEB-TS computation with O3 proton acceptor. Selected images are shown (A – C).

Table 5.3. Selected bond distances (Å) and angles (°) for for the selected structures on the potential energy profile with axial-O3′ TS obtained by an NEB-TS optimization.

	Co···O1	Co–O2	Co–O5	Co–N1	Co–N2	Co–N3	∠N1–Co–N5	∠N2–Co–N3
A	2.88	1.99	2.20	1.86	1.82	1.85	147.1	158.9
B	3.87	2.23	1.94	1.85	1.82	1.81	169.0	165.1
C	4.02	2.41[a]	1.94	1.83	1.81	1.82	173.4	166.8

[a] The distance between Co center and dissociated O2 atom.

The NEB calculation performed with a DFT-optimized intermediate species shows an uphill in energy (Figure 5.12). The Co complex structures over this barrier exhibit several structural changes (A′ – E′). First, the bond length of Co–O2 increases as O2 moves towards the axial position from the equatorial position due to the alteration in the binding mode. Secondly, bond angles of ∠N1–Co–O5 and ∠N2–Co–N3 are getting larger while going towards the intermediate. Notably, the bond angle of ∠N2–Co–N3 is going through significant changes (from 148.2° from RC to 166.9° from E′ in Figure 5.12). Taken together, the elongation and dissociation of Co–O1 bond arises considerable conformational alterations, and the first saddle point accounts for these structural changes. Additional geometric parameters are shown in Appendix A5, Table A5.6.

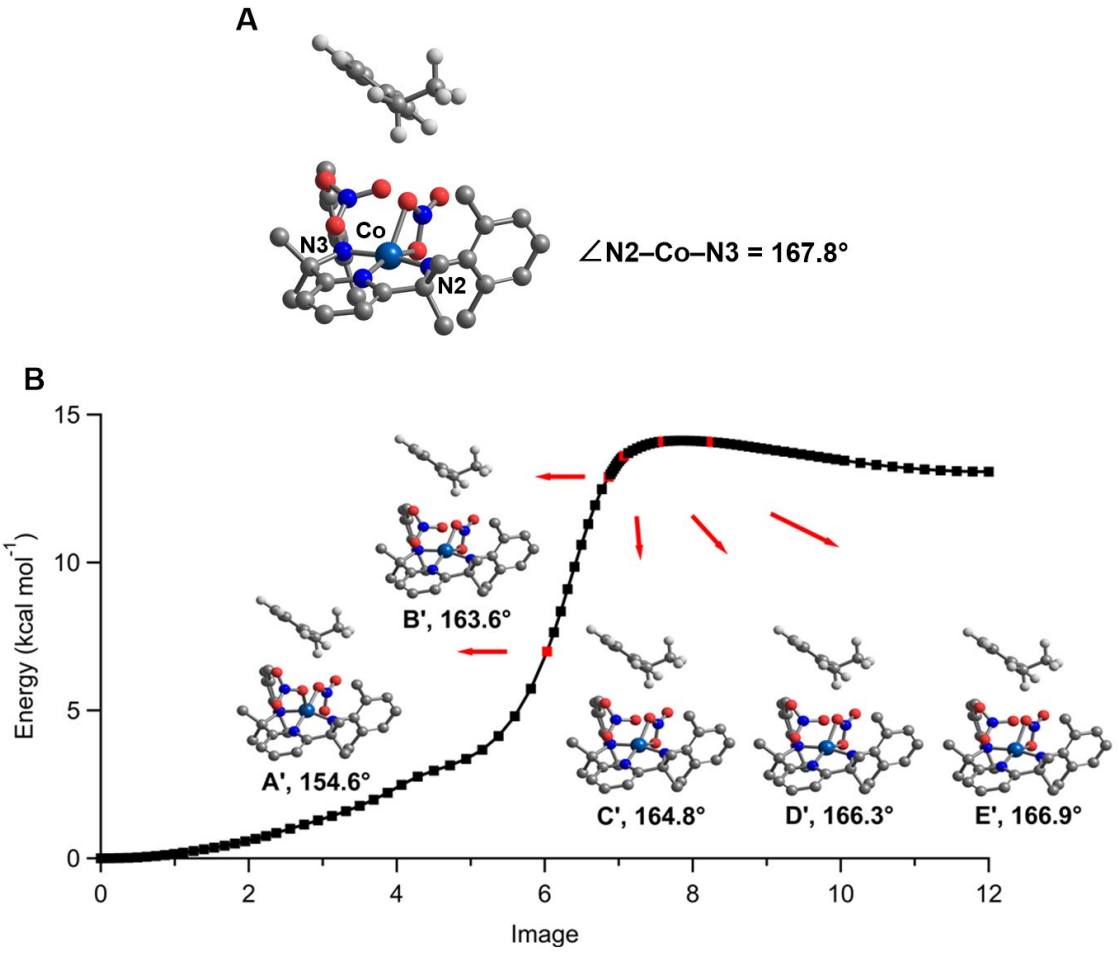

Figure 5.12. (A) DFT-optimized structure of intermediate species from the reaction coordinate of $[Co^{IV}(ONO_2)_2(NNN)]$ and EtBn. The bond angle of ∠N2–Co–N3 is indicated. (B) Potential energy profile for formation of the intermediate species. Selected images are beside the reaction coordinate (A′ – E′) that show dissociation of the axial nitrate ligand as well as the changes in ∠N2–Co–N3.

Table 5.4. Selected bond distances (Å) and angles (°) for reactant complex (RC), intermediate, transition state (TS), and product complex (PC).[a]

	Co–O1	Co–O2	Co–O5	Co–N1	Co–N2	Co–N3	∠N2–Co–N3
RC	1.93	1.92	2.86	1.86	1.86	1.82	148.2
Intermediate	–	2.12	2.00	1.86	1.82	1.81	167.8
TS (axial-O3′)	–	2.61	1.93	1.83	1.80	1.80	168.5
PC	–	2.18	1.97	1.85	1.85	1.85	161.9

[a] Atom labels are referred to what is shown in Figure 5.6A.

After the first saddle point, there is another small increment of energy before the TS (Figure 5.11). This additional energy can be ascribed to the structural changes that occur with the bidentate nitrate ligand. As an example, the structure B in Figure 5.11 shows a longer distance for Co–O2 bond by 0.11 Å and a slightly shorter distance for Co–O5 bond by 0.06 Å than those of structure A (Table 5.3). Eventually, the elongation of Co–O2 bond leaves the nitrate ligand in a monodentate binding fashion (structure C in Figure 5.11). Further, the axial-O3′ TS shows distinct bond lengths and angles from the other TS structures (Table 5.1). First, the bond lengths of O–H and C–H are the same (1.32 Å), which does not indicate a late transition state. Secondly, the largest bond angle of ∠N2–Co–N3 is observed in that structure (168.5°). The activation parameters are determined for the TS on the basis of enthalpy and entropy values of the infinitely separated reactants (axial-O3′ in Table 5.5). The activation enthalpy is 22.9 kcal mol^{-1}, which is 7.8 kcal mol^{-1} higher than the experimental value. Additionally, the difference in the entropy of activation between the experimental and theoretical methods is marginal (1.1 kcal mol^{-1}; Tables 5.5). As a result, although the TS obtained using the NEB method does not provide significant improvements in activation parameters, the presence of intermediate species may suggest a different mechanism for the proton and electron transfer. Changes in electronic structures among the calculated TS structures will be inspected to confirm this possibility.

Table 5.5. Experimental and calculated activation parameters at 298.15 K from the TS structure (axial-O3′) obtained using an NEB-TS method for the reaction of $[Co^{IV}(ONO_2)_2(NNN)]$ and EtBn.[a]

	$\Delta H^{\ddagger}$	$T\Delta S^{\ddagger}$	$\Delta G^{\ddagger}$
Experimental	15.1	−6.9	22.0
axial-O3′	22.9	−6.0	29.0

[a] All values are in kcal mol^{-1}.

Another computational investigation was performed to introduce more variations in activation enthalpies among the TSs, since the calculated values of activation parameters for the reaction of $[Co^{IV}(ONO_2)_2(NNN)]$ with EtBn are similar among the six TSs. To this goal, 9,10-dihydroanthracene (DHA) was chosen for further computational studies, as this compound has a weak C–H bond strength relative to that of EtBn (78 vs. 86.4 kcal mol^{-1}, respectively[10]). Kinetic experiments were carried out to collect experimental activation parameters for DHA oxidation reaction by $[Co^{IV}(ONO_2)_2(NNN)]$ (Table 5.6). The experimental activation parameters for this oxidation reaction are significantly different from the values collected for the oxidation reaction of $[Co^{IV}(ONO_2)_2(NNN)]$ and EtBn. About five times smaller enthalpy of activation is obtained, while approximately two times larger entropy of activation is measured (3.3 vs. 15.1 kcal mol^{-1} and −14.3 vs. −6.9 kcal mol^{-1}, respectively). Additionally, this activation enthalpy is lower than the experimentally determined $\Delta H^{\ddagger}$ for those reactions of DHA and other metal complexes which cleave stronger C–H bonds that $[Co^{IV}(ONO_2)_2(NNN)]$ does not.[47, 50] However, the activation entropy value is larger than the values for those more reactive metal species. As an example, $[LCu^{III}(OH)]^{-}$ (L = *N*,*N*′-bis(2,6-diisopropylphenyl)-2,6-pyridinedicarboxamide) shows 5.4(2) kcal mol^{-1} and −30(2) e.u. (−9.0 kcal mol^{-1} for $T\Delta S^{\ddagger}$ at 298.15K) for $\Delta H^{\ddagger}$ and $\Delta S^{\ddagger}$, respectively, which can activate the C–H bond of cyclohexane at −25 °C. In another case 9 kcal mol^{-1} for $\Delta H^{\ddagger}$ and −26 e.u. for $\Delta S^{\ddagger}$ (−7.8 kcal mol^{-1} for $T\Delta S^{\ddagger}$ at 298.15K) were reported from the oxidation reaction of $[Mn^{IV}(O)(N4py)]^{2+}$ and DHA. To reveal the reason behind those counterintuitive experimental activation parameters, TSs of DHA oxidation reaction by $[Co^{IV}(ONO_2)_2(NNN)]$ was theoretically explored (*vide infra*).

Table 5.6. Selected bond distances (Å) and angles (°) for the computed TS structures of the C–H bond oxidation reaction of $[Co^{IV}(ONO_2)_2(NNN)]$ and DHA.[a]

	$\Delta H^{\ddagger}$	$T\Delta S^{\ddagger}$[b]	$\Delta G^{\ddagger}$
Experimental	3.3	−14.3[c]	17.6
axial-O1	17.4	−8.7	26.1
axial-O3	11.0	−7.9	18.9
equatorial-O2	17.5	−9.6	27.1
equatorial-O4	12.1	−8.7	20.8

[a] All values are in kcal mol^{-1}.
[b] Entropy values are calculated at 298.15 K.
[c] −48 cal mol^{-1} K^{-1} (e.u.).

In the same way introduced earlier, the same four oxygen atoms were adopted as proton acceptors (O1 – O4; see Figure 5.7B). TSs with O1, O2, and O4 acceptors, labeled as axial-O1, equatorial-O2, and equatorial-O4, are obtained from TS optimizations using each approximated TS structure according to the relaxed surface scans. For the TS with O3 acceptor, an NEB computation was applied, followed by TS optimization to achieve a TS with only single imaginary frequency (Figure 5.13).

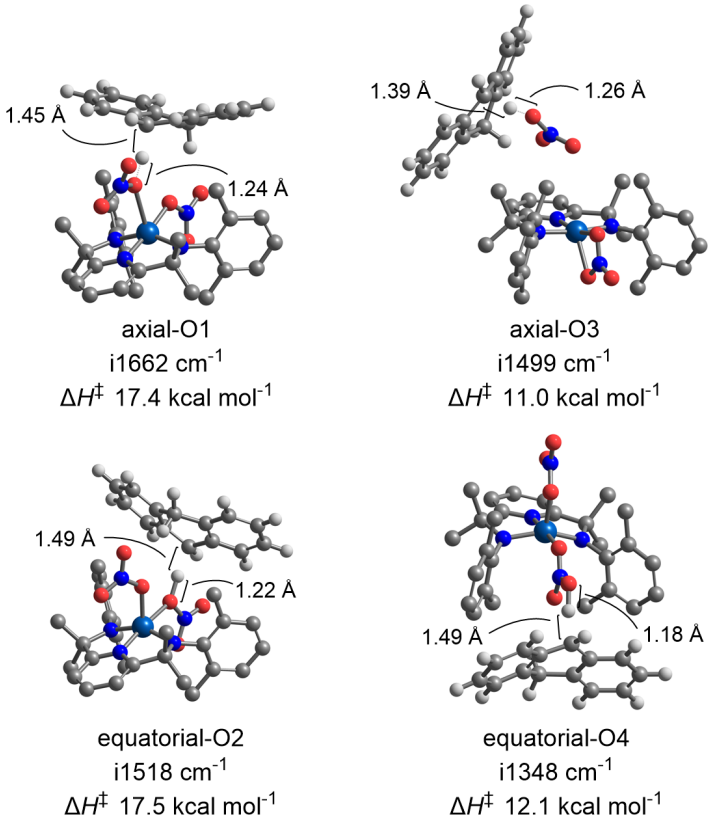

Figure 5.13. Calculated TS structures with different oxygen atoms as proton acceptors for the C–H bond oxidation reaction of [$Co^{IV}(ONO_2)_2$(NNN)] and DHA. The imaginary frequencies from each TS optimization and $\Delta H^{‡}$ are indicated.

Table 5.7. Selected bond distances (Å) and angles (°) for the computed transition state structures of the C–H bond oxidation reaction of [$Co^{IV}(ONO_2)_2$(NNN)] and DHA.[a]

	O–H	C···H	Co–O1	Co–O2	∠N1–Co–O2	∠N2–Co–N3	τ_5[b]
axial-O1	1.24	1.45	2.42	1.91	174.1	152.3	0.36
axial-O3	1.26	1.39	–	1.98	166.4	167.5	*0.02*
equatorial-O2	1.22	1.49	2.02	2.10	174.5	152.2	0.37
equatorial-O4	1.18	1.49	2.01	1.98	178.1	150.0	0.47

[a] Atom labels are referred to what is shown in Figure 5.6A.
[b] Index of the degree of trigonality = $(\beta - \alpha) \div 60$; where β and α are the largest angles.[48, 49]

The lengths of O–H and C–H bonds among the TSs show smaller ranges than those in the TSs with EtBn, for example, 1.18 – 1.26 and 1.15 – 1.32 Å for O–H bond distance ranges in TSs with DHA and EtBn, respectively. (Tables 5.2 and 5.7). Similar to the TSs with EtBn, the distances of Co–O1 bond are smaller in the TSs with equatorial proton acceptors than those of TSs with axial proton acceptors by ca. 0.4 Å. Other than that bond distance, there are no clear distinctions between the TSs with the equatorial and axial proton acceptors (Table 5.7). Theoretically collected activation parameters using these TSs show larger differences among the activation enthalpy values (1.1 – 6.5 kcal mol^{-1}) than those observed in the TSs for EtBn oxidation reaction (1.3 – 4.0 kcal mol^{-1}) as intended. However, both calculated $\Delta H^{\ddagger}$ and $T\Delta S^{\ddagger}$ values show more discrepancies with the experimentally determined values (Table 5.6). The calculated enthalpies of activation are larger than the experimental value by 8 – 14 kcal mol^{-1}, and the differences for the entropies of activation between computational and experimental parameters are around 6 kcal mol^{-1}. These variations are larger than those observed in activation parameters for EtBn oxidation (Tables 5.1 and 5.5). To find the possible reasons for these larger variations, the potential energy profile from an NEB computation with O3 proton acceptor was inspected (Figure 5.14).

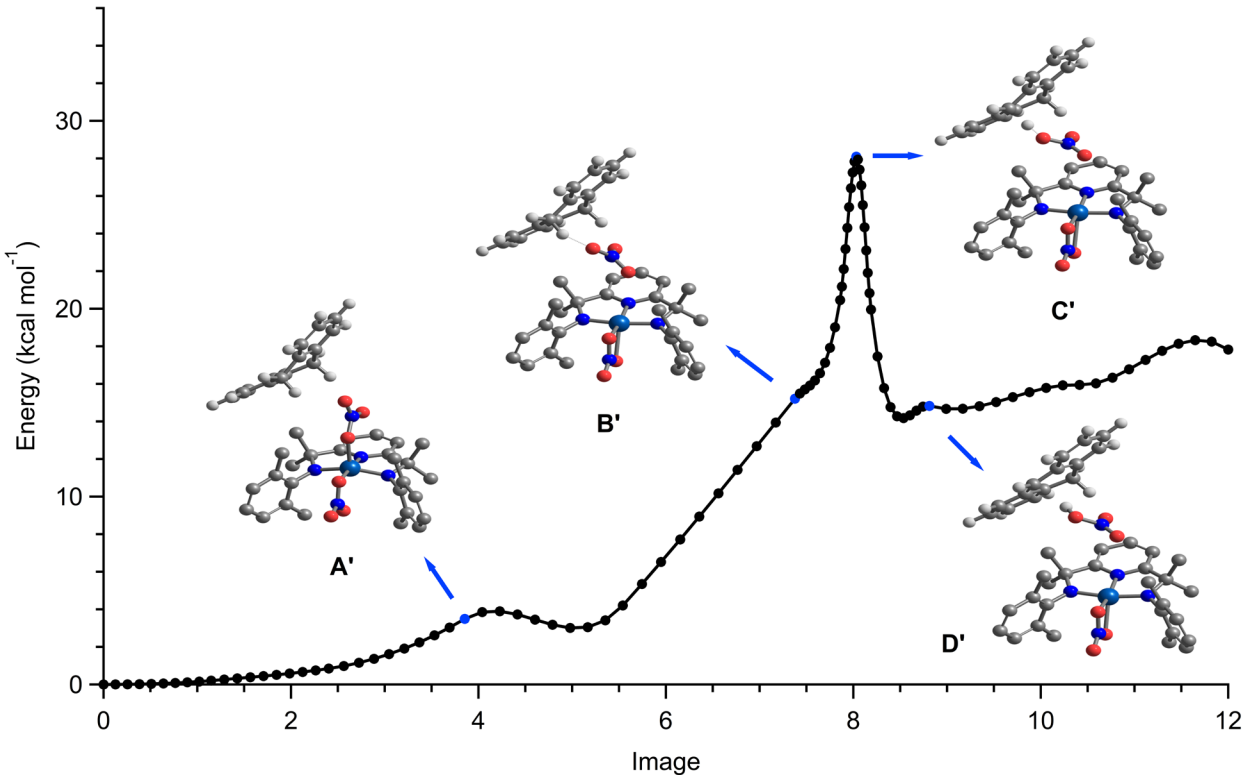

Figure 5.14. Potential energy profile for the reaction coordinate of $[Co^{IV}(ONO_2)_2(NNN)]$ and DHA obtained from a converged NEB-TS computation with O3 proton acceptor. Selected images are shown (A′ – D′).

Table 5.8. Selected bond distances (Å) and angles (°) for the selected structures on the potential energy profile of $[Co^{IV}(ONO_2)_2(NNN)]$ with axial-O3 proton acceptor and DHA computed by a NEB-TS method.

	Co-O1	Co–O2	Co–O5	Co–N1	Co–N2	Co–N3	∠N1–Co–O5	∠N2–Co–N3
RC	2.00	1.92	2.75	1.87	1.85	1.83	126.1	152.0
A′	2.02	1.93	2.54	1.86	1.86	1.86	119.5	152.7
B′	3.47	1.96	2.21	1.86	1.82	1.82	130.6	168.3
C′	3.89	1.95	2.35	1.84	1.82	1.81	131.9	169.0
D′	4.07	1.98	2.16	1.86	1.85	1.85	133.3	167.0
PC	4.60	1.97	2.16	1.85	1.85	1.84	129.5	165.7

The potential energy profile of [$Co^{IV}(ONO_2)_2(NNN)$] (with O3 proton acceptor) and DHA has one TS and one saddle point before the TS. At the saddle point, with a very low potential energy, is attributed to the changes with O5 atom based on the distance of Co–O5 bond (altered by 0.21 Å). Dissociation of the axial nitrate ligand and the corresponding structural changes in the equatorial nitrate contribute to the increase in potential energy after the saddle point. In contrast, there is no noticeable structural difference in the Co complex before and after TS, which implicates the spike of the energy at this TS is produced solely by the proton and an electron transfer from DHA to the dissociated nitrate ligand (structures B′ and C′ in Figure 5.14). The PC used in this NEB calculation lies higher in energy than RC; therefore, the overall reaction is endothermic, which does not correspond to the experimental findings. Possible reasons for this discrepancy are currently being sought by applying different level of theory. Altogether, the results of NEB calculations show the dissociation of axial nitrate ligand prior to the proton and electron transfer step, as the NEB computation results for [$Co^{IV}(ONO_2)_2(NNN)$] and EtBn (*vide supra*). Although axial-O3 and equatorial-O4 TSs show lower $\Delta H^{\ddagger}$ values than axial-O1 and equatorial-O2 by 5.3 – 6.5 kcal mol^{-1}, they are much higher than the experimental $\Delta H^{\ddagger}$ value by ca. 8 – 9 kcal mol^{-1}. Further NEB calculations, with additional investigations on PC, for TSs with other proton acceptor O atoms may be beneficial to compare and interpret these data.

5.4 Conclusion

The electronic structure of [$Co^{IV}(ONO_2)_2(NNN)$] was explored using multiple spectroscopic techniques and different computational methods. The EPR spectrum of [$Co^{IV}(ONO_2)_2(NNN)$] and calculations through DFT and CASSCF with NEVPT2 corrections

suggest an unpaired electron is located at Co^{IV} d_z^2 orbital. The XANES data of $[Co^{IV}(ONO_2)_2(NNN)]$ are consistent with the XRD structure. Possible transition state structures were explored computationally to better understand the CPET mechanism of $[Co^{IV}(ONO_2)_2(NNN)]$ towards C–H bond activation. All calculated activation parameters from TS structures are fairly similar to each other and to the experimentally determined values for ethylbenzene oxidation. However, calculated parameters show somewhat different values from the experimental activation parameters of DHA oxidation. This discrepancy may reflect a significant amount of multireference character required in calculations or a different mechanism, e.g., stepwise proton and electron transfer process. Furthermore, NEB calculations show a saddle point before the TS of each oxidation reaction. It is unclear at the moment how it affects the electronic structure of $[Co^{IV}(ONO_2)_2(NNN)]$, but the changes in electronic structures will be inspected. CASSCF calculations with NEVPT2 corrections are undergoing to examine the multireference character of TS structures. It will be beneficial to see any differences in NEB calculations with different functionals. Additionally, another set of computations would be needed to account for the lower $\Delta H^{\ddagger}$ and larger $\Delta S^{\ddagger}$ than those of other highly reactive metal complexes, which can include a different mechanism for proton and electron transfer, e.g., a stepwise mechanism.

5.5 Notes and References

1. Gandeepan, P.; Müller, T.; Zell, D.; Cera, G.; Warratz, S.; Ackermann, L., 3d Transition Metals for C–H Activation. *Chemical Reviews* **2019,** *119* (4), 2192-2452.

2. Xue, X.-S.; Ji, P.; Zhou, B.; Cheng, J.-P., The Essential Role of Bond Energetics in C–H Activation/Functionalization. *Chemical Reviews* **2017,** *117* (13), 8622-8648.

3. Moselage, M.; Li, J.; Ackermann, L., Cobalt-Catalyzed C–H Activation. *ACS Catalysis* **2016,** *6* (2), 498-525.

4. Trammell, R.; Rajabimoghadam, K.; Garcia-Bosch, I., Copper-Promoted Functionalization of Organic Molecules: from Biologically Relevant Cu/O2 Model Systems to Organometallic Transformations. *Chemical Reviews* **2019,** *119* (4), 2954-3031.

5. Olivier-Bourbigou, H.; Breuil, P. A. R.; Magna, L.; Michel, T.; Espada Pastor, M. F.; Delcroix, D., Nickel Catalyzed Olefin Oligomerization and Dimerization. *Chemical Reviews* **2020,** *120* (15), 7919-7983.

6. Ballhausen, C. J.; Gray, H. B., The Electronic Structure of the Vanadyl Ion. *Inorganic Chemistry* **1962,** *1* (1), 111-122.

7. Gray, H. B.; Winkler, J. R., Living with Oxygen. *Accounts of Chemical Research* **2018,** *51* (8), 1850-1857.

8. Cho, J.; Sarangi, R.; Annaraj, J.; Kim, S. Y.; Kubo, M.; Ogura, T.; Solomon, E. I.; Nam, W., Geometric and electronic structure and reactivity of a mononuclear 'side-on' nickel(iii)–peroxo complex. *Nature Chemistry* **2009,** *1* (7), 568-572.

9. Andris, E.; Navrátil, R.; Jašík, J.; Srnec, M.; Rodríguez, M.; Costas, M.; Roithová, J., M−O Bonding Beyond the Oxo Wall: Spectroscopy and Reactivity of Cobalt(III)-Oxyl and Cobalt(III)-Oxo Complexes. *Angewandte Chemie International Edition* **2019,** *58* (28), 9619-9624.

10. Massie, A. A.; Sinha, A.; Parham, J. D.; Nordlander, E.; Jackson, T. A., Relationship between Hydrogen-Atom Transfer Driving Force and Reaction Rates for an Oxomanganese(IV) Adduct. *Inorganic Chemistry* **2018,** *57* (14), 8253-8263.

11. Kim, Y.; Kim, J.; Nguyen, L. K.; Lee, Y.-M.; Nam, W.; Kim, S. H., EPR spectroscopy elucidates the electronic structure of [Fe^{V}(O)(TAML)] complexes. *Inorganic Chemistry Frontiers* **2021,** *8* (15), 3775-3783.

12. Hong, S.; Pfaff, F. F.; Kwon, E.; Wang, Y.; Seo, M.-S.; Bill, E.; Ray, K.; Nam, W., Spectroscopic Capture and Reactivity of a Low-Spin Cobalt(IV)-Oxo Complex Stabilized by Binding Redox-Inactive Metal Ions. *Angewandte Chemie International Edition* **2014,** *53* (39), 10403-10407.

13. Collins, T. J.; Powell, R. D.; Slebodnick, C.; Uffelman, E. S., Stable Highly Oxidizing Cobalt Complexes of Macrocyclic Ligands. *Journal of the American Chemical Society* **1991,** *113* (22), 8419-8425.

14. Adamian, V. A.; D'Souza, F.; Licoccia, S.; Di Vona, M. L.; Tassoni, E.; Paolesse, R.; Boschi, T.; Kadish, K. M., Synthesis, Characterization, and Electrochemical Behavior of (5,10,15-Tri-X-phenyl-2,3,7,8,12,13,17,18-octamethylcorrolato)cobalt(III) Triphenylphosphine Complexes, Where X = p-OCH3, p-CH3, p-Cl, m-Cl, o-Cl, m-F, or o-F. *Inorganic Chemistry* **1995,** *34* (3), 532-540.

15. Will, S.; Lex, J.; Vogel, E.; Adamian, V. A.; Van Caemelbecke, E.; Kadish, K. M., Synthesis, Characterization, and Electrochemistry of σ-Bonded Cobalt Corroles in High Oxidation States. *Inorganic Chemistry* **1996,** *35* (19), 5577-5583.

16. Goetz, M. K.; Hill, E. A.; Filatov, A. S.; Anderson, J. S., Isolation of a Terminal Co(III)-Oxo Complex. *Journal of the American Chemical Society* **2018,** *140* (41), 13176-13180.

17. Goetz, M. K.; Anderson, J. S., Experimental Evidence for pKa-Driven Asynchronicity in C–H Activation by a Terminal Co(III)–Oxo Complex. *Journal of the American Chemical Society* **2019,** *141* (9), 4051-4062.

18. Hill, E. A.; Kelty, M. L.; Filatov, A. S.; Anderson, J. S., Isolable iodosylarene and iodoxyarene adducts of Co and their O-atom transfer and C–H activation reactivity. *Chemical Science* **2018,** *9* (19), 4493-4499.

19. Wang, B.; Lee, Y.-M.; Tcho, W.-Y.; Tussupbayev, S.; Kim, S.-T.; Kim, Y.; Seo, M. S.; Cho, K.-B.; Dede, Y.; Keegan, B. C.; Ogura, T.; Kim, S. H.; Ohta, T.; Baik, M.-H.; Ray, K.; Shearer, J.; Nam, W., Synthesis and reactivity of a mononuclear non-haem cobalt(IV)-oxo complex. *Nature Communications* **2017,** *8* (1), 14839.

20. Stoll, S.; Schweiger, A., EasySpin, a comprehensive software package for spectral simulation and analysis in EPR. *Journal of Magnetic Resonance* **2006,** *178* (1), 42-55.

21. McAlpin, J. G.; Stich, T. A.; Ohlin, C. A.; Surendranath, Y.; Nocera, D. G.; Casey, W. H.; Britt, R. D., Electronic Structure Description of a [Co(III)3Co(IV)O4] Cluster: A Model for the Paramagnetic Intermediate in Cobalt-Catalyzed Water Oxidation. *Journal of the American Chemical Society* **2011,** *133* (39), 15444-15452.

22. Stich, T. A.; Krzystek, J.; Mercado, B. Q.; McAlpin, J. G.; Ohlin, C. A.; Olmstead, M. M.; Casey, W. H.; David Britt, R., Structural insights into $[Co4O4(C5H5N)4(CH3CO2)4]^{+}$, a rare Co(IV)-containing cuboidal complex. *Polyhedron* **2013,** *64*, 304-307.

23. Ravel, B.; Newville, M., ATHENA, ARTEMIS, HEPHAESTUS: data analysis for X-ray absorption spectroscopy using IFEFFIT. *Journal of Synchrotron Radiation* **2005,** *12* (4), 537-541.

24. Neese, F., The ORCA program system. *WIREs Computational Molecular Science* **2012,** *2* (1), 73-78.

25. Weigend, F.; Ahlrichs, R., Balanced basis sets of split valence, triple zeta valence and quadruple zeta valence quality for H to Rn: Design and assessment of accuracy. *Physical Chemistry Chemical Physics* **2005,** *7* (18), 3297-3305.

26. Grimme, S.; Ehrlich, S.; Goerigk, L., Effect of the damping function in dispersion corrected density functional theory. *Journal of Computational Chemistry* **2011,** *32* (7), 1456-1465.

27. Grimme, S.; Antony, J.; Ehrlich, S.; Krieg, H., A consistent and accurate ab initio parametrization of density functional dispersion correction (DFT-D) for the 94 elements H-Pu. *The Journal of Chemical Physics* **2010,** *132* (15), 154104.

28. Tao, J.; Perdew, J. P.; Staroverov, V. N.; Scuseria, G. E., Climbing the Density Functional Ladder: Nonempirical Meta--Generalized Gradient Approximation Designed for Molecules and Solids. *Physical Review Letters* **2003,** *91* (14), 146401.

29. Schäfer, A.; Horn, H.; Ahlrichs, R., Fully optimized contracted Gaussian basis sets for atoms Li to Kr. *The Journal of Chemical Physics* **1992,** *97* (4), 2571-2577.

30. Schäfer, A.; Huber, C.; Ahlrichs, R., Fully optimized contracted Gaussian basis sets of triple zeta valence quality for atoms Li to Kr. *The Journal of Chemical Physics* **1994,** *100* (8), 5829-5835.

31. Weigend, F., Accurate Coulomb-fitting basis sets for H to Rn. *Physical Chemistry Chemical Physics* **2006,** *8* (9), 1057-1065.

32. Angeli, C.; Cimiraglia, R.; Evangelisti, S.; Leininger, T.; Malrieu, J. P., Introduction of n-electron valence states for multireference perturbation theory. *The Journal of Chemical Physics* **2001,** *114* (23), 10252-10264.

33. Duboc, C.; Phoeung, T.; Zein, S.; Pécaut, J.; Collomb, M.-N.; Neese, F., Origin of the Zero-Field Splitting in Mononuclear Octahedral Dihalide MnII Complexes: An Investigation by Multifrequency High-Field Electron Paramagnetic Resonance and Density Functional Theory. *Inorganic Chemistry* **2007,** *46* (12), 4905-4916.

34. Wijeratne, G. B.; Zolnhofer, E. M.; Fortier, S.; Grant, L. N.; Carroll, P. J.; Chen, C.-H.; Meyer, K.; Krzystek, J.; Ozarowski, A.; Jackson, T. A.; Mindiola, D. J.; Telser, J., Electronic Structure and Reactivity of a Well-Defined Mononuclear Complex of Ti(II). *Inorganic Chemistry* **2015,** *54* (21), 10380-10397.

35. Neese, F., Prediction and interpretation of the 57Fe isomer shift in Mössbauer spectra by density functional theory. *Inorganica Chimica Acta* **2002,** *337*, 181-192.

36. Carpenter, G. B.; Clark, G. S.; Rieger, A. L.; Rieger, P. H.; Sweigart, D. A., Dithiolenes Revisited - an Electron-Spin-Resonance Study of Some 5-Co-Ordinate Cobalt Complexes and the Crystal-Structures of [Co(S2C2(CF3)(2))(2)(P(OPh)(3))] and [Co(S2C2(CF3)(2))(2)(PPh(3))]. *J Chem Soc Dalton* **1994,** (20), 2903-2910.

37. Harmer, J.; Van Doorslaer, S.; Gromov, I.; Bröring, M.; Jeschke, G.; Schweiger, A., A Pulse EPR and ENDOR Investigation of the Electronic Structure of a σ-Carbon-Bonded Cobalt(IV) Corrole. *The Journal of Physical Chemistry B* **2002,** *106* (10), 2801-2811.

38. Sarangi, R., X-ray absorption near-edge spectroscopy in bioinorganic chemistry: Application to M–O2 systems. *Coordination Chemistry Reviews* **2013,** *257* (2), 459-472.

39. Fujita, E.; Furenlid, L. R.; Renner, M. W., Direct XANES Evidence for Charge Transfer in Co−CO2 Complexes. *Journal of the American Chemical Society* **1997,** *119* (19), 4549-4550.

40. Lahanas, N.; Kucheryavy, P.; Lockard, J. V., Spectroscopic Evidence for Room Temperature Interaction of Molecular Oxygen with Cobalt Porphyrin Linker Sites within a Metal–Organic Framework. *Inorganic Chemistry* **2016,** *55* (20), 10110-10113.

41. Schrapers, P.; Mebs, S.; Goetzl, S.; Hennig, S. E.; Dau, H.; Dobbek, H.; Haumann, M., Axial Ligation and Redox Changes at the Cobalt Ion in Cobalamin Bound to Corrinoid Iron-Sulfur Protein (CoFeSP) or in Solution Characterized by XAS and DFT. *PLOS ONE* **2016,** *11* (7), e0158681.

42. Sarangi, R.; Cho, J.; Nam, W.; Solomon, E. I., XAS and DFT Investigation of Mononuclear Cobalt(III) Peroxo Complexes: Electronic Control of the Geometric Structure in CoO2 versus NiO2 Systems. *Inorganic Chemistry* **2011,** *50* (2), 614-620.

43. Yu, R. P.; Darmon, J. M.; Milsmann, C.; Margulieux, G. W.; Stieber, S. C. E.; DeBeer, S.; Chirik, P. J., Catalytic Hydrogenation Activity and Electronic Structure Determination of Bis(arylimidazol-2-ylidene)pyridine Cobalt Alkyl and Hydride Complexes. *Journal of the American Chemical Society* **2013,** *135* (35), 13168-13184.

44. Corcos, A. R.; Villanueva, O.; Walroth, R. C.; Sharma, S. K.; Bacsa, J.; Lancaster, K. M.; MacBeth, C. E.; Berry, J. F., Oxygen Activation by Co(II) and a Redox Non-Innocent Ligand: Spectroscopic Characterization of a Radical–Co(II)–Superoxide Complex with Divergent Catalytic Reactivity. *Journal of the American Chemical Society* **2016,** *138* (6), 1796-1799.

45. Van Leest, N. P.; Tepaske, M. A.; Oudsen, J.-P. H.; Venderbosch, B.; Rietdijk, N. R.; Siegler, M. A.; Tromp, M.; Van Der Vlugt, J. I.; De Bruin, B., Ligand Redox Noninnocence in $[Co^{III}(TAML)]^{0/-}$ Complexes Affects Nitrene Formation. *Journal of the American Chemical Society* **2020,** *142* (1), 552-563.

46. Padden, K. M.; Krebs, J. F.; Trafford, K. T.; Yap, G. P. A.; Rheingold, A. H.; Borovik, A. S.; Scarrow, R. C., Probing the Structure of Immobilized Metal Sites in Porous Organic Hosts by X-ray Absorption Spectroscopy. *Chemistry of Materials* **2001,** *13* (11), 4305-4313.

47. Rice, D. B.; Massie, A. A.; Jackson, T. A., Experimental and Multireference ab Initio Investigations of Hydrogen-Atom-Transfer Reactivity of a Mononuclear Mn^{IV}-oxo Complex. *Inorganic Chemistry* **2019,** *58* (20), 13902-13916.

48. Addison, A. W.; Rao, T. N.; Reedijk, J.; Van Rijn, J.; Verschoor, G. C., Synthesis, structure, and spectroscopic properties of copper(II) compounds containing nitrogen–sulphur donor ligands; the crystal and molecular structure of aqua[1,7-bis(N-methylbenzimidazol-2′-yl)-2,6-dithiaheptane]copper(II) perchlorate. *J. Chem. Soc., Dalton Trans.* **1984,** (7), 1349-1356.

49. Blackman, A. G.; Schenk, E. B.; Jelley, R. E.; Krenske, E. H.; Gahan, L. R., Five-coordinate transition metal complexes and the value of τ5: observations and caveats. *Dalton Transactions* **2020,** *49* (42), 14798-14806.

50. Dhar, D.; Yee, G. M.; Spaeth, A. D.; Boyce, D. W.; Zhang, H.; Dereli, B.; Cramer, C. J.; Tolman, W. B., Perturbing the Copper(III)–Hydroxide Unit through Ligand Structural Variation. *Journal of the American Chemical Society* **2016,** *138* (1), 356-368.

Chapter 6

Future Directions

6.1 Introduction

Sustainable transition metal catalysts are an important component to achieve environmental friendly chemical production. Given the demands for sustainable catalysts in many industrial processes, earth-abundant transition metals have gained attention from researchers in recent years as substitutes of precious metals. In this dissertation I investigated and reported structure and reactivity correlations of high-valent manganese and cobalt complexes. Following the general background of the subject in chapter 1, chapters 2 – 4 contain structural features of mono- or multinuclear high-valent manganese species and their reactivities. In chapter 5 the oxidation state and electronic structure of a high-valent cobalt complex were investigated. Transition state structure calculations for the C–H bond oxidation reactions of the cobalt complex were performed in an effort to reveal the mechanism of C–H bond activation by the complex. In this chapter future directions are briefly discussed on the basis of experimental and computational results in the previous chapters.

6.2 Preparation of High-valent Manganese Complexes

Manganese is often found as Mn^{II}, Mn^{III}, and Mn^{IV} ions in biological systems. Among those oxidation states, high-valent manganese ions are found in a couple of manganese-dependent redox enzymes, e.g., the oxygen evolving complex (OEC) in photosystem II, which catalyzes water oxidation to generate molecular oxygen under ambient conditions. In the catalytic cycle of water oxidation, high-valent Mn-oxo units (Mn^{IV} and Mn^{V}) are proposed for O–O bond formation.[1] Moreover, several synthetic Mn^{IV}-oxo complexes show strong oxidation reactivities towards C–H bond activation.[2, 3] Although oxidation reactivities of high-valent manganese

complexes have shown interesting results, mononuclear Mn^{IV}-oxo complexes have been only prepared in TFE or a mixed solvent system, such as 1:1 MeCN:TFE. As a result, there are limits to use Mn^{IV}-oxo complexes for practical applications due to the toxic and corrosive properties of this fluorinated solvent. To better understand and use the oxidizing ability of a mononuclear Mn^{IV}-oxo complex, preparation of the high-valent complex in solvents other than TFE is necessary. In preparation of $[Mn^{IV}(O)(^{DMM}N4py)]^{2+}$ in acetonitrile and water, a less harmful and more applicable solvent system than TFE, formation of the high-valent manganese complex is observed. Interestingly, different intermediates are found depending on the amount of CAN used. It is presumed that different ratios of Mn^{II}:CAN induce different yields of $[Mn^{IV}(O)(^{DMM}N4py)]^{2+}$, which is unstable and transforms into another intermediate by reacting with $[Mn^{II}(OTf)(^{DMM}N4py)]^{+}$, $[Mn^{III}(OH)(^{DMM}N4py)]^{2+}$, or a Brønsted/Lewis acid available in solution.

The EPR spectrum of the new intermediate (intermediate A; Figure 6.1) from the reaction of $[Mn^{II}(OTf)(^{DMM}N4py)](OTf)$ and 4 equiv. CAN is attributed to a mononuclear $S = 3/2$ Mn^{IV} complex with a broad resonance spanning over the $g = 2.6 - 5.7$, albeit without the ^{55}Mn hyperfine coupling.[4] This spectrum does not resemble the EPR spectra of Mn^{IV}-oxo species bearing neutral pentadentate ligands, which display less resolved low-field signals.[3, 5, 6] Instead, several Mn^{IV}-oxo complexes supported by different ligands and with a variety of geometries exhibit comparable EPR spectra. An EPR spectrum of a Mn^{IV}-oxo complex shows a low-field resonance at $g = 3.7$.[7] This complex contains a neutral tetradentate N4 ligand, and $[Mn^{IV}(O)(OCH_3)(L^{N4})]^{+}$ (L^{N4} = *N*-benzyl-1-(pyridin-2-yl)-*N*-((1-(pyridin-2-ylmethyl)pyrrolidin-2-yl)methyl)methanamine; Figure 6.2) is proposed from a coldspray ionization time-of-flight mass spectrometry (CSI-TOF MS) technique. Another example is an oxo(porphyrinato)manganese(IV) complex, $[Mn^{IV}(O)(T_{piv}PP)]$ ($T_{piv}PP$ = *meso*-tetra(α,α,α,α-*o*-pivalamidophenyl)porphyrin), prepared from $[Mn^{III}Br(T_{piv}PP)]$

and KO_2 in a THF:DMF mixed solvent (Figure 6.2).[8] This Mn^{IV}-oxo complex displays an intense low-field signal ($g \approx 4$) with hyperfine splitting at $g \approx 2$ in its EPR spectrum, which is remarkably similar to the EPR spectrum from the new intermediate. Based on these examples, the intermediate A possesses a mononuclear Mn^{IV} center but it is different from $[Mn^{IV}(O)(^{DMM}N4py)]^{2+}$ (Figure 6.1).

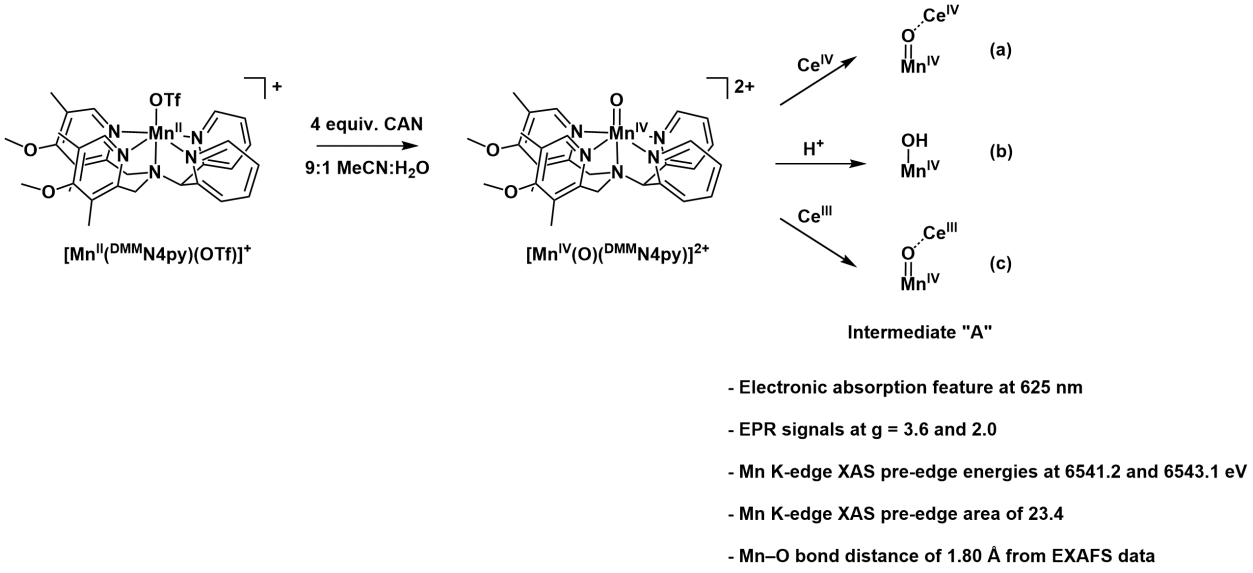

Figure 6.1. Reaction scheme of $[Mn^{II}(OTf)(^{DMM}N4py)](OTf)$ and 4 equiv. CAN in 9:1 (v/v) MeCN:H_2O and possible core structures for the final product, intermediate A. Spectroscopic features of the intermediate A are briefly described.

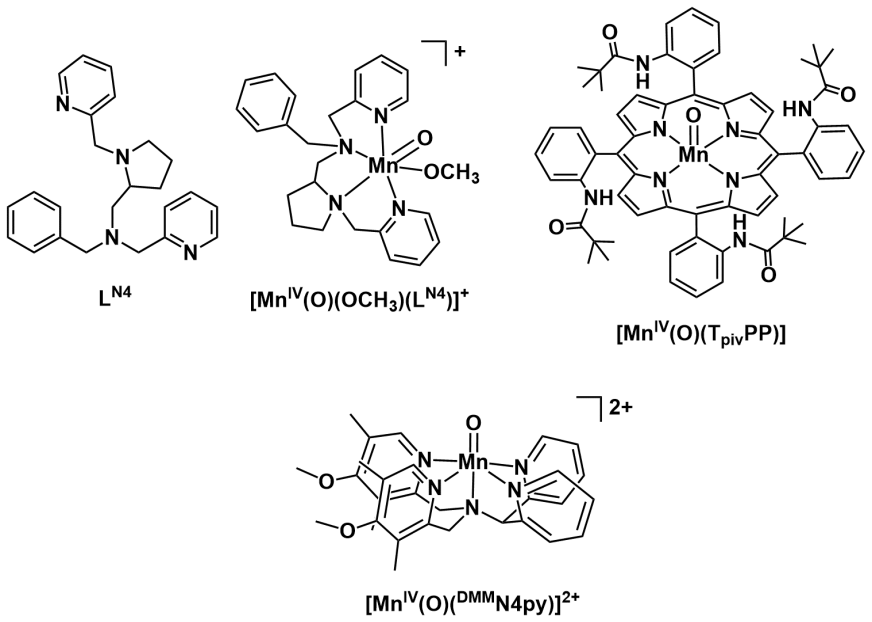

Figure 6.2. Chemical structures of L^{N4} ligand, $[Mn^{IV}(O)(OCH_3)(L^{N4})]^{+}$, $[Mn^{IV}(O)(T_{piv}PP)]$, and $[Mn^{IV}(O)(^{DMM}N4py)]^{2+}$.

The geometry of the intermediate A can be explored by theoretical methods. Time-dependent DFT (TD-DFT) calculations have been utilized to analyze transitions in electronic absorption and pre-edge spectra for 3d metal complexes.[5, 9-12] A series of manganese species, for example, have been studied computationally to reproduce and identify manganese K-pre-edge features.[13] As an example, preliminary pre-edge calculations for $[Mn^{IV}(OH)_2(^{DMM}N4py)]^{2+}$ were performed, which predicts a much smaller pre-edge area (9.5) than the experimental value (23.4; Figure 6.3). Furthermore, electronic structures of manganese complexes in different coordinating environments offer profound insight into the pre-edge features of manganese model complexes. Therefore, it is informative to theoretically investigate electronic absorption and pre-edge spectra of the intermediate A by using a set of possible Mn^{IV} complexes (Figure 6.1).

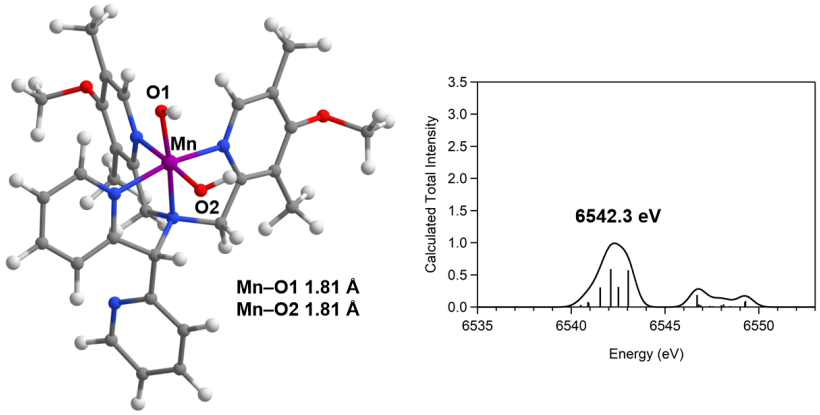

Figure 6.3. DFT-optimized structure of $[Mn^{IV}(OH)_2(^{DMM}N4py)]^{2+}$ and a TD-DFT-calculated pre-edge region of $[Mn^{IV}(OH)_2(^{DMM}N4py)]^{2+}$.

Several experiments can provide additional information to characterize the intermediate A. EPR characterization on the manganese species formed by reacting $[Mn^{IV}(O)(^{DMM}N4py)]^{2+}$ and 2 equiv. CAN (Chapter 3) to confirm whether the same intermediate is generated with the one from $[Mn^{II}(OTf)(^{DMM}N4py)](OTf)$ and 4 equiv. CAN in 9:1 (v/v) MeCN:H_2O (Figure 6.4). Additionally, examining the effects of acid present in the solution of $[Mn^{IV}(O)(^{DMM}N4py)]^{2+}$, considering 2 equiv. NH_4^+ in 1 equiv. CAN, can give further information to assign the identity of the intermediate A. The effects of acid can be investigated spectroscopically by recording electronic absorption and EPR spectra of $[Mn^{IV}(O)(^{DMM}N4py)]^{2+}$ treated with an acid (e.g., NH_4NO). Similarly, the effects of a Lewis acid, $Ce^{III}(NO_3)_3$, on $[Mn^{IV}(O)(^{DMM}N4py)]^{2+}$ have been inspected using electronic absorption spectroscopy. When 1.5 equiv. PhIO in 19:1 (v/v) MeCN:TFE is added to a 1 mM solution of $[Mn^{II}(OTf)(^{DMM}N4py)](OTf)$ in 19:1 (v/v) MeCN:H_2O, a 52% formation of $[Mn^{IV}(O)(^{DMM}N4py)]^{2+}$ is observed. The electronic absorption spectrum of a new intermediate generated by adding 2 equiv. $Ce^{III}(NO_3)_3$, to $[Mn^{IV}(O)(^{DMM}N4py)]^{2+}$ shows a feature at 630 nm, which resembles the electronic absorption feature of the intermediate A (625 nm; Figure 6.4). It

may be useful to examine a reaction in which both $Ce^{III}(NO_3)_3$ and NH_4NO_3 are added to $[Mn^{IV}(O)(^{DMM}N4py)]^{2+}$, since the reaction of $[Mn^{II}(OTf)(^{DMM}N4py)](OTf)$ with 4 equiv. CAN occurs in an acidic solution. Lastly, it will be informative to study a possible equilibrium state between the Mn^{IV}-oxo complex and a Ce^{III} ion as the Que group reported for two Fe^{IV}-oxo complexes (Chapter 3), by changing the amounts of H_2O and NO_3^- in the solution.[14] Additionally, collecting ESI-MS data for the intermediate prepared at a cryogenic temperature might be helpful to find potential manganese species for the intermediate A.

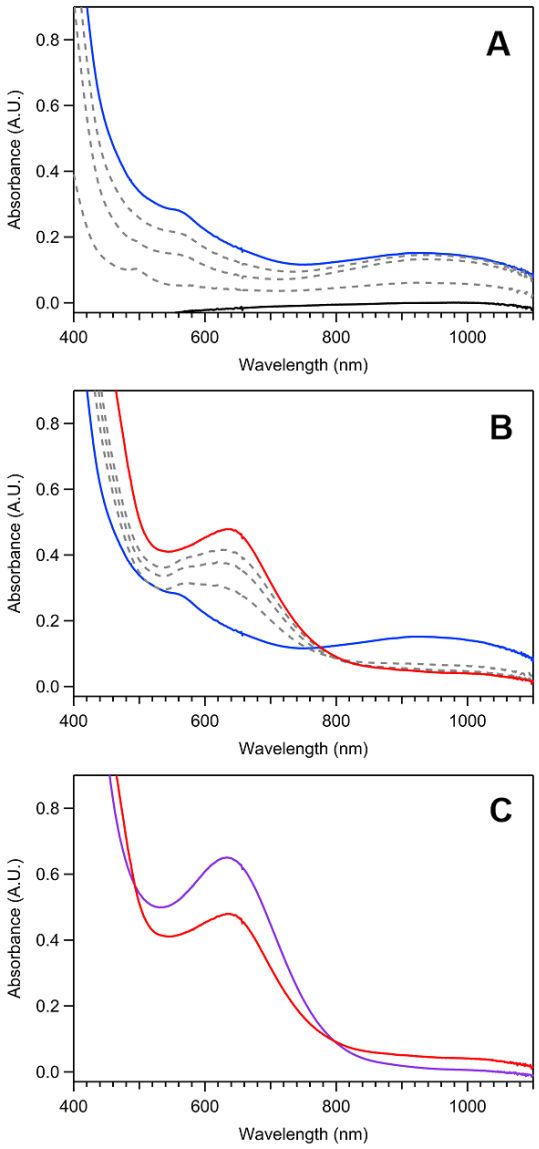

Figure 6.4. (A) Formation of $[Mn^{IV}(O)(^{DMM}N4py)]^{2+}$ in 19:1 (v/v) MeCN:H_2O (blue) from the reaction of 1.5 equiv. PhIO in 19:1 (v/v) MeCN:TFE and a 1 mM solution of $[Mn^{II}(OTf)(^{DMM}N4py)](OTf)$ in 19:1 (v/v) MeCN:H_2O (black) at 3 °C. Dashed gray traces show the corresponding transitions. (B) Electronic absorption spectra of $[Mn^{IV}(O)(^{DMM}N4py)]^{2+}$ (blue) and after adding 2 equiv. $Ce^{III}(NO_3)_3{\cdot}6H_2O$ at 3 °C (red). (C) Comparison of electronic absorption spectra of the intermediate from the reaction of $[Mn^{IV}(O)(^{DMM}N4py)]^{2+}$ and 2 equiv. $Ce^{III}(NO_3)_3{\cdot}6H_2O$ (red) and the intermediate A from the reaction of 1 mM $[Mn^{II}(OTf)(^{DMM}N4py)](OTf)$ with 4 equiv. CAN in 19:1 (v/v) MeCN:H_2O (purple) at 3 °C.

6.3 Equatorial Ligand Field Effects on Reactivity of High-valent Manganese Intermediates

From the experimental data shown in Chapter 4, the new Mn^{IV}-oxo complex, $[Mn^{IV}(O)(N3pyQ)]^{2+}$, shows an average equatorial ligand field strength and rates of C–H bond oxidation between those of $[Mn^{IV}(O)(2pyN2Q)]^{2+}$ and $[Mn^{IV}(O)(N4py)]^{2+}$. These results clearly indicate that the equatorial ligand field strength in a pentadentate system is modulated by different functional groups on the ligand, which further influences C–H bond activation reactivity of the Mn^{IV}-oxo core. Further investigations of the equatorial ligand field effects on the reactivity will be beneficial to prepare Mn^{IV}-oxo complexes that can activate unreactive C–H bonds with high BDEs. One of the interesting subjects related to the equatorial ligand field effects on the reactivity of Mn^{IV}-oxo core is the correlation between steric effects and equatorial ligand field effects of Mn^{IV}-oxo complexes. Specifically, there is a lack of information about how equatorial ligand field strength changes depending on the location of steric hindrance on a neutral pentadentate N5 ligand.

Sastri, de Visser, and co-workers investigated steric effects of the secondary coordination sphere on the reactivity of the Fe^{IV}-oxo complexes bearing neutral pentadentate N5 ligands.[15] They inspected these effects where the equatorial ligand field effects are designed to be nearly identical between two different ligands, ^{Me}N4py and N4py^{Me} (Figure 6.5). The only difference is the positions of two methyl groups on pyridines of each ligand. XRD structures of the Fe^{II} complexes show that the averaged $Fe–N_{equatorial}$ bond distances of the two complexes differ only by 0.02 Å, suggesting that the equatorial ligand field strengths of the complexes are marginally different. However, the reaction rates of $[Fe^{IV}(O)(N4py^{Me})]^{2+}$ are higher than those of $[Fe^{IV}(O)(^{Me}N4py)]^{2+}$; e.g., 20 and 400 times faster rates were observed for hydrogen and oxygen atom transfer reactions (with ethylbenzene and dibenzothiophene, respectively). The authors proposed that the deviation in the reaction rates of the complexes can be caused by steric effects from the secondary

coordination sphere based on their computational studies. The transition state calculations of $[Fe^{IV}(O)(^{Me}N4py)]^{2+}$ with a substrate show that the average bond distance of Fe–$N_{a,b}$ and Fe–$N_{c,d}$ are 2.130 and 2.216 Å, respectively, in the transition state structure of $[Fe^{IV}(O)(^{Me}N4py)]^{2+}$ for ethylbenzene oxidation. In contrast, only a marginal difference is shown between the corresponding bond distances (2.202 and 2.185 Å, respectively) in the transition state structure of $[Fe^{IV}(O)(N4py^{Me})]^{2+}$ in the same oxidation reaction.

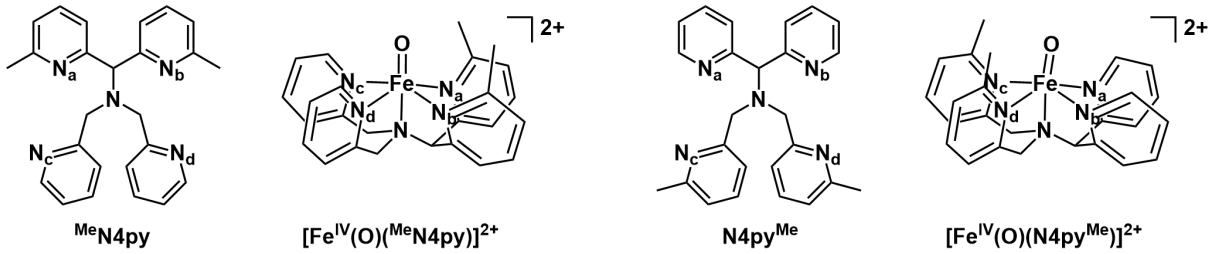

Figure 6.5. Structures of $^{Me}N4py$, $[Fe^{IV}(O)(^{Me}N4py)]^{2+}$, $N4py^{Me}$, and $[Fe^{IV}(O)(N4py^{Me})]^{2+}$.

As described above, steric effects at different locations on a ligand may change the reactivities of Fe^{IV}-oxo species; however, this correlation between steric effects and equatorial ligand field effects has not been studied for the reactivity of Mn^{IV}-oxo species. In general, the oxidation reactivities of Fe^{IV}-oxo and Mn^{IV}-oxo complexes have shown comparable trends; e.g., a weak equatorial ligand field strength enhances oxidation reactivities.[3, 16-19] On the contrary, in some cases Fe^{IV}-oxo and Mn^{IV}-oxo complexes possess opposite reactivities with the identical ligand scaffold.[6] Additionally, several pentadentate N5 ligands were developed to study the oxidation reactivities of Mn^{IV}-oxo complexes, but often functional groups are attached to the two 2-methylpyridine groups on the ligands due to the relative ease of ligand synthesis.[3, 19] Due to these

reasons, it will be beneficial to investigate and compare the reactivities of Mn^{IV}-oxo complexes with two different ligands which have the same functional groups on the two 2-methylpyridine or the two counter pyridine groups. As in the case of the Fe^{IV}- oxo complexes introduced above, reactivity studies with these two Mn^{IV}-oxo complexes will provide critical information with respect to designing Mn^{IV}-oxo complexes with strong oxidation reactivities.

6.4 Mechanism of C–H Bond Activation by a High-valent Co Complex

The first-row transition metals with a high number of d-electrons have been of interest to many researchers developing catalysts as the transition metals show properties different from those first-row transition metals with a low number of d-electrons. However, there are a paucity of reactivity studies using the transition metals with metal-centered high oxidation states, holding back progress in this area. In the investigations of $[Co^{IV}(ONO_2)_2(NNN)]$ (Chapter 5), the complex exhibits a unique EPR spectrum that supports its high oxidation state on the metal center. This feature provides an excellent platform to study the oxidative reactivity of high-valent Co species, and DFT-based computational studies show minor differences in activation parameters from possible transition states. Further theoretical studies described below need to be conducted to elucidate the mechanism of C–H bond activation process by $[Co^{IV}(ONO_2)_2(NNN)]$.

Preliminary CASSCF/NEVPT2 calculations using an active space of 15 electrons in 11 orbitals for selected transition states show different multireference characters among the transition states (Figure 6.6). All calculations converge to an $S = 1/2$ ground state. The lowest NEVPT2 total energy for the ground state is found with axial-O1′ among the three transition states. The total

energy of axial-O1′ is lower than those of the axial-O1 and axial-O3′ by 3.3 and 13.0 kcal mol^{-1}, respectively. For transition states axial-O1 and axial-O1′, three electron configurations correspond to approximately 30% each for the ground state. Specifically, three electrons are found over the C–H···O σ-antibonding, Co d_z^2, and Co d_{yz} MOs (Figure 6.7). The three configurations that contribute to the ground state differ in the occupancy of the C–H···O σ-antibonding and Co d_z^2 MOs. The configurations are $(\sigma^*)^2(d_z^2)^0$, $(\sigma^*)^0(d_z^2)^2$, and $(\sigma^*)^1(d_z^2)^1$. This pattern thus reveals a distribution of two electrons (one alpha, one beta) over two MOs. In these two transition states, the coordinating oxygen of NO_3^- also serves as the proton acceptor at the axial position (O1; chapter 5). Although the axial nitrate ligand is dissociated in axial-O1′, the proton acceptor O1 is still in relatively close proximity to the Co center (Co···O1 = 2.69 Å). Only one transition state (axial-O3′) from the preliminary CASSCF/NEVPT2 calculations shows a dominant single reference ground state (87%). In this transition state, a non-coordinating oxygen from NO_3^- serves as the proton acceptor (O3), and this oxygen atom has no interaction with the Co center (Co···O3 = 4.57 Å). Therefore, the significant multireference characters for axial-O1 and axial-O1′ can be attributed to the proximity of the proton-accepting oxygen atom to the Co center in the transition state. Furthermore, remarkably small differences in energy are found between the ground and first excited states (S = 1/2 and 3/2, respectively; 0 – 300 cm^{-1}). In each case, the triplet state has a dominant $(\sigma^*)^1(d_z^2)^1(d_{yz})^1$ state, which is related to the S = 1/2 state by a spin flip of an electron from the σ^*/d_z^2 MOs. For transition state axial-O3′, the triplet and singlet states are degenerate. Other transition states, axial-O1 and axial-O1′, also have energies between the ground and the first

excited states of 85 – 300 cm^{-1} (Figure 6.6). Additionally, in transition state axial-O1, the C–H···O σ-antibonding and d_z^2 MOs show strong interactions, while these MOs have no mixing in the other transition states. This difference can be attributed to the transition state structure of axial-O1, where the axial nitrate ligand remains bound to the Co center. If the axial nitrate ligand is dissociated from the Co center, the transition state does not show mixing between the C–H···O σ-antibonding and d_z^2 MOs. These differences among the transition states might imply the significance of the position of proton-accepting oxygen atom on the nitrate ligand. Further analysis of the CASSCF/NEVPT2 results and comparisons of spin density and activation parameters for each transition state will give more insight on the oxidation reactivity of $[Co^{IV}(ONO_2)_2(NNN)]$.

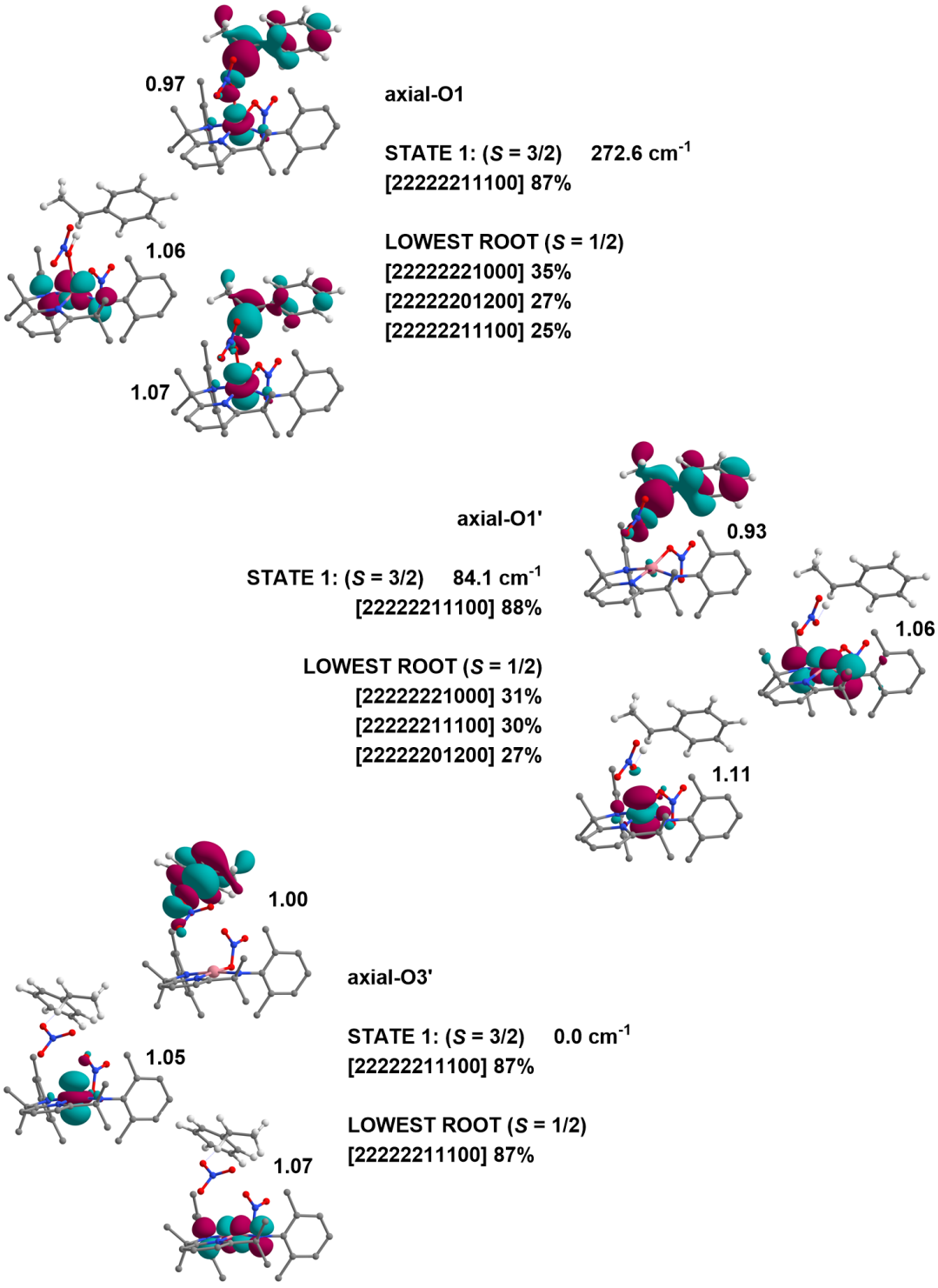

Figure 6.6. State-specific CASSCF/NEVPT2 results of three transition states for the ethylbenzene oxidation reaction. Electron configurations of the first excited and ground states are shown for each transition state. Surface contour plots show MOs that contain an unpaired electron in the ground state with their occupation number.

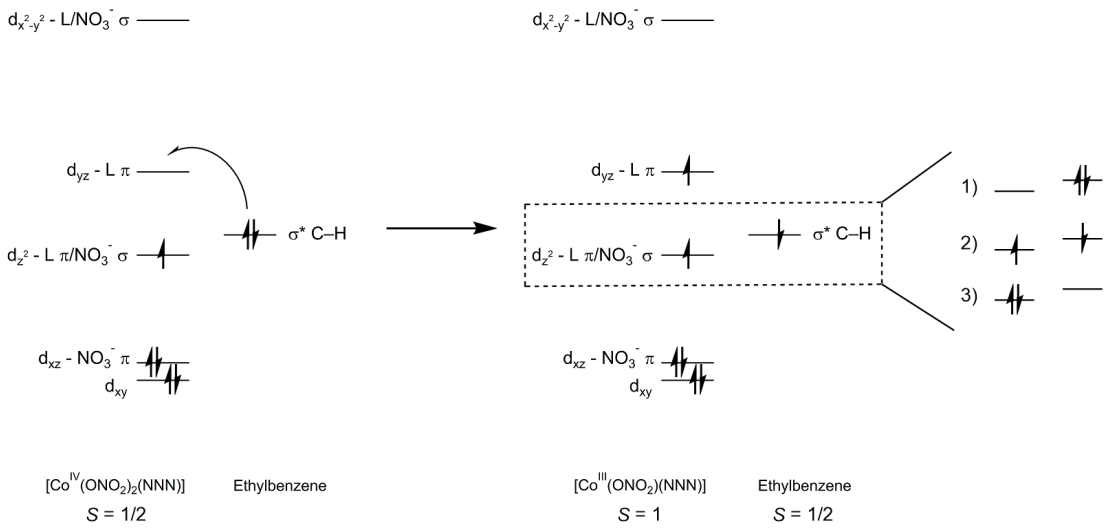

Figure 6.7. Schematic MO diagrams of the reactant complex (left) and transition state (right) for the transition states axial-O1 and axial-O1′. Multireference character is shown by three different electron configurations with the d_z^2 and σ* C–H MOs.

Additionally, it could be informative to investigate the C–H bond activation mechanism of [$Co^{IV}(ONO_2)_2$(NNN)] from the perspective of a stepwise process. Additional experimental data using a broader range of BDEs indicate a linear correlation between the rates of C–H bond activation and the pK_a of substrates, instead of the rates and the BDE values of substrates. Therefore, computational studies on the stepwise process using possible reactant and product complexes will be useful to interpret the C–H bond activation mechanism of the high-valent Co complex. This information could further help to better understand the C–H bond activation of the first-row late transition metals, given that a few number of studies have been done in this area.

6.5 Final Comments

Earth-abundant transition metals have been getting more attention lately as our society is seeking for environmentally sustainable and benign ways to use limited resources in industry. In organic transformations, earth-abundant transition metals are full of potential to be used as catalysts with high selectivity as they do in metalloenzymes in nature. However, more investigations are needed to utilize earth-abundant transition metals for specific reactions with high selectivity due to their characteristic chemical properties including variable oxidation states and distinctive electronic structures. In this dissertation I describe the observed properties and reactivities of several high-valent manganese complexes and a cobalt complex and provide insight and further ways to better understand their structure-reactivity correlations. This information can help pave the way to develop transition metal catalysts for organic transformation reactions and contribute to a sustainable society.

6.6 Notes and References

1. Cox, N.; Pantazis, D. A.; Neese, F.; Lubitz, W., Biological Water Oxidation. *Accounts of Chemical Research* **2013,** *46* (7), 1588-1596.

2. Wu, X.; Seo, M. S.; Davis, K. M.; Lee, Y.-M.; Chen, J.; Cho, K.-B.; Pushkar, Y. N.; Nam, W., A Highly Reactive Mononuclear Non-Heme Manganese(IV)–Oxo Complex That Can Activate the Strong C–H Bonds of Alkanes. *Journal of the American Chemical Society* **2011,** *133* (50), 20088-20091.

3. Massie, A. A.; Denler, M. C.; Cardoso, L. T.; Walker, A. N.; Hossain, M. K.; Day, V. W.; Nordlander, E.; Jackson, T. A., Equatorial Ligand Perturbations Influence the Reactivity of Manganese(IV)-Oxo Complexes. *Angewandte Chemie International Edition* **2017,** *56* (15), 4178-4182.

4. Pecoraro, V. L., Manganese redox enzymes. New York, N.Y. : VCH: New York, N.Y., 1992.

5. Massie, A. A.; Denler, M. C.; Singh, R.; Sinha, A.; Nordlander, E.; Jackson, T. A., Structural Characterization of a Series of N5-Ligated Mn^{IV}-Oxo Species. *Chem-Eur J* **2020,** *26* (4), 900-912.

6. Denler, M. C.; Massie, A. A.; Singh, R.; Stewart-Jones, E.; Sinha, A.; Day, V. W.; Nordlander, E.; Jackson, T. A., Mn^{IV}-Oxo complex of a bis(benzimidazolyl)-containing N5 ligand reveals different reactivity trends for Mn^{IV}-oxo than Fe^{IV}-oxo species. *Dalton Transactions* **2019,** *48* (15), 5007-5021.

7. Du, J.; Miao, C.; Xia, C.; Lee, Y.-M.; Nam, W.; Sun, W., Mechanistic Insights into the Enantioselective Epoxidation of Olefins by Bioinspired Manganese Complexes: Role of Carboxylic Acid and Nature of Active Oxidant. *ACS Catalysis* **2018,** *8* (5), 4528-4538.

8. Charnock, J. M.; Garner, C. D.; Trautwein, A. X.; Bill, E.; Winkler, H.; Ayougou, K.; Mandon, D.; Weiss, R., Characterization of an Oxo(porphyrinato)manganese(IV) Complex by X-ray Absorption Spectroscopy. *Angewandte Chemie International Edition in English* **1995,** *34* (3), 343-346.

9. Colmer, H. E.; Howcroft, A. W.; Jackson, T. A., Formation, Characterization, and O-O Bond Activation of a Peroxomanganese(III) Complex Supported by a Cross-Clamped Cyclam Ligand. *Inorganic Chemistry* **2016,** *55* (5), 2055-2069.

10. Leto, D. F.; Jackson, T. A., Mn K-Edge X-ray Absorption Studies of Oxo- and Hydroxo-manganese(IV) Complexes: Experimental and Theoretical Insights into Pre-Edge Properties. *Inorganic Chemistry* **2014,** *53* (12), 6179-6194.

11. Rice, D. B.; Wijeratne, G. B.; Jackson, T. A., Mn K-edge X-ray absorption studies of mononuclear Mn(III)–hydroxo complexes. *JBIC Journal of Biological Inorganic Chemistry* **2017,** *22* (8), 1281-1293.

12. Leto, D. F.; Massie, A. A.; Rice, D. B.; Jackson, T. A., Spectroscopic and Computational Investigations of a Mononuclear Manganese(IV)-Oxo Complex Reveal Electronic Structure Contributions to Reactivity. *Journal of the American Chemical Society* **2016,** *138* (47), 15413-15424.

13. Roemelt, M.; Beckwith, M. A.; Duboc, C.; Collomb, M.-N.; Neese, F.; DeBeer, S., Manganese K-Edge X-Ray Absorption Spectroscopy as a Probe of the Metal–Ligand Interactions in Coordination Compounds. *Inorganic Chemistry* **2012,** *51* (1), 680-687.

14. Draksharapu, A.; Rasheed, W.; Klein, J. E. M. N.; Que Jr, L., Facile and Reversible Formation of Iron(III)–Oxo–Cerium(IV) Adducts from Nonheme Oxoiron(IV) Complexes and Cerium(III). *Angewandte Chemie International Edition* **2017,** *56* (31), 9091-9095.

15. Mukherjee, G.; Alili, A.; Barman, P.; Kumar, D.; Sastri, C. V.; de Visser, S. P., Interplay Between Steric and Electronic Effects: A Joint Spectroscopy and Computational Study of Nonheme Iron(IV)-Oxo Complexes. *Chemistry – A European Journal* **2019,** *25* (19), 5086-5098.

16. Sastri, C. V.; Sook Seo, M.; Joo Park, M.; Mook Kim, K.; Nam, W., Formation, stability, and reactivity of a mononuclear nonheme oxoiron(iv) complex in aqueous solution. *Chemical Communications* **2005,** (11), 1405-1407.

17. Leto, D. F.; Ingram, R.; Day, V. W.; Jackson, T. A., Spectroscopic properties and reactivity of a mononuclear oxomanganese(iv) complex. *Chemical Communications* **2013,** *49* (47), 5378-5380.

18. Massie, A. A.; Sinha, A.; Parham, J. D.; Nordlander, E.; Jackson, T. A., Relationship between Hydrogen-Atom Transfer Driving Force and Reaction Rates for an Oxomanganese(IV) Adduct. *Inorganic Chemistry* **2018,** *57* (14), 8253-8263.

19. Rasheed, W.; Draksharapu, A.; Banerjee, S.; Young Jr, V. G.; Fan, R.; Guo, Y.; Ozerov, M.; Nehrkorn, J.; Krzystek, J.; Telser, J.; Que Jr, L., Crystallographic Evidence for a Sterically Induced Ferryl Tilt in a Non-Heme Oxoiron(IV) Complex that Makes it a Better Oxidant. *Angewandte Chemie International Edition* **2018,** *57* (30), 9387-9391.

Appendix A2

A2.1 Supporting tables

Table A2.1. Cartesian coordinates for DFT-optimized structure of **1**

	x	y	z
Mn	4.74811234593949	-0.24489653296645	0.75201628046105
Mn	7.14488786603876	0.65705446404843	-0.10615424827234
O	5.69802476592918	0.54534955647761	1.47230860963387
O	6.23806754024326	-0.15327938757126	-0.80690256463998
N	2.94557086657214	1.60128687938632	0.70945355060675
N	3.68669791697456	0.82333541478247	-1.87384499916901
N	5.07677761706487	2.90162858170284	-0.41830082335392
N	3.31605303985366	-1.04243755285765	0.30574579328178
C	1.96672903240201	1.82612350281751	-0.41889609691425
H	1.01785093614240	1.30169226660179	-0.16669358912776
H	1.68730213386735	2.89921904634850	-0.45399987601479
C	2.46136637290133	1.39594761046522	-1.77948922689309
C	1.66112829335416	1.56922404980334	-2.92344039678541
H	0.66741083960654	2.03264110787212	-2.83062130033447
C	2.13875731584459	1.14413288203278	-4.16987376762292
H	1.52356373548853	1.27295426796788	-5.07326428540782
C	3.41123339198681	0.55015479303407	-4.24825355850575
H	3.82180829724770	0.20159855578090	-5.20664436890120
C	4.15365941240657	0.40828338383196	-3.07458987173160
H	5.15486154484199	-0.04615500654332	-3.06211150241434
C	3.38925952936814	2.88983336629541	1.31322591043301
H	2.52616807610505	3.49688993824075	1.65826594695158
H	4.00017357168641	2.64237992846968	2.20685034769749
C	4.23459294622738	3.65872023895172	0.32249988246340
C	4.17017819312960	5.05325571045903	0.17303575460931
H	3.47278986872329	5.64497322886073	0.78505354727396
C	4.99854122023058	5.67362796574516	-0.77665819747843
H	4.96110457820513	6.76426433184906	-0.91998893682430
C	5.85825246899386	4.87795295716922	-1.55145571828723
H	6.50889530923131	5.32185483056769	-2.31894990008845
C	5.86307965451764	3.49268727503668	-1.33806593283791
H	6.51039393861458	2.82355834280220	-1.92527220691175
C	2.41106343421285	0.65699919518002	1.77497979270425
H	3.23105700881112	0.60550548885988	2.52290634388656
C	1.15933287001570	1.15314419784181	2.49464017145013
N	0.02276276669936	1.19628942376014	1.76732011254271
C	1.20662220844134	1.54083979481099	3.84659580968550
H	2.14779007255882	1.48701131090902	4.41608913060708
C	0.02377289099601	1.98743345185255	4.46258739802538
H	0.02382836071938	2.28952189276884	5.52089590049830
C	-1.15406488719086	2.03631327282488	3.70413256695086
H	-2.10322607770817	2.37547155376643	4.14471309163123
C	-1.10212816673600	1.63278091221626	2.35719101859034
H	-2.00749894773193	1.65323663425736	1.72810902295287
C	2.29903703046613	-0.72769779342639	1.14267391387683
C	1.26700657749258	-1.64058606798021	1.41161826525707
H	0.45104101327702	-1.36734921183848	2.09305103959162
C	1.28483118488337	-2.89459884144703	0.77882767274462
H	0.47895240565746	-3.62031889921758	0.96660532493188

C	2.33077212211872	-3.19943384326861	-0.10648644207290
H	2.36933800324549	-4.16205391917553	-0.63681813420935
C	3.33040949713173	-2.23976084523370	-0.31105537870481
H	4.17268069197998	-2.42237342767999	-0.99570090674735
N	8.85468752146290	-1.16787730554773	-0.06054863462230
N	6.66384580936605	-2.20338327540068	1.08947884048474
N	8.28798772992453	1.39177800436126	0.36798355880493
C	9.89168377114983	-1.40365648157868	1.01198137068392
H	10.82350036976206	-0.86786795695724	0.71497780475369
H	10.16775620780115	-2.47764139161025	1.02671469078657
C	9.44590122527742	-0.97285592255879	2.38826009140783
N	8.22839637909349	-0.39297116600493	2.49709516955601
C	10.26632403991457	-1.14449717630081	3.51692266220363
H	11.25480450990956	-1.61614947116963	3.41087167822669
C	9.81063715503451	-0.70482462202276	4.76716940339421
H	10.43895683663021	-0.83017922121672	5.66200047227538
C	8.54361283984463	-0.10053917081993	4.86089380975073
H	8.15192029193613	0.25970531302082	5.82294323363737
C	7.78064150290992	0.03705857943753	3.69947579638767
H	6.78225333942692	0.49791496132031	3.69685056646833
C	8.34028525399260	-2.44979513538736	-0.63131162269095
H	7.75921279768754	-2.19795005268005	-1.54230789952461
H	9.16453598265505	-3.12975324206127	-0.92928387570459
C	7.41585062861778	-3.08687271375244	0.37644043664936
C	7.29497787104081	-4.46771175410873	0.58087514979849
H	7.91584531573397	-5.16572445345611	-0.00012478570788
C	6.38416083267785	-4.94001303609119	1.54150028578451
H	6.28122983360308	-6.02041163088366	1.72461363041301
C	5.62364742673631	-4.01405235862129	2.27279360467474
H	4.90969076778133	-4.34171198962911	3.04203140414345
C	5.79372326193751	-2.64773925002111	2.01854539577482
H	5.23420445167485	-1.87446546315258	2.56196119490747
C	9.31988707587064	-0.19703318419358	-1.14378765618108
H	8.48790486879719	-0.20488940439960	-1.87891944179111
N	11.74567696166061	-0.50025515805693	-1.15511161830604
C	10.60025892270437	-0.60237151676104	-1.86320949586240
C	10.56977904347115	-1.05715663645784	-3.19437789699842
H	9.62061142217125	-1.11796219956777	-3.74962164151853
C	11.78183575747383	-1.41849276187559	-3.81004298410633
H	11.79617916673151	-1.77060148781129	-4.85266584504539
C	12.96951357205735	-1.31550317151069	-3.07255469657913
H	13.94070328616762	-1.58248386780121	-3.51489406572849
C	12.89947334835401	-0.85291090009777	-1.74519071878359
H	13.81158393713283	-0.75483343843769	-1.13356768627939
C	9.31631093019940	1.18143041547709	-0.50168514438133
C	10.23692726008406	2.20067086776263	-0.77663468418094
H	11.06474564834986	2.01414051127454	-1.47319289658850
C	10.10069803602503	3.44250436343881	-0.13330808230404
H	10.82405899689432	4.24849860951565	-0.32915350644982
C	9.04441818540480	3.63338059739801	0.77060118020082
H	8.91118813181825	4.58497444439564	1.30489451647119
C	8.15275334163992	2.57848711865023	0.99480908851848
H	7.30467247433036	2.66071190470846	1.68751787408847

Table A2.2. Cartesian coordinates for DFT-optimized structure of **2**

	x	y	z
Mn	2.43730015782682	2.34474927158971	5.44814903301329
Mn	4.27565015954234	0.45619561308709	4.88317622120335
O	4.19343149956327	1.94980917693712	5.87831978973993
O	2.55406950121213	0.81514576915559	4.44185794067332
N	2.28194312079564	4.13722733112088	6.67285836806415
N	0.47315762334842	2.80031644962667	5.04141061174017
N	2.90720760356834	4.04959150874219	4.04351930952812
N	1.54816775079138	1.63203671197857	7.43297581656185
C	0.90600207728020	4.73553734959304	6.49506808829236
H	0.47678563597425	4.91788751834148	7.50327016830095
H	1.01745163410159	5.74099841884284	6.04012553867144
C	-0.03446916017790	3.90997482752012	5.64168444175462
C	-1.37441192675267	4.28660643620171	5.46570348804019
C	-2.21041867123882	3.47990203944529	4.62659401328321
C	-1.66845620269396	2.32719280174296	3.97925371706890
C	-0.32034071384106	2.05410071437996	4.24917917494570
H	0.16613411719787	1.17975541021630	3.79044879000306
C	3.34557288400964	5.06139662821003	6.17815532217712
H	3.28451725242658	6.04050734844535	6.69254989106021
H	4.32161062807084	4.60527498390847	6.44522538115217
C	3.23705534130231	5.20564083462319	4.67345854229849
C	3.44343885935282	6.40566614559439	3.97586607554029
C	3.25327023146751	6.39765367313284	2.55128356752329
C	2.88881979267836	5.18866947336085	1.88777757542939
C	2.73960690592806	4.05984216370043	2.71396332536726
H	2.45977313074146	3.09662267972077	2.25756511849602
C	2.56656825809693	3.71493558163810	8.10375305364873
H	3.59783870566117	3.30425289244786	8.05479995892761
C	2.57287433443493	4.85111690271595	9.12358985944327
N	1.38792388586540	5.43906238995617	9.39521118031394
C	3.77083137843129	5.25175048582503	9.74564462554754
H	4.72164316710467	4.74814101002195	9.51055856907990
C	3.73162701637505	6.29924603863975	10.68228809513761
H	4.65004138864629	6.62938758237524	11.19105408121548
C	2.50089303077951	6.91133187156755	10.95743486742192
H	2.42067221201511	7.73254147897339	11.68484627796115
C	1.35744472582201	6.44566462672081	10.28397469925856
H	0.36982701122287	6.89755855847800	10.47530786887761
C	1.65117551176258	2.53911530029399	8.43111771566265
C	0.99947813132968	2.35129022360355	9.66030067649941
H	1.09245098440183	3.10068721202477	10.45673468067742
C	0.21463634136769	1.20071877471877	9.84357447670709
H	-0.31314901146758	1.03744450106881	10.79543326153076
C	0.10413471001070	0.27368708454989	8.79574336737309
H	-0.50984163044231	-0.63297674527637	8.89665408504994
C	0.79313920250411	0.53256930065018	7.60321469732896
H	0.74375990113039	-0.15507873217074	6.74512059786853
N	4.41199633269107	-1.28207551026832	3.72372393613265
N	3.80658349910528	-0.93259562776164	6.28383075717085
N	5.01855664308517	1.24852308154014	3.15474405216508
C	5.78875392039372	-1.89387056289060	3.83261789947512
H	6.19679602962091	-1.99268948965349	2.80222470624430

H	5.68829670927195	-2.93214171148829	4.20924879437831
C	6.73374769951473	-1.11235109710650	4.72235388389386
N	6.22584303337734	-0.00117026807205	5.29875580725300
C	8.07267052183674	-1.52752163027547	4.91002008213773
C	8.86990351024363	-0.74373388932934	5.79746730990284
C	8.34018907333828	0.46044179121603	6.36284205260408
C	7.01404852541224	0.77304962312846	6.07966600022251
H	6.53368648129809	1.67058288895945	6.49622056537382
C	3.35595856852516	-2.18125807607377	4.28356599205507
H	2.37533914512221	-1.77242858810349	3.96411205686346
H	3.45320633838283	-3.20448055016615	3.87102419829101
C	3.44681003732456	-2.14897960696036	5.79551711627206
C	3.15810245758137	-3.24806911534725	6.63178817600726
C	3.35951112219665	-3.05780964207714	8.03453837021270
C	3.71998568822593	-1.77094371034724	8.54011250181080
C	3.92746300707950	-0.74871701609566	7.61470765114693
H	4.21982783636914	0.26057221400964	7.93412086670619
C	4.07336215133833	-0.81084603581568	2.31353154392321
H	3.02254516044937	-0.46332719810589	2.40340884359808
N	5.35027015849903	-2.33090808884556	0.87315235308299
C	4.12707562499500	-1.88729347811352	1.23603118289362
C	2.94295901184085	-2.38121882657606	0.65646925789933
H	1.96031637115788	-1.99022837973856	0.96344543655639
C	3.03773140159098	-3.37240650362970	-0.33620772159799
H	2.13145600976695	-3.77339032860054	-0.81490823952605
C	4.30800039267339	-3.83342797898639	-0.70862997850043
H	4.43158320591365	-4.60334048619154	-1.48452631177126
C	5.43449240281155	-3.28169335056076	-0.07186368090448
H	6.45094043213535	-3.61435976491013	-0.34056268766897
C	4.90652850983709	0.43742083800735	2.06715011776878
C	5.48184576702657	0.79949010325881	0.84252528246069
H	5.39301252281198	0.12882525139114	-0.02180681309349
C	6.18818954178654	2.01069049637602	0.74862062348618
H	6.65887084509833	2.30295128151061	-0.20217988188296
C	6.29730099353676	2.82905442826674	1.88260334704962
H	6.85026876936127	3.77872951604723	1.85451337336880
C	5.69475273542622	2.41046736170410	3.07496388478118
H	5.74552905472574	3.00072268979121	3.99959913139654
C	3.84474913549685	7.70433264462906	4.62713996178209
H	3.10872512921760	8.50317207192536	4.40406446862198
H	3.95686995191528	7.62592344180296	5.72273097296624
H	4.80842166372990	8.06628703515464	4.21385206768744
C	2.67339967482011	5.00647991355082	0.39983665854313
H	3.56827987909531	5.27281784660330	-0.19549816458794
H	2.44153528992436	3.94562079117340	0.18394243897016
H	1.82741577757509	5.60468900150343	0.01068447456996
O	3.47724910477059	7.60892787900655	2.00494676888231
C	3.13380118920089	7.99669889871983	0.65442398060771
H	3.77033104223271	7.48552697030395	-0.09042917121421
H	2.06156243282321	7.81922058157042	0.44944563268203
H	3.33502945577252	9.08213252374178	0.61603855257272
O	-3.46234507458143	3.96657872564817	4.53947557594125
C	-4.59413716346161	3.27686947865659	3.96038428003588
H	-4.49915605169202	3.19083093586389	2.86272276428271
H	-4.73700530965869	2.28401857579998	4.42625769085678

H	-5.46222011821806	3.91714344659995	4.19820997441378
C	-1.97404311244758	5.50726865946436	6.11552842696351
H	-2.88781808141164	5.23941996438070	6.68313575633076
H	-1.27774641230282	6.01699058560304	6.80396645023232
H	-2.30196851716818	6.23939907762390	5.34879976895116
C	-2.39361933827063	1.41557966446962	3.01177485704585
H	-1.69730876097133	0.64380469511558	2.63078741860992
H	-3.24721700195094	0.88282792512759	3.47264408510310
H	-2.78008744701704	1.96447074150529	2.13094457346063
O	10.14846487256509	-0.97603663041743	6.15015809372300
C	10.75249243251830	-2.29139807126838	6.23289673325916
H	10.00632467216927	-3.05756663203211	6.51409571038478
H	11.25501582027179	-2.55944922947929	5.28494090940215
H	11.51360648851807	-2.20871735761607	7.03034274025577
C	8.60738381393867	-2.71137203323388	4.13203199976303
H	9.66915208173587	-2.57339527519589	3.86335599083824
H	8.52580605227688	-3.66832984847201	4.68894240572683
H	8.06055166119933	-2.84490254091899	3.17986155263875
C	9.19282784209069	1.33105922765968	7.24301819864226
H	8.63169847334441	2.21459671172929	7.60107352033103
H	9.56499539189636	0.76641791079406	8.12210717650667
H	10.09544165470815	1.68085369519124	6.70171732285612
C	3.88884063864778	-1.54873768456123	10.01711113585321
H	2.95231580357488	-1.77552289266710	10.56603344559709
H	4.65794380895148	-2.23008489668185	10.43482662429919
H	4.18483642449692	-0.50610865122365	10.23767240699701
C	2.57874378226333	-4.52397604934656	6.05528896183806
H	3.32922893756275	-5.33121941247653	5.93171807219207
H	1.77783084578415	-4.91826622530146	6.70808845047252
H	2.11449224373111	-4.35145633118360	5.06724424767343
O	3.18707738695444	-3.98526652612785	8.99658560544762
C	3.45233614805379	-5.40051142288427	8.81543220473367
H	2.55293173229960	-5.93875427796772	8.46422307750888
H	4.30068674690865	-5.55750851187410	8.12282091000357
H	3.72470460980872	-5.77204509414488	9.82002320864513

Table A2.3. EXAFS fitting parameters for **1**.[a]

fit	Mn···Mn			Mn–O			Mn–N1			Mn–N2			Mn···C			R - factor
	n	*r*(Å)	σ^2	*n*	*r*(Å)	σ^2	*n*	*r*(Å)	σ^2	*n*	*r*(Å)	σ^2	*n*	*r*(Å)	σ^2	
1	1	2.64	2.54	2	1.83	4.99	4	2.18	13.8							0.272
2	1	2.63	2.43	2	1.82	4.53	3	2.14	11.9				7	2.91	8.54	0.145
3	**1**	**2.63**	**2.42**	**2**	**1.82**	**4.78**	**2**	**2.12**	**7.92**				**7**	**2.91**	**8.32**	**0.153**
4	1	2.63	2.51	2	1.82	4.79	2	2.12	7.80				6	2.91	7.22	0.159
5	1	2.63	2.61	2	1.82	4.81	2	2.12	7.66				5	2.91	6.09	0.169

[a] Fourier transform range: k = 2 – 14 Å^{-1}. Debye-Waller factors are reported in units of 10^{-3} Å^2.

Table A2.4. EXAFS fitting parameters for **2**.[a]

fit	Mn···Mn			Mn–O			Mn–N1			Mn–N2			Mn···C			R - factor
	n	*r*(Å)	σ^2	*n*	*r*(Å)	σ^2	*n*	*r*(Å)	σ^2	*n*	*r*(Å)	σ^2	*n*	*r*(Å)	σ^2	
1	1	2.66	2.91	2	1.89	10.6	4	2.26	11.4							0.230
2	1	2.65	3.19	2	1.85	8.35	3	2.19	9.66	1	4.59	26.1	5	2.92	4.20	0.119
3	1	2.65	2.95	2	1.84	8.17	3	2.19	9.86	1	-6.07	49.9	6	2.92	5.73	0.116
4	1	2.65	2.40	2	1.81	5.23	3	2.18	5.32	1	1.98	0.49	7	2.91	5.71	0.108
5	1	2.66	3.48	2	1.82	6.00	2	2.23	2.39	2	2.06	5.51	5	2.93	2.75	0.105
6	**1**	**2.65**	**2.96**	**2**	**1.82**	**6.03**	**2**	**2.22**	**2.52**	**2**	**2.05**	**6.06**	**6**	**2.92**	**4.21**	**0.107**
7	1	2.65	2.56	2	1.81	6.04	2	2.21	2.51	2	2.03	6.34	7	2.92	5.59	0.110

[a] Fourier transform range: k = 2 – 12.5 Å^{-1}. Debye-Waller factors are reported in units of 10^{-3} Å^2.

A2.2 Supporting figures

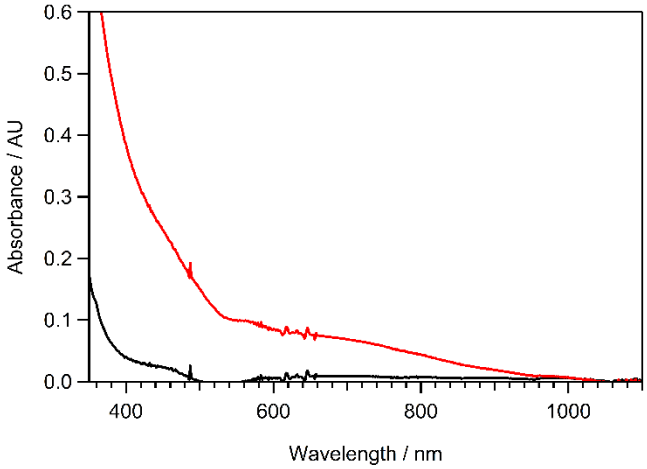

Figure A2.1. Electronic absorption spectra showing the reaction of $[Mn^{II}(OH_2)(2pyN2Q)](OTf)_2$ (black line) with 5 equiv. H_2O_2 and 0.5 equiv. Et_3N (red line) in H_2O at 3 °C.

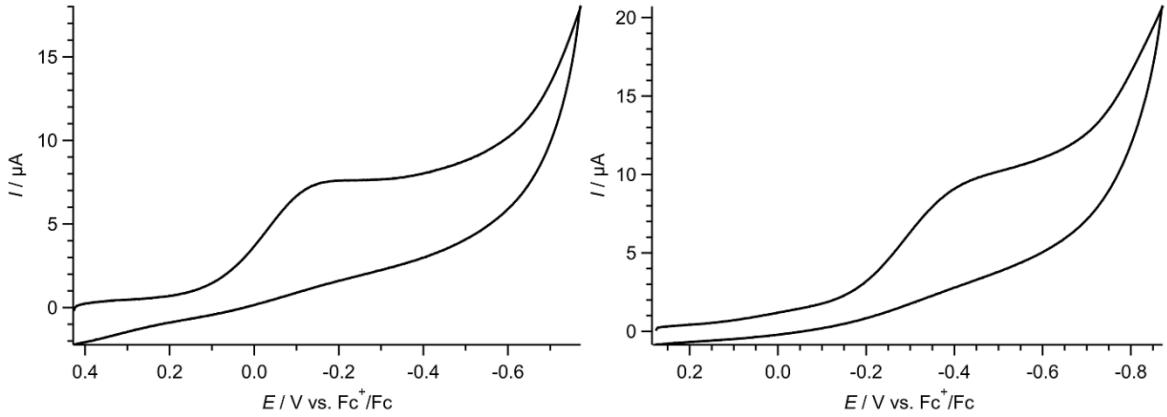

Figure A2.2. Cyclic voltammograms of **1** (left) and **2** (right) collected with a narrower scan window. These scans, where **1** and **2** were not subjected to oxidizing potentials, lack the minor features seen in Figure 2.7.

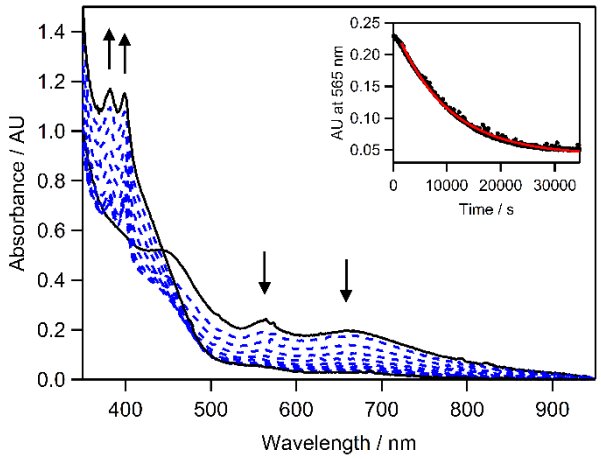

Figure A2.3. Representative electronic absorption spectra showing the reaction of **1** with 50 equiv. 2,4,6-tri-*tert*-butylphenol at 25 °C. Inset: the decay profile showing the change in absorbance at 565 nm versus time (black solid circles) and a fit to a pseudo-first-order model (solid red trace).

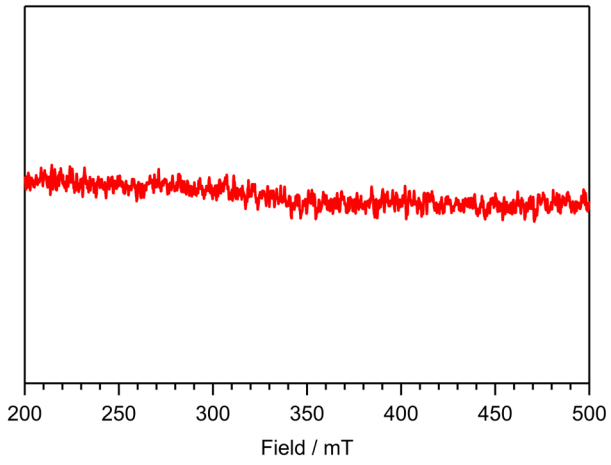

Figure A2.4. Representative EPR spectrum from complete reaction solution of **1** with 50 equiv. 2,4-di-*tert*-butylphenol at 25 °C. Experimental conditions are the same as in Figure 2.3 captions.

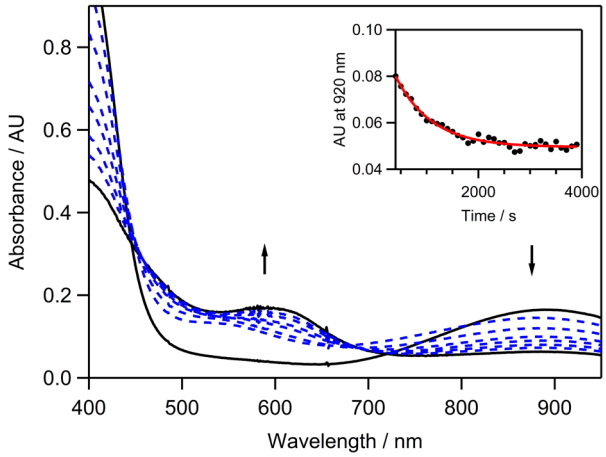

Figure A2.5. Electronic absorption spectral changes of 0.5 mM $[Mn^{IV}(O)(^{DMM}N4py)]^{2+}$ reacting with 10 equiv. 4-*tert*-butylphenol in CF_3CH_2OH at –40 °C. Inset: the decay profile showing the change in absorbance at 565 nm versus time (black solid circles) and a fit to a pseudo-first-order model (solid red trace).

Appendix A3

A3.1 Supporting figures

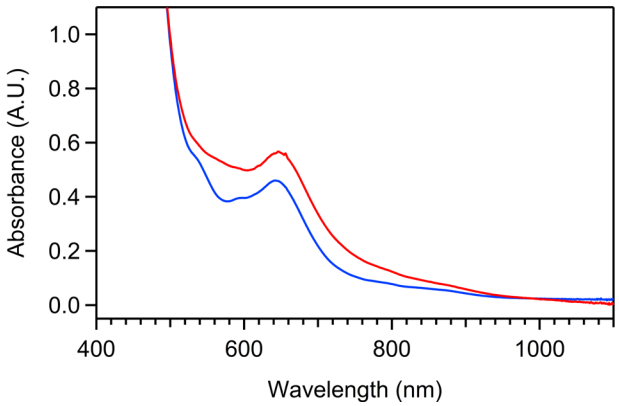

Figure A3.1. Direct comparison between two intermediates prepared from the reaction of $[Mn^{II}(OTf)(^{DMM}N4py)](OTf)$ and 2 equiv. CAN at 0 °C (red) and $[Mn^{III}Mn^{IV}(\mu\text{–}O)_2(^{DMM}N4py)_2]^{3+}$ and 2 equiv. CAN at room temperature (blue).

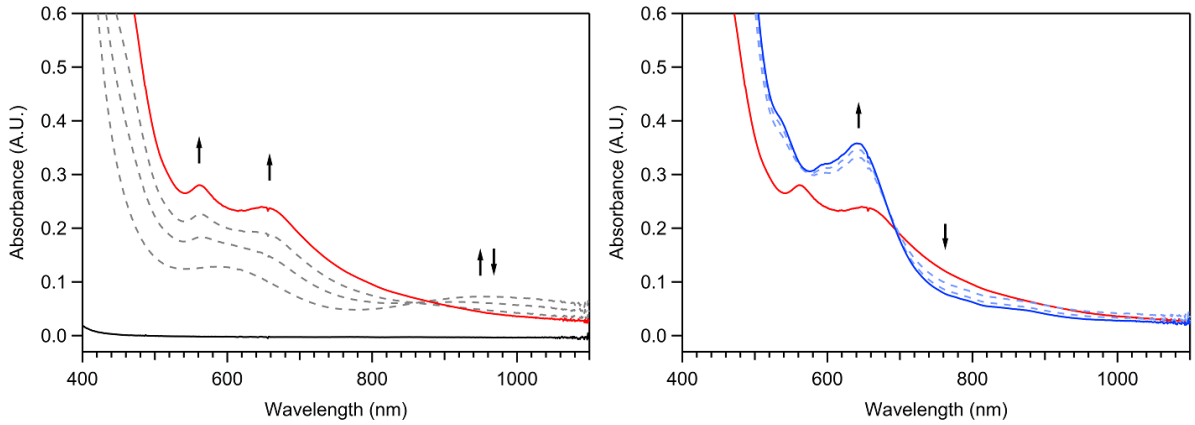

Figure A3.2. Electronic absorption spectra from the reaction of $[Mn^{II}(OTf)(^{DMM}N4py)](OTf)$ (black) and 2 equiv. CAN in 9:1 (v/v) MeCN:H_2O at room temperature (red; left). Spectral changes after additional 2 equiv. CAN was added to the intermediate in the red trace (blue; right).

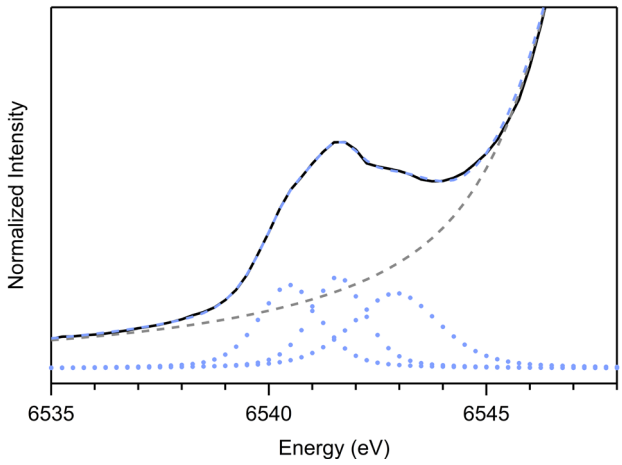

Figure A3.3. Experimental pre-edge region of $[Mn^{IV}Mn^{IV}(\mu\text{–}O)_2(^{DMM}N4py)_2]^{4+}$ (black). The fit functions (dotted light blue), the fit of the pre-edge peak (dashed light blue), and background (dashed gray) are shown.

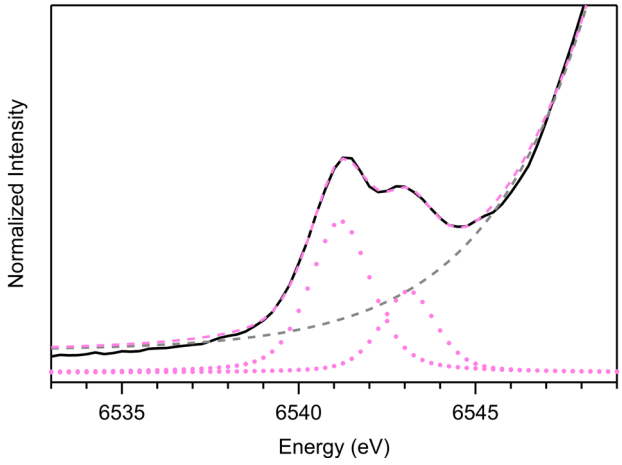

Figure A3.4. Experimental pre-edge region of the intermediate complex from the reaction of $[Mn^{II}(OTf)(^{DMM}N4py)](OTf)$ and 4 equiv. CAN (black). The fit functions (dotted pink), the fit of the pre-edge peak (dashed pink), and background (dashed gray) are shown.

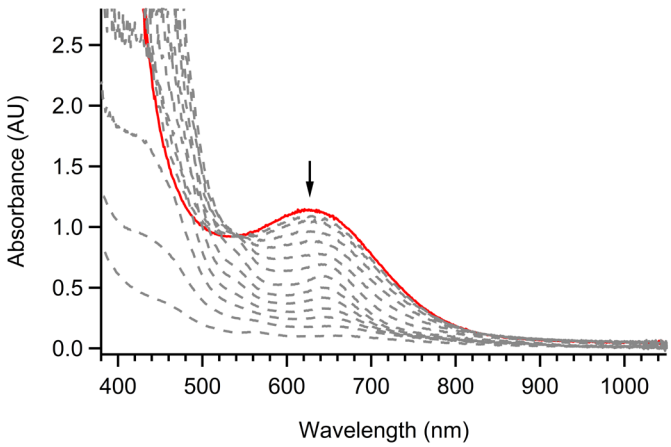

Figure A3.5. Electronic absorption spectra showing the intermediate (red) from the reaction of a 2 mM solution of [Mn^{II}(OTf)(^{DMM}N4py)](OTf) and 4 equiv. CAN in 9:1 (v/v) MeCN:H_2O at room temperature and the decay process of the intermediate (dashed gray).

Appendix A4

A4.1 Supporting figures

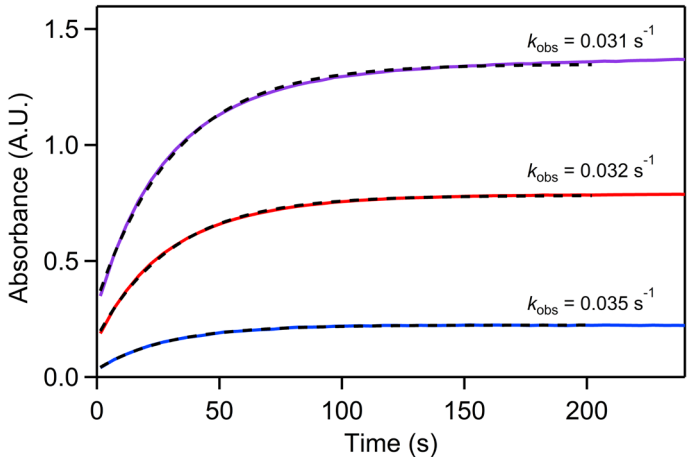

Figure A4.1. Time traces at 390 nm (purple), 467 nm (red), and 1050 nm (blue) with corresponding rates in absorbance increase for the formation reaction of $[Mn^{IV}(O)(N3pyQ)]^{2+}$ in TFE solution at 25 °C.

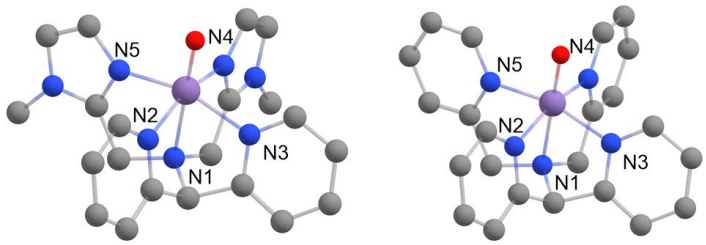

$[Mn^{IV}(O)(2pyN2I)]^{2+}$ $[Mn^{IV}(O)(N4py)]^{2+}$

	$[Mn^{IV}(O)(2pyN2I)]^{2+}$	$[Mn^{IV}(O)(N4py)]^{2+}$
Mn–N1 (Å)	2.36	2.12
Mn–N2 (Å)	2.13	2.02
Mn–N3 (Å)	2.04	2.02
Mn–N4 (Å)	1.97	2.00
Mn–N5 (Å)	1.97	2.00
avg. Mn–$N_{equatorial}$ (Å)	2.0021	2.0132
O-Mn-N1 (°)	177.6	179.2

Figure A4.2. DFT-optimized structures and selective metric parameters of $[Mn^{IV}(O)(2pyN2I)]^{2+}$ and $[Mn^{IV}(O)(N4py)]^{2+}$.[1] Hydrogens are omitted for clarity in the structures. Grey, blue, red, and purple atoms indicate carbon, nitrogen, oxygen, and manganese, respectively.

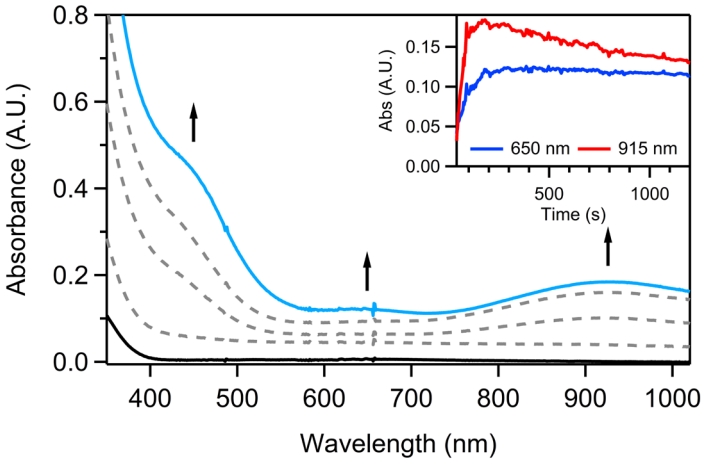

Figure A4.3. Formation of $[Mn^{IV}(O)(2pyN2I)]^{2+}$ (cerulean) from 1 mM $[Mn^{II}(2pyN2I)(OTf)]^{+}$ (black) and 10 equiv. PhIO in 1:1 TFE:CH_2Cl_2 solution at 25 °C. Time traces at 650 nm (blue) and 915 nm (red) are shown in the inset.

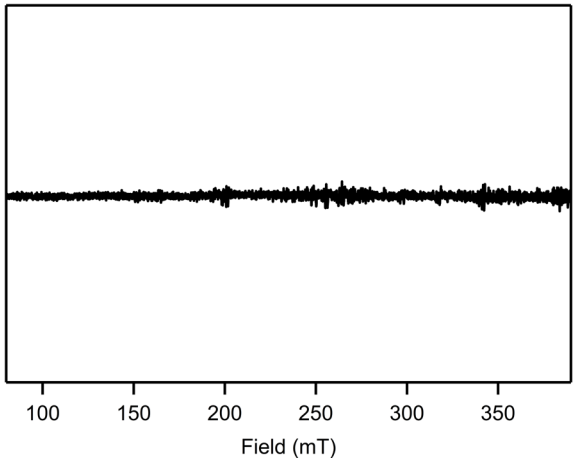

Figure A4.4. X-band EPR spectrum from 1 mM $[Mn^{II}(2pyN2I)(OTf)]^{+}$ and 10 equiv. PhIO in TFE where the 650 nm electronic absorption band at its maximum absorbance. Experimental conditions: 9.64 GHz microwave frequency, 4 G modulation amplitude, 100 kHz modulation frequency, 20 dB power attenuation, 40 dB receiver gain, 5.12 ms time constant, and 7.3 K temperature.

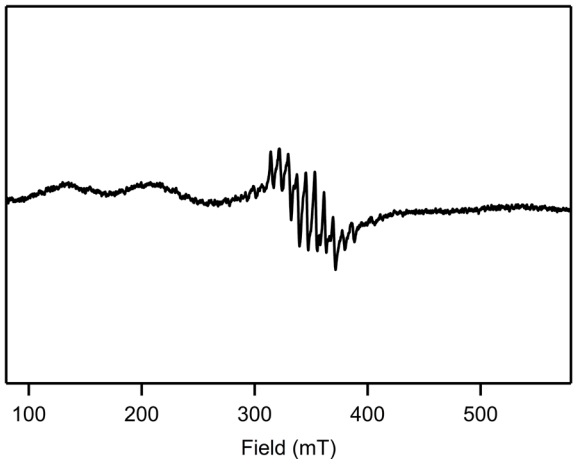

Figure A4.5. X-band EPR spectrum from 5 mM $[Mn^{II}(2pyN2I)(OTf)]^{+}$ and 10 equiv. PhIO in TFE. Experimental conditions: 9.64 GHz microwave frequency, 4 G modulation amplitude, 100 kHz modulation frequency, 14 dB power attenuation, 20 dB receiver gain, 40.96 ms time constant, and 13 K temperature.

A4.2 Notes and References

1. DFT-optimized structures are from unpublished calculations by Jaycee Mayfield.

Appendix A5

A5.1 Supporting figures

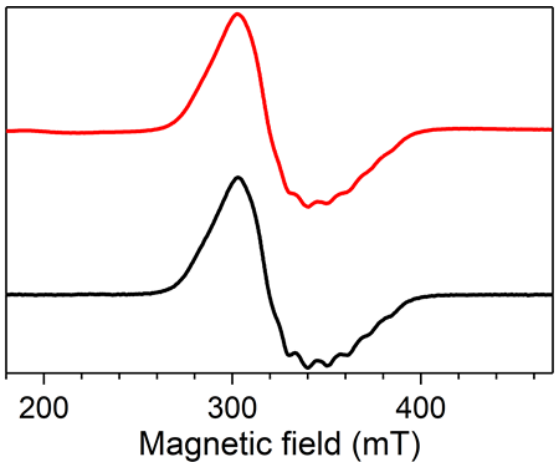

Figure A5.1. EPR spectra of [$Co^{IV}(ONO_2)_2(NNN)$] collected at 10 K (red) and 30 K (black). Experimental conditions are the same as those stated in the caption of Figure 5.3.

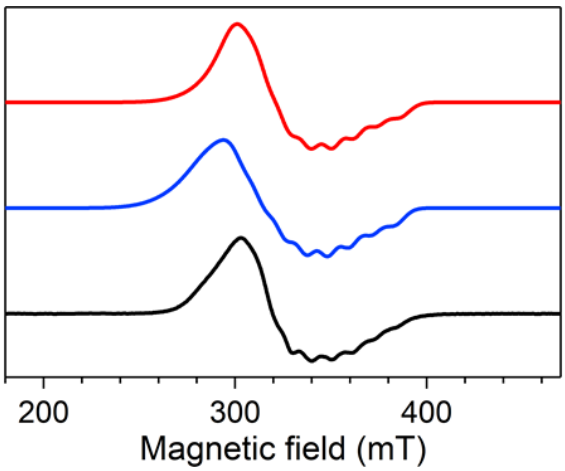

Figure A5.2. Experimental EPR spectrum of [$Co^{IV}(ONO_2)_2(NNN)$] (black) and spectra simulated with no constraints (red) and simulated using the *g* values from the CASSCF/NEVPT2 calculations (blue). Simulation parameters for the red simulation are as follows: g = [2.08, 2.00, 2.23]; S = 0.5; Nucs = '^{59}Co'; A = [129.7540, 320, 185]; gStrain = [0.0020, 0.0020, 0.0011]; AStrain = [110, 50, 305.3790]; HStrain = [653.2610, 270, 610]. Simulation parameters for the blue simulation are as follows: g = [2.07, 2.01, 2.39]; S = 0.5; Nucs = '^{59}Co'; A = [129.7540, 320, 185]; gStrain = [0.0020, 0.0020, 0.0011]; AStrain = [110, 50, 305.3790]; HStrain = [653.2610, 270, 610].

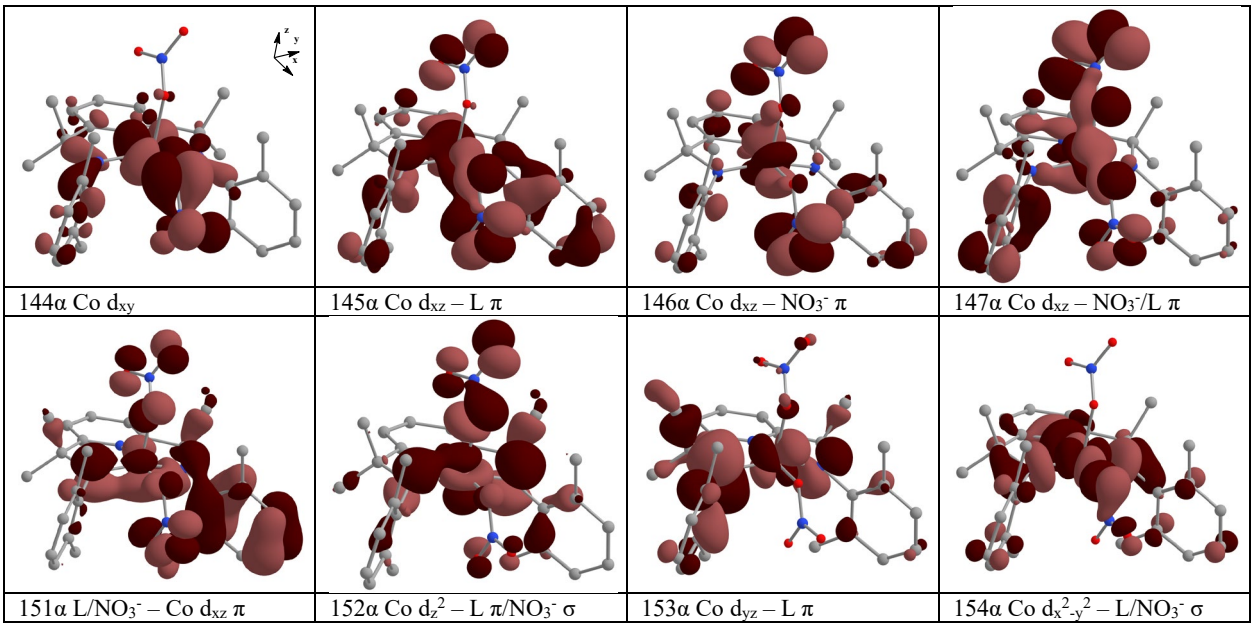

Figure A5.3. Surface contour plots of selected α-spin Kohn-Sham MOs of $[Co^{IV}(ONO_2)_2(NNN)]$ with corresponding orbital descriptions.

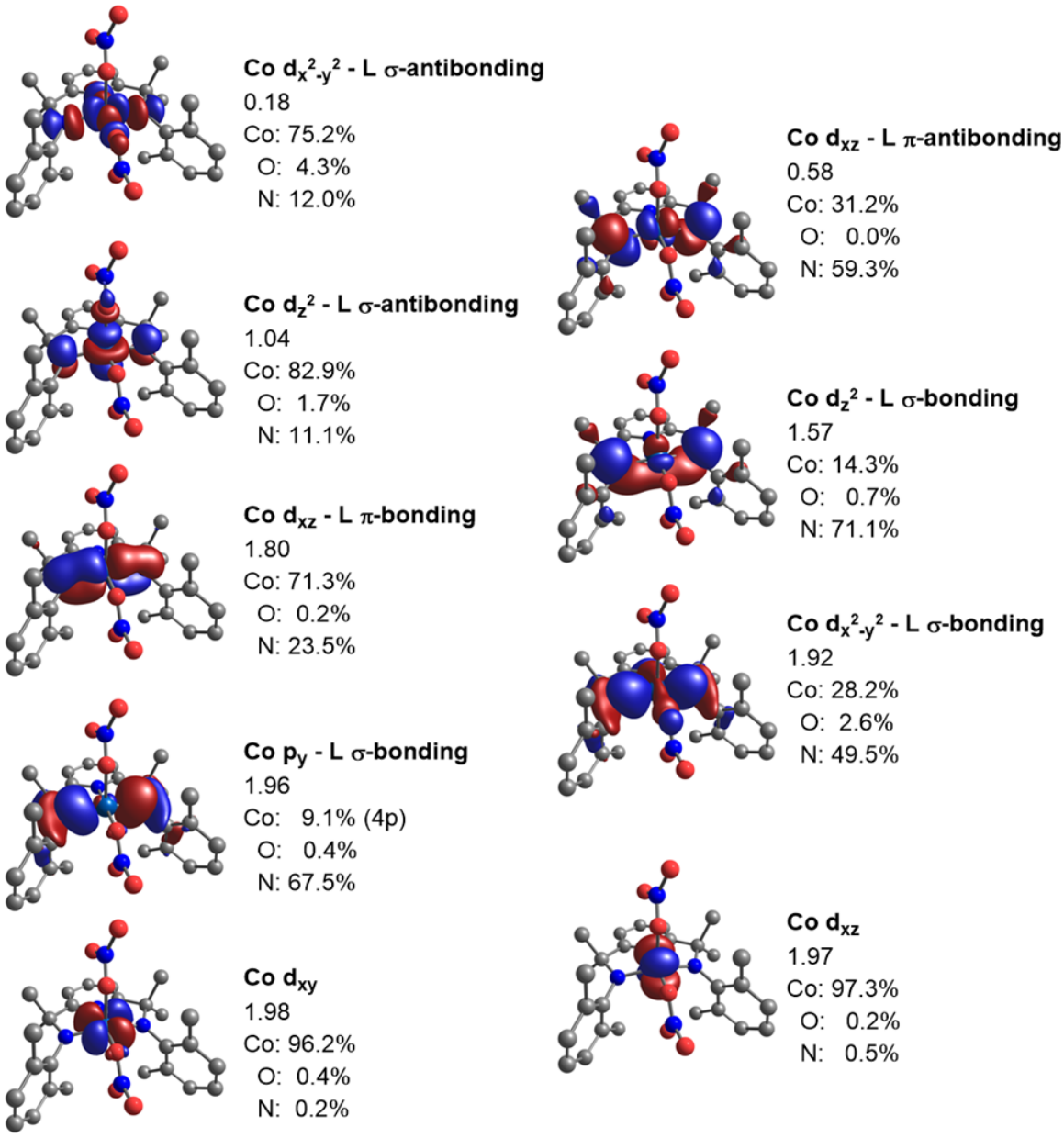

Figure A5.4. Surface contour plots of the CASSCF natural orbitals for the CAS(13,9) calculations. The occupation number and percent compositions are displayed adjacent to each natural orbital.

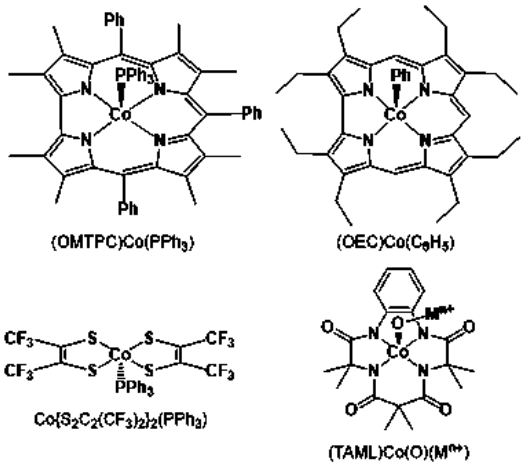

Figure A5.5. Chemical structures of square pyramidal Co^{IV} complexes. For (TAML)Co(O)(M^{n+}), M^{n+} = Sc^{3+}, Y^{3+}, Ce^{3+}, Zn^{2+}. See Table A5.2 for more information for these complexes.

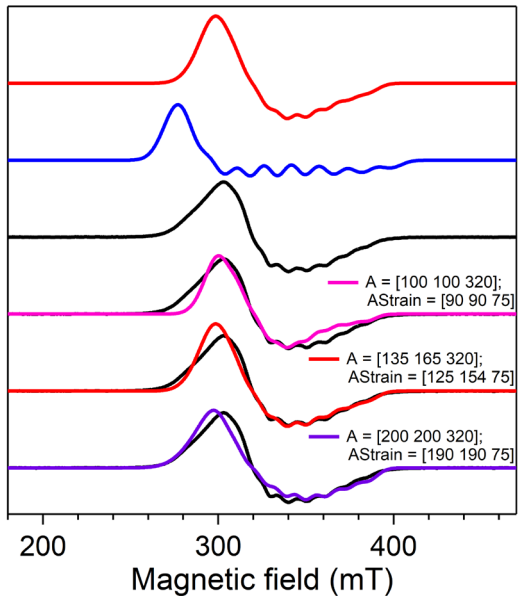

Figure A5.6. Experimental EPR spectrum of [$Co^{IV}(ONO_2)_2$(NNN)] (black) and spectra simulated with no constraints (red) and simulated using the *g* and *A* values from the CASSCF/NEVPT2 calculations (blue). Spectra simulated with varied *A* and Astrain values that show acceptable range of *A* values affecting the breadth of the EPR signal (pink, purple). Simulation parameters for the red simulation are as follows: *g* = [2.23, 2.08, 2.00]; S = 0.5; Nucs = '^{59}Co'; *A* = [135, 165, 320]; lw = [8]; gStrain = [0.0011, 0.002, 0.002]; AStrain = [125, 154, 75]; HStrain = [450, 453, 180]. Simulation parameters for the blue simulation are as follows: *g* = [2.391, 2.069, 2.013]; S = 0.5; Nucs = '^{59}Co'; *A* = [61, 326, 451]; lw = [8]; gStrain = [0.0011, 0.002, 0.002]; AStrain = [55, 154, 75]; HStrain = [450, 453, 180]. Simulation parameters for the rest of simulations are as follows: *g* = [2.23, 2.08, 2.00]; S = 0.5; Nucs = '^{59}Co'; lw = [4]; gStrain = [0.0011, 0.002, 0.002]; HStrain = [410, 453, 270] (*A* and AStrain are varied as noted in the inset).

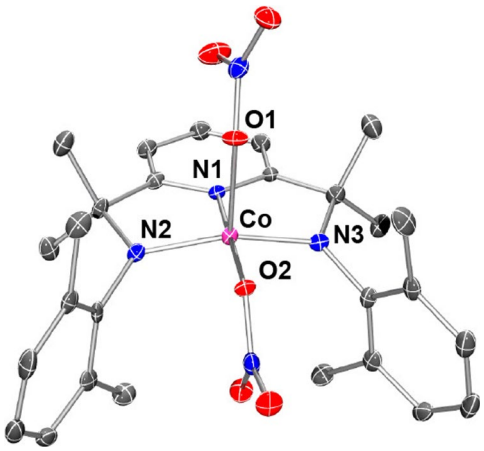

Figure A5.7. Crystal structure of [$Co^{IV}(ONO_2)_2(NNN)$] (selected bond lengths and angle: Co−N1, 1.863 Å; Co−N2, 1.831 Å; Co−N3, 1.834 Å; Co−O1, 2.100 Å; Co−O2, 1.927 Å; O1−Co−O2, 81.96°). Thermal ellipsoids are drawn at the 50% probability level. Hydrogen atoms (except the one on the hydroxyl group) are ignored for clarity.

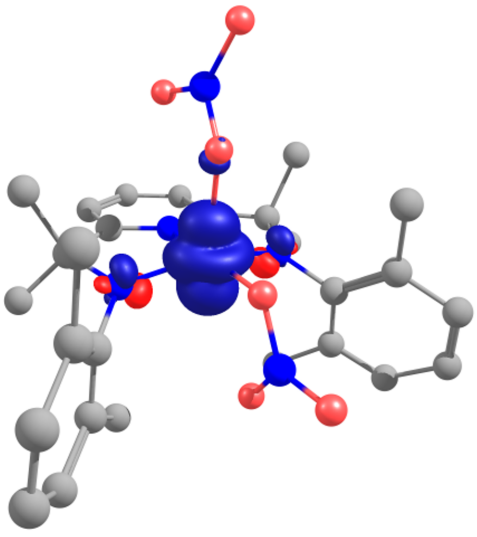

Spin Populations	
Co:	1.009
O_{axial}:	0.010
$O_{equatorial}$:	0.001
N_{am}:	-0.009, -0.0089
N_{py}:	0.000

Figure A5.8. Spin density isosurface plot of [$Co^{IV}(ONO_2)_2(NNN)$] and spin populations obtained from CASSCF computations. The blue and red colors represent positive and negative spin density, respectively. The contour value for this plot is 0.005.

A5.2 Supporting tables

Table A5.1. Molecular Orbital Energies, Descriptions, Occupations, and Compositions (%) for $[Co^{IV}(ONO_2)_2(NNN)]$.

Orbital	Energy (eV)	Orbital description	Occup.	Spin	Compositions			
					Co 3d	O_{ax} 2p	O_{eq} 2p	N 2p
144α	-6.4881	Co d_{xy}	1.0	↑	59.5	0.2	13.6	1.3
145α	-6.3964	Co d_{xz} – L/NO_3^- π	1.0	↑	22.9	0.2	6.1	7.6
146α	-6.3213	Co d_{xz} – NO_3^- π	1.0	↑	36.7	1.2	0.7	1.6
147α	-6.1115	Co d_{xz} – NO_3^-/L π	1.0	↑	20.5	6.6	4.9	2.6
151α	-5.7801	L/NO_3^- π – Co d_{xz}	1.0	↑	13.2	4.3	2.3	17.2
152α	-5.2926	Co d_z^2 – L π /NO_3^- σ	1.0	↑	31.0	14.6	1.2	25.9
153α	-4.4985	Co d_{yz} – L π	0.0	↑	29.0	0.5	0.1	46.2
154α	-3.0506	Co $d_{x^2-y^2}$ – L/NO_3^- σ	0.0	↑	53.1	0.0	6.1	16.3
145β	-6.1186	Co d_{xy}/d_{xz} – L π	1.0	↓	36.6	0.3	5.7	3.2
146β	-6.0641	Co d_{xz} – NO_3^-/L π	1.0	↓	36.9	5.8	1.1	3.3
149β	-5.9632	Co d_{xz}/d_{xy} – NO_3^- π	1.0	↓	20.0	3.2	1.0	2.5
150β	-5.8606	Co d_{xy} – L π	1.0	↓	33.9	0.5	3.6	4.9
151β	-5.6524	Co d_{xz}/d_{yz} – L π	1.0	↓	28.8	1.9	0.3	30.2
152β	-4.3059	Co d_{yz}/d_{xz} – L π	0.0	↓	40.8	0.9	0.1	35.9
153β	-3.7555	Co d_z^2 – L π/NO_3^- σ	0.0	↓	62.4	7.7	0.4	14.0
154β	-2.4833	Co $d_{x^2-y^2}$ – L/NO_3^- σ	0.0	↓	52.2	0.0	4.9	13.2

Table A5.2. *g*- and *A*-values for Square Pyramidal Co(IV) Complexes.[a,b]

Compound	g_1	g_2	g_3	A^c	Method[d]	Ref
(OMTPC)Co(PPh_3)	2.14	2.00	1.89	–	spectral analysis	1
(OEC)Co(C_6H_5)[e]	2.12	2.01	1.94	–	spectral analysis	2
	1.9670	2.1122	2.0043	72, 8, 10	simulation	3
Co{$S_2C_2(CF_3)_2$}$_2$(PPh_3)[f]	2.034	2.031	1.992	207	simulation	4
(TAML)Co(O)(M^{n+})[g]	2.57	2.16	2.03	156	simulation	5
[$Co^{IV}(ONO_2)_2$(NNN)]	2.23	2.08	2.00	320	simulation	This work

[a] See Figure A5.5 for the structure of each complex.

[b] Ligand abbreviations and formula are as follows: OMTPC = 5,10,15-triphenyl-2,3,7,8,12,13,17,18-octamethylcorrole; OEC = 2,3,7,8,12,13,17,18-octaethylcorrole; TAML = Tetraamidomacrocyclic ligand; $M^{n+} = Sc^{3+}$, Y^{3+}, Ce^{3+}, Zn^{2+}.

[c] *A* values are expressed in MHz, with 1×10^{-4} cm^{-1} = 3 MHz used for conversion.

[d] "Spectral analysis" means the *g* values were reported from analysis of the signal positions in the EPR spectrum; "Simulation" indicates that the *g*- and *A*-values were determined through a computer simulation of the EPR spectrum.

[e] *A* values are reported as $|A_1|$ = 72 MHz, $|A_2|$ = 8 MHz, and $|A_3|$ = 10 MHz.

[f] The *A* value for this complex is A_I.

[g] For this complex, the principal components of the *g*-matrix were assigned, with $g_1 = g_x$, $g_2 = g_y$, and $g_3 = g_z$, and $A = A_y$.

Table A5.3. Roots, Ground Configurations, and g-values from CASSCF NEVPT2 Calculations for $[Co^{IV}(ONO_2)_2(NNN)]$.[a]

CAS	State weighting	Roots	Ground Configuration	*g* values
(9,7)	State averaged	Sextet:1 Quartet: 15 Doublet: 10	42% [2221110] 13% [2222100]	1.990 2.051 2.165
(13,9)	State averaged	Sextet:1 Quartet: 15 Doublet: 10	36% [222221200] 22% [222221020] 17% [222222100]	1.985 2.098 2.322
(13,9)	State specific	Sextet:1 Quartet: 15 Doublet: 10	61% [222222100] 12% [222220120]	1.987 2.055 2.385
(13,9)	State averaged	Sextet:1 Quartet: 24 Doublet: 25	30% [222221200] 24% [222222100] 19% [222221020]	2.005 2.105 2.343
(13,9)	State specific	Sextet:1 Quartet: 24 Doublet: 25	61% [222222100] 12% [222220120]	2.013 2.069 2.391

[a] The positions of the hydrogen atoms were optimized using DFT computations.

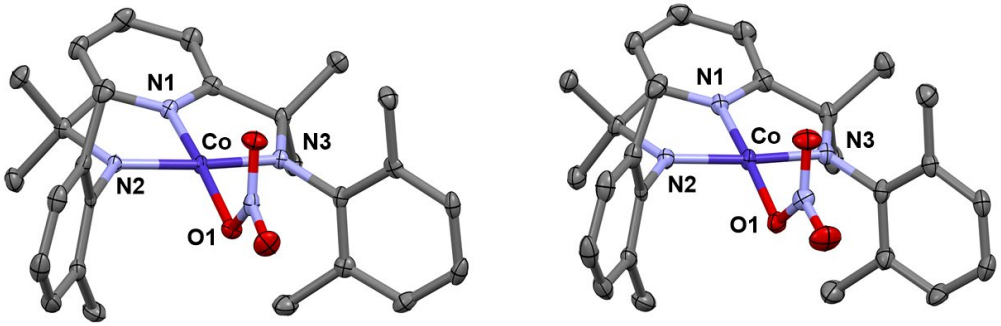

XRD1 XRD2

Table A5.4. Geometric parameters of two XRD structures of $[Co^{III}(ONO_2)(NNN)]$.

	XRD1	XRD2
Co–O1	1.925(2)	1.929(2)
Co–N1	1.821(2)	1.824(3)
Co–N2	1.790(2)	1.788(3)
Co–N3	1.783(2)	1.790(3)
∠N1–Co–O1	175.7(1)	176.1(1)
∠N2–Co–N3	170.2(1)	170.1(1)

Table A5.5. Pre-edge and edge energies (eV) of $[Co^{III}(OH)(NNN)]$, $[Co^{III}(ONO_2)(NNN)]$, and $[Co^{IV}(ONO_2)_2(NNN)]$.

	Pre-edge (1s → 3d)	Edge
$[Co^{III}(OH)(NNN)]$	7709.22 7710.20	7721.2
$[Co^{III}(ONO_2)(NNN)]$	7709.19 7710.20	7720.9
$[Co^{IV}(ONO_2)_2(NNN)]$	7709.77	7720.6

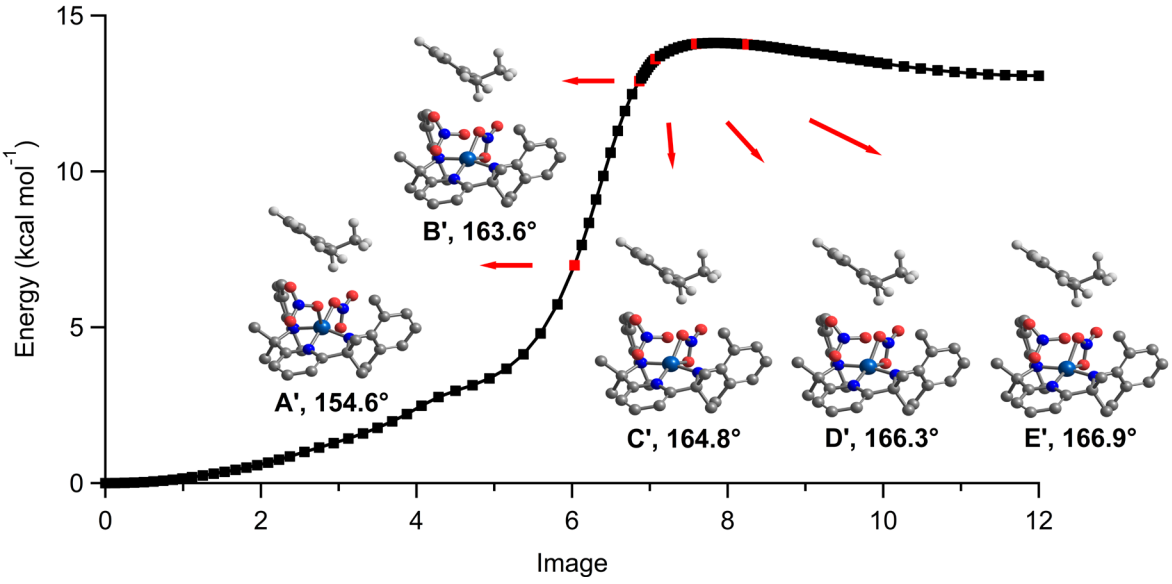

Table A5.6. Selected geometric parameters for structures found over the potential energy profile towards the intermediate species before axial-O3′ transition state.

	Co–O2	Co–O5	Co–N1	Co–N2	Co–N3	∠N1–Co–O2	∠N1–Co–O5	∠N2–Co–N3
A′	1.92	2.53	1.86	1.83	1.86	173.9	129.3	154.6
B′	1.97	2.22	1.87	1.84	1.82	160.0	138.7	163.6
C′	1.99	2.18	1.86	1.83	1.82	156.7	141.4	164.8
D′	2.03	2.10	1.86	1.82	1.82	150.8	146.7	166.3
E′	2.06	2.06	1.86	1.82	1.81	146.8	150.6	166.9

Table A5.7. Cartesian coordinates for a structure of [Co^{III}(OH)(NNN)] where the positions of the hydrogen atoms have been optimized by DFT computations.

Co	-0.00117642806157	-0.00162409615856	-0.00278949860345
O	-1.79339380058969	-0.00142132824919	-0.00427398003911
N	1.85162040205424	-0.02459525649757	-0.18482838535994
N	0.23022296612922	1.81940460683724	0.12604667986121
N	0.16838182803243	-1.82696601836047	-0.00364783728948
C	2.51682682395020	1.14799382894109	-0.14803372263148
C	3.90063131460410	1.14077022584758	-0.26009745064659
C	4.56153331924249	-0.06621730879007	-0.41381450517929
C	3.84331093286932	-1.25521155802552	-0.46862206701026
C	2.45951568872553	-1.21601838557340	-0.32471382467976
C	1.62056226080427	2.35357335427890	0.00848860004907
C	2.04472173123639	3.15084256622480	1.25669982167497
C	1.81658209260799	3.24242976784231	-1.23286527474567
C	-0.83198219787108	2.75683700737925	0.28765082076353
C	-1.52514825117093	3.23577863965634	-0.84239284906007
C	-2.55893887665011	4.16241104863666	-0.67560707407758
C	-2.93164956788925	4.59344012304035	0.58522565181544
C	-2.32802541090968	4.03439794478849	1.69811531569768
C	-1.29921182239611	3.09775334743913	1.57104396319100
C	-1.23435953252572	2.70551811177142	-2.22061381540739
C	-0.77737868845061	2.42521366512761	2.82423785628421
C	1.51623464447511	-2.39176009065409	-0.32870454037773
C	1.54736965749058	-3.05360466034568	-1.72661358812928
C	2.01478457870328	-3.42435730364213	0.70162592474122
C	-0.88266278295669	-2.75865428634786	0.26779685291617
C	-1.76751510127885	-3.17098499957232	-0.77125924543052
C	-2.74992222291792	-4.11608198956700	-0.47073703076570
C	-2.89602761952370	-4.62975584347795	0.81052048870273
C	-2.09188358530332	-4.15478229839938	1.83548500734028
C	-1.10872811123793	-3.18947076770264	1.57953449689650
C	-1.71831145680951	-2.59373318044721	-2.16240833701513
C	-0.37130427481125	-2.59827867526984	2.75592041045074
H	-2.09979584130919	0.92105238884373	0.08326752784620
H	4.45945210163855	2.08035267152525	-0.22330311640054
H	5.65174657905977	-0.08407711878516	-0.50556577695024
H	4.35882173873755	-2.21093751377216	-0.59795322145882
H	1.37504283171326	4.01537285977883	1.40001885008651
H	3.07118835685864	3.53104825543510	1.12538767839135
H	2.01475202708213	2.51813586252593	2.15684078985546
H	1.61407996113547	2.68038135863880	-2.15693512250035
H	2.85686136584670	3.60602729755353	-1.26091941059159
H	1.14890808071760	4.11933626049420	-1.18701327744790
H	-3.08322671865111	4.53231927137545	-1.56439949347365
H	-3.73564441259939	5.32847939157407	0.70347465209670
H	-2.67109073915873	4.30516316366155	2.70358856318004
H	-2.16466388817341	2.66387919637512	-2.81207049123996
H	-0.79945062588541	1.69413812291157	-2.16547406717653
H	-0.52605398955377	3.34651774697013	-2.77460098684277
H	0.01036400006199	3.02286412216400	3.31669148528351
H	-0.34837369000275	1.43749280840981	2.58671680546100
H	-1.59654559800778	2.29704093332015	3.55124607996307
H	0.87607086612326	-3.92800715666294	-1.74512314306435

H	2.57175832325059	-3.39711693348218	-1.94534976421908
H	1.23494299029122	-2.33956970467333	-2.50446433949226
H	2.14447732400167	-2.96719929801500	1.69365696733183
H	2.98545465137756	-3.83186197227771	0.37512185090201
H	1.30312165014644	-4.26281272516972	0.78013542345317
H	-3.42797597332006	-4.44093940575371	-1.26920133426237
H	-3.66771989021055	-5.38028755581244	1.01671030472839
H	-2.24164088901071	-4.50063897273815	2.86484621612963
H	-1.29253635051465	-1.57741503387423	-2.14295611287857
H	-2.73517918538467	-2.54879311803132	-2.58730757867307
H	-1.10418154726105	-3.20794110947054	-2.84545542332708
H	0.39153008248278	-3.28971415932445	3.15698794566889
H	-1.08025134342336	-2.38920977591385	3.57577066467835
H	0.13250824237013	-1.65854634853064	2.47802199100675

Table A5.8. Cartesian coordinates for a DFT-optimized structure of $[Co^{IV}(ONO_2)_2(NNN)]$.

Co	2.07202413882736	12.89675803826336	13.19613471932387
O	3.48765370387964	11.92869476458046	14.37870621260135
O	4.60593611761136	11.33600388328250	16.14375068095771
O	2.64162628877813	12.27015135464263	16.39727009298413
O	3.42141251530645	12.49324880856217	11.86730351245024
O	2.06570485850783	13.37070960339654	10.37423488748516
O	4.01058613717507	12.55626198994223	9.76983713260203
N	0.77387506244983	13.27719463798650	14.47840843711156
N	0.99585421961507	11.45604803227950	12.84722057734073
N	2.40689675069095	14.68787855948616	13.31000900135956
N	3.56777064230583	11.84957574571747	15.68472992310308
N	3.14949568711363	12.82242385710252	10.61984302794965
C	-0.12271687180228	12.31992251424569	14.77829508921256
C	-1.05478522935198	12.54426607696873	15.79335078940355
H	-1.78463204855401	11.77416548809914	16.05366701320893
C	-1.03908149175901	13.77860569798047	16.45928165385072
H	-1.76103337798693	13.97680694281844	17.25657408184369
C	-0.11647122704249	14.76792443239626	16.09015648571400
H	-0.10891721022699	15.74262947438011	16.58348515509725
C	0.79294951020409	14.48540558255390	15.06879356624802
C	0.00942807811665	11.08079967278556	13.91732315685102
C	0.64497541294023	9.92669606288045	14.74305063767442
H	1.65692791371159	10.19161514149711	15.07443987961869
H	0.01465823991347	9.72470375561493	15.62472295969707
H	0.68896171676494	9.01784084621984	14.12368771907287
C	-1.36357584839480	10.60629783400953	13.40457667485290
H	-1.23516576027839	9.77604646068278	12.69275307573401
H	-1.94869917151782	10.23172425340081	14.25998039174513
H	-1.93068001597116	11.41505047648679	12.92493566018875
C	0.90102030164026	10.84796371570583	11.57160571358774
C	1.80503427314673	9.79806684216086	11.24422935714027
C	1.68639520898668	9.19009581088821	9.98251764435132
H	2.36765986839244	8.37120293315240	9.72549067551687
C	0.72333995132800	9.61505814966553	9.05907851518392
H	0.64975047579589	9.12853895589346	8.08068231438446
C	-0.12519005197631	10.68269391041050	9.37691859215224
H	-0.84841591333914	11.04573578393764	8.63793771270361
C	-0.04705111650854	11.32620272397153	10.62233314674818
C	2.85066068943662	9.30957505067395	12.21787002579310
H	3.09848004903413	10.07798875570330	12.96414026526776
H	2.49717037531696	8.41185737936324	12.75718541413057
H	3.76821949107701	9.02548454701787	11.67636245071878
C	-0.89695860954576	12.54937099632915	10.87562696173524
H	-0.71650404622269	13.29576209217523	10.08383405161649
H	-0.66189819248979	13.02367270181585	11.84015069317026
C	1.84046097725423	15.41574651763527	14.50048887881017
C	3.01003602065590	15.58486722218357	15.51221163281352
H	3.75481016571339	16.28035087866043	15.09552232455777
H	2.60888314763338	16.01209705679682	16.44582468447848
H	3.48305229050140	14.61894081505368	15.73251432699240
C	1.24538328405559	16.80808178439193	14.21376394681261
H	0.31282267955566	16.74530281956186	13.63772034761419
H	1.02753169415506	17.29782864123122	15.17633019128412

H	1.97409895526789	17.43275416013692	13.67431925330147
C	3.10536433816998	15.43996746095939	12.32934814201582
C	4.53015076251459	15.41071580747368	12.32299254844501
C	5.20335202231703	16.18332073821438	11.36104184491023
H	6.29903548340668	16.18293486429215	11.36096564688199
C	4.50412750927107	16.93789772718302	10.41195560246894
H	5.05046672601314	17.52970127146616	9.67007621718249
C	3.10497654310528	16.90651134377883	10.39318119974972
H	2.55502046080992	17.45341172000259	9.61909276676828
C	2.38047683235095	16.15556299792685	11.33277071976058
C	5.33173966349475	14.61415989472569	13.32446883660059
H	4.75550419782668	13.77035111859675	13.72940006767646
H	5.65150130196467	15.24809270698159	14.17085492688559
C	0.87971624477110	16.05666864887170	11.18866683950086
H	0.39484718818170	17.03055067042374	11.37506128117895
H	0.62954313599288	15.75655901605174	10.15731270687635
H	0.44756915898874	15.30802196988806	11.86765323963219
H	6.24403328902225	14.22201100827917	12.84581307951255
H	-1.97254756809272	12.30118080210536	10.85546701780492

Table A5.9. Cartesian coordinates for structure of [$Co^{IV}(ONO_2)_2(NNN)$] where the positions of the hydrogen atoms have been optimized by DFT calculations.

Co	3.09820396021807	6.31262975341963	3.94165365823409
O	1.66284788907659	7.20647299053663	2.69636952994185
O	1.04869070603364	8.45263891500986	1.03632862310972
O	2.58805451413765	6.95507193445658	0.72545224305047
O	1.78628054930546	6.72086818728666	5.29217693771210
O	3.20286250427190	5.83660112762897	6.70632031467228
O	1.37911429518565	6.78477394698492	7.42088877555125
N	4.40548727253108	5.91562294360647	2.67488252776424
N	4.18848954393841	7.74441498423384	4.29327232788022
N	2.70212935587885	4.53095582780726	3.79276550334704
N	1.77149906966237	7.54150834801501	1.44929404132479
N	2.13900664713897	6.43230545615565	6.52030811965974
C	5.33167929364238	6.84210093653844	2.39456009033400
C	6.27591437090134	6.58808707951416	1.42314542599405
H	7.03844499531958	7.34107984833310	1.17957614780059
C	6.24067792774796	5.37041327671894	0.76438898180748
H	6.98572591798219	5.15169304250462	-0.01658536861956
C	5.28164063398050	4.41925394997297	1.08407678627344
H	5.25715422694555	3.44720946836704	0.57231552640716
C	4.36136585495592	4.72018124783292	2.06530283438037
C	5.20770759744008	8.09212059888837	3.23372903294599
C	4.58498001272789	9.23168780412501	2.39087141981665
H	3.58725923991283	8.97215214450547	2.00380411194663
H	5.24051443844008	9.46385575732434	1.52706993684622
H	4.49625883038837	10.14334104197249	3.01360850282041
C	6.57934758013037	8.57225454193102	3.73420055750834
H	6.46103068654000	9.41566834704535	4.44032254883191
H	7.17151625746366	8.94222224299148	2.87344632262815
H	7.15982655066141	7.77462157583321	4.22978273270337
C	4.27212350164289	8.41978121724518	5.55013407345909
C	3.34217816903495	9.43753061947958	5.84305018653635
C	3.49191303125689	10.12531039245150	7.04801874489958
H	2.78499358252329	10.93688376497665	7.28485545657326
C	4.48654131035594	9.78029938848989	7.95203488012710
H	4.58029860168987	10.32753251926387	8.90317429994017
C	5.33201700532296	8.72691024539609	7.67194581772450
H	6.07693799752885	8.41322308259453	8.42272137821305
C	5.23746597008612	8.01375790051075	6.49141172399006
C	2.18599447400227	9.77973682853573	4.94388523331722
H	2.06882570527664	9.07756471476765	4.10148099808282
H	2.28572440746910	10.80679074142568	4.53055131441546
H	1.24306032899552	9.75612001022723	5.52533679307720
C	6.08286192504312	6.77952545473504	6.30972320975883
H	5.85437930115623	6.06074607262766	7.12311632463357
H	7.16759912299242	7.00906524247476	6.37282714166681
H	5.88426195472096	6.25531314592335	5.35822410479232
C	3.26109119892905	3.82154481331522	2.58254546098759
C	2.11850395886431	3.74771410657970	1.54328355982942
H	1.31875382696477	3.08117061094393	1.91780967769943
H	2.50092884985307	3.32457088250032	0.59207798462214
H	1.70542845433290	4.74910922991849	1.33466420736667
C	3.78910792086728	2.40775192403154	2.83397375098935

H	4.69928052204784	2.39565617231654	3.45953530955003
H	4.03481403707022	1.92725286656520	1.86573670501564
H	3.01642403472674	1.78138037476548	3.31973199122607
C	2.04069490728833	3.74984252991453	4.79340247179249
C	0.63641765234340	3.75903519637776	4.84101507290441
C	0.01738875128573	2.97318164681772	5.81234950505518
H	-1.08495818799607	2.96831404436990	5.85240226583725
C	0.73525542413982	2.19814551129283	6.68851650374675
H	0.21101509064313	1.57802057522516	7.43339253716852
C	2.11317082052267	2.23331460371215	6.66494328179810
H	2.69499014730117	1.66352074716120	7.40817389048826
C	2.79321199888623	3.03490069564897	5.75062886254111
C	-0.20369986435799	4.52297798577643	3.85699823879418
H	0.31750935046601	5.40870561438893	3.45105330381775
H	-1.13966426558275	4.86889488163672	4.33801834357223
H	-0.50482665309195	3.88398621570281	2.99931871878196
C	4.28849790658600	3.16108032916794	5.87901777652292
H	4.79701172404900	2.18133599437342	5.75778075148322
H	4.53944540178995	3.53349861346049	6.89241307167283
H	4.72003988041415	3.87856417337078	5.15983688285592

Table A5.10. Cartesian coordinates of a calculated TS structure with axial-O1 for EtBn oxidation reaction.

Co	2.36285710681981	12.87173080768407	13.16800521208869
O	3.96374816674287	12.09917691808097	14.55640583336226
O	4.60313125055231	10.62175805697045	16.11093318299854
O	2.70962464630053	11.70340293249432	16.33683236106301
O	3.85217045765567	12.57450287032781	11.99796484336774
O	2.68084996143335	13.42777754379420	10.33697762055997
O	4.75641728615476	12.79087338530929	10.02361585714346
N	0.98463057142160	13.13894954662571	14.39050337304108
N	1.36766931775012	11.37734624134716	12.70263644404272
N	2.64099958525840	14.68802609689374	13.42621610360606
N	3.74675262055295	11.41757528752407	15.76682246188063
N	3.75236755414261	12.95173399356558	10.72206895858187
C	0.05160986253869	12.17777447442757	14.53637514182114
C	-0.96200450404435	12.33875496887948	15.48626468237250
C	-0.99252150727382	13.50956541461291	16.25418514036249
C	-0.03007917030795	14.50760487452498	16.04350056448056
C	0.95785958949541	14.29964278946149	15.07874752214451
C	0.21353816740893	11.01491180195861	13.57928151590534
C	0.46910424796249	9.71382077479329	14.38136959409605
C	-1.10271840869178	10.83207464000739	12.78241128316101
C	1.63022059398268	10.55156543193245	11.56840687159118
C	2.53637013755808	9.45605918622215	11.66711539215648
C	2.78707289461001	8.67216983256209	10.52761737491994
C	2.17510554733223	8.95301793127811	9.30264381566702
C	1.31262527913252	10.04761844554661	9.20295414684895
C	1.03169432660125	10.86364627948672	10.31305173224077
C	3.25594319945066	9.11370024618446	12.94862762683683
C	0.11996201752431	12.05288124462401	10.11505314531478
C	2.06398932582962	15.26043512126223	14.68044882995513
C	3.13457244308393	15.27844532904512	15.80632030646293
C	1.51074173234352	16.69066848936924	14.50888434401418
C	3.19146355746716	15.57681737766097	12.46329985634983
C	4.58096174709189	15.87065604082292	12.46011092086927
C	5.08791058608103	16.75891102645330	11.49536672584210
C	4.25059984538430	17.34751169752082	10.54355054901752
C	2.88922194258959	17.02677362867586	10.52993427937813
C	2.34183238465588	16.13597705237086	11.46654208323995
C	5.52583736580802	15.24346189650419	13.45650818527851
C	0.88247194585006	15.75966458199484	11.35375136022856
H	-1.71891086545416	11.56110729894385	15.61712924755500
H	-1.77660605257689	13.65345286277386	17.00398177403019
H	-0.05183931668080	15.43885415295264	16.61523312206438
H	1.37684480841027	9.79641582388478	14.99451816118677
H	-0.38651060512692	9.50888616673284	15.04824640714628
H	0.57103586716370	8.86762522137850	13.68394596531811
H	-0.95627844711765	10.07275684796549	11.99748959776539
H	-1.90492669812890	10.48234736701262	13.45441881980259
H	-1.42114588180996	11.77486703648972	12.31566970030517
H	3.48929780121913	7.83516654781278	10.61150905299806
H	2.38704402962157	8.33483376855967	8.42360415122389
H	0.85411240435413	10.29590022603876	8.23877046746710
H	3.36580544723081	10.00299564069287	13.58106575930830

H	2.71695217130315	8.34610610018304	13.53072246929115
H	4.25551637168958	8.71083351727056	12.73113678412663
H	0.41611426371354	12.60357963259445	9.20786394764150
H	0.17766711170627	12.74571465755850	10.96517917233197
H	-0.93035037229540	11.73217583178680	9.98555515541528
H	3.91526849095515	16.01477204399239	15.56133903429016
H	2.67436059136436	15.56305930606021	16.76876092158274
H	3.59438371318539	14.28569375842399	15.91237533551907
H	0.67020412896850	16.71982779076171	13.80057467766344
H	1.16390502210298	17.07812206967964	15.48200956794346
H	2.30671064820914	17.35666563281134	14.14030936835416
H	6.16164428052996	16.97989410066187	11.49096870404572
H	4.66227591951818	18.03543776657120	9.79745118039259
H	2.23534618140707	17.45529188447456	9.76149715806122
H	5.06325521490639	14.36824965056350	13.93227542840140
H	5.81019276282792	15.95737218445083	14.25206513554592
H	6.45735244674063	14.93005949460395	12.95540174266511
H	0.22526537930433	16.63242912836671	11.52450152653397
H	0.67190041597612	15.37853246628153	10.34049096866077
H	0.61526570640606	14.97046560559371	12.07256137736320
C	6.56157145967529	10.45094335194880	13.09695651021891
C	6.94151287190380	9.28541702060504	13.82307963034650
C	7.04660657126950	8.05183481948688	13.18167586165213
C	6.77713143683849	7.94144368569138	11.80332935921734
C	6.38838162094480	9.07887244639560	11.07259375444718
C	6.26776355567167	10.31480385439042	11.70686987294884
C	6.45603591238507	11.75928793520601	13.71425842615908
C	7.22885764639062	12.13099596104369	14.95869644239758
H	7.14664000275640	9.35970971089543	14.89479268837073
H	7.33976314732886	7.16474457449195	13.75305012722741
H	6.86253691585872	6.96952104405185	11.30564558892849
H	6.16491902999583	8.99794601382790	10.00425435570950
H	5.94132940179515	11.19526227351776	11.14346082643587
H	5.07679102221287	11.82162135476624	14.15294153200920
H	6.31914656424019	12.57070679860728	12.98504336021742
H	6.87896691007628	13.09482955987358	15.36523883141652
H	8.30579977623938	12.24512281402910	14.71864644104632
H	7.14359254054403	11.37312293844196	15.75421226695810

Table A5.11. Cartesian coordinates of a calculated TS structure with axial-O1′ for EtBn oxidation reaction.

Co	2.23220917810950	12.93450320757700	13.09730695083066
O	4.15665174346825	12.08522241148104	14.78059071558874
O	4.64252579378646	10.43995292490457	16.20739728309880
O	2.80989028280915	11.62316143654818	16.44352165061893
O	3.75561112575079	12.61949735270233	11.98736700294601
O	2.67463908037506	13.41698079944641	10.23344518466080
O	4.77630331805353	12.81438144965226	10.06723862717159
N	0.92304292840400	13.16422196909616	14.36554301943381
N	1.35745043608070	11.39319655684193	12.72675924032421
N	2.55380328340991	14.69565143340397	13.36599132499652
N	3.86171376272219	11.32800193725785	15.88926866828265
N	3.72752590748267	12.96923251774874	10.69882713209644
C	0.03222232369620	12.17211189743711	14.56539912753113
C	-0.93956450216818	12.30447181271585	15.56012488358138
C	-0.97614323701915	13.48183927078719	16.31979898407528
C	-0.05971893358168	14.51065307091408	16.05691174951475
C	0.88931340787207	14.32709247931266	15.04966783175348
C	0.19824789021997	11.01561440713392	13.60303523683377
C	0.49886854209155	9.71714217266816	14.38963263924898
C	-1.11954424199758	10.81448185260527	12.81657287967387
C	1.60396801550437	10.58010266841452	11.57555792413883
C	2.54764603169786	9.51751169664203	11.66316269952091
C	2.78341245848461	8.72973951463368	10.52350986877472
C	2.12837914536969	8.98412116698154	9.31456067187792
C	1.24165812456215	10.06003773111053	9.22715087422936
C	0.96993723987129	10.87841414554955	10.33802711658125
C	3.32311810463857	9.23061613626093	12.92507382151831
C	0.05013935652433	12.06370548953304	10.15291713450767
C	1.94842389696830	15.31070137404473	14.59627229382740
C	3.04271491284573	15.40309476337029	15.69399454385509
C	1.34281742758566	16.71164838564012	14.37505754625977
C	3.14828325038698	15.57592939342152	12.41485913066845
C	4.54462759762232	15.82811018064550	12.44456576732768
C	5.09035730514191	16.71427601694708	11.49875753590410
C	4.28890311789643	17.32910027524080	10.53332637963045
C	2.92280358473367	17.03403278232200	10.48184001147353
C	2.33343597939911	16.15160719294737	11.40045260203117
C	5.45941832134951	15.15598400839737	13.44010385051030
C	0.87412470212325	15.79197680740046	11.23823303744244
H	-1.65952658267574	11.50070552480533	15.73501905168887
H	-1.72679510080416	13.60387438855714	17.10649562671336
H	-0.08529382100553	15.44437857812980	16.62464421762463
H	1.40777480975421	9.82592553463576	14.99697165508015
H	-0.34759588111798	9.48810848101293	15.05971276263178
H	0.61731525798810	8.87812134372955	13.68612853081694
H	-0.97374196392993	10.05580558871666	12.03100734491718
H	-1.90716876703537	10.45638929895124	13.50091452495313
H	-1.45781599011704	11.75269845856353	12.35482501486671
H	3.51247935758565	7.91494649575934	10.59349961707472
H	2.33058827023753	8.36314389534489	8.43534064611157
H	0.75823748767560	10.29444913084490	8.27182595832088
H	3.52353448396861	10.16122060741886	13.47313239319388

H	2.78180300336288	8.54791458276032	13.60128493854471
H	4.28143401671455	8.75093690137349	12.68140561348043
H	0.33030090507970	12.61032570815437	9.23830458350638
H	0.12440004884261	12.76432896269533	10.99622118124140
H	-1.00217522637114	11.74276036847727	10.04442539187838
H	3.80678277228484	16.13616401581553	15.39300424986780
H	2.59266725107864	15.73740744932820	16.64491281275966
H	3.51401198581283	14.42078574384720	15.84357447657141
H	0.48781544707049	16.68220171967159	13.68455206402420
H	0.99887279776586	17.12244740109577	15.33945402811112
H	2.10680900509099	17.39188014946784	13.96686539921959
H	6.16904922925916	16.90774301503987	11.51863093302515
H	4.73292068440671	18.01342240657041	9.80278438606061
H	2.29757341876476	17.47491917033041	9.69688121812833
H	4.97301098399348	14.28160092936030	13.89265456162121
H	5.75745472021075	15.84533005518174	14.25176530777194
H	6.38476369135107	14.82975328381999	12.93611151887247
H	0.22122163865903	16.67204573951228	11.38427575102843
H	0.69801169361848	15.41134347287459	10.21826020414978
H	0.57154264990291	15.00397341380727	11.94431971719342
C	6.65523394766983	10.42285198756028	13.16593986212949
C	6.99531754826823	9.18786331895167	13.78740730047289
C	7.04784597564991	8.00933646357008	13.04316380444270
C	6.76174052914756	8.02549246026719	11.66399345649514
C	6.40813242730824	9.23390280725062	11.03678376339405
C	6.34206268915389	10.41546914401303	11.77475478039777
C	6.60364442883573	11.67885147548871	13.89571262764151
C	7.40393533455114	11.90650714646564	15.15943931126547
H	7.21152442371839	9.16426345499262	14.85929799715060
H	7.31229074960110	7.06701717826846	13.53462409918451
H	6.80568062438691	7.09648068384532	11.08538795953165
H	6.16791248877376	9.25235467236262	9.96911652232688
H	6.03627167883959	11.34786357321554	11.28842947380587
H	5.27464240572936	11.76457664057705	14.35585916264326
H	6.52219227560418	12.55361029833063	13.23389939312603
H	7.13253158851206	12.86939141326279	15.62409205621464
H	8.48815451513368	11.93963393554083	14.92884252780250
H	7.24450942942261	11.11202484064516	15.90689627858323

Table A5.12. Cartesian coordinates of a calculated TS structure with axial-O3 for EtBn oxidation reaction.

Co	1.49820252931136	13.01564427107010	13.17903351871692
O	2.39378613449943	11.81858831405008	15.01440334053052
O	3.28509343981516	11.75522672663694	17.04291620599512
O	1.44362206130498	12.86461461965954	16.69832972540719
O	2.99378963858257	12.17701808496227	12.32939933515322
O	2.21215978196776	13.14530590788017	10.52003149207955
O	3.98913755781881	11.86214034745645	10.40584558018599
N	0.07486687780803	13.74701977176441	14.12774255205958
N	0.24080560594622	11.75598251082306	12.67942769686095
N	2.24128645986547	14.69680213511389	13.41787296365148
N	2.32010946504868	12.16882940729147	16.21107798792860
N	3.07321887776835	12.40473411542612	11.02011169680610
C	-1.03669593442077	12.99676986361824	14.27842684631981
C	-2.08879340757368	13.47547890870211	15.06238624870038
C	-1.96782893810832	14.73876689723477	15.65938961953116
C	-0.81091947382904	15.50148768588227	15.45467967916857
C	0.21630828272951	14.97461638461256	14.66604634794718
C	-0.97241600248059	11.66781728238188	13.54501772135146
C	-0.78787286118850	10.52969632684269	14.58747831247834
C	-2.28092384313046	11.40774136976132	12.76880449986401
C	0.28124126594013	11.00273998814987	11.47642154995447
C	0.93640390834701	9.74247514029364	11.44156729128445
C	0.94901100929927	9.01526929992759	10.23855389862285
C	0.34336616834080	9.51789203945774	9.08329465479799
C	-0.25312357082972	10.78289601454416	9.11117065780558
C	-0.28009770077304	11.54936912421207	10.28703601233655
C	1.63624389926010	9.18347205978737	12.65680733393019
C	-0.83809980185658	12.95345732338352	10.23510270147380
C	1.51803606124394	15.66025601265900	14.30164928481759
C	2.32559099489321	15.97951511915498	15.58659452303859
C	1.19356203435979	17.00847469711676	13.60865213510092
C	3.41720963920053	15.13846372597956	12.74590384559006
C	4.69080576141823	14.82290672873799	13.30495043532474
C	5.85171523192072	15.25357740297206	12.64362927594788
C	5.78054878081020	15.96216279879245	11.43838621697068
C	4.53281958874362	16.21884134413750	10.86738470181536
C	3.33984400172183	15.80581786423101	11.49090343642863
C	4.82176388921124	13.97725517684014	14.54521276177875
C	2.03576357187695	16.03995200496883	10.76237080235513
H	-2.99002246042322	12.87270336676969	15.20063691052088
H	-2.78159413145575	15.13296554872101	16.27592485801634
H	-0.70594539326786	16.49379918089220	15.90075289585664
H	0.16131407729854	10.65645050981291	15.12726149203230
H	-1.61944906154613	10.53205729566344	15.31391667957330
H	-0.77868371092817	9.55843962705896	14.06857177464279
H	-2.18368172050849	10.48835336450939	12.17017508853854
H	-3.11433751543614	11.26743713420645	13.47810863060499
H	-2.52999358941504	12.24223705984338	12.09807453625249
H	1.45617800783845	8.04383971114891	10.21225132049985
H	0.36382389574104	8.93891245508037	8.15388948143468
H	-0.68441555506714	11.20302884853155	8.19505800178739
H	1.84155093745908	9.98047881917508	13.38497670073210

H	1.03096711192215	8.40494669649580	13.15769508876327
H	2.59064116867994	8.71479919143749	12.36240322667199
H	-0.33102773540332	13.52477528950837	9.43935239331487
H	-0.67470787133058	13.48499065930438	11.18480279027453
H	-1.92017200316016	12.95373273164026	10.00774468415329
H	3.29412546985908	16.42426062242971	15.30484863618897
H	1.77810110976662	16.70999608731869	16.20734566240372
H	2.49350397412083	15.07404388899059	16.18602593496826
H	0.49356279402434	16.87311667805249	12.77270976329888
H	0.74033303887313	17.70198817866845	14.33731607450092
H	2.12291361164738	17.46529356836585	13.23274395439970
H	6.82598280643824	15.01062714355021	13.08306849035793
H	6.69648195795350	16.28767789796152	10.93362876468743
H	4.46974290468408	16.73179610004271	9.90064713120215
H	4.38937542053267	12.98198497117000	14.36103056491617
H	4.29850417010670	14.40605214656671	15.41136841194512
H	5.88098964422410	13.84617057172102	14.81276084031912
H	1.76252867833289	17.11112771177609	10.75635057033699
H	2.13640336030472	15.71420527878636	9.71438455186230
H	1.21613117756011	15.46437672025802	11.21365186120033
C	5.76181100675405	10.50685684924702	15.10222892316187
C	6.98192951985358	11.11425851085522	15.52847671878686
C	7.82888148234151	11.73939087412789	14.61655820897959
C	7.47642897614474	11.80311509943606	13.25363703706392
C	6.27046535198063	11.22905363136477	12.81295682307868
C	5.42817737439936	10.58585686234665	13.71887767195095
C	4.88901492219792	9.88346872619239	16.07776216040446
C	3.87888906946488	8.82422727353323	15.69659007433986
H	7.24992204105320	11.07270566931343	16.59040444413123
H	8.76650385484889	12.18806126105912	14.96185227591736
H	8.13296936455764	12.31122742822003	12.53980224364723
H	5.96291487043563	11.30753117045569	11.76634583987222
H	4.48257174047657	10.17342880315152	13.36168344260821
H	4.02353597701354	10.98147745826495	16.47890306316303
H	5.35638841841716	9.74098911082172	17.06690274428072
H	3.22405433652041	8.58055110823687	16.54996307435708
H	4.38983923569113	7.88916056654075	15.38868676146905
H	3.24220390356016	9.14250274485708	14.85675383641824

Table A5.13. Cartesian coordinates of a calculated TS structure with axial-O3′ for EtBn oxidation reaction.

Co	-0.98484221067952	0.49299552419258	-0.42143388017419
O	-0.42606002798012	-2.22473051740113	2.87106726244265
O	1.25714475988033	-0.84727484448352	3.33124812816554
O	-0.78126023405304	-0.12174028084823	3.38088183602807
O	1.00638231621720	-1.16743217490158	-0.14937303126854
O	0.20462798551120	-0.02969681409551	-1.84323955802124
O	1.93206216474848	-1.34786045853487	-2.13492214584836
N	-2.18455413654606	1.06588187665712	0.82954697140275
N	-2.19294404553041	-0.80404712757963	-0.76187257529668
N	-0.06946644904241	1.99054656138503	-0.00931000554424
N	-0.05693319740157	-1.09541373841539	3.17846539600145
N	1.09043296043247	-0.88369150600969	-1.36918308308799
C	-3.30456960479239	0.33921300475052	1.02903960490156
C	-4.20925488986504	0.72657911736029	2.01935046421978
C	-3.93934171380415	1.87893659298988	2.77122953304851
C	-2.79039944183131	2.63639607927486	2.50234077611335
C	-1.91591788206021	2.20460513175354	1.50390209040841
C	-3.44641484040068	-0.81890628123762	0.06196791367114
C	-3.61871702634205	-2.14366744857905	0.83881288676157
C	-4.69903996381151	-0.58320787510867	-0.81957464195701
C	-2.12565125270529	-1.70254665088550	-1.87207992222661
C	-1.63377158146068	-3.02621658739935	-1.70742759388445
C	-1.59650952388875	-3.87475576904019	-2.82932591893901
C	-2.00104263584444	-3.43600065208053	-4.09207225492334
C	-2.41484645059339	-2.11071236362083	-4.25619714599658
C	-2.47141955290799	-1.22466576325892	-3.16803015466899
C	-1.08726884001017	-3.54236099733627	-0.39514125841916
C	-2.85725358756076	0.21495382273287	-3.42127262668038
C	-0.66795085903290	2.90962321010394	1.01253695948145
C	0.28781729079175	3.19919314546093	2.19032066902558
C	-1.08209560442805	4.25319763508213	0.35781895870532
C	1.09674206503962	2.44112188142686	-0.70291158609911
C	2.38941573844194	2.19395765814286	-0.16516871727534
C	3.51372232678860	2.64581503955184	-0.88052451206480
C	3.38375905049753	3.30221053911877	-2.10691426438181
C	2.11105177483209	3.47872782461780	-2.65817855886703
C	0.95740570740678	3.04383950711975	-1.98474840491653
C	2.61097978104094	1.40496990211116	1.10377002561259
C	-0.38395814884478	3.18959612121257	-2.66590967968319
H	-5.11253567190036	0.13765800654975	2.19902566128919
H	-4.63097069111670	2.19365460444203	3.55847046179172
H	-2.57620534285106	3.55019131186582	3.06266920404935
H	-2.76690375014109	-2.31996234287314	1.51086576355162
H	-4.54344977195806	-2.09850543238618	1.43970676873302
H	-3.71473733611370	-2.98085753362401	0.12995441891158
H	-4.75845289555532	-1.36310606731805	-1.59630148328196
H	-5.61028315699792	-0.63638846016859	-0.19996699808507
H	-4.66068603676659	0.40426106844961	-1.30316098856009
H	-1.21614342715109	-4.89490896302639	-2.70139908841526
H	-1.95973615018381	-4.11271440656946	-4.95211785048480
H	-2.68321923752511	-1.74045842235488	-5.25253842087816
H	-0.89482511648842	-2.72941178514914	0.31600336291766

H	-1.77334436688828	-4.26819059550077	0.07731308036955
H	-0.13506833124665	-4.06805572741491	-0.57823954154916
H	-2.32400101970718	0.59826201624925	-4.30738093532808
H	-2.59860330752215	0.85345546333957	-2.56230919580323
H	-3.94063839131876	0.31948918017205	-3.61462770298710
H	1.20840531292353	3.67230922193690	1.81443756518067
H	-0.19597811428813	3.90341982258818	2.88901373963069
H	0.53533249652089	2.27719206524310	2.73395318079982
H	-1.83727180619763	4.09126108533187	-0.42582354377908
H	-1.50345280063049	4.92997127577638	1.12047283094148
H	-0.19648991645835	4.73514363298769	-0.08796559718175
H	4.50942489625991	2.44931839621577	-0.46607803362251
H	4.27224851700551	3.64267887457617	-2.64940382733131
H	2.00181634443899	3.94343359471081	-3.64502485774430
H	1.72063402896004	0.83151060442712	1.38931033915050
H	2.89596285757841	2.05551221210097	1.94942976763593
H	3.43738167208470	0.69687204686135	0.94496775281127
H	-0.74947069973237	4.23236989981009	-2.63227662098202
H	-0.30167682151395	2.90044861616569	-3.72691796689202
H	-1.14123657287810	2.54585855872047	-2.19269786447349
C	3.94445454035084	-2.01702623448127	1.92652946909998
C	4.90309506224485	-1.28182137891839	2.67988406964856
C	5.90271869680532	-0.54608958937503	2.04496823564613
C	5.96788561183683	-0.51614097549495	0.63897404460752
C	5.02211817460742	-1.22613010153856	-0.12327170612252
C	4.01956921010281	-1.96307883089612	0.50765499009816
C	2.90131896777085	-2.77221843887158	2.62150737930346
C	2.13152384256132	-3.86124664995766	1.90547721488386
H	4.84665170740520	-1.30264460105640	3.77406376319902
H	6.63468735293869	0.01008679530646	2.63976696901622
H	6.74764307353008	0.06853387634655	0.13937418945402
H	5.05069171015888	-1.18738031981527	-1.21642795193754
H	3.27283004058332	-2.47722145921651	-0.09959949124543
H	2.00803861449075	-1.85291248945934	2.92336915283610
H	3.17499667986597	-3.01416982457356	3.66387838923383
H	1.37343858597264	-4.30365461836466	2.56891239684239
H	2.82468666865995	-4.66397174588324	1.58303348997552
H	1.61776584726230	-3.47205756011437	1.01305405931086

Table A5.14. Cartesian coordinates of a calculated TS structure with equatorial-O2 for EtBn oxidation reaction.

Co	1.44412122081287	13.30082927646869	12.80485659397423
O	2.83633100672805	12.54110694510838	14.11495640594774
O	3.52769278839443	11.68295775869441	15.99387538047114
O	1.55699940817421	12.63925317570377	15.92210554109289
O	2.83163768802977	12.50372604276192	11.56959822853141
O	1.84162772132956	13.27828681796103	9.74605991264931
O	3.81987495994496	12.34807181400704	9.56594606090326
N	0.14964822426376	14.08381058947799	13.89323804546455
N	0.14516099941795	11.99973918388906	12.57826480667845
N	2.04464242844543	15.04666019982944	12.67490526518438
N	2.62144685464128	12.28061556395532	15.39630438050123
N	2.83435150021664	12.72878246135825	10.16364977836488
C	-0.95717719619767	13.37874998971724	14.18924067868652
C	-1.91515530110274	13.92937914467896	15.04620523496488
C	-1.70240423063069	15.21192981585157	15.56653679266622
C	-0.55478586217318	15.93141312907822	15.20317527503940
C	0.36593499798645	15.33814665398607	14.33747289885917
C	-1.03003254890793	12.03195385305269	13.50114928736464
C	-0.97559708238764	10.90879295460075	14.56790652835329
C	-2.37613159956949	11.91404822550360	12.74488534548881
C	0.22034906787047	10.94494456345614	11.62279962066282
C	0.88354160222424	9.72102543589613	11.92960309030961
C	0.93867302195891	8.71064992660973	10.95212504317535
C	0.37449843082775	8.88876884131806	9.68528211779067
C	-0.24195248359517	10.10416801851293	9.37611193319403
C	-0.32618712507131	11.14323434791378	10.31969033761250
C	1.55641310033431	9.47478646702615	13.25980358087952
C	-0.98896781278342	12.43756001016491	9.90639167141078
C	1.64840706781400	15.94565347412385	13.80071691644151
C	2.72462179641932	15.90944249818195	14.92048803711478
C	1.43367206961140	17.41110520547084	13.37226260070455
C	2.73957900954057	15.58698245903632	11.56283992221440
C	4.15879558676442	15.53256308511620	11.50378586768334
C	4.81113503946831	16.06310480799922	10.37647143606603
C	4.09040523197841	16.63882789761004	9.32544590984175
C	2.69237896161367	16.66283705512891	9.37717948817920
C	1.99691619377313	16.13003800856983	10.47464678880653
C	4.97220693570720	14.90875487177246	12.60912356587649
C	0.48574929091404	16.09693330554282	10.44358930535201
H	-2.81471689562020	13.36224232728928	15.29892086367899
H	-2.43858564176824	15.65867875751278	16.24189029530872
H	-0.38077551842086	16.94191891866395	15.58142028140298
H	-0.04298300545310	10.96458151988331	15.14526344265609
H	-1.82643567182364	11.01500483997944	15.26335229595232
H	-1.06037024115876	9.92838000265415	14.07292372837835
H	-2.38244627296044	10.99404961725788	12.13815479650134
H	-3.20839285727324	11.85269477400633	13.46643905702247
H	-2.54491011610890	12.77985611841542	12.08870835800429
H	1.44854212927093	7.77107165447451	11.19554604231190
H	0.43290879888048	8.09153004057728	8.93672592141390
H	-0.66171447487875	10.26506776821681	8.37634459655358
H	1.85521770826931	10.41917939776010	13.73404794051340

H	0.89454751134656	8.93735686691307	13.96022209472215
H	2.45111797429196	8.84535888529975	13.12260631644235
H	-0.64466373419298	12.73642780874607	8.90287578712229
H	-0.75223286485774	13.24797137833476	10.60940322502680
H	-2.08727095582753	12.32313611492580	9.85799514276053
H	3.64169184750362	16.40420902281081	14.56554842393140
H	2.36082760469956	16.44304272762533	15.81575971851625
H	2.95795227190737	14.87196122376823	15.19410395627849
H	0.59803940199240	17.51371887910880	12.66479704790934
H	1.22032975302103	18.03183636234700	14.25901064399459
H	2.34912146465466	17.79938998183340	12.89851824114838
H	5.90490984525895	16.01078558429301	10.32731038229205
H	4.61588192310723	17.04677064249434	8.45538257939223
H	2.12203968031520	17.07992620788784	8.53897991698022
H	4.37697457009967	14.19458609588896	13.19589969848486
H	5.35965442250659	15.67623222581987	13.30472946746417
H	5.84574709211635	14.38565131481815	12.19007602937520
H	0.05784433378526	17.11598504199048	10.46981216027031
H	0.13639198698046	15.61953173892378	9.51216675440698
H	0.08162838059295	15.52552927230816	11.29298677967115
C	5.91058574796576	11.48269580455376	12.44772745379855
C	6.15374155220011	11.95455009926243	13.77322430072459
C	7.30787145883668	12.67856369821722	14.06989657400581
C	8.23975151818453	12.97652530283889	13.05912790483617
C	8.00461179158052	12.54101192162143	11.74057656310512
C	6.85968286840594	11.80576240472098	11.43479643521200
C	4.70823130165865	10.71877631517293	12.17976444908719
C	4.60921199188442	9.72759590121670	11.04471415342849
H	5.41494624163924	11.73936498766933	14.55283467784279
H	7.48299624792190	13.02102127012219	15.09511445940579
H	9.14186927064670	13.55161413945975	13.29335295760029
H	8.72386792660855	12.78061666758124	10.95012120426352
H	6.68173327196348	11.48013749342712	10.40595986603805
H	3.74593274868031	11.76735996790769	11.83972735226853
H	4.15819209334228	10.44397863205326	13.09127258497124
H	3.55722964079105	9.49761151811651	10.80699826253559
H	5.09730276162817	8.77480903665860	11.33755580560269
H	5.09563015301912	10.08348285143537	10.12359333488223

Table A5.15. Cartesian coordinates of a calculated TS structure with equatorial-O4 for EtBn oxidation reaction.

Co	1.61941591332007	13.27139262448507	12.51850225640479
O	2.81665537027474	12.10473546326668	13.66957979253669
O	3.45807996830756	11.00518548548136	15.42946107155934
O	1.64502819801057	12.23011238642008	15.55425696395820
O	3.03978418715651	12.76554239089000	11.23060726101419
O	2.09457459788684	13.87336920194781	9.58228237539761
O	3.97604082162924	12.73513995282200	9.28219589692551
N	0.27075451437089	13.78899714982915	13.67988212724715
N	0.31102782156613	12.15292606695840	11.85093182038462
N	2.25025930773605	14.97303439286231	12.84575842074997
N	2.62357858575485	11.77004533083182	14.94220379315611
N	2.96867144405544	13.16754432235786	10.04156079368270
C	-0.83612824153012	13.02571871549007	13.74876643014387
C	-1.84008531315770	13.35798475573607	14.66162578149793
C	-1.67270302312338	14.49315799712121	15.46707017936173
C	-0.52570465182608	15.28745769466085	15.33029814623057
C	0.44833690538373	14.91149823835920	14.40205658040636
C	-0.83288183445112	11.86666813298371	12.76776962366180
C	-0.58814396937069	10.54053637482849	13.53610305680504
C	-2.19457179055493	11.76744767712702	12.04611853133887
C	0.38581188833499	11.50843524632045	10.58608634142551
C	1.17820541044988	10.33746703703937	10.40665463654740
C	1.27306148903948	9.77512780778760	9.12004523407111
C	0.61397195634063	10.33983706760731	8.02338271016411
C	-0.13212939940599	11.51020982604024	8.19878392706205
C	-0.24478495202385	12.11892631763772	9.46034811771252
C	1.94125784036934	9.69885868976015	11.54333881553524
C	-0.97273658247566	13.43941428384909	9.56906819462690
C	1.73766811518817	15.64429675124041	14.07516178755286
C	2.73948101302485	15.47557823804489	15.24776513161292
C	1.46422623185853	17.15136230747270	13.87664816458033
C	3.18910996654882	15.62551490758382	12.00072421055367
C	4.58580938882671	15.37438071635902	12.13370061307733
C	5.47185728706956	15.99150708548768	11.23224642484183
C	5.01025922395601	16.82877453020130	10.21132736188715
C	3.63674154147547	17.04247460310277	10.06373524997441
C	2.71096110286275	16.44325839501585	10.93399791213182
C	5.13799156608258	14.43997476218949	13.18443992494511
C	1.23581136482735	16.63349054599738	10.66434363376573
H	-2.73937020525808	12.74155860135170	14.73840066234344
H	-2.44617649209775	14.76938628151589	16.19031527219682
H	-0.39100200047180	16.18908664433968	15.93325652958626
H	0.38588367764094	10.55928078310053	14.04219949196622
H	-1.37676307185959	10.39009704378804	14.29373905017522
H	-0.61988493815013	9.69807277402952	12.82686784406976
H	-2.13102588181026	11.03170974996613	11.22810244006117
H	-2.96793003011718	11.42220519267350	12.75294301298712
H	-2.50865484736719	12.73675846409669	11.63337116929424
H	1.88807905799079	8.87799425090842	8.98461622066442
H	0.69907470534434	9.88177841211965	7.03192611770869
H	-0.62179734411212	11.98126147198462	7.33790053425058
H	2.21567253348741	10.43153981342951	12.31607683755991

H	1.34698667688258	8.90216585408121	12.02646114865626
H	2.86471456204137	9.23160304808252	11.16361314254753
H	-0.66602411306121	14.11017772049666	8.74874201296282
H	-0.74412876487495	13.93730457779363	10.52286410558128
H	-2.06734883128924	13.30844175481392	9.49348554307275
H	3.65742912847608	16.04297432774688	15.02693235097221
H	2.30117928493357	15.86974625075777	16.18120899920891
H	2.98788886613549	14.41654602220875	15.39616150339275
H	0.63730648896350	17.32532447715237	13.17328733981606
H	1.20573887493902	17.61643362024780	14.84307627298216
H	2.37106816308017	17.64608369653380	13.49273247051699
H	6.54485266214547	15.79017246231966	11.33079633305531
H	5.71676068797963	17.29022519810938	9.51302286848339
H	3.26543268995713	17.65539256476387	9.23569993431597
H	4.41351553001928	13.65817724001539	13.45551385785693
H	5.40964822965668	14.98621348551985	14.10599886542647
H	6.05451840252303	13.95259947756349	12.81305804805640
H	0.89968884350875	17.64781686575940	10.94737756542976
H	1.03393397531248	16.50795134193706	9.58753471477398
H	0.63349206715559	15.89850658616652	11.21905741169275
C	3.27709172266437	14.54410242639771	6.57205399274571
C	4.34517589668898	15.46146954588617	6.34472927231813
C	4.10652246315684	16.83271205635044	6.25182209613279
C	2.80187602337730	17.34140253670372	6.38423970345957
C	1.73279300931324	16.45598209527136	6.61801523293856
C	1.96415299718828	15.08605657193818	6.71625225062354
C	3.48333305987405	13.11918283546554	6.69405608771237
C	4.72768976275776	12.42489293575475	6.19258897734439
H	5.36669340856348	15.08390629976196	6.23938770728900
H	4.94287852792232	17.51691365001774	6.07298673952456
H	2.61986296828485	18.41837513917891	6.30819184656398
H	0.71399123780141	16.84434162230247	6.72206397276381
H	1.13357815199054	14.39807742342478	6.90398554371725
H	2.56110457297313	12.51730924369318	6.67874237356494
H	3.70044574602115	12.99730672462418	8.20173546644657
H	4.74951988316887	11.37314345691879	6.52320266204551
H	5.65472390503166	12.90814656560637	6.54886370830436
H	4.76656481172783	12.42655234211849	5.08325540029777

Table A5.16. Cartesian coordinates of a DFT-optimized reactant complex (RC) for NEB calculations in EtBn oxidation reaction.

Co	1.36509396188250	12.96831735005101	13.47069547670731
O	1.82354435923873	11.83502253927484	14.96683139020178
O	2.16836998651180	11.38279990557601	17.05299938805694
O	1.42132085146607	13.37652902938179	16.53316418948438
O	2.83290800799838	12.02583293061450	12.67399813949067
O	2.20171321411264	12.88160833665086	10.74175879726436
O	3.88898284657513	11.48621046691063	10.84465432026280
N	-0.08652037745444	13.85712129413127	14.22666788668798
N	0.04155400621824	11.79501524950395	12.90573213734076
N	2.08480121043259	14.63346804865239	13.39751244422956
N	1.79911126157214	12.23636921077921	16.25241538870179
N	2.98274031850671	12.13957082579733	11.35105355877697
C	-1.23197188946532	13.17057416087074	14.38763644265829
C	-2.29115779773242	13.76288109282901	15.08054053442855
C	-2.13724134318036	15.07463666900961	15.55209414050714
C	-0.95551826383837	15.78197200316628	15.29218243734288
C	0.07606127422702	15.13690587499219	14.60517236490757
C	-1.21563082425924	11.80738030904416	13.71737967291614
C	-1.15458107203793	10.67604731773623	14.77982922952643
C	-2.49677538062797	11.61297072008309	12.87707607168675
C	0.10895981212971	11.00068290213921	11.73479693546221
C	0.69967210249995	9.70873204598698	11.78919150538123
C	0.71317476497854	8.93486095637059	10.61559122782503
C	0.18311216240712	9.42127884325829	9.41695238739596
C	-0.34472960465160	10.71631395844126	9.36472220321770
C	-0.37632206000448	11.53164129155503	10.50527491688855
C	1.31335764523907	9.15339835340925	13.05218340614183
C	-0.84550942294619	12.96260707747833	10.37808274121000
C	1.38842795580880	15.73633848998150	14.15106474994337
C	2.23937448816567	16.20622584774732	15.35775735039210
C	1.08800022834519	16.97724721445574	13.27441478714878
C	3.33737010234503	14.95581893059062	12.79211406443877
C	4.54075738474279	14.61167261663308	13.47668695993586
C	5.76328840774848	14.99302462539983	12.90199576028771
C	5.81705961787471	15.65020341958294	11.66761969459360
C	4.63448053566511	15.90545415263994	10.97081077571156
C	3.37998017071358	15.55833464202178	11.50421774265866
C	4.54530818037457	13.81201703730064	14.75518126667801
C	2.15313346892604	15.76897775534785	10.64457237478302
H	-3.22286287214555	13.21397547147570	15.23827879528540
H	-2.95184626877097	15.55592637756263	16.10175305005735
H	-0.83687928844280	16.81844168162318	15.61787595294812
H	-0.21842297001287	10.71939836618766	15.35154633758627
H	-2.01049504736823	10.76890971123146	15.47044240579787
H	-1.21813716714180	9.70072439956299	14.27278637268796
H	-2.42771697838197	10.67649265650072	12.30203506175767
H	-3.36698142224587	11.53812472509461	13.55055395742044
H	-2.66358653480962	12.44781249357554	12.18195756684584
H	1.16317240966949	7.93632211433417	10.64937685370443
H	0.20955037921958	8.80258093875370	8.51384243600853
H	-0.71378312819160	11.11856990780673	8.41442993007587
H	1.46902864149929	9.93214636856466	13.80988125678247

H	0.67799002614140	8.36023408894466	13.48838307682452
H	2.29084318977652	8.69862785200868	12.82217603655529
H	-0.24733887290534	13.47880934005702	9.60847075251312
H	-0.72055072507431	13.51602901313705	11.32111551558578
H	-1.90517471187282	13.01692871196937	10.06876584368744
H	3.21680651755937	16.56528210487195	14.99714685779290
H	1.72314752077274	17.04304919080876	15.85829788650115
H	2.37742376134671	15.39236583018484	16.08031876402800
H	0.40273509930438	16.73606820904537	12.45022782911713
H	0.62299697421294	17.75448087614453	13.90332206487650
H	2.02646927439725	17.38301388541750	12.86671591951173
H	6.68593927468583	14.74145677937521	13.43375749110267
H	6.78335592031468	15.93100030447338	11.23563336781490
H	4.67175939885260	16.36507068417092	9.97652507891327
H	4.11318975724943	12.81625852562826	14.57317832967941
H	3.95732012323458	14.28244888678822	15.55599934087645
H	5.57623121187122	13.67012442849088	15.11226315283574
H	1.93377178899123	16.84297432051091	10.50476264335329
H	2.32980695713899	15.33108697440132	9.64861067518429
H	1.27057297200673	15.27338589134869	11.06939466169974
C	6.05920847041766	10.67969638327064	14.59968365205578
C	6.94123510540030	11.01544276667159	15.64414996289086
C	8.07261771757605	11.81114888566765	15.40796948663288
C	8.34449180561651	12.27941919010304	14.11406448103405
C	7.47364621677220	11.94904277604660	13.06353540847509
C	6.34174587210857	11.15964994487506	13.30442149115707
C	4.83999585785976	9.81608776049297	14.84804949198637
C	5.03228094661133	8.36441560329600	14.37286235185573
H	6.72953928296219	10.65776082836157	16.65892909518022
H	8.74281651767748	12.06596928767071	16.23677068792366
H	9.22803023085483	12.89980498938871	13.92606664327587
H	7.66689841710002	12.32011563495342	12.05113751872627
H	5.65238082066460	10.93706099364737	12.48315009886042
H	3.97447477724793	10.25727056135419	14.32526149763202
H	4.59577097173759	9.82481708332188	15.92482160843847
H	4.12717701037099	7.76287512419957	14.57170809648610
H	5.88330546010958	7.88542574262730	14.88914450342428
H	5.23551301752273	8.32941883860197	13.28769879727706

Table A5.17. Cartesian coordinates of a DFT-optimized product complex (PC) for NEB calculations in EtBn oxidation reaction.

Co	1.31849659855563	13.09499064565085	12.88035727719441
O	1.70779638017822	10.50024417570774	16.17541915761153
O	3.23584071154942	12.13555066037273	16.32287148515781
O	1.20529767760644	12.41866903318248	17.11869174137137
O	2.94783357941506	11.71098872194394	13.30897903243671
O	2.45180157282073	12.52998366094015	11.37528375400387
O	4.12136504007751	11.09312881719751	11.53962438290183
N	0.17043662420884	13.69488364941556	14.19657880047603
N	-0.02136504872038	11.86910967734253	12.53872088381159
N	2.20419185185091	14.68297034870974	13.19507087322164
N	1.93504878791646	11.63574154464429	16.55498771653755
N	3.22726943805726	11.74073507903340	12.05427739977232
C	-0.97294933549792	13.00602896741314	14.42027622838343
C	-1.84082977475983	13.42414963211584	15.43147149203670
C	-1.52614781269654	14.57593488015135	16.16548120158912
C	-0.37875064393418	15.31421131531985	15.84562270485508
C	0.46205945574727	14.85488694441815	14.82939461724960
C	-1.20358926334361	11.86834491672615	13.44649335584936
C	-1.37756418633352	10.53511895423038	14.21188638945229
C	-2.51055578547799	12.15944463818542	12.66106639277463
C	-0.03334202483463	10.99565204304757	11.41318540448776
C	0.44327979247791	9.65781291536629	11.51216022730705
C	0.40017429819181	8.83341017296903	10.37273683177145
C	-0.07148446918828	9.30781989464632	9.14636194532612
C	-0.47345894992216	10.64263161653010	9.03732340837240
C	-0.44914213707858	11.50327907471793	10.14714738139278
C	1.05295439436245	9.09954668909171	12.77870936684852
C	-0.82955698948049	12.95302188204188	9.94981486542432
C	1.67917347384436	15.56588696024567	14.27471949616450
C	2.69996010724162	15.83209161536004	15.40635980573320
C	1.22371125125280	16.92994803200409	13.68972493697093
C	3.31755261628579	15.13122064235190	12.42686681374829
C	4.65135404778195	14.88488457940536	12.85914066655185
C	5.72017770908659	15.33776357094682	12.06400244944437
C	5.49767755910979	15.99863375312582	10.85340738313208
C	4.18630039712425	16.18200345997056	10.40272026224411
C	3.08735071919995	15.74595089614102	11.16133338223598
C	4.96666849860802	14.10107028159331	14.11062841400919
C	1.69710785122443	15.90865589749535	10.59072145784796
H	-2.75563036012472	12.86119958531470	15.63395305004204
H	-2.18872005720696	14.91245563215332	16.96856979346969
H	-0.14074324846093	16.24041487149126	16.37493904049780
H	-0.49439166256852	10.31203389312940	14.82667987691522
H	-2.26147567540519	10.59204775113551	14.87093856333610
H	-1.54183756770443	9.71688419173744	13.49311620488041
H	-2.63446996136075	11.40429138798197	11.86747807244829
H	-3.38456785389336	12.10558337228898	13.33241624756881
H	-2.47962495261768	13.15892701618903	12.20205843538785
H	0.76774741694738	7.80371578573759	10.45458821587994
H	-0.09382807097294	8.65035093599375	8.27068407842447
H	-0.79809301699057	11.03808416492904	8.06761536984094
H	1.30352049064563	9.89452067627983	13.49291197886946

H	0.37604477832412	8.38341733446766	13.27871803235906
H	1.97842551813210	8.55219268000087	12.53280820977949
H	-0.33463693531110	13.35721075656273	9.05039065776656
H	-0.52713870402222	13.56264545247316	10.81459795106088
H	-1.91951857848660	13.07308365710556	9.80912988972790
H	3.59581380742759	16.31847489782666	14.98941531752284
H	2.25875604835008	16.51345237051379	16.15453824713294
H	2.98953964727573	14.89854340187681	15.90832521946614
H	0.41211031683100	16.79120569486304	12.95967066086413
H	0.86832987162204	17.59788012621100	14.49306905379629
H	2.07873909441980	17.41241076531722	13.18794615652174
H	6.74463685685568	15.14259588342015	12.40234841187782
H	6.34276025455179	16.34114903237984	10.24650267070790
H	4.00393211261148	16.65677564939870	9.43142398639087
H	4.06977609341620	13.61592384892926	14.51190763305550
H	5.40049544030017	14.74365278580701	14.89746401937943
H	5.71011061580710	13.32066747758128	13.88593327129446
H	1.34481215613676	16.95407901084110	10.66456568848105
H	1.68851535928903	15.63228273786930	9.52278610689609
H	0.97560564412680	15.26867148986625	11.12050884978853
C	6.13653114550421	10.63070539522866	15.18763848709765
C	6.75109500950070	11.43552233042752	16.20012186152728
C	7.81529601256238	12.28300411436433	15.90241689713302
C	8.31471594829588	12.36264069660799	14.58780733261528
C	7.72317906767539	11.58617333126629	13.57321361013659
C	6.65256206790018	10.73985192344854	13.85759315669172
C	5.05873581574012	9.75599135356137	15.52108270148876
C	4.39972192934684	8.80565988628151	14.57191906846749
H	6.36882697616725	11.37455391306474	17.22565914111290
H	8.26632814753211	12.88850397375575	16.69595162120329
H	9.15211692020916	13.02868416269006	14.35562057591153
H	8.09732190240858	11.65322043120171	12.54621330461859
H	6.19274195852834	10.16194267426323	13.05260572963859
H	3.68903834281261	11.41164708351637	15.79911773812020
H	4.81498172538755	9.65915731231810	16.58904415119364
H	3.40074652015927	8.51660943517927	14.93564207419757
H	4.99569929479677	7.87318999969460	14.46797411578536
H	4.28838432501949	9.23932142569676	13.56463208592167

Table A5.18. Cartesian coordinates of intermediate complex from the reaction coordinate of $[Co^{IV}(ONO_2)_2(NNN)]$ and EtBn (axial-O3′).

Co	-0.99448121516148	0.59324133947179	-0.45200674938781
O	-0.85389969669956	-1.73692456803733	2.93833132598146
O	0.27837107574838	0.00588964635456	3.58625479653083
O	-1.87871252687017	-0.06521574780772	3.88812082416829
O	0.72105326107131	-0.64395826639693	-0.58572847165698
O	-0.11703863135574	0.43039621244605	-2.24183237423711
O	1.66369381814468	-0.83529911163157	-2.57723207667039
N	-2.21293768773957	1.13088466986293	0.84501027313192
N	-2.18295517044665	-0.74915125144006	-0.74084656118667
N	-0.09863639450152	2.09342269157442	0.03519380609243
N	-0.81845588137201	-0.59792341842423	3.47469976012456
N	0.81649813928793	-0.38317256851916	-1.84086290816506
C	-3.33868797931704	0.40228538523076	1.00713389191673
C	-4.29268089732596	0.81529490566881	1.93766886496842
C	-4.05841376384909	1.98432566727731	2.67229033333032
C	-2.89534112090770	2.73345774958462	2.45305447630882
C	-1.97133097474185	2.28149851755201	1.51068027630948
C	-3.42799891432593	-0.79081757695975	0.08471850256383
C	-3.55329553061297	-2.09547355408586	0.90945825509192
C	-4.68076574117269	-0.64789414360132	-0.81982560156316
C	-2.00219103377016	-1.74370234274480	-1.74664631417329
C	-1.36044957996070	-2.97433163773703	-1.43305095582699
C	-1.20390929535123	-3.92274737078141	-2.46039680336315
C	-1.63471991176508	-3.66685205661221	-3.76427978637916
C	-2.20077817140886	-2.42575952221960	-4.07261315967502
C	-2.37925853147345	-1.44171902719107	-3.08722220016663
C	-0.79539221103333	-3.28489379976927	-0.06611016517281
C	-2.92365399395216	-0.09075988425907	-3.49467610844587
C	-0.69546939533112	2.97108478484551	1.08685566681321
C	0.23489085341993	3.17466728952333	2.30683063556322
C	-1.03939889419083	4.35959162858408	0.48367111633248
C	1.13281667170176	2.48593228475858	-0.56840222574794
C	2.36841953426471	2.08566388008855	0.01304475354261
C	3.56000140696034	2.46320238271074	-0.63280663929939
C	3.54482620372543	3.19648615679157	-1.82161638172079
C	2.32182270644818	3.53515256114900	-2.41031566939261
C	1.10219087352616	3.17571979928235	-1.81482153032266
C	2.45771918108058	1.23145518146322	1.25359553424314
C	-0.18718249705643	3.50124442967091	-2.53540375435392
H	-5.19960687124503	0.22600934932881	2.09199475264108
H	-4.78678287712692	2.31437363201565	3.41863959784683
H	-2.70435276070931	3.65283724074909	3.01159393876274
H	-2.73519973721895	-2.17882619156153	1.63913932337578
H	-4.51456234512763	-2.08501234855231	1.45066088495119
H	-3.55248081478497	-2.96208236945498	0.22981876663593
H	-4.69828238196986	-1.46852908602827	-1.55475864706345
H	-5.59247846724088	-0.71299643392655	-0.20319762297034
H	-4.67976781832492	0.31562824660252	-1.35048719594024
H	-0.71132372829006	-4.87260983241711	-2.22344683882470
H	-1.49850648085561	-4.41970557752049	-4.54759214658620
H	-2.49383279292239	-2.19860297263885	-5.10394936480685
H	-0.75468142073454	-2.40393032099732	0.58651470833068

H	-1.38815573770379	-4.06400070822281	0.44548495290890
H	0.22954932751486	-3.67595279893268	-0.17281648946893
H	-2.41941422722849	0.25333428207749	-4.41284319089134
H	-2.75869640655223	0.66525618158158	-2.71251433805995
H	-4.00718172449859	-0.13709086478872	-3.70766661341142
H	1.18992368439773	3.61038604832386	1.97452392789430
H	-0.24252329916910	3.88455367274035	3.00345186994406
H	0.41052749400029	2.22498941665573	2.83130689363844
H	-1.77128170769439	4.26717438515717	-0.33234731301271
H	-1.46021045454522	5.01050620793375	1.26792803621903
H	-0.11992438413877	4.82759725515793	0.09720117673374
H	4.51135710378462	2.14189624686046	-0.19493173897269
H	4.48504326840107	3.47549150594405	-2.30882696292990
H	2.30376674835066	4.07000379198926	-3.36681972102041
H	1.50173562994892	0.75976095406085	1.51539386704927
H	2.79803721063909	1.82201121133161	2.12256144749001
H	3.19813564947197	0.43371030225043	1.09548735527009
H	-0.43807028035262	4.57467531562727	-2.45361239720002
H	-0.08704417407725	3.26467954537649	-3.60751271166686
H	-1.03229309215941	2.92023211424670	-2.13684342488446
C	3.79159727606417	-2.08557975196908	1.46291367832558
C	4.84201911446143	-1.55158870959031	2.23260754685167
C	5.90225469376907	-0.85815688581639	1.62875493712857
C	5.93078441878284	-0.68917616032281	0.23690367180487
C	4.89453106074226	-1.22419105209856	-0.54510507701189
C	3.84107611717729	-1.91831445033198	0.06317169256705
C	2.62065687482964	-2.79456537581266	2.11152424724199
C	2.57263749301718	-4.30111097414957	1.80446749911027
H	4.81610606825733	-1.66523045489281	3.32270490439114
H	6.70502872221770	-0.44379993250262	2.24896927407493
H	6.75428663197562	-0.14294043359828	-0.23630649652968
H	4.89540421071877	-1.08690820918811	-1.63165959341683
H	3.02544246935652	-2.30339155992362	-0.55636027991801
H	1.68282920802343	-2.32091634489905	1.77191593881657
H	2.65908357967181	-2.63950654435857	3.20373014372832
H	1.67981582173941	-4.76363440572337	2.26078798442148
H	3.46855558503642	-4.81659547585688	2.19394448098437
H	2.53220643863470	-4.48445299560740	0.71558000934173

Table A5.19. Cartesian coordinates of a calculated TS structure with axial-O1 for DHA oxidation reaction.

Co	2.10023399548103	12.86636954486028	12.89605644702025
O	4.09143071626647	12.07989231991004	14.02276502765671
O	4.70058229697619	10.86026851796051	15.79183109213583
O	3.42929095183302	12.62055281703262	16.06516462912431
O	3.21083703159601	12.33580819414794	11.43756037553968
O	1.58558118562124	12.95098819790729	10.08158236226559
O	3.45339626036050	12.12433658841514	9.27892607976893
N	1.15928132477183	13.32831801570725	14.43244504450609
N	1.03198310468212	11.36024262467782	12.96435060247713
N	2.34405852019346	14.68770079669631	12.76477549440364
N	4.07828961579864	11.83571142847002	15.39236645471845
N	2.72073401401370	12.47981081715414	10.20564455660912
C	0.39810323002256	12.38856540920012	15.02727801063222
C	-0.24642572234272	12.68669203989880	16.23108841474084
C	-0.10429557422605	13.97039903956532	16.77493110795569
C	0.65440447884755	14.93685479482205	16.09979483329101
C	1.28176233085162	14.58588822394015	14.90228128856298
C	0.32039188156244	11.08838396051970	14.24874388545811
C	1.03162021773020	9.95503413447946	15.03431151651852
C	-1.16130191285229	10.68440438851548	14.06414905314340
C	0.77029263119271	10.51348922299294	11.85088064652363
C	1.62686915386135	9.41188172294999	11.58236111964785
C	1.34427204096315	8.58343003984981	10.48227891412963
C	0.24949319213520	8.83242652365950	9.64944329596768
C	-0.56089332653429	9.94594102368880	9.89188035541769
C	-0.31087873031742	10.80810024996597	10.97218088018638
C	2.84234892689251	9.12404269432561	12.42469482191782
C	-1.16118120153253	12.04700967108170	11.12661104091972
C	2.11835599433310	15.48278483758553	14.01037639359446
C	3.47595973522444	15.77693363964070	14.70421945085873
C	1.39252566025894	16.82494670164065	13.76959569655953
C	2.70743357056873	15.38366500354911	11.57941730583667
C	4.07476088425357	15.52178036796799	11.22134555072340
C	4.40185311788052	16.22419098192391	10.04774116823345
C	3.40974551850332	16.77281593967173	9.23080672270300
C	2.06369589128329	16.58984858007521	9.56461301039857
C	1.68870750610197	15.88662282225203	10.72032310160901
C	5.17997760901649	14.91434757394398	12.04520475440593
C	0.22201459736321	15.63030882822797	10.97621163812893
H	-0.85564760554980	11.92892753134500	16.73039560262632
H	-0.60021553436816	14.22369797454692	17.71703886465057
H	0.75512837809833	15.95020234558072	16.49668048287808
H	2.10520016151669	10.15786989237192	15.14557409641843
H	0.58453486728766	9.84470589861972	16.03763375452982
H	0.90749888990500	9.00516536815267	14.49110610884238
H	-1.22945114247799	9.81855971272033	13.38644793980542
H	-1.59331855582661	10.39412415549005	15.03695773408838
H	-1.75721445562716	11.50980500427173	13.64972685412812
H	2.01101617510808	7.73813765461832	10.27573901742820
H	0.04605675334939	8.17851694479102	8.79463355996989
H	-1.39226954360199	10.17437211788969	9.21490616124293
H	3.18726688815547	10.02672714017168	12.94569154828652

H	2.64433550336983	8.34637101775651	13.18400361066333
H	3.65748004685835	8.75226516457761	11.78782428015072
H	-1.19039157318064	12.59925362017708	10.17275251064493
H	-0.74906891706722	12.71994268209769	11.89244583304883
H	-2.20255423880256	11.79329382917268	11.39762355022309
H	4.06962023372792	16.45320860272464	14.06951937551725
H	3.30522736669739	16.26821377547103	15.67820907826494
H	4.03272393618462	14.84418355237312	14.86860569627767
H	0.36575742687486	16.67178899584631	13.40785770990284
H	1.35088757837116	17.39955125383403	14.71043332334024
H	1.94709928202688	17.42209495490510	13.02851770015216
H	5.45807303210276	16.32548226118311	9.77267695606754
H	3.68253236525796	17.31563058165847	8.31945848176357
H	1.27937740354873	16.97454317978095	8.90234750644565
H	4.79224693820542	14.15767054041149	12.73953439184800
H	5.72079980146492	15.67832133022698	12.63251383321828
H	5.91526120705208	14.43609732713479	11.38253034836177
H	-0.32334986617279	16.56799784762191	11.18951673812512
H	-0.23711038653390	15.17479333023813	10.08288404329896
H	0.07953208582161	14.93771213812829	11.81835829238547
C	6.24520488398598	9.79258957089123	12.67981348727142
C	6.23243919971786	9.69147307815187	11.25798325786417
C	6.36818445419452	10.94376359510921	10.42896215429121
C	7.16305107099089	12.03487229893700	11.09988238899229
C	7.16177022998581	12.11920863942677	12.52264951105344
C	6.47904044515200	11.09219973418092	13.30516986193633
C	6.06428015366976	8.62342851944142	13.46161808369829
C	5.90529917826832	7.37917003445001	12.85323311179905
C	5.91212366258271	7.27957716775302	11.44920832991082
C	6.07128653990952	8.43154910282252	10.66436442575169
C	7.88527385698462	12.98192202713511	10.35936517073367
C	8.59314958828849	14.01074742549607	10.99837710684266
C	8.57876461636735	14.10851574474855	12.40212966957512
C	7.86620450060202	13.17511902817409	13.15379541987939
H	6.78703689185421	10.71055500219631	9.43508921674035
H	5.34437707277259	11.34003130861839	10.23210868855493
H	6.75846797795609	11.05107455199362	14.36821066103989
H	5.14689626548451	11.58999904192912	13.59820573499486
H	6.06004381006244	8.71399574473074	14.55243259400219
H	5.77652771988882	6.48159111973128	13.46684083844685
H	5.79130674455876	6.30381763275022	10.96710172759946
H	6.07155161709926	8.35193273378338	9.57156898292483
H	7.89366874534552	12.91097657481348	9.26605264809611
H	9.15451927051496	14.73824499404928	10.40289107431573
H	9.12771553418390	14.91267538328289	12.90285086207497
H	7.85741874916656	13.23806994063837	14.24780886272243

Table A5.20. Cartesian coordinates of a calculated TS structure with axial-O3 for DHA oxidation reaction.

Co	-1.36457176965377	0.53292811163345	-1.77501365047626
O	-1.02879065625019	0.47444914127968	-3.72299083795616
O	-3.07907740353909	0.55611380905068	-3.07816526751437
O	-2.63461628406104	0.48694696175557	-5.24264022932003
N	-1.22018697898843	0.57290234435046	0.07481407013917
N	-1.32789572603818	-1.28099513583501	-1.54902396202026
N	-1.19729879655841	2.34866314121029	-1.63691644068182
N	-2.27930768753671	0.50512077002259	-4.08408975959349
C	-1.11912035355845	-0.60339147764110	0.73454424747845
C	-0.93547675496179	-0.60367654108874	2.11866314745372
C	-0.84458590568089	0.62473483854819	2.78619200217814
C	-0.88732110163090	1.82378936502710	2.06396188362443
C	-1.05866179338744	1.77142628618844	0.67928821898809
C	-1.18117343398613	-1.81675482068112	-0.16577443812982
C	0.13359990718176	-2.62428880630855	-0.02899921477601
C	-2.36035858091782	-2.72534984436233	0.26065805708458
C	-1.36857205829035	-2.20228904099234	-2.63348274218142
C	-0.16585858755089	-2.48559209481798	-3.34332166188169
C	-0.21283169215183	-3.40022362393867	-4.40815450645116
C	-1.41358487337623	-4.00269957983256	-4.79747005882358
C	-2.59919933908987	-3.66178911818158	-4.14174693460138
C	-2.60660707087997	-2.75323718697530	-3.06777203778544
C	1.14403915322840	-1.80463883297048	-3.01744582657489
C	-3.93583285692953	-2.36288369973419	-2.45894705557479
C	-1.02847473858492	2.94069761781982	-0.27867495631562
C	0.33951511411564	3.66179215681847	-0.15379054431371
C	-2.15065997094990	3.94699390173227	0.07544085155312
C	-1.16627628018679	3.21558560031896	-2.76668550877367
C	0.05987403217570	3.38329380962961	-3.47558641080619
C	0.08315453141264	4.24192868797906	-4.58669780451631
C	-1.07177580735022	4.89970574286887	-5.02220903626672
C	-2.28323228782776	4.67088202099414	-4.36534296744116
C	-2.36105335836371	3.82215555821362	-3.24608095452331
C	1.31914174418364	2.63618096075779	-3.09822211101905
C	-3.72023187219058	3.55252766959656	-2.63780537579542
H	-0.85000283608146	-1.54370019762433	2.66766071893878
H	-0.70670429476303	0.63903096565543	3.87073397427781
H	-0.76052847629298	2.78679722850918	2.56433872072628
H	1.00893456576839	-1.99917987786468	-0.24780477676513
H	0.22898145427891	-3.00981348250478	0.99976402453874
H	0.10745296776286	-3.47814144109022	-0.72568140593305
H	-2.43592087026595	-3.58250835983534	-0.42682754715949
H	-2.17203687085524	-3.11235599697798	1.27687724319330
H	-3.31229526448881	-2.17480376411153	0.26253552115487
H	0.71210575736496	-3.62363478238333	-4.95229587228968
H	-1.42980260461621	-4.70988128887714	-5.63353069748260
H	-3.55169377799625	-4.08862771699430	-4.47671496693654
H	1.00248459851005	-0.92836840838390	-2.36818927791033
H	1.84251299216754	-2.49137635577813	-2.50613215347182
H	1.63199137158486	-1.46958509817067	-3.94800570004482
H	-4.65029495194459	-2.10728663480738	-3.25947021050971
H	-3.83815645773133	-1.48647782167095	-1.80472269602285

H	-4.37418840260239	-3.19400052588342	-1.87694414614491
H	0.40570817298217	4.44590374323551	-0.92563769105936
H	0.42218720357700	4.14088397163554	0.83652521498445
H	1.16570437957089	2.94791920994761	-0.26998559325917
H	-3.13710538745628	3.46137454314792	0.08148871841081
H	-1.96057907934003	4.37489257436955	1.07448097966757
H	-2.15418317041290	4.77072777924009	-0.65565142834692
H	1.02573678583521	4.37527726199365	-5.13003805793809
H	-1.03381706509705	5.56154784540875	-5.89390427297600
H	-3.20254302603534	5.14008712022904	-4.73459139209857
H	1.10603004404121	1.79211097725517	-2.42756265770698
H	2.04562631120847	3.29502230894700	-2.58925729649799
H	1.80778732688773	2.24371001995207	-4.00556220716885
H	-4.10829403124438	4.43971454778157	-2.10493155660073
H	-4.44109957527458	3.30456213717573	-3.43496216491759
H	-3.68949693149249	2.70599600932837	-1.93930504827498
O	2.05862833402893	0.63827948327456	-0.08738167257521
O	2.97028764428734	-1.01368176274900	0.99729028919330
O	2.39921194828063	0.84188203770092	2.06999876955980
N	2.45008128220402	0.22490400417494	1.00428554915637
C	4.16742856524717	-1.18949387471917	4.14113083913942
C	3.59426721295760	-0.27290690801996	5.06640215180408
C	2.08989572138126	-0.19192349167250	5.19591265137529
C	1.36010077427567	-1.46243377094286	4.82126927303911
C	1.95792679445893	-2.36215849383025	3.89222369798917
C	3.30122034589366	-2.08822915033622	3.37872406013452
C	5.57362057236997	-1.20292232328226	3.96810509527036
C	6.39380458986599	-0.34751869879861	4.70345821796394
C	5.82390337158371	0.54201096342283	5.63177680168305
C	4.43250179471706	0.57135960292887	5.80639761028084
C	0.09281116438658	-1.75651166353252	5.34574483145497
C	-0.61234779311885	-2.90258959689774	4.94568696531852
C	-0.03811292018387	-3.78049041623425	4.00961837329199
C	1.23527787438984	-3.51475429952205	3.49244421305700
H	1.80354319468954	0.13308974528390	6.21182276308114
H	1.74628228316416	0.60850098853400	4.50554003597470
H	3.80903995743830	-2.95348565867498	2.92369178476415
H	3.10026451153047	-1.41227770056242	2.18125465618874
H	6.01175357540298	-1.90381612896773	3.24884464763210
H	7.47925471722840	-0.37328088415870	4.56180690494676
H	6.46288474845776	1.21113205399164	6.21731821146740
H	3.98969691607627	1.26724608538305	6.52851221551946
H	-0.35118459871005	-1.07735185193667	6.08354102758975
H	-1.60082686118959	-3.11317487516328	5.36700936674014
H	-0.57897274198324	-4.67599414875614	3.69680352594213
H	1.69656570149446	-4.21023444922716	2.78355866025468

Table A5.21. Cartesian coordinates of a calculated TS structure with equatorial-O2 for DHA oxidation reaction.

Co	2.11196668567260	12.88965218349252	13.04958581840514
O	3.80478766075987	12.20656085296602	13.90355746370645
O	5.24032575834895	11.99549931824124	15.52160570130641
O	3.48610626578637	13.27510441476797	15.81700372444345
O	3.23983535744717	12.26212582110897	11.39076624764776
O	1.43397808866353	12.79233894269936	10.24630830371762
O	3.09278504592093	11.84525020314603	9.18289732910686
N	0.96208433034491	13.45312639810205	14.42125603366893
N	1.09704333197143	11.33710369061733	13.18210849200582
N	2.28965966492242	14.71545135035733	12.77926205313501
N	4.18404152980813	12.51396496717997	15.13144044949682
N	2.53782479020549	12.30006745156536	10.16393462331058
C	0.20442293763166	12.52714553279769	15.04073614955227
C	-0.63905736614515	12.90489361687714	16.08778634867975
C	-0.69881188622728	14.25633408222510	16.45461975108718
C	0.06641153378133	15.19859402677950	15.75704850441723
C	0.89778463932881	14.76385648797037	14.72012661855030
C	0.39892073186939	11.13085530694459	14.48750976983798
C	1.28430851547462	10.34054795110060	15.49219261784694
C	-0.94960337072665	10.39601773489590	14.34565262257742
C	0.91331863225679	10.38213415371295	12.14729383847067
C	1.79939293852445	9.27812226734765	12.01467806462123
C	1.59175875245746	8.36552509793336	10.96542469486577
C	0.53915945518643	8.52878829978877	10.05861681557107
C	-0.31945237834624	9.62548697707668	10.18614511638044
C	-0.15081986628017	10.56564637697406	11.21691642277726
C	2.94400601868238	9.06102839849254	12.97181456144959
C	-1.09146162353940	11.74740770667880	11.29496740506811
C	1.75080275983806	15.63792116820256	13.83159955392547
C	2.85728031788681	16.31137285511926	14.68658937084237
C	0.87317058691744	16.76665655561582	13.23387377522151
C	3.02178421048124	15.31372364434622	11.71295111541200
C	4.43782059442214	15.45516928123928	11.80840955207779
C	5.12440250070275	16.10738685351632	10.76933787610923
C	4.45836591504952	16.56694854510336	9.62838613443178
C	3.08033028064536	16.36979870155827	9.51362847934531
C	2.34055920574933	15.75347065435943	10.53980207374349
C	5.22854319497299	14.87573785902176	12.95419653402135
C	0.84943284426265	15.58990947857461	10.33999676807954
H	-1.24400539666233	12.15416257958889	16.60243344901028
H	-1.35420927945448	14.57599108747118	17.27064181994539
H	0.01675425383405	16.26099966311883	16.00879674673063
H	2.29432694816623	10.76830097361205	15.54159671884810
H	0.83296309398296	10.37938842346192	16.49869112832661
H	1.35221542009859	9.28737157832026	15.18278222579353
H	-0.79503959950877	9.42589446698902	13.84743881132974
H	-1.37681235200309	10.20085298235164	15.34388271700008
H	-1.67447278034250	10.98286791117907	13.76329728546114
H	2.28020353646299	7.51993922679450	10.86221026424714
H	0.39684490385348	7.81037052101471	9.24410259274664
H	-1.13289472660179	9.76966710286367	9.46557618709787
H	3.32619761925923	10.01243549445216	13.37044971512975

H	2.63035461076949	8.43867428060826	13.82915520071504
H	3.76119671532040	8.52306920268342	12.47281604225378
H	-1.21121214540346	12.20742989541010	10.30016668245210
H	-0.71132657758986	12.51423840543709	11.98673632885984
H	-2.09634824963283	11.43496778344634	11.63529043068820
H	3.52621441450746	16.89551011362926	14.03376540002799
H	2.39004690157511	17.00411975951300	15.40788191373604
H	3.43221993059892	15.56086303247433	15.24634441164301
H	-0.02416305729791	16.36338907844685	12.74423804892830
H	0.55603795728440	17.45360340493884	14.03643874499844
H	1.45830756958950	17.34639556277819	12.50251530815673
H	6.20607100588007	16.24527728727570	10.86455047756696
H	5.01392613984824	17.06769457968273	8.82812016219968
H	2.55264085673523	16.70396174134534	8.61263050365490
H	5.44952756965468	13.81370564322017	12.76222289834250
H	4.68481841367969	14.91109165584346	13.90321292362738
H	6.19121261520975	15.39764996271144	13.06849360866258
H	0.33592583851397	16.56770487249216	10.38141156006482
H	0.64787896781050	15.15507655442227	9.34708724888384
H	0.41020996705013	14.92857714181694	11.09848883867508
C	6.34644460977874	9.49036351486184	12.15701421044723
C	5.68076056372365	9.93005168991018	10.97516678760667
C	5.67297861436667	11.35235563869698	10.64411783707991
C	6.71762434242251	12.19154133902626	11.21910804744093
C	7.36219081194436	11.78741714887301	12.42449217092104
C	6.91174893209868	10.51846857417838	13.10515115607081
C	6.44225440179291	8.11601957754468	12.41542676358043
C	5.87839025421721	7.17576298312918	11.53940529332317
C	5.19562014455287	7.60858410810350	10.38758509798889
C	5.09067066005635	8.97246509133722	10.11232668106116
C	7.13799224271533	13.38099358931504	10.57265571702892
C	8.17191446365691	14.15067515157572	11.10342607195478
C	8.79153417012514	13.75975544490667	12.30446770760950
C	8.38363533317846	12.58614616466918	12.95534598842594
H	5.39661884729086	11.59035335781852	9.60848236169713
H	4.36116825512432	11.84186662672680	11.15271688292114
H	7.73125651431494	10.08772858935127	13.70565524031926
H	6.12195364990428	10.80183902495690	13.83779990510854
H	6.96779254385329	7.77625883951561	13.31503521494778
H	5.96848445777982	6.10603977337123	11.75538676924704
H	4.75066594775032	6.87707544246210	9.70504871365477
H	4.56326742220475	9.31971117361177	9.21816369695596
H	6.64127322079889	13.68372339272544	9.64516914369968
H	8.50020155256304	15.05894334933426	10.58718220885780
H	9.59871684992680	14.36606894835148	12.72866987128647
H	8.87400052396036	12.27894428774922	13.88559729003992

Table A5.22. Cartesian coordinates of a calculated TS structure with equatorial-O4 for DHA oxidation reaction.

Co	2.07943814089072	12.91259491116810	13.17074607931084
O	3.29790822818063	12.31489176215556	11.72485795188062
O	1.94721321069103	12.87246847595446	10.07694211900377
O	3.90412001137743	11.90128761202195	9.69825156355636
N	0.89586281219181	13.47945802351584	14.48072782736505
N	0.94409177276387	11.46005452075810	13.09719363419310
N	2.37567468923477	14.71362935855221	12.95925764114990
N	2.98029790897067	12.39654691511254	10.50620142288377
C	0.03199627945566	12.57997584196798	14.98892631819276
C	-0.81885410732437	12.96107870277971	16.02897151949540
C	-0.76544575384011	14.28203431638978	16.49628610418431
C	0.11167059878469	15.20059672663053	15.90383360055058
C	0.94510197877820	14.76692432400221	14.86949633700159
C	0.10953203806230	11.22290939771232	14.31130732042516
C	0.80898801526782	10.21009038472146	15.25715674005459
C	-1.30482690489549	10.69431887846611	13.99021714063005
C	0.84684587976695	10.59644694468528	11.97540190271912
C	1.76553290032777	9.52242308230024	11.80070545780403
C	1.65773531569598	8.72666234670724	10.64598383401673
C	0.67709529581445	8.96993807504377	9.67980676325115
C	-0.20045452440879	10.04614057061257	9.84386735596609
C	-0.12084141424682	10.88369093520205	10.96784510757633
C	2.86186716607298	9.23190787109461	12.79850426030393
C	-1.01705108936706	12.09927952523558	11.04319335504509
C	1.92938394103524	15.60340933495947	14.07545535867559
C	3.12944328813033	15.99851648336141	14.97434020825364
C	1.24099154069826	16.89662033473110	13.58172688202433
C	3.10228038524910	15.28972149590450	11.87737984647026
C	4.52742668548848	15.28258889679127	11.86721363903353
C	5.19674046572251	15.86208429173976	10.77392602107658
C	4.49631107128777	16.42479485458519	9.70325451129128
C	3.09978601913809	16.37693061355662	9.69414953988331
C	2.38433651114383	15.79896283743860	10.75536595950560
C	5.34557457218348	14.64513755132427	12.96604682610695
C	0.88092146252139	15.68764533689114	10.63390560982925
H	-1.51538757935587	12.23873348189174	16.46212465479233
H	-1.42227893067049	14.60069552804918	17.31151989117116
H	0.14710682022832	16.24050222009063	16.23840772005494
H	1.84317104455849	10.51601629291587	15.46142015941261
H	0.26181837865195	10.14257599756702	16.21342636937451
H	0.81389100858063	9.21476839799282	14.78572318879475
H	-1.23075074781037	9.78371412242942	13.37427874664991
H	-1.82684048187043	10.43102182946438	14.92571430285422
H	-1.90742702249683	11.44065222948258	13.45300681961128
H	2.37243330337051	7.90819024793174	10.50238069780344
H	0.61843065679002	8.34695817653452	8.78277262263391
H	-0.94448876197756	10.26267732089024	9.06910201269072
H	3.14453184869325	10.12671526742759	13.37140025845130
H	2.55063448981307	8.45073028603617	13.51638266846233
H	3.75726618634520	8.85487158528555	12.27705973822945
H	-0.99478957306850	12.64719571416513	10.08557569099422
H	-0.68810640976940	12.78657088884644	11.83710198262065

H	-2.06913655214411	11.81917004048984	11.23361096952569
H	3.83386557135547	16.61229296404411	14.39028429177012
H	2.77447028677723	16.59642220219460	15.83178986719516
H	3.63784254853603	15.10363009709479	15.35685535660233
H	0.29254154043877	16.67898939432627	13.07001779831571
H	1.03304674187750	17.55865868197229	14.43924271238382
H	1.90913871770453	17.43473519808463	12.89028489742378
H	6.29287127775179	15.85346773336805	10.76693967073807
H	5.03725450275596	16.86742291898137	8.86015789110241
H	2.54559964247402	16.76075232285119	8.83209882271120
H	4.78500861870058	13.85482371541457	13.48407827898037
H	5.66615438083653	15.38859268488687	13.71776381407457
H	6.25881043285966	14.19677000735612	12.54124533793421
H	0.38844632479707	16.66752423564535	10.77029141178696
H	0.61704692599925	15.32539383751277	9.62604147804485
H	0.47254304418137	14.98426312452522	11.37405380280865
O	3.59809068848086	12.13030898174984	14.23700775426712
O	4.77031750291593	11.64769377670692	15.99860787582120
O	2.98688851432691	12.89959580395491	16.23287363353953
N	3.78526092569001	12.23695911902912	15.55217959285643
C	2.42926972356366	10.88478196494587	6.81229020289744
C	1.03404093879926	11.14856893886904	6.68874835327786
C	0.52421665555606	12.53189571634766	7.02248913318671
C	1.51640585675128	13.63451239643455	6.72815111165562
C	2.90963075306194	13.34677673583749	6.81447533458100
C	3.34448344912994	11.98354802528192	7.09964095663072
C	2.89690553669326	9.56252591674643	6.60322108069953
C	2.02013550364930	8.54239242500086	6.23281831016847
C	0.65150597908662	8.81994915260736	6.06502792972800
C	0.17018100819946	10.11744930779644	6.29962096214492
C	1.10045713292796	14.92922175522479	6.39285455333580
C	2.03450863553524	15.94798850037107	6.14737719019501
C	3.40951991015509	15.67398329513685	6.25009853069340
C	3.84065215437631	14.39125235602211	6.58828369059955
H	-0.43869479273272	12.72710083989351	6.51970699482318
H	0.31496337551063	12.54894867875824	8.11414423684977
H	4.41022957600196	11.77453224628683	6.91795024074357
H	3.51874733894911	11.97632945769807	8.58309381137992
H	3.96738163236812	9.35591869697540	6.71256674857264
H	2.40059893996955	7.53004277330941	6.06124614580620
H	-0.03838085145064	8.02723717415271	5.75759074837425
H	-0.89814208268608	10.33167634414662	6.17843685161209
H	0.02820549159047	15.14281945990547	6.31169966999931
H	1.69097301934221	16.95176897253761	5.87636325767456
H	4.14284303706919	16.46550415141607	6.06362730941768
H	4.91133382141027	14.17298375702273	6.66650310374823

Table A5.23. Cartesian coordinates of a DFT-optimized reactant complex (RC) for NEB calculations in DHA oxidation reaction.

Co	2.41364070877143	13.26939020597032	13.08914684442855
O	3.54025247591525	12.87613052027639	11.59123514036965
O	1.63369781216440	12.74112429792610	10.50420551078676
O	3.53360747113056	12.39221980756716	9.46173694850977
N	1.28103509874159	13.65253073220157	14.52522255551687
N	1.90650287556310	11.52544258452569	13.45451655281679
N	2.03654994198814	14.99454578170733	12.61624931747595
N	2.87445818143373	12.65728162229543	10.45632955801784
C	0.88185211666410	12.63547858274938	15.30931208812702
C	0.11045461377648	12.90360041507184	16.44276622290304
C	-0.24262994363820	14.23151440249020	16.71936100048885
C	0.15963911602209	15.25951069768475	15.85576700052231
C	0.93305325960353	14.93344386442743	14.73926166948525
C	1.35744135581992	11.27928852929985	14.82637830254661
C	2.52266780026561	10.78589467289359	15.72715573545939
C	0.22735111602045	10.23261088952811	14.89483309141738
C	1.79650977131006	10.51945399812582	12.46666829308141
C	2.94578448292192	9.73763218878949	12.16043489476834
C	2.81721553956237	8.72142273379042	11.19955422084429
C	1.60402896407417	8.49285400245626	10.54033723227804
C	0.49802130276269	9.30478971153765	10.81364715100427
C	0.57414653694932	10.33622018906838	11.76171659476301
C	4.26283996669609	9.96275640102948	12.85993609052332
C	-0.59821820828477	11.27507127736193	11.92935269650094
C	1.44866386937082	15.88065061133807	13.67784354143321
C	2.59184239064561	16.75925186162094	14.25615602810661
C	0.31965873258948	16.81549017905958	13.19326310403681
C	2.31618830551602	15.57546961234992	11.34750191384989
C	3.64823006773492	15.96920081005879	11.03232041805155
C	3.88372554776723	16.56369055044703	9.78086585678466
C	2.85619539447172	16.74131454420528	8.84983133772829
C	1.56776983553220	16.28856476051321	9.14838993438355
C	1.27451937363009	15.68838540782501	10.38311664798714
C	4.80500348520380	15.77694844302996	11.98418928758725
C	-0.10464106316184	15.10777422981671	10.59963262622224
H	-0.21022036190487	12.08791347068080	17.09532277298129
H	-0.84514674860657	14.46435232772989	17.60263208624836
H	-0.12308676041870	16.29768881104712	16.04667769724777
H	3.40132992542593	11.43111312889358	15.62029574757749
H	2.20586417251086	10.78260994136834	16.78253563557206
H	2.79964580449678	9.75846114693568	15.44790296974984
H	0.55999791812042	9.29272786367406	14.42790034042374
H	-0.00234253104608	10.02105484462732	15.95259532938224
H	-0.69219788959495	10.57374478182364	14.39938427896338
H	3.69318995466248	8.10783647667939	10.96195881060116
H	1.52921631531100	7.69912372290873	9.78966416838202
H	-0.43670362291063	9.16057926181041	10.25993798570468
H	4.42255990226043	11.02718132113740	13.08550939515697
H	4.30369595244896	9.40828972041807	13.81399910950371
H	5.09360289595701	9.60456408499364	12.23068611620969
H	-0.82706125084057	11.75206533130806	10.96143990354782
H	-0.37867832586677	12.08024895257500	12.64690538918829

H	-1.50519233161463	10.73740524677492	12.26011575457776
H	2.95049919130643	17.44643517889138	13.47365472396984
H	2.20256252076903	17.35446420686282	15.09951932894817
H	3.41965232113878	16.13616911037940	14.61766316489065
H	-0.58825875775121	16.25753422475392	12.92629022049565
H	0.06938720720784	17.52347777913278	14.00072784383168
H	0.65730835726978	17.39904545649519	12.32266935524548
H	4.90444397383268	16.87705495226981	9.53530630596209
H	3.06703565604416	17.20070371618149	7.87856373722042
H	0.77130425205544	16.36984132160206	8.40001749135444
H	4.63286604252489	14.94077213246237	12.67550844711097
H	4.99410613807016	16.68791109023625	12.58058618513652
H	5.72285215666475	15.56196800768659	11.41383768057274
H	-0.87632624755961	15.89801327441677	10.63060650436154
H	-0.34986060668954	14.43265720214926	9.76317601554556
H	-0.15684805065305	14.51649958905749	11.52453149968661
O	4.17307892636020	13.16933258344820	14.02860330755396
O	5.68205710057237	13.57764042693831	15.52854313711441
O	3.59921630807265	14.08801916595161	15.97701843672407
N	4.48721813154780	13.64043078359635	15.23647129805294
C	7.69738272046603	10.89419055613277	16.78075201906644
C	7.16980763792172	11.42086654247558	17.97905017973023
C	5.68106104867864	11.28419553310964	18.23011651845019
C	5.15233620870432	9.95236188316164	17.73745606690782
C	5.68534890000366	9.42150837178934	16.54149081195402
C	6.74521791204712	10.22139833154340	15.81247516372833
C	9.07112706893199	11.01318024690201	16.51807266685797
C	9.92001497378489	11.65494029569980	17.43039879829334
C	9.39609337867868	12.17761949425554	18.62118428496447
C	8.02627919030170	12.05536662968750	18.89238482884848
C	4.15956400706702	9.23791794854493	18.42835535199791
C	3.68378881239537	8.01297697500024	17.93875995373262
C	4.21646426239383	7.48292593138593	16.75477429980673
C	5.21897718066433	8.18352565377983	16.06792608904489
H	5.44849570501447	11.42416924478390	19.29933267551583
H	5.16132449356249	12.10196476627022	17.68742671938984
H	7.29236136477461	9.58537168224527	15.09672057564266
H	6.24600962040692	11.01185617996247	15.21313638939430
H	9.47837280082738	10.59953558683548	15.58812960324128
H	10.99007056065651	11.74262442933013	17.21353438827084
H	10.05422967450593	12.67554497488227	19.34140208884777
H	7.61424890509734	12.45956444872967	19.82452191494961
H	3.75733458886279	9.64723699403101	19.36279595754880
H	2.90898867497929	7.46684828795992	18.48778767344613
H	3.86194148400137	6.51973681487849	16.37234115597744
H	5.65009489056041	7.76228743967204	15.15249224077455

Table A5.24. Cartesian coordinates of a DFT-optimized product complex (PC) for NEB calculations in DHA oxidation reaction.

Co	1.72049477906227	13.13777402922597	12.53749439399056
O	2.03497033713460	12.89530872742032	10.60519108072703
O	-0.01174155876155	13.09058921971008	11.24412939691898
O	0.42244534054804	12.80833087158313	9.09449153615107
N	1.81295123803538	13.34114518001523	14.37680930177624
N	1.74795236570916	11.33426641536184	12.93488592987853
N	1.94678467374303	14.96826687934470	12.52338125681878
N	0.78250477158061	12.92557264134545	10.24800444066790
C	1.82600181853623	12.22979974425602	15.14992627242775
C	1.90544881222023	12.35541198767697	16.53844512927077
C	2.01287549997047	13.63527943876997	17.10037589860561
C	2.07907815776557	14.75979532830645	16.26606628621257
C	1.98694427983274	14.58523845682486	14.88319287631625
C	1.80378966034358	10.93624669996340	14.36535083923785
C	3.10350668164829	10.14965326391876	14.67361883725079
C	0.60255690297529	10.06817233958487	14.81449715692251
C	1.76596613017259	10.31228436735451	11.94575623288833
C	3.00399471999523	9.96746421545008	11.32705524056110
C	3.02167091916463	8.95146161467678	10.35762968243264
C	1.84682433061674	8.29862980099791	9.96918106662408
C	0.62676434850917	8.69330674705001	10.52343329970585
C	0.55805186769969	9.70655939928546	11.49764075164401
C	4.28867038628707	10.69757875655428	11.64725306284688
C	-0.80478587027997	10.14819357016156	11.98503502028808
C	2.11666701814628	15.66233391219506	13.82777596298661
C	3.53369548847472	16.28901374981062	13.93268241923528
C	1.06986025785581	16.77524158728332	14.07513604731765
C	1.97807059683017	15.73984501495811	11.32823263480295
C	3.19332056365047	15.83004612248529	10.58764120882951
C	3.21751737496941	16.59482309273691	9.40968811962035
C	2.06878342095583	17.23864079884656	8.93803928795605
C	0.86363572330103	17.08506411761018	9.62776590495109
C	0.78866754701367	16.32903296566894	10.81206387122483
C	4.44126398968732	15.08792212315901	11.00630728933701
C	-0.56628657075217	16.13233200855497	11.45628088041759
H	1.90296309643418	11.45997652183249	17.16429551525693
H	2.06872094108476	13.75541133789771	18.18688210444109
H	2.20931299972459	15.76210070486703	16.68214955225427
H	3.98882262927293	10.75381083310647	14.43446403138307
H	3.14179841254033	9.86577323775464	15.73674875949141
H	3.12556129984184	9.23123862051701	14.06447271643805
H	0.56123069930009	9.15358233256957	14.20198377702788
H	0.73146174215304	9.76746371290259	15.86912094943301
H	-0.34652165073835	10.61443029936099	14.71316520854570
H	3.97498366048319	8.68706247863960	9.88504725478552
H	1.87868052048095	7.51099544722124	9.20866619859611
H	-0.30463044893220	8.22631866534603	10.18202532142451
H	4.08265452440577	11.67321695706169	12.11373353468520
H	4.93241169521227	10.12091523787321	12.33625494873080
H	4.86656094785099	10.87065630786349	10.72429674802503
H	-1.47087314443178	10.31926216744767	11.12232465228797
H	-0.74181059803559	11.08634913297694	12.55192391056787

H	-1.27885237936246	9.37783071162842	12.62063080462729
H	3.66263867579894	17.01904757462473	13.11665414296269
H	3.65479082086677	16.81724420318803	14.89445639320364
H	4.31002751632067	15.51492814913787	13.85174988519643
H	0.05175617854629	16.36337931187810	14.12609659977777
H	1.28851062031164	17.29485772985177	15.02421785603051
H	1.11979384850624	17.51573505956794	13.26094600584672
H	4.15387696962801	16.66432078402946	8.84373630554198
H	2.10556447516813	17.82767351912267	8.01530425369997
H	-0.05286759626449	17.54025492364350	9.23416161543558
H	4.20067589025501	14.25970706388119	11.68890982275684
H	5.16147351599942	15.74841488285106	11.52227544614524
H	4.94949479383060	14.67319695125063	10.11997663608759
H	-0.93644516273757	17.06751085676805	11.91522687169286
H	-1.30060116972333	15.82603852937111	10.69220065842732
H	-0.53445433055462	15.34830665335227	12.22445584089414
O	6.15879708462629	13.58916933199607	13.67240064806972
O	6.65401988952397	11.62429672485520	14.54194898370127
O	5.24799291513300	13.02710785056176	15.59097617704213
N	5.95697523562644	12.86268680375741	14.61231450730635
C	7.26361325305822	11.10810782309090	17.69190681112171
C	6.43156179439332	11.93700587761607	18.50870861331748
C	4.97328963252805	11.58969181337187	18.70477941210978
C	4.56591543555211	10.19387262512262	18.28984281973976
C	5.43180076716092	9.40833078978027	17.46626980743480
C	6.73469249870710	9.90002268009222	17.13128787952139
C	8.61191692246704	11.50427091940303	17.45757992170424
C	9.12242301567312	12.67055306454224	18.01990696554893
C	8.30210415476002	13.47296235890983	18.83605796479714
C	6.97004657434295	13.10002819540855	19.07156546702176
C	3.32056739466707	9.67075461665323	18.66234630362648
C	2.89924017287991	8.40481726061925	18.22391046734247
C	3.73964596707553	7.63570999977595	17.39676084292541
C	4.98838775644406	8.12893550719312	17.02669869747858
H	4.67631015004406	11.77509908604689	19.75397980479875
H	4.37803550183888	12.30689610328607	18.09983628835707
H	7.39614091827923	9.26386271503096	16.53045782533274
H	6.45336969892700	11.19286527710887	15.41893365464199
H	9.24501316718855	10.87110062459866	16.82647818003563
H	10.16080161461215	12.96094075347884	17.83056043068439
H	8.70037025433174	14.38874115509904	19.28449718862840
H	6.33387739874857	13.73280116921413	19.70125682683562
H	2.66572354599861	10.26276858311514	19.31301825017713
H	1.92116664978509	8.01820802660056	18.52761081517426
H	3.41403830614947	6.65075164880655	17.04750151642130
H	5.65129833359515	7.53159952731340	16.39140599053803

A5.3 Notes and References

1. Adamian, V. A.; D'Souza, F.; Licoccia, S.; Vona, M. L. D.; Tassoni, E.; Paolesse, R.; Boschi, T.; Kadish, K. M., Synthesis, Characterization, and Electrochemical Behavior of (5,10,15-Tri-X-phenyl-2,3,7,8,l2,13,17,18-octamethylcorrolato)cobalt(III) Triphenylphosphine Complexes, Where X = p-OCH3, p-CH3, p-Cl, m-Cl, o-Cl, m-F, o-F, or H. *Inorg. Chem.* **1995,** *34*, 532-540.

2. Will, S.; Lex, J.; Vogel, E.; Adamian, V. A.; Caemelbecke, E. V.; Kadish, K. M., Synthesis, Characterization, and Electrochemistry of ó-Bonded Cobalt Corroles in High Oxidation States. *Inorg. Chem.* **1996,** *35*, 5577-5583.

3. Harmer, J.; Doorslaer, S. V.; Gromov, I.; Broring, M.; Jeschke, G.; Schweiger, A., A Pulse EPR and ENDOR Investigation of the Electronic Structure of a ó-Carbon-Bonded Cobalt(IV) Corrole. *J. Phys. Chem. B* **2002,** *106*, 2801-2811.

4. Carpenter, G. B.; Clark, G. S.; Rieger, A. L.; Rieger, P. H.; Sweigart, D. A., Dithiolenes Revisited: An Electron Spin Resonance Study of some Five-coordinate Cobalt Complexes and the Crystal-Structures of [Co{S2C2(CF3)2}2{P(OPh)3}] and [Co{S2C2(CF3)2}2(PPh3)]. *J. Chem. Soc. Dalton Trans.* **1994,** *20*, 2903-2910.

5. Hong, S.; Pfaff, F. F.; Kwon, E.; Wang, Y.; Seo, M.-S.; Bill, E.; Ray, K.; Nam, W., Spectroscopic Capture and Reactivity of a Low-Spin Cobalt(IV)-Oxo Complex Stabilized by Binding Redox-Inactive Metal Ions. *Angew. Chem. Int. Ed.* **2014,** *53*, 10403-10407.